Jacques-Noël Levadoux
Mohsen M. Baligh

Pore Pressure During Cone Penetration in Clays

MIT Sea Grant
College Program

Massachusetts
Institute of Technology
Cambridge,
Massachusetts 02139

MITSG 80-12

PORE PRESSURES DURING
CONE PENETRATION IN CLAYS

by

Jacques-Noël Levadoux

Mohsen M. Baligh

Sea Grant College Program
Massachusetts Institute of Technology
Cambridge, Massachusetts 02139

Report No. MITSG 80-12
Index No. 80-312-Cim
April 1980

ABSTRACT

Deep quasi-static cone penetration provides a superior exploration tool for soil stratification and identification, especially in offshore work. In order to estimate the shearing resistance and the consolidation and/or permeability characteristics of soils, a better understanding of the mechanism of cone penetration is needed.

This report utilizes the strain path method to investigate the mechanism of cone penetration in clays with the specific objective of estimating pore pressures in the soil during penetration. Deformations and strains are determined assuming that the soil provides no shearing resistance. Deviatoric stresses and shear-induced pore pressures are determined from specially developed soil behavior models and the strain paths of soil elements. Approximate values of the total stresses and pore pressures in the soil are then computed from equilibrium considerations. An evaluation of the predicted pore pressure fields in Boston Blue Clay (BBC) by means of results of special conical pore pressure probes indicate surprisingly excellent agreement for various overconsolidation ratios ($1.3<OCR<3$) after the excess pore pressures, Δu, are normalized by the shaft pore pressure, $(\Delta u)_{sh}$.

Additional interesting aspects of this study include: applicability of cavity expansion approaches to deep penetration and pile installation problems, likelihood of soil hydrofracture due to pile installation, evaluation of a deviatoric stress model capabilities in predicting the undrained behavior of BBC in various laboratory tests, development and evaluation of a shear induced pore pressure model for clays subjected to undrained loading along general strain paths.

ACKNOWLEDGEMENTS

The authors are indebted to their MIT colleagues who contributed to the success of this research: Charles C. Ladd, Professor; Dr. Robert T. Martin, Senior Research Associate; Dr. Amr Azzouz, Research Associate; Jack Germaine, Research Assistant.

The authors are especially indebted to Dr. A. Azzouz for invaluable help in preparing the final manuscript.

This report describes the results of research done as a part of the MIT Sea Grant College Program with support from the Office of Sea Grant in the National Oceanic and Atmospheric Administration, U.S. Department of Commerce, through grant number NA79AA-D-00101, and from the Massachusetts Institute of Technology. The U.S. Government is authorized to produce and distribute reprints for governmental purposes notwithstanding any copyright notation that may appear herein.

RELATED SEA GRANT REPORTS

MIT/Marine Industry Collegium. RISKS AND COSTS FOR OCEAN STRUCTURES: OPPORTUNITY BRIEF #17. MITSG 79-18. 13 pp. $3.50.

MIT/Marine Industry Collegium. TOWARDS IMPROVED TECHNIQUES FOR PREDICTING SOIL STRENGTH: OPPORTUNITY BRIEF #16. MITSG 79-17. 19 pp. $3.50.

Baligh, Mohsen M., Vitoon Vivatrat and Charles C. Ladd. EXPLORATION AND EVALUATION OF ENGINEERING PROPERTIES FOR FOUNDATION DESIGN OF OFFSHORE STRUCTURES. MITSG 79-8. 268 pp. $8.00.

Chryssostomidis, Marjorie. OFFSHORE PETROLEUM ENGINEERING: A BIBLIOGRAPHIC GUIDE TO PUBLICATIONS AND INFORMATION SOURCES. MITSG 78-5. 366 pp. $45.00.

The Sea Grant Marine Resources Information Center maintains an inventory of technical publications. We invite orders and inquiries to:

Marine Resources Information Center
MIT Sea Grant College Program
Massachusetts Institute of Technology
Building E38-302
Cambridge, Massachusetts 02139
(617) 253-5944

FOREWORD

A three-year research program entitled, "In Situ Evaluation of Geotechnical Properties of Marine Sediments," sponsored primarily by the National Oceanic and Atmospheric Administration through its MIT Sea Grant Program, was initiated in July, 1978 by the Constructed Facilities Division of MIT. Matching funds for this research were provided by FUGRO, Inc., Consulting Engineers, and by Instituto Tecnologico Venezolano del Petroleo.

The objective of this research is to provide the geotechnical designer with more reliable methods for estimating in situ properties of marine sediments for foundation design.

The electric (Dutch) cone penetrometer and the conical piezometer probe represent a new generation of in situ testing devices which are particularly valuable offshore because of their simplicity, consistency, and economy.

Previous efforts at MIT concentrated on:

1. Evaluating the capability of cone penetration in establishing stratification, determing variability, and performing soil identification (Baligh et al. 1980), and
2. Estimating the undrained shear strength of clays (Baligh et al. 1978; Baligh and Vivatrat, 1979).

This report investigates the pore pressures that develop in clay deposits due to cone penetration. These pore pressures are

important for understanding the mechanism of penetration and for estimating the coefficients of consolidation and permeability from the pore pressure decay that takes place after interrupting cone penetration (Baligh and Levadoux, 1980).

TABLE OF CONTENTS

LIST OF TABLES

LIST OF FIGURES

CHAPTER 1

INTRODUCTION

Cone penetration testing provides an efficient and reliable method for soil exploration which is especially suited for offshore work. Continuous measurements are obtained as the cone is pushed into the soil and hence the test is valuable for determining stratification and variability in a large variety of soils ranging from dense sands to soft clays. Furthermore, the similarity with pile foundations makes cone penetration results particularly attractive for the design of piles.

Like most in situ tests, cone penetration lacks the ideal conditions offered by laboratory tests, and hence poses significant interpretation problems. However, recent hardware developments (Wissa et al., 1975) enabled reliable measurements of pore pressures generated by cone penetration which, together with the conventional cone resistance measurements, offer a better tool for determining soil stratification, assess soil variability and, in addition, provide more reliable methods for soil identification (Baligh et al., 1980)

This research represents part of a continuing effort at M.I.T. to develop a better understanding of the mechanism of cone penetration in clays, through theoretical

and experimental studies, aimed at providing reliable methods of interpreting cone penetration results especially with regard to engineering soil properties for field predictions and design purposes. Past research (Baligh, et al., 1978) was primarily concerned with the undrained shear strength of clays. This research is primarily aimed at estimating the in situ consolidation and/or permeability characteristics of clays from the pore pressure decay that takes place after steady cone penetration.

This report estimates the excess pore pressures in saturated clays during steady cone penetration. A separate report (Baligh and Levadoux, 1980) presents excess pore pressure dissipation analyses and measurements for estimating the in situ consolidation (and/or permeability) properties of soils from the pore pressure decay that takes place after steady cone penetration is interrupted.

Chapter 2 describes the application of the "strain path method" to deep steady cone penetration in clays. The "strain path method" (Baligh et al., 1978) is an approximate method for systematically elucidating and solving problems which are basically strain-controlled. In this approach, the strain path of selected elements is estimated from a deformation pattern (velocity field) chosen on the basis of kinematic requirements. Laboratory tests are then conducted or, alternatively, appropriate constitutive laws used, to determine the deviatoric stresses

in these elements when subjected to the estimated strain paths. The octahedral (isotropic) stresses are then estimated by integrating the equilibrium equations. Finally, Chap. 2 discusses the limitations of the method and suggests means to assess the accuracy of solutions.

Chapter 3 performs the first step in the strain path method by determining the displacements and strains in saturated clays due to deep steady cone penetration (assuming that the soil offers no shearing resistance, i.e., behaves as an incompressible ideal fluid) and compares predictions with limited laboratory model test data.

Chapter 4 generalizes an analytical soil behavior model (Iwan, 1967; Mroz, 1967; and Prevost, 1977) capable of incorporating the difficult anisotropic, elastoplastic, path-dependent stress-strain-strength properties of inviscid saturated clays subjected to undrained loading conditions in order to account for the complicated strain paths imposed by cone penetration. Predictions of the model are evaluated by comparisons with laboratory test results on Boston Blue Clay.

Chapter 5 reviews existing methods for predicting the excess pore pressures generated by undrained shearing of saturated clays, proposes a new analytical model to estimate the pore pressures during undrained straining of clays and evaluates predictions with laboratory test results.

Chapter 6 determines the excess pore water pressures in the soil during steady cone penetration based on the strain path method (Chapter 2), the strain paths corresponding to an ideal fluid (Chapter 3), the deviatoric stress model (Chapter 4) and the shear induced pore pressure model in Chapter 5 using soil parameters appropriate to normally consolidated Boston Blue Clay. Predictions are compared to field measurements of penetration pore pressures at different locations on the cone and the shaft behind it as well as measurements around driven piles in different soils with various overconsolidation ratios.

Finally, Chapter 7 summarizes the main conclusions reached in this report.

CHAPTER 2

THE STRAIN PATH METHOD

2.1 INTRODUCTION

The prediction of foundation performance is one of the most challenging aspects of geotechnical engineering. Because of the complexity of soil behavior and soil variability, complete solutions to practical problems are not available and the engineer relies on empirical and/or simplified rational approaches. For example, the prediction of foundtion settlement on sand deposits by means of the standard penetration test results (N-values) represents an empirical method (Terzaghi and Peck, 1967) whereas predictions according to the stress path method (Lambe, 1967) are based on a more rational, yet simplified, method. Reliable empirical methods require very large data bases and are difficult to adapt to slightly different or new situations. Simplified methods require engineering judgement in selecting the input parameters and in interpreting the results.

The "stress path method" (Lambe, 1967) provides an integrated and systematic framework for elucidating and solving stability and deformation problems. The application of the stress path method to deformation problems consists of the following steps: 1) estimate the stress history at selected locations in the soil mass and the stress increments caused by the foundation on the basis of equilibrium

requirements; 2) conduct laboratory tests on samples obtained from those locations in order to subject the soil to the same stress path expected in the actual problem, and; 3) integrate the strains obtained from laboratory tests to predict displacements.

The stress path is an approximate method because, even under ideal conditions of sampling and testing capabilities involving an infinite number of samples, the compatibility of strains is not satisfied.* A compatible strain field would be obtained if and only if the estimated stress increments were identical to those actually experienced in the field. The latter depends on soil behavior and cannot, therefore, be known a priori.

The stress path method proved successful for predicting the performance of surface structures, e.g., excavations, shallow foundations, natural slopes, earth dams, etc.,... (Lambe and Marr, 1979). The success of the stress path method in solving shallow foundation problems** is due to the essentially stress-controlled characteristic of surface problems where stress increments can be predicted with sufficient accuracy by simplified methods (e.g., analytical or numerical elastic analyses).

On the other hand, attempts to use the stress path method

---

*The deformations depend on the path of integration of the strains.

**Where the depth of the foundation soil below ground surface is "small" compared to its lateral extent.

for deep foundations encountered major problems caused by the difficulties of estimating incremental stresses. Lambe and Horn (1965) utilized the stress paths obtained from triaxial extension tests (assuming $\Delta\sigma_v = 0$ and $\Delta\sigma_\theta = \Delta\sigma_r$) to provide insight into the problem of pile installation in clays. D'Appolonia (1971) and Hagerty and Garlanger (1972) applied this insight to predict pore pressures caused by pile installation. Vijayvergia and Focht (1972) extended the concept further and relied on the "Rankine passive earth pressure" to formulate the very popular semi-empirical λ-method for pile design in clays, especially offshore. The Rankine passive state follows directly from the use of triaxial extension tests, but actually has little in common with the stress state in the soil caused by pile driving because: 1) the vertical stress can change significantly (i.e., $\Delta\sigma_v \neq 0$) and, more importantly, 2) the tangential stress, σ_θ, is far from being equal to the radial stress, σ_r, during soil shearing (i.e., $\Delta\sigma_\theta \neq \Delta\sigma_r$).

In deep penetration problems, experimental observations (Rourk, 1961; Vesic, 1963; Robinsky and Morrison, 1964; Szechy, 1968; and others) indicate that soil deformations caused by penetration of a rigid indenter are similar in different soils even though the penetration resistance can be drastically different (i.e., soil stresses are very different).

This implies that deep steady cone penetration problems are basically strain-controlled and that the associated deformations are not very sensitive to soil behavior. Baligh (1975) outlined an approximate method that he later called the "strain path method" (Baligh et al., 1978) for solving these problems. In this approach, the strain path of selected elements is estimated from a deformation pattern (velocity field) chosen on the basis of kinematic requirements. Laboratory tests are then conducted or, alternatively, appropriate constitutive laws used, to determine the deviatoric stresses in these elements when subjected to the estimated strain paths. The octahedral (isotropic) stresses are then estimated by integrating the equilibrium equations.

Figure 2.1 compares the strain and stress path methods to identify their strong similarities. As indicated in Fig. 2.1, the strain path method is approximate because the estimated stresses will not, in general, satisfy the equilibrium requirements, unless the estimated strain field is identical to the actual one.

In this Chapter, the application of the strain path method to deep steady cone penetration in clay is described. The limitations of the method are discussed and means to assess the accuracy of the solution are proposed.

2.2 APPLICATION OF THE STRAIN PATH METHOD TO DEEP STEADY CONE PENETRATION IN CLAY

2.2.1 General Description

Deep steady cone penetration is an axisymmetric steady state problem i.e., for an observer moving with the cone, the deformation pattern, the strain and stress fields in the soil do not vary with time. Accordingly, by using a cylindrical coordinate system, the process of cone penetration is reduced to a flow problem where soil particles move along streamlines around the cone (Fig. 2.2). A solution to the problem consists of the strains and the stresses of soil elements along different streamlines.

Figure 2.3 describes the steps for evaluating stresses and pore pressures in the soil due to deep steady cone penetration in clay by means of the strain path method. These steps, to be later reviewed in details, consist of:

1) Estimate a velocity field* satisfying the conservation of volume (or mass) requirement and the boundary conditions.
2) From the velocity field determine the soil deformations by integration along streamlines. Compare with experimental model or field test results (if possible).

---

*The velocity field describes the velocity of soil particles as they move around the cone.

3) Compute the strain rates, $\dot{\varepsilon}_{ij}$, along the streamlines by differentiating the velocities with respect to the spacial coordinates.

4) Integrate the strain rate, $\dot{\varepsilon}_{ij}$, along streamlines to determine the strain path (ε_{ij}) of different soil elements.

5) Estimate the initial stresses, $(\sigma_{ij})_o$, and initial pore pressures, u_o, in the soil prior to cone penetration.

6) Compute the deviatoric stresses, s_{ij} ($= \sigma_{ij} - \delta_{ij}\, \sigma_{oct}$)* and the shear induced pore pressures, Δu_s, along streamlines by means of:

   a) a model to determine s_{ij} for a given strain path (ε_{ij}), and;

   b) a model to determine Δu_s for a given strain path (ε_{ij}).

7-a) From equilibrium considerations, compute the total stresses, σ_{ij} ($= s_{ij} + \delta_{ij}\, \sigma_{oct}$), given the deviatoric stresses, s_{ij}. This requires the determination of the octahedral stresses, σ_{oct}.

7-b) From s_{ij} and Δu_s, compute the effective stresses, $\bar{\sigma}_{ij}$.

---

*δ_{ij} = Kronecker delta: = 0 when $i \neq j$; = 1 when $i = j$ and, $\sigma_{oct} = 1/3\ \sigma_{ii}$.

8) From σ_{oct} and Δu_s determine the pore pressure u.

The important steps in the method (Fig. 2.3) are discussed below.

2.2.2 Velocity Field

The strain path method hinges on the assumption that soil deformations during deep cone penetration can be estimated with a reasonable degree of accuracy. Figure 2.3 recommends that deformations be obtained from velocities by integration rather than the more obvious alternative of estimating deformations (e.g., from laboratory penetration tests) and then derive velocity and strains by differentiation. This avoids the significant errors caused by the process of numerical differentiation associated with the limited accuracy of existing deformation measurements.

Most of the existing experimental results consist of crude visual observations of deformations during cone penetration by means of photographs (Rourk, 1961; Randolph et al., 1979). More precise measurements obtained by X-ray techniques are currently conducted at Cambridge University, England (Randolph, 1979). Arthur and Phillips (1975) evaluated the accuracy of the X-ray technique under ideal conditions (providing maximum accuracy) by analyzing the same radiograph twice, i.e., a case of uniform zero deformations and strains. Using a 10 x 12 grid of lead shots spaced at 10 mm, they obtain an average vertical strain equal to zero, thus showing that no consistent error occured in deformation measurements.

However, the standard deviation of strains was 0.3%. This means that when the results are based on measurements of a lead shot at a single location (as in non uniform fields), there is a 32% chance of obtaining an error in strain in excess of $\pm$0.3% and a 5% chance of obtaining an error in strain in excess of $\pm$0.6% (assuming a normal distribution of data about the mean). Such errors might be acceptable in some soils subjected to special loading conditions but, in other cases, such strains are sufficient to reach the peak strength and hence cannot, in general, be tolerated. In penetration experiments in clays, the X-ray technique is further complicated by:

a) the inevitable variability of the soil in the model test. This adds to the errors in the estimated deformation and strain fields caused by penetration which are highly non uniform;

b) the limited size of the clay container. The diameter of the consolidometer containing the clay must be small ($\simeq$ 20 cm) to require a reasonable exposure time and yield sufficient image sharpness. On the other hand, the radius of the consolidometer must be large compared to that of the model pile in order to minimize the boundary effects, and;

c) the density of the lead shots in the clay. In order to measure the large strain gradients accurately, a large number of lead shots is required,

especially near the cone tip. On the other hand, a high density of lead shots might cause excessive changes in the mechanical properties of the clay (because of interaction between lead shots and clay).

Consequently, it is recommended that soil deformations during steady cone penetration in clay obtained from experimental measurements be used to evaluate velocity fields rather than to estimate strain fields.

In this study, strains are derived from velocity fields obtained for an inviscid incompressible (or perfect) fluid. Chapter 3 describes the analytical methods used to derive these velocity fields which, for clays, will be approximate. Solutions involving materials with more complex behavior such as viscous fluids are still under investigation at M.I.T.

2.2.3 Stress-Strain Relationships

The strain paths of soil elements during cone penetration are very complicated (see Chapter 3) and cannot be duplicated by existing laboratory tests. Therefore, a soil model is used herein to determine soil stresses during penetration. For reasons discussed in Chapter 4, an incremental total stress model was considered appropriate for the undrained penetration problem. During undrained shearing, the behavior of clays is not affected by the octahedral normal total stress, $\sigma_{oct} (= \frac{1}{3} \sigma_{ii})$ and, hence, only the deviatoric components of

stresses, s_{ij}, need to be considered:

$$s_{ij} = \sigma_{ij} - \sigma_{oct}\,\delta_{ij} \qquad (2.1)$$

in which σ_{ij} is the total stress tensor and δ_{ij} is the kronecker delta ($\delta_{ij} = 1$ for $i = j$, and; $\delta_{ij} = 0$ for $i \neq j$).

By following a soil element along its streamline, the soil model thus provides the deviatoric stress path corresponding to its strain path. This process is repeated along a number of streamlines and the deviatoric stress field is thus evaluated at as many discrete points as desired.

2.2.4 Pore Pressure-Strain Relationships

In order to evaluate the pore pressure distribution in the soil during steady undrained cone penetration, the excess pore pressure, Δu, is separated into two components: the first corresponds to changes in octahedral normal total stress, $\Delta\sigma_{oct}$, and the second results from the shear deformations of the soil, Δu_s (see Chapter 5):

$$\Delta u = \Delta\sigma_{oct} + \Delta u_s \qquad (2.2)$$

$\Delta\sigma_{oct}$ is obtained from equilibrium considerations (see next section) and the shear-induced pore pressure, Δu_s, is evaluated by means of a new model (similar to the deviatoric stress model) as a function of the strain path of soil elements.

2.2.5 Effective Stresses, Total Stresses and Pore Pressures

The changes in effective stresses, $\Delta\bar{\sigma}_{ij}$, are evaluated from the changes in deviatoric stresses, Δs_{ij}, and the shear

induced pore pressure, Δu_s:

$$\Delta\bar{\sigma}_{ij} = \Delta s_{ij} - \Delta u_s \cdot \delta_{ij} \qquad (2.3)$$

Evaluation of the total stresses, σ_{ij}, and pore pressures, u, requires determination of the octahedral normal total (or isotropic) stress, σ_{oct}. This is achieved by integrating the equilibrium equations as described in Appendix A.

The changes in pore pressure, Δu, and total stresses, $\Delta\sigma_{ij}$, are given by:

$$\Delta u = \Delta\sigma_{oct} + \Delta u_s \qquad (2.4)$$

and

$$\Delta\sigma_{ij} = \Delta s_{ij} + \Delta\sigma_{oct}\ \delta_{ij} \qquad (2.5)$$

2.3 DISCUSSION

The strain path method is an approximate method to systematically simplify and analyze problems where the strains are principally governed by kinematic requirements and, thus, are not very sensitive to material properties. The expansion of a cylindrical cavity in an incompressible cross-anisotropic infinite medium represents one problem where solutions by the strain path method are exact* because soil strains are independent of material properties. In more complicated problems (e.g., cone penetration in clays) where strains are "slightly" dependent on material properties, solutions based on simplified strain fields are approximate. Like all

*Provided an appropriate soil model is available.

approximate solutions, results of the strain path method require treatment of the following:

1) The source of approximation (i.e., why is the solution approximate?) in order to provide a better understanding of the reasons behind the resulting errors and, hence answer the following questions (2) and (3) rationally.

2) The effects of approximation (i.e., how important are the simplifications made). This requires criteria and methods to evaluate the degree of approximation.

3) The methods to improve solutions (i.e.; how to reduce the effects of simplifications).

1) Source of approximation

In the strain path method, the simplification in the strain field is the source of deviation from exactness.* Appendix A shows that the deviatoric stress field predicted by means of the strain path method is the exact solution to a cone penetration problem where a fictitious field of body forces is applied.

2) Effects of approximation

The degree of approximation of predictions obtained by the strain path method can be evaluated analytically by

*Provided an appropriate soil model is available.

comparing:

a) the octahedral total normal stresses, σ_{oct}, obtained by integration along different paths (see Chapter 6), and;

b) the magnitude of the fictitious body forces compared to the stress gradients (see Appendix A). Small fictitious body forces indicate better results.

Ultimately, the effects of approximations and the practical value of the method are judged by comparing predictions with laboratory and/or field measurements. For example, application of the method to cone penetration can be evaluated by comparing:

a) the predicted vs. experimental deformations in model tests (say), and;

b) the predicted vs. measured point resistance and pore pressures at different locations (on the tip, on the shaft behind the tip and in the soil around the cone) by means of field measurements (see Chapter 6). However, these comparisons are complicated on one hand by experimental difficulties and on the other hand by the selection of an adequate soil model and the appropriate soil parameters required to perform predictions.

3) Methods of improving solutions

Approximate solutions obtained by the strain path method can be improved by successive iterations on the velocity field until the stress field is sufficiently close to satisfying the equilibrium requirements. A possible iterative procedure consists of: a) evaluate the fictitious body forces from the deviatoric stress field; b) estimate a new velocity field (utilizing the same idealized material, e.g., an ideal fluid) after taking the fictitious body forces field into consideration (with a negative sign), and; c) repeat the necessary steps to evaluate a new stress field (see Fig. 2.3).

In this study, no attempt was made to establish the validity of this iterative procedure or to prove its superiority over other possible techniques. Therefore, solutions presented subsequently correspond to an initial velocity field without corrections (iterations).

2.4 SUMMARY

Deep steady cone penetration in clay is essentially a "strain-controlled" problem where strains and deformations are primarily imposed by kinematic requirements. For this type of problem, Baligh (1975) proposes an approximate method of solution called the "Strain path method". This method is based on concepts similar to the "stress path method" (Lambe, 1967) and consists of four basic steps: a) estimate the initial stresses; b) estimate an approximate strain field satisfying conservation of volume, compatibility and boundary

velocity requirements; c) evaluate the deviatoric stresses at a selected number of elements by performing laboratory tests on samples subjected to the same strain paths or, alternatively, by using an appropriate soil behavioral model, and; d) estimate the octahedral (isotropic) stresses by integrating the equilibrium equations.

In this chapter, application of the strain path method to deep steady cone penetration is discussed in details (Fig. 2.3). It is recommended to estimate the velocity fields from solution of cone penetration in simple materials (e.g., perfect fluid). Because of the complexity of the strain paths of soil elements during cone penetration, the deviatoric stresses and shear-induced pore pressures are evaluated by means of behavioral soil models. The deviatoric stress field predicted by means of the strain path method is the exact* solution to a cone penetration problem where a fictitious field of body forces is applied. Consequently, the octahedral (isotropic) normal total stresses obtained by integration of the equilibrium equations and neglecting the fictitious body forces is path dependent. Evaluation of the degree of approximation of the solution obtained with the strain path method is achieved by comparing: a) the predicted soil deformations to experimental measurements; b) the magnitude of the fictitious body forces to the stress

*Provided the soil model is adequate.

gradients; c) the isotropic stress fields obtained by integration along different paths, or; d) stress and pore pressure predictions with laboratory and/or field measurements.

Stress Path Method	Strain Path Method
APPLICATIONS	
Surface Problems	Deep Problems
STEPS	
1. Estimate initial stresses 2. Estimate incremental stresses 3. Perform stress path tests on samples (or use adequate soil model) to obtain strains at selected locations. 4. Estimate deformations by integrating strains	1. Estimate initial stresses 2. Estimate incremental strains 3. Perform strain path tests on samples (or use adequate soil model) to obtain deviatoric stresses at selected locations. 4. Estimate octahedral (isotropic) stresses by integrating equilibrium equations.
APPROXIMATION	
In step 2, stresses are approximate thus leading to strains not satisfying compatibility requirements. i.e., deformations in step 4 depend on strain integration path.	In step 2, strains are approximate thus leading to stresses not satisfying all equilibrium conditions. i.e., octahedral stresses in step 4 depend on equilibrium integration path.

Figure 2.1 Comparison of stress path and strain path methods.

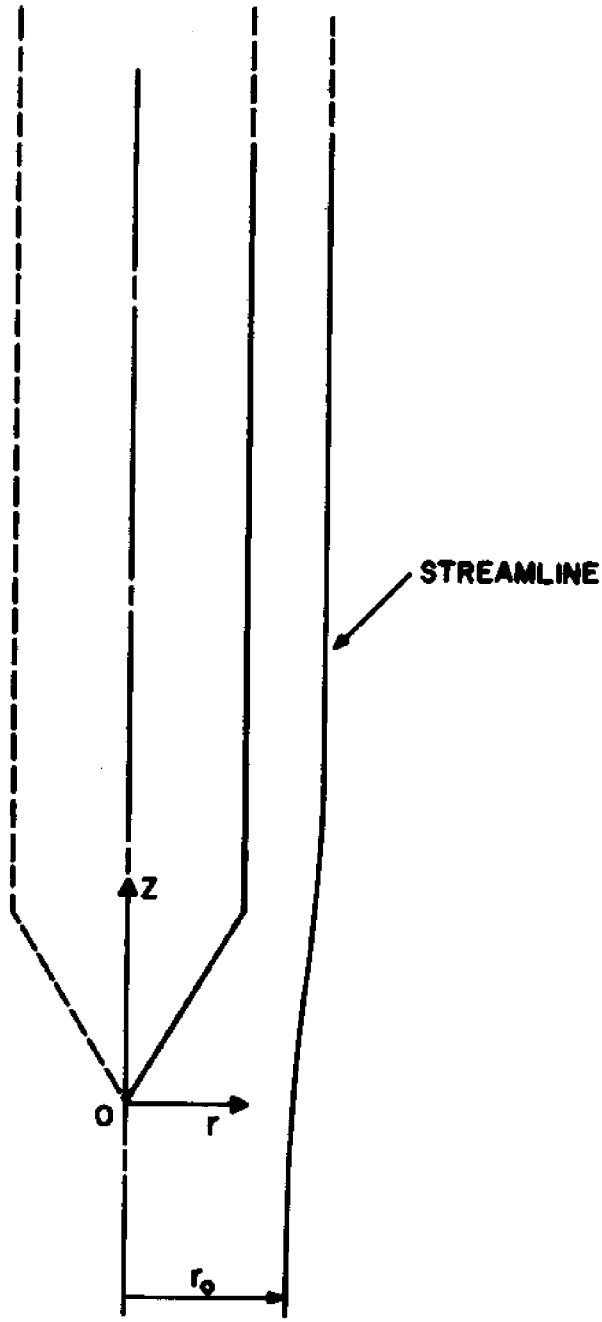

Figure 2.2 Problem geometry and coordinate system for deep steady cone penetration.

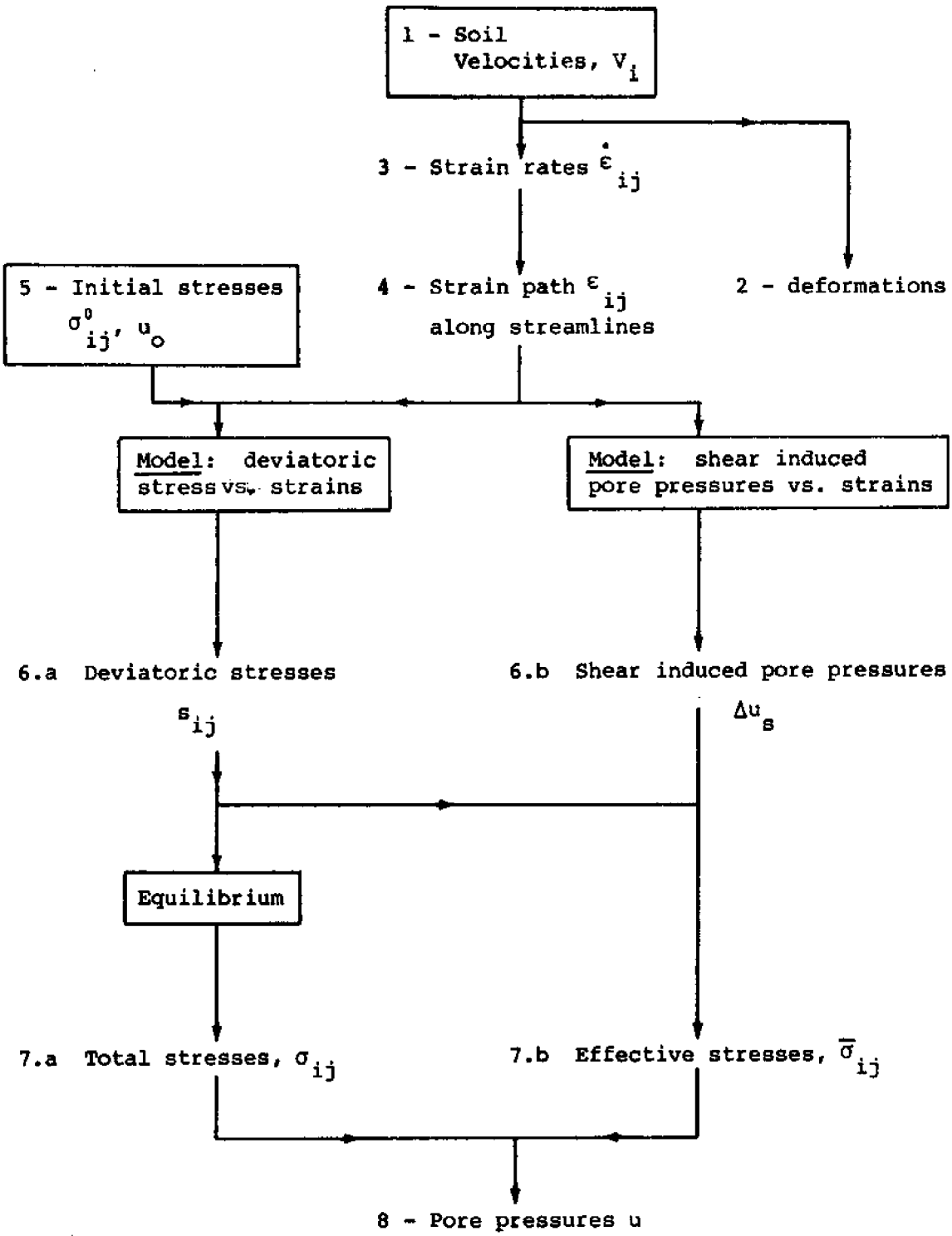

Figure 2.3 Application of the strain path method to deep steady cone penetration: Flow Chart.

CHAPTER 3

STRAIN FIELD

This chapter presents numerical solutions for the irrotational steady flow of an incompressible inviscid fluid around a cone penetrometer (or pile) under conditions of axial symmetry (i.e., properties and flow characteristics are independent of the tangential coordinate). Distortions and strains are obtained by superimposing the effect of a suitable distribution of sources and sinks to a uniform flow. This method of solution has been described by Weinstein (1948), Rouse (1959), Shames (1962), and others and was used to determine the flow around the so-called "Rankine-body" (ovoidal body of revolution). Problem formulation is carried out using Eulerian axes where field variables are expressed in terms of coordinates fixed in space (with respect to the cone).

3.1 STREAM FUNCTIONS

The method of sources and sinks uses the superposition principle by adding the stream functions corresponding to combinations of sources and sinks to that of a uniform flow, Fig. 3.1. For steady incompressible axisymmetric flow, the stream function $\psi(r,z)$ is a convenient mathematical expression describing different particle paths (streamlines) when ψ = const. For the sake of simplicity, sources and sinks will hereafter be referred to as sources with a (+ ve)

sign to indicate a source and a (- ve) sign to indicate a sink. Sources are located on the axis of the cone as shown in Fig. 3.1. In cylindrical coordinates (r,z), the stream function ψ_o for a uniform flow of velocity V_o parallel to the z-axis is given by:

$$\psi_o(r,z) = - \tfrac{1}{2} V_o r^2 \qquad (3.1)^*$$

The stream function ψ_s corresponding to a line source of length ℓ, with a total strength m (uniformly distributed over its length) and located at $z = z_s$ is given by:

$$\psi(r,z) = m \left(1 + \frac{\rho^B - \rho^T}{\ell}\right) \qquad (3.2)^*$$

in which:

$$\rho^B = \{(z - (z_s - \ell/2))^2 + r^2\}^{\frac{1}{2}} \qquad (3.3)$$

and

$$\rho^T = \{(z - (z_s + \ell/2))^2 + r^2\}^{\frac{1}{2}} \qquad (3.4)$$

The geometry of the cone penetrometer is prescribed by a finite number of "body points" which, for simplicity have the same z-coordinate as the line source centers, Fig. 3.1. The stream function at the i^{th} body point (r_i, z_i) due to the superposition of the uniform velocity V_o (at infinity) and of the n line sources $(0, z_k)$ distributed

---

*Stream functions are completely defined except for an additive constant which is herein dropped to cancel the stream function along the streamline represented by the negative z-axis.

along the symmetry axis is given by:

$$\psi_i = -\tfrac{1}{2} V_o\, r_i^2 + \sum_{k=1}^{n} m_k \left(1 + \frac{\rho_{ik}^B - \rho_{ik}^T}{\ell_k}\right) \qquad (3.5)$$

in which ℓ_k and m_k are the length and strength of the k^{th} line source, respectively, and ρ_{ik}^B and ρ_{ik}^T are the distances of the i^{th} body point to the end points of k^{th} line source. The body points are located on the boundary streamline and thus the stream function must vanish at their locations:

$$\sum_{k=1}^{n} m_k \left(1 + \frac{\rho_{ik}^B - \rho_{ik}^T}{\ell_k}\right) = \tfrac{1}{2} V_o\, r_i^2 \quad ; \quad i = 1,2,\ldots,n \qquad (3.6)$$

Equations 3.6 represent n linear equations which can be easily solved numerically to obtain the source strengths $m_1, \ldots, m_n$. The stream function ψ at any location (r,z) is then given by the following equations:

$$\psi(r,z) = -\tfrac{1}{2} V_o\, r^2 + \sum_{k=1}^{n} m_k \left(1 + \frac{\rho_k^B - \rho_k^T}{\ell_k}\right) \qquad (3.7)$$

$$\rho_k^B = \left[(z - (z_k - \ell_k/2))^2 + r^2\right]^{\frac{1}{2}} \qquad (3.8)$$

$$\rho_k^T = \left[(z - (z_k + \ell_k/2))^2 + r^2\right]^{\frac{1}{2}} \qquad (3.9)$$

3.2 VELOCITY FIELD AND DEFORMED GEOMETRY

The velocity components V_r and V_z in the meridian plane (the third velocity component, V_θ, vanishes because of axial symmetry) are determined from the stream function ψ by the expressions:

$$V_r = \frac{1}{r}\frac{\partial \psi}{\partial z} \; ; \quad V_z = -\frac{1}{r}\frac{\partial \psi}{\partial r} \tag{3.10}$$

Substituting (3.7) into (3.10), we get:

$$V_r = \frac{1}{r}\sum_{k=1}^{n} \frac{m_k}{\ell_k}\left[\frac{z - (z_k - \ell_k/2)}{\rho_k^B} - \frac{z - (z_k + \ell_k/2)}{\rho_k^T}\right] \tag{3.11}$$

$$V_z = V_o - \sum_{k=1}^{n} \frac{m_k}{\ell_k}\left[(\rho_k^B)^{-1} - (\rho_k^T)^{-1}\right] \tag{3.12}$$

Deformations are obtained from velocities by numerical integration. A material point M_i with initial coordinates r_i° and z_i° (far enough in front of the tip) has, at any time t, the coordinates:

$$r_i^t = r_i^\circ + \int_o^t V_r(r_i^\tau, z_i^\tau)\, d\tau \tag{3.13}$$

$$z_i^t = z_i^\circ + \int_o^t V_z(r_i^\tau, z_i^\tau)\, d\tau \tag{3.14}$$

Another method could have been used to determine streamlines by solving the implicit equation:

$$\psi(r,z) = -\tfrac{1}{2} V_o r_o^2 \qquad (3.15)$$

where $\psi(r,z)$ is given by Eq. 3.7, and r_o is the radial coordinate of the given streamline far ahead of the cone. By varying z, and solving Eq. 3.15 for r, different streamlines are determined for various r_o. However, in order to determine strain fields, the numerical integration procedure (Eqs. 3.13 and 3.14) proved more convenient.

3.3 STRAIN FIELD

In an orthogonal cartesian frame of reference, the components of the rate of deformation tensor, D_{ij} (also called stretching tensor), are defined in terms of the gradients of the velocity components, V_i, by the expression (see Malvern, 1969):

$$D_{ij} = \tfrac{1}{2}\left(\frac{\partial V_i}{\partial x_j} + \frac{\partial V_j}{\partial x_i}\right) \qquad (3.16)^*$$

In penetration problems considered herein, this tensor can be directly obtained by differentiating Eqs. 3.11 and 3.12. In order to determine the large strains associated with penetration problems, we introduce the natural strain increment tensor:

---

*Cylindrical coordinates will later be introduced for applications to penetration problems.

$$d\,\varepsilon_{ij} = D_{ij} \cdot dt \qquad (3.17)$$

and, for convenience, define the natural strain components ε_{ij}, at any time t by the expression:

$$\varepsilon_{ij} = \int d\varepsilon_{ij} = \int D_{ij} \cdot dt \qquad (3.18),$$

where the integration is conducted by following the material point through its path along a streamline. Estimates of the natural strains will prove very useful in visualizing the degree of straining in the soil due to penetration, and in portraying the strain history of different soil elements.

3.3.1 Rate of Deformation

Using cylindrical coordinates, the non-vanishing components of the rate of deformation tensor, D_{ij}, in axisymmetric problems are given by (Malvern, 1969):

$$D_{rr} = \frac{\partial V_r}{\partial r} \; ; \; D_{zz} = \frac{\partial V_z}{\partial z} \; ; \; D_{\theta\theta} = \frac{V_r}{r} \quad \text{and;}$$

$$D_{rz} = \tfrac{1}{2}\left(\frac{\partial V_r}{\partial z} + \frac{\partial V_z}{\partial r}\right) \qquad (3.19)$$

Substituting Eqs. 3.11 and 3.12 into Eq. 3.19, the components of the rate of deformation tensor are obtained, Table 3.1.

3.3.2 Strain Field

Integration of Eq. 3.18 is analytically intractable and was, therefore, performed numerically by following a streamline (from a starting point far ahead of the cone) and

computing natural strain increments corresponding to small time intervals dt. The natural strains in a soil element, at a given time t, are then simply obtained by adding the components of natural strain increments.

3.3.3 Computer Program

In order to compute deformations, strain-increments and strains, a computer program was developed. A listing of this program (written in Fortran IV) together with a description of its use are given in Appendix B. Input data consist of the cone geometry (half angle and radius), the cylinder length and the number of sources over the cone and cylinder lengths (sources are equally spaced along the cone and cylinder axes), respectively. A radius of curvature can also be assigned to smooth the cone-cylinder transition. The program first solves the linear equations 3.6, using the elimination method, to determine the sources strength. For different streamlines, deformations, strain increments and strains are then computed using Eqs. 3.13, 3.14, 3.17 and 3.19, respectively, with the forward integration method. Special program modes are available to check stability and accuracy of solutions.

3.3.4 Graphical Representation of Strain Paths

In axially symmetric problems, the (natural) strains are described by four non-vanishing components: ε_{rr}, ε_{zz}, $\varepsilon_{\theta\theta}$ and ε_{rz}. Bearing in mind that the soil treated herein is incompressible, the three normal strains must satisfy the condition of no volume change:

$$\varepsilon_{rr} + \varepsilon_{zz} + \varepsilon_{\theta\theta} = 0 \qquad (3.20)^*$$

Therefore, the strain tensor can be uniquely defined by three components (or three linearly independent combinations of the components) only. In order to develop a graphical representation of different states of strain and follow the strain path of various soil elements, we utilize the E_i - space, $\{E_1, E_2, E_3\}$ (Prevost, 1978) defined as:

$$E_1 = \varepsilon_{zz} \; ; \; E_2 = \frac{1}{\sqrt{3}} (\varepsilon_{\theta\theta} - \varepsilon_{rr}) \text{ and, } E_3 = \frac{2}{\sqrt{3}} \varepsilon_{rz} \qquad (3.21)$$

Figure 3.2 shows a strain point in the three-dimensional E_i - space where its distance from the origin is proportional to the octahedral shear strain γ_{oct}:

$$[E_1^2 + E_2^2 + E_3^2]^{\frac{1}{2}} = \sqrt{2}\, \gamma_{oct} \qquad (3.22)$$

$$\gamma_{oct} = {}^1/_3 [(\varepsilon_{rr} - \varepsilon_{zz})^2 + (\varepsilon_{zz} - \varepsilon_{\theta\theta})^2 + (\varepsilon_{\theta\theta} - \varepsilon_{rr})^2 + 6\, \varepsilon_{rz}^2]^{\frac{1}{2}} \qquad (3.23)$$

The value of γ_{oct} is a good measure of the level of straining to which a soil element is subjected. Furthermore, the strain paths of conventional strain controlled tests move along the three axes (triaxial test along E_1, pressuremeter test

---

*Eq. 3.20 is applicable to infinitesimal strain. However, in view of the definition of the natural strains ε_{ij} as expressed by Eq. 3.18 and, since $D_{rr} + D_{zz} + D_{\theta\theta} = 0$ (for imcompressible material, Table 3.1) Eq. 3.20 is also valid for large values of ε_{ij}.

along E_2, and Direct Simple Shear test along E_3, Fig. 3.2).

3.4 RESULTS

This section presents results of analyses conducted to estimate deformations and strains in the soil caused by penetrometers (or piles) with cylindrical shafts having the same diameter as the conical tip. Penetrometers with 18° tips were analyzed using 20 sources along the cone axis and 80 sources along the cylinder axis (the cylinder length is 4 times the cone length). Penetrometers with 60° tips were analyzed using 10 and 120 sources, respectively, and a cylinder length 12 times that of the cone. In order to achieve numerically stable solutions, the geometry of existing Dutch cone penetrometer with 60° tips was slightly altered by introducing a circular arc with a radius of curvature equal to 3 times the cylinder radius at the cone-cylinder transition. The effect of the smooth transition between cone and cylinder is believed to alter the deformations and strains of the soil in its vicinity but not at some distance away. The integration of rates of deformation was started at a distance of 200 radii in front of the cone apex with an integration inteval initially equal to 10 radii and decreasing to 2% of the cylinder radius ahead of the pile. From thereon, the integration interval was kept constant at 2%. Further reduction of the above integration interval showed no noticeable change in the results.

3.4.1 Predicted Deformations

The predicted deformation patterns around cones with 18° and 60° tip angles are shown in Figs. 3.3 and 3.4, respectively. The deformed grids illustrate the magnitude and distribution of the shear strains ε_{rz} (which are the easiest shear strains to visualize). The sharp (18°) cone cuts its way through the soil and causes smaller strains than the blunt (60°) cone which causes severe straining in its vicinity. The present analysis assumes a frictionless soil-probe interface and, hence, is believed to underestimate actual soil distortions.

Figures 3.5 and 3.6 illustrate soil displacement paths, at selected initial locations, due to cone penetration for 18° and 60° tip angles, respectively. Clearly, the soil is monotonically deformed radially away from the cone. On the other hand, the soil is initially pushed down in the direction of penetration and is then pushed up after passage of the cone base.

3.4.2 Experimental Deformation and Comparison with Predictions

A thorough check on the accuracy of the predicted deformations is prevented by the lack of well controlled experimental data. Figure 3.7 shows the deformation pattern obtained by Rourk (1961) due to penetration of a flat ended model pile into bentonite (with a water content of 300%). A rigid conical wedge of soil located ahead of the pile can

be easily detected. The wedge moves with the pile and has an apex angle of approximately 90°. Soil distortions near the pile are more pronounced than the predicted deformations for a 60° tip, Fig. 3.4.

In comparing theoretical predictions and experimental deformations, in Fig. 3.7 we note that:

(a) The rigid soil wedge moving with the model pile is much blunter ($\simeq 90°$) than the maximum tip angle ($= 60°$) analyzed herein. The analyses have shown that soil straining increases with the cone angle; and, (b) the experiments reported by Rourk were conducted in a container made of stiff cardboard jackets with a diameter equal to six times that of the model pile. Such close boundaries reduce soil movements in the downward and radial directions but have a more important effect on the stresses and penetration resistance, especially for undrained conditions.

More recently, better experimental results were reported by Randolph et al. (1979). The deformed grid reproduced in Fig. 3.8a is obtained by jacking a "C" shaped half closed-ended pile into one-dimensionally consolidated kaolin against a transparent perspex wall which allows photographs to be taken. The displacement field, displacement path, and radial displacements in Figs. 3.8b, 3.8c and 3.8d, respectively, are obtained by comparing the deformed grid (Fig. 3.8a) with the initial grid before penetration. The accuracy of the measurements can be assessed in Fig. 3.8d

where a scatter of ±10% is observed for the radial displacements. The experimental results indicate that:

(1) the general deformation trends are as predicted. In particular, the conservation of volume requirement governs the radial displacements behind the tip. Furthermore, the predicted tendency for the particles to return to their initial elevation after passage of the tip (Figs. 3.5 and 3.6) is also confirmed by the experimental results shown in Fig. 3.8.c, especially for soil particles with an initial radius $r_o > 1.25$ R (R = pile radius), and;

(2) the measurements are not sufficiently accurate to provide neither the displacements close to the pile axis nor the strains at any location in the field.

A new generation of experiments is currently underway at Cambridge University where the pile is modelled by a cylinder ended with a conical tip and pushed along the axis of a large diameter cylinder of clay. These experiments which include deformation measurement by the X-Ray technique and pore pressure monitoring should provide a better experimental insight into the cone penetration problem.

3.4.3 Strain Paths

Section 3.3.3 indicates that the strain paths of soil elements due to cone penetration can be conveniently described in the E_i strain space (Eqs. 3.21). Figures 3.9 and 3.10 show the strain path projections (in the E_i-space) of three soil elements (located at r_o/R = 0.2, 0.5 and 1.0;

where r_o is the initial radial coordinate of the element and R is the cylinder radius) for 18° and 60° tip angles, respectively. These figures illustrate the complexity of the strain path caused by cone penetration. Of particular interest is the strain path projection on the $\{E_1, E_3\}$ plane which illustrate strains totally neglected by the cavity expansion technique often used to analyse deep penetration problems. For the sake of comparison and illustration, Figs. 3.9 and 3.10 also show the directions and typical magnitudes (at the end of the test) of strain paths encountered in common laboratory and field tests.*

Comparison of Figs. 3.9 and 3.10 reveals that the 18° and 60° cone tips produce the same type of strains in the soil with the latter causing much higher levels of E_1 and E_3-strains. The E_1- strain ($= \varepsilon_{zz}$) is produced by triaxial tests* (TC or TE) and the E_3- strain ($= \frac{2}{\sqrt{3}} \varepsilon_{rz}$) is produced by the direct simple shear (DSS) test.* However, the predominant strain is the E_2- strain [$= \frac{1}{\sqrt{3}} (\varepsilon_{\theta\theta} - \varepsilon_{rr})$] produced by the pressuremeter test* and hence provides some justification for current approaches of modelling cone (and pile) penetration by means of the expansion of a cylindrical cavity (Esrig et al., 1977, 1978, 1979; Carter et al, 1978; Kirby et al., 1977, 1979; etc....). Further examination of Figs. 3.9 and 3.10 indicates that:

*Under ideal testing conditions.

1. Strain levels: The strains caused by cone penetration are much higher than normally encountered in laboratory tests (≃ 20% in TC, TE and DSS) and in the pressuremeter test (≃ 10%). Since the peak strength is reached at relatively low strains (≃ 0.35% in TC, ≃ 10% in TE for Boston Blue Clay; see Chapter 4) the post-peak behavior of the clay appears to be of importance in determining cone penetration resistance;

2. Straining reversals: The permanent (residual) strains caused by cone penetration are not monotonically reached but all three strains (E_1, E_2 and E_3) reverse direction after soil elements pass the base of the cone. The magnitude of the strain reversal is significant (5 to 20% next to the cone and can, therefore, have an important effect on both the cone resistance and the residual stresses left in the soil after penetration (see Chapter 4).

3.4.4 Strain Contours

Contours of the radial normal strain*, ε_{rr}, vertical (longitudinal) normal strain, ε_{zz}, meridional shear strain, ε_{rz}, maximum shear strain $\gamma_{max} = \frac{1}{2}(\varepsilon_1 - \varepsilon_3)$** and octahedral shear strain, γ_{oct} (Eq. 3.23) are given in Figs. 3.11 through 3.15, for cones with 18° and 60° tip angles. These contours

---

*These strains are the natural strains obtained by integration of the natural strain increments; Eq. 3.18.

**ε_1 and ε_3 are the major and minor principal strains, respectively.

show the magnitude and the extent of straining due to steady cone penetration and further indicate the complexity of the strain field around the tip.* The blunt cone (60°) causes higher level of strains than the sharp cone (18°), especially in the soil ahead of the tip. On the other hand, behind the tip, the strain contours become parallel to the shaft axis, thus indicating that a uniform condition has been reached. These residual strain contours which are very similar for blunt (60°) and sharp (18°) cones are compared to strains predicted by the expansion of a cylindrical cavity** in the upper part of Figs. 3.11, 3.14 and 3.15. Further examination of the strain contours shows that:

(1) The radial normal strains, ε_{rr} (Fig. 3.11) are moderately tensile ahead of the cone and then become compressive behind the vicinity of the cone apex. The residual strains ε_{rr} in soil elements close to the shaft (up to a distance of one half the shaft radius) are slightly underpredicted by the cylindrical cavity expansion whereas the inverse occurs in soil elements further away from the axis;

(2) The vertical (longitudinal) normal strains ε_{zz}, shown in Fig. 3.12 are nonexistent during cavity expansion. These strains are generally small (as compared to the radial

---

*The strain field for which contours are drawn in Figs. 3.11 through 3.15 is limited to 5 R in the radial direction, 4 R ahead and 10 R behind the cone apex where most of the large straining occurs (R = shaft radius).

**The cylindrical cavity is expanded from a zero radius to a final radius equal to that of the cone penetrometer shaft.

strain magnitudes in Fig. 3.11), and compressive ahead of the cone base. A concentration of tensile ϵ_{zz} occurs in the vicinity of the cone base where a sharp change in velocity directions takes place. The vertical normal strains, ϵ_{zz} require large distances behind the cone to attain residual values (especially at some distance from the shaft). These residual strains are positive (compressive) near the shaft, decrease with radius, reach a minimum negative (tensile) value and then increase again to vanish at large distances from the shaft.

(3) The meridional shear strains, ϵ_{rz}, shown in Fig. 3.13 are nonexistent during cavity expansion. In spite of a frictionless soil-probe interface ϵ_{rz} strains are large in the vicinity of the cone (where the soil particles experience a change in direction of motion), are sharply reduced after passing the cone base and, the residual values are quite significant along the shaft, especially for the 60° cone.

(4) Contours of maximum shear strain, γ_{max} (Fig. 3.14) and octahedral shear strain, γ_{oct} (Fig. 3.15) are very similar and provide a good indication of the average shear strain experienced by soil elements during cone penetration. The residual values are virtually identical when predicted by simple cavity expansion, except in the immediate vicinity of the shaft where the amount of shearing is slightly larger during cone penetration (especially for the 60° cone).

3.4.5 Strain Rate Contours

The strength and stiffness of clays depend on the rate of undrained shearing. Ladd et al. (1977) estimate that the undrained shear strength measured in triaxial compression tests on sensitive and plastic clays increases 10 ± 5% per log cycle of strain rate for typical strain rates employed in the laboratory. Since cone penetration causes large strains concentrated in narrow zones, an adequate estimate of the strain rates during cone penetration is important when results are compared with laboratory tests typically sheared at a rate of axial strain $\dot{\varepsilon}_v$ = 0.5%/hr (which corresponds to an octahedral shear strain rate $\dot{\gamma}_{oct}$ = 0.35%/hr)*. Using a cone radius R = 1.78 cm (i.e., a projected area of 10 cm^2), and a penetration velocity of 2 cm/sec corresponding to the present standard adopted for cone penetration tests (Report of the Subcommittee on Standardization of Penetration Testing in Europe, 1977), contours of the octahedral shear strain rate, $\dot{\gamma}_{oct}$, are given in Fig. 3.16. The dotted areas in Fig. 3.16 represent locations where $\dot{\gamma}_{oct}$ is larger than 5000%/hr. Clearly, cone penetration shears very large volumes of soil at much higher rates than normally encountered in laboratory strength tests.

3.5 DISCUSSION AND CONCLUSIONS

The method of "sources and sinks" of the potential theory is utilized to predict the velocity, strain and deformation

* $\gamma_{oct} = \frac{1}{\sqrt{2}} \cdot \varepsilon_v$ in triaxial tests.

fields caused by the deep steady penetration of cones (or piles) with 18° and 60° tips. The principal advantage of this prediction method is to provide analytic expressions for the strain rates, everywhere in the soil, which can be accurately integrated to obtain strains and deformations. This avoids the important errors associated with differentiating displacement fields to obtain the strains.* However, the proposed method presents the following difficulties:

a) The number of possible source configurations (i.e., the number and the locations of sources along the cone and cylinder axes) is infinite and, therefore, numerous trials are required to obtain an acceptable solution. Numerical instability occurs when the sources are too closely spaced.

b) The method is best suited for slender bodies (i.e., sharp cones) and encounters difficulties when discontinuities in slope away from the symmetry axis (i.e., at the base of the cone) are encountered. The 60° conical tip** is probably the maximum cone angle that can be treated by this method without the need for a ring source located at the slope discontinuity (i.e., at the cone-cylinder transition). However, in the present study, the considerable additional computational effort did not seem justified, in view of the small expected improvement in the solution.

---

*As in the case of experiments where deformations are measured and the strains are then computed.

**To obtain an acceptable solution, the 60° cone was slightly modified by fitting a circular arc (with a radius equal to 3 times that of the cylinder) at the cone-cylinder transition.

Due to the lack of reliable experimental results, predictions cannot be evaluated accurately. However, qualitative comparisons with experimental results obtained by Rourk (1961) and Randolph et al., (1979) indicate that the predicted deformations are reasonable.

The predicted strain paths and the strain contours reflect the complexity of the cone penetration process and emphasize that: (1) no single laboratory test can adequately impose the strain paths encountered during cone penetration; (2) strains, stresses and pore pressures predicted by the cylindrical cavity expansion theory can lead to important errors because of: (a) strain reversals that take place behind the tip and; (b) the shear strain ε_{rz} and the vertical (longitudinal) normal strain ε_{zz} which are neglected by cavity expansion. Therefore, in order to predict the point resistance and the stress field in the soil caused by steady cone penetration, a comprehensive soil model (Chapter 4) is needed.

$$D_{zz} = \sum_{k=1}^{n} \frac{m_k}{\ell_k} \left[\frac{\Delta z_k^T}{(\rho_k^T)^3} - \frac{\Delta z_k^B}{(\rho_k^B)^3} \right]$$

$$D_{rr} = \frac{1}{r^2} \cdot \sum_{k=1}^{n} \frac{m_k}{\ell_k} \left[\frac{\Delta z_k^B \cdot ((\rho_k^B)^2 + r^2)}{(\rho_k^B)^3} - \frac{\Delta z_k^T \cdot ((\rho_k^T)^2 + r^2)}{(\rho_k^T)^3} \right]$$

$$D_{\theta\theta} = \frac{1}{r^2} \cdot \sum_{k=1}^{n} \frac{m_k}{\ell_k} \left[\frac{\Delta z_k^T}{\rho_k^T} - \frac{\Delta z_k^B}{\rho_k^B} \right]$$

$$D_{rz} = r \cdot \sum_{k=1}^{n} \frac{m_k}{\ell_k} \left[(\rho_k^T)^{-3} - (\rho_k^B)^{-3} \right]$$

In which : $\rho_k^B = [(\Delta z_k^B)^2 + r^2]^{\frac{1}{2}}$; $\rho_k^T = [(\Delta z_k^T)^2 + r^2]^{\frac{1}{2}}$

and ; $\Delta z_k^B = z - (z_k - \ell_k/2)$; $\Delta z_k^T = z - (z_k + \ell_k/2)$

Notes: See Fig. 3.1 for definitions;
signs according to Soil Mechanics conventions.

Table 3.1 Components of the Rate of Deformation Tensor.

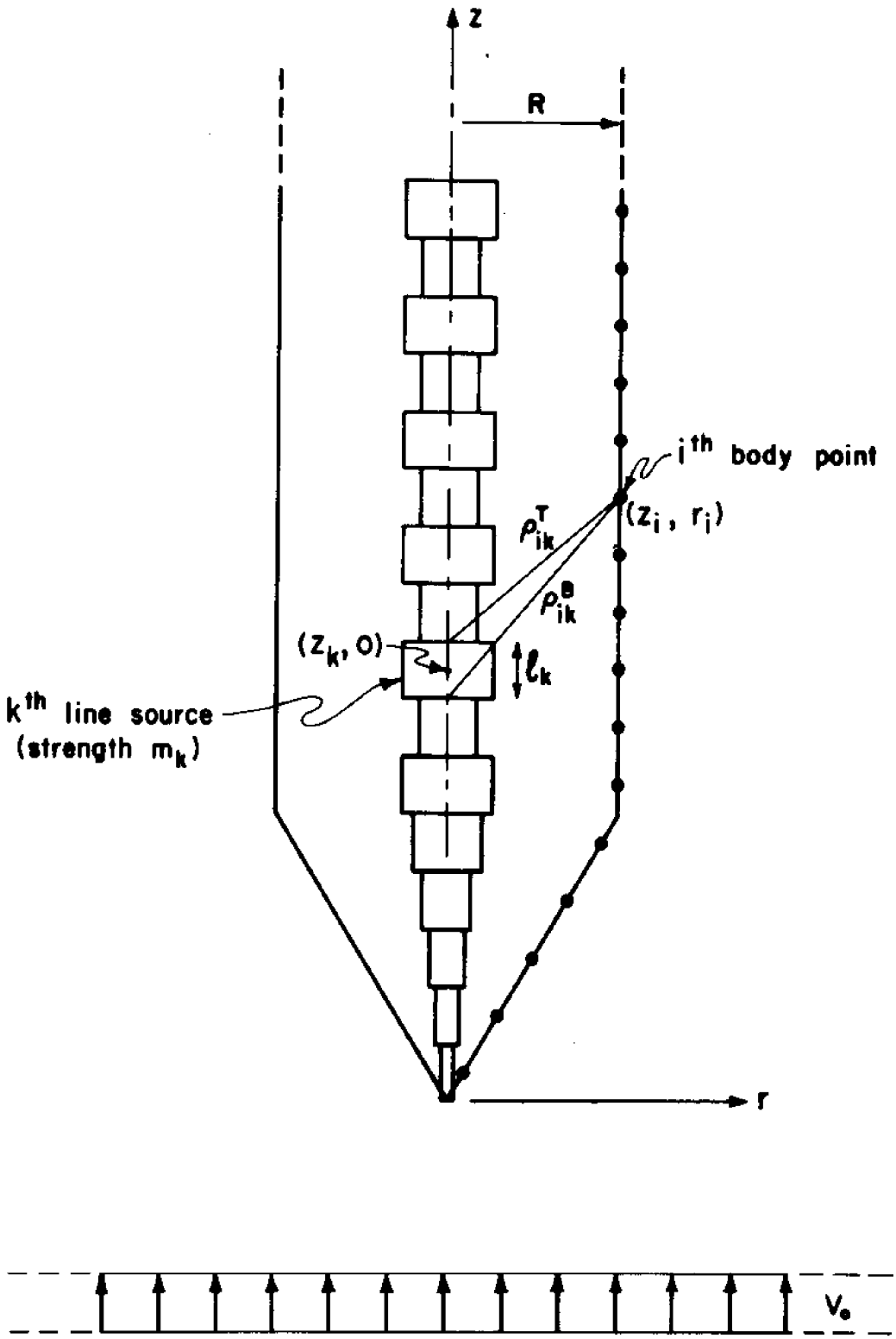

Figure 3.1 Problem description

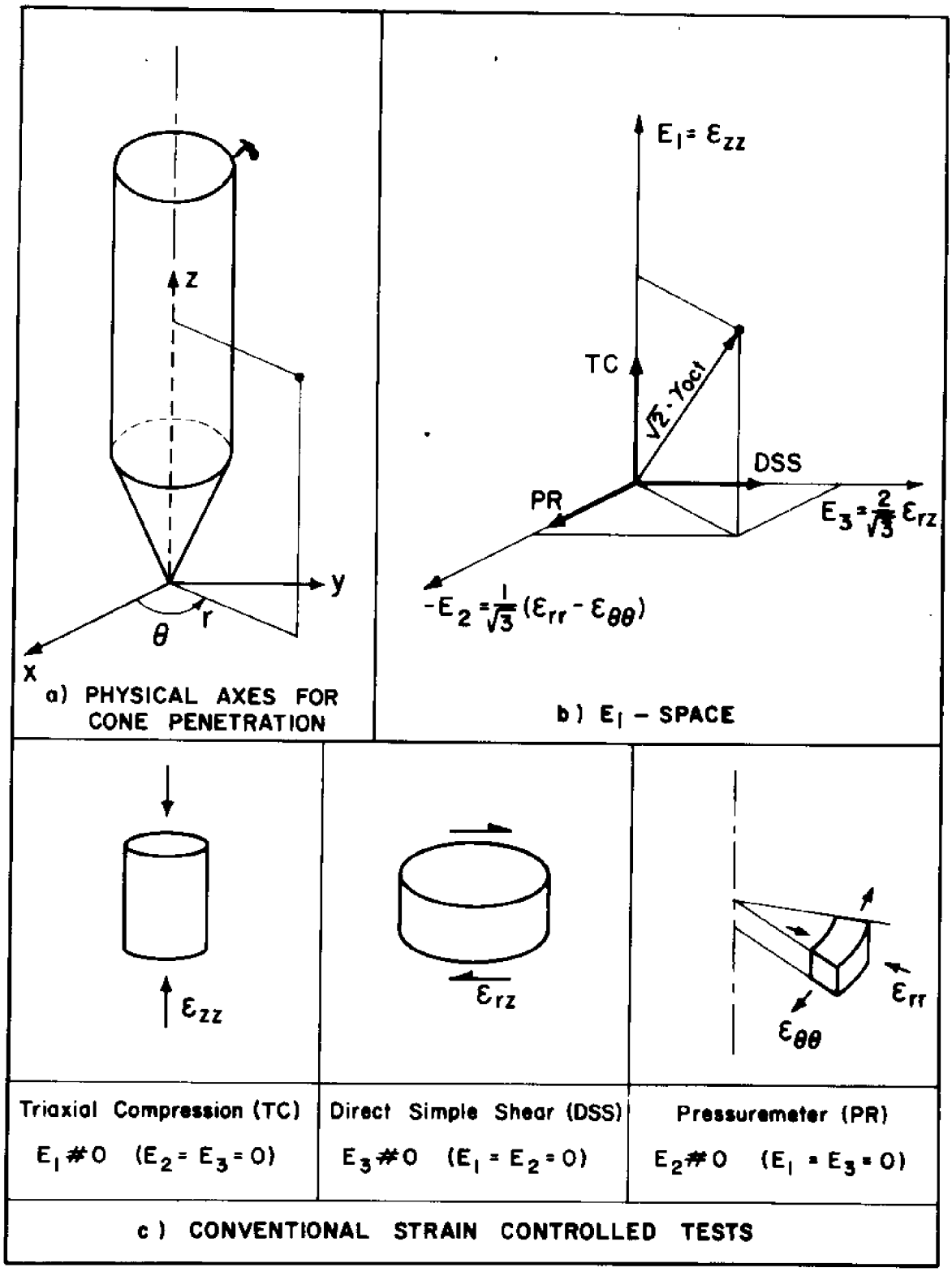

Figure 3.2 Strain representation in the E_i-space

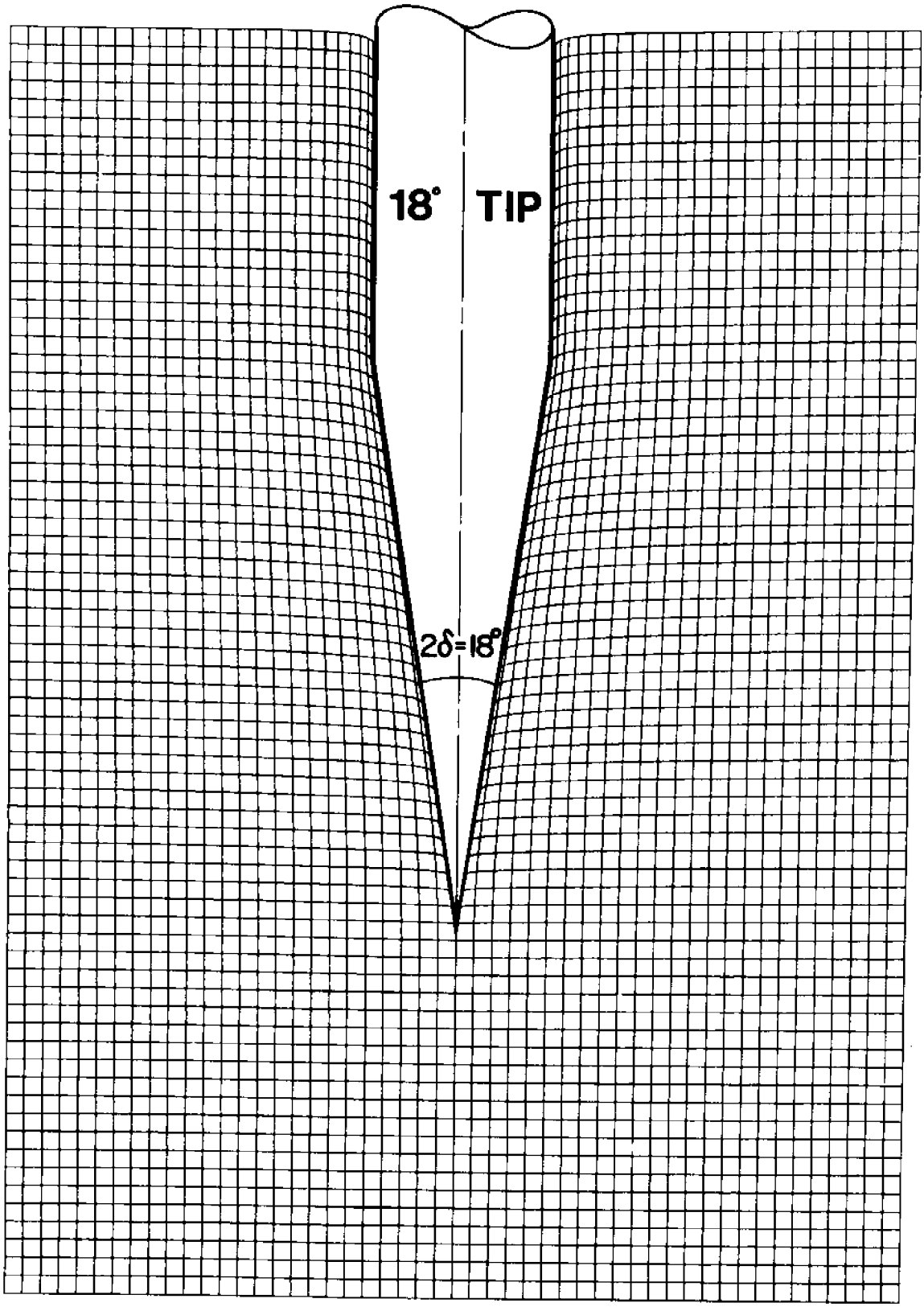

Figure 3.3 Predicted deformation pattern around an 18°cone

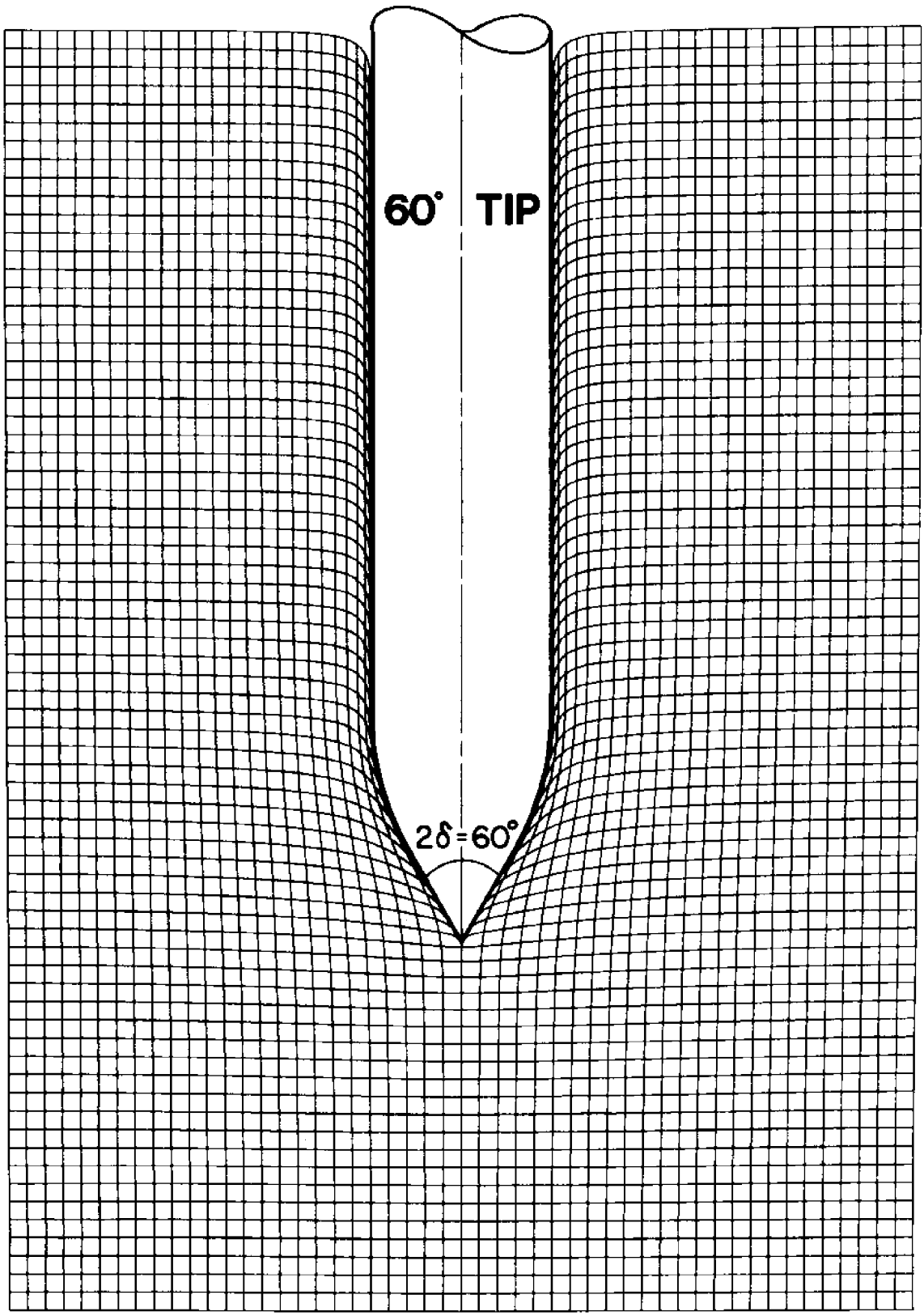

Figure 3.4 Predicted deformation pattern around a 60° cone

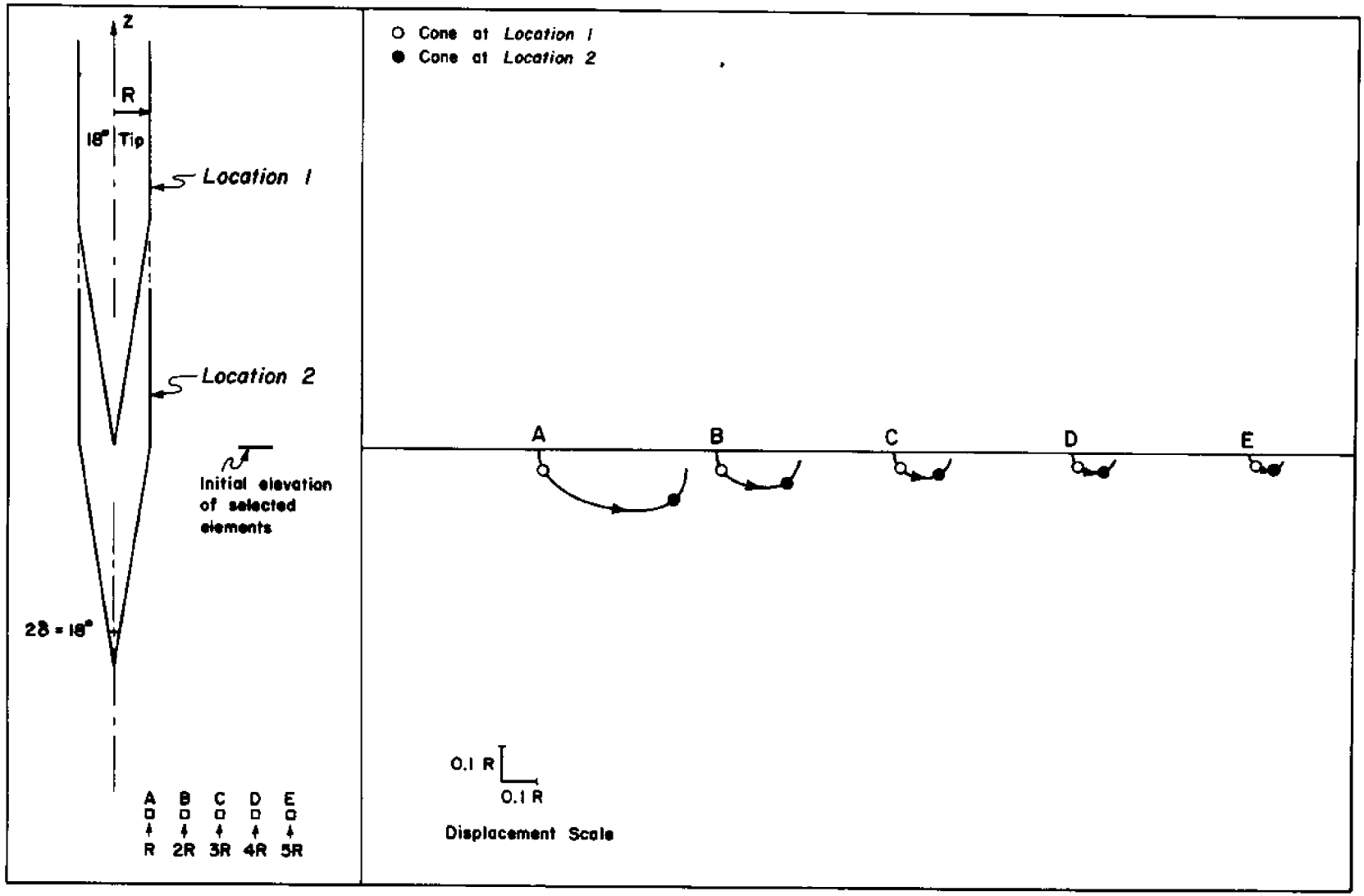

Figure 3.5 Soil displacements during penetration of an 18° cone

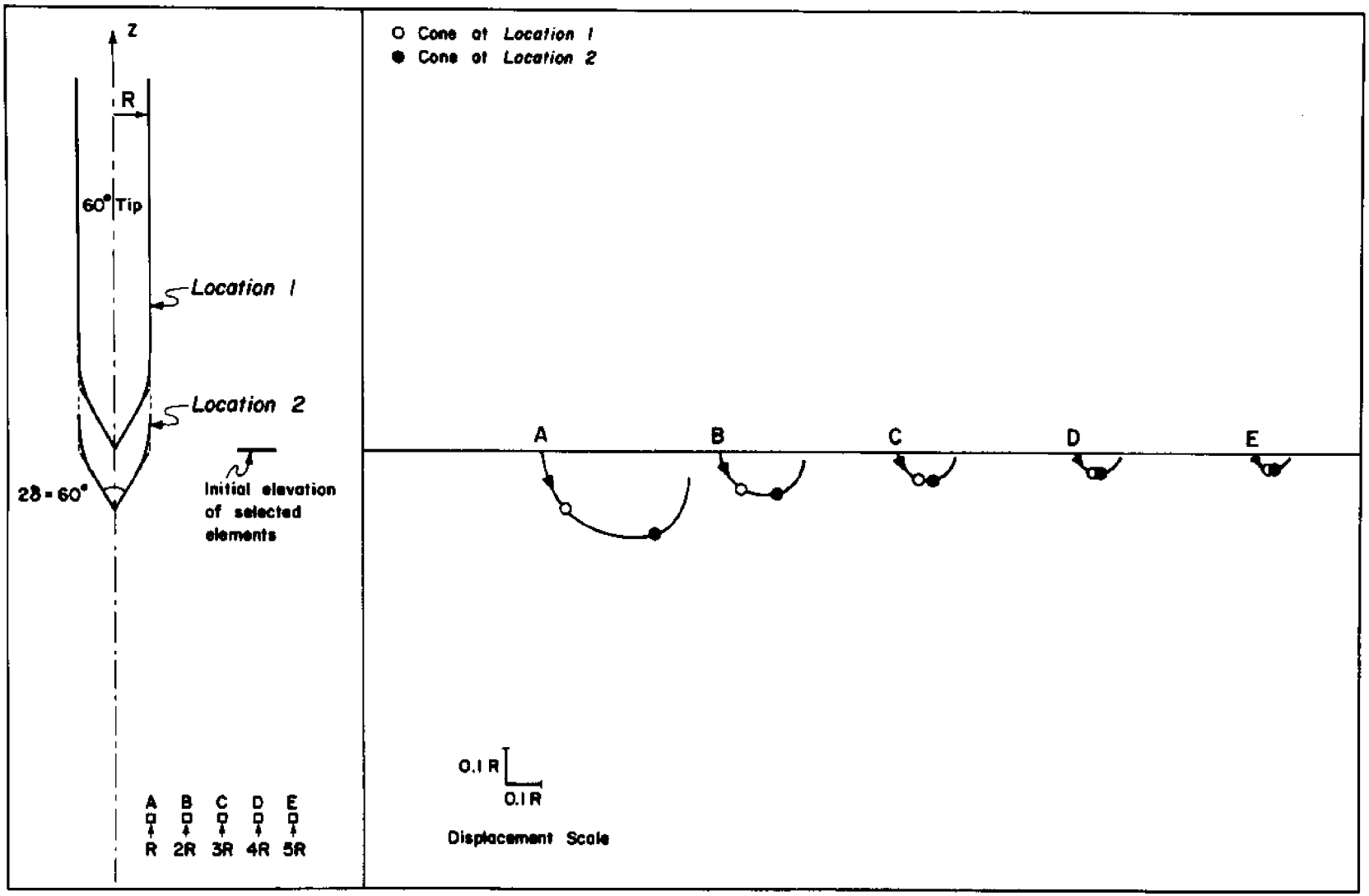

Figure 3.6 Soil displacements during penetration of a 60° cone

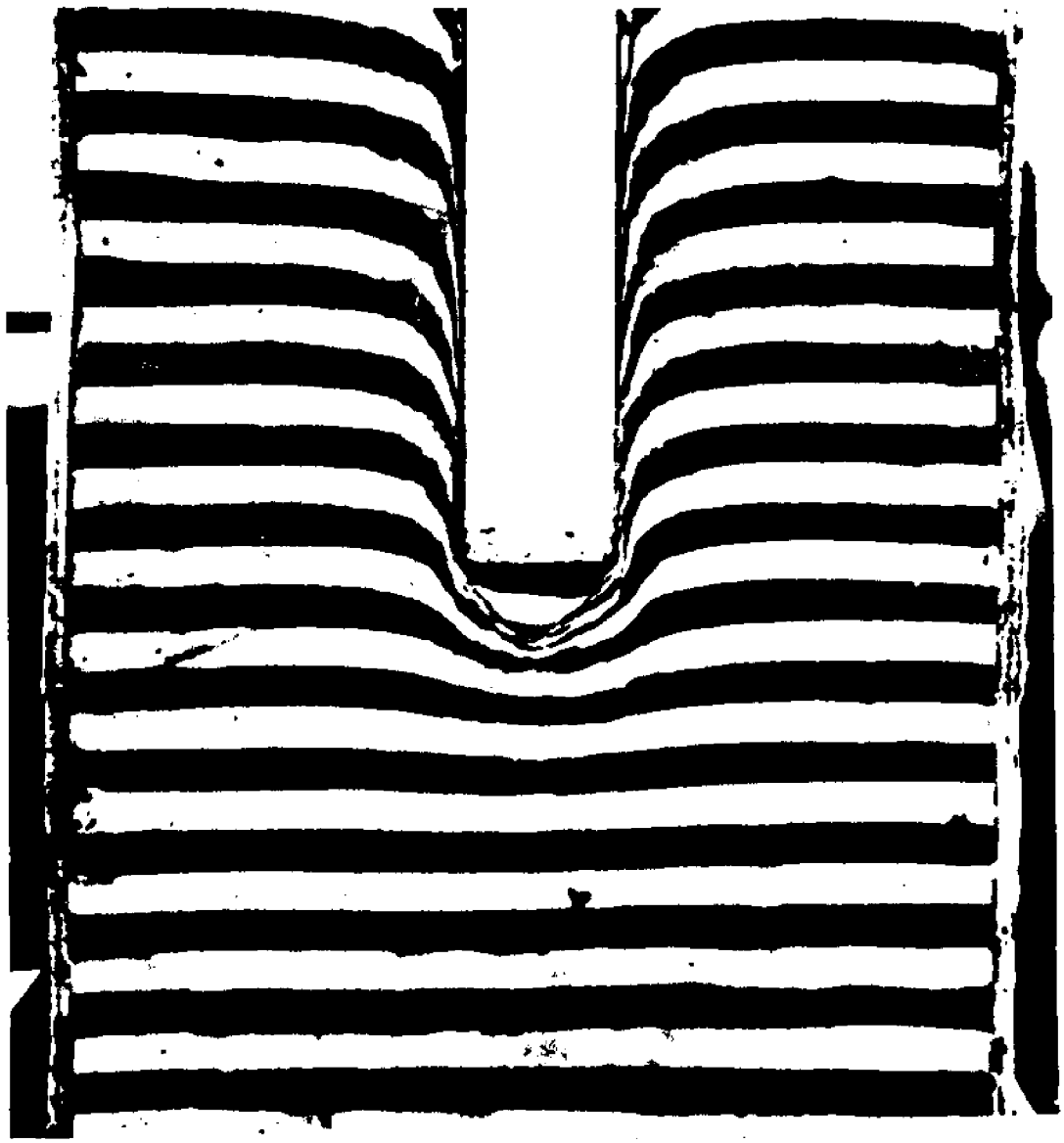

Figure 3.7 Experimental deformation pattern in bentonite due to cone penetration of a flat-ended model pile (after Rourk, 1961)

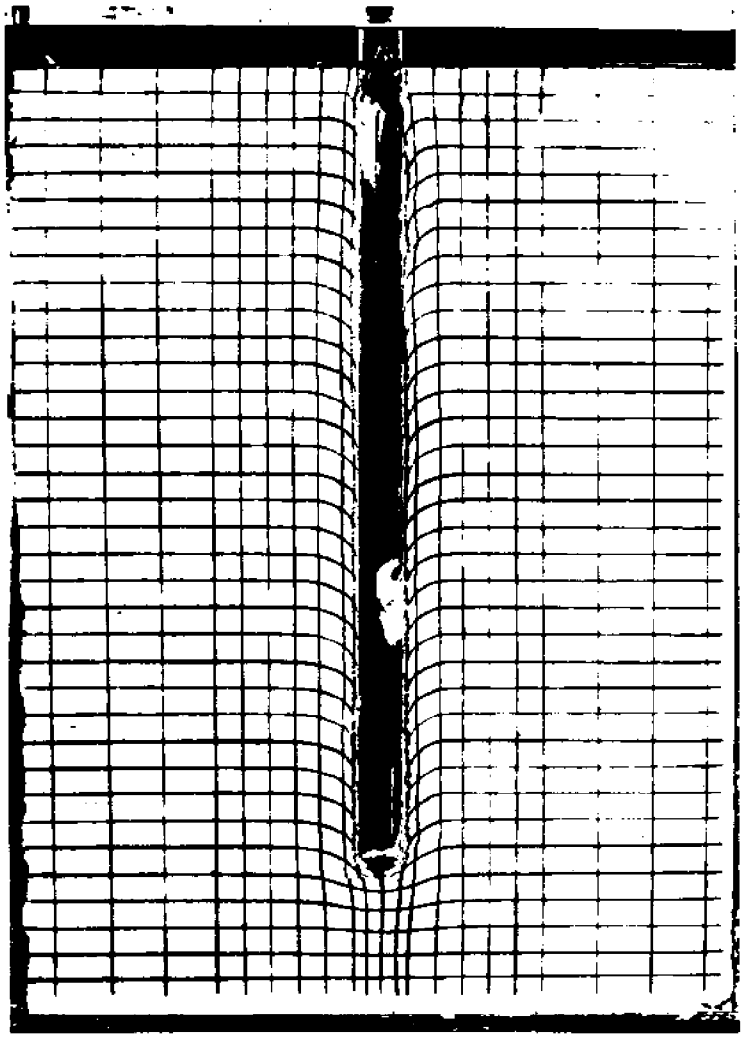

a) deformed grid

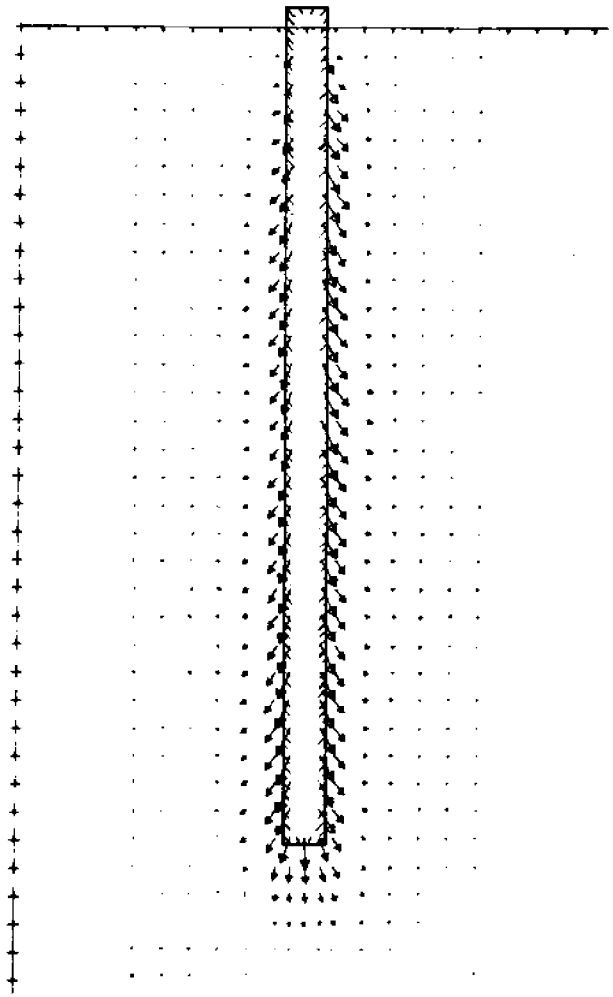

b) displacement field

Figure 3.8 Experimental results of a model pile test in kaolin (after Randolph et al., 1979)

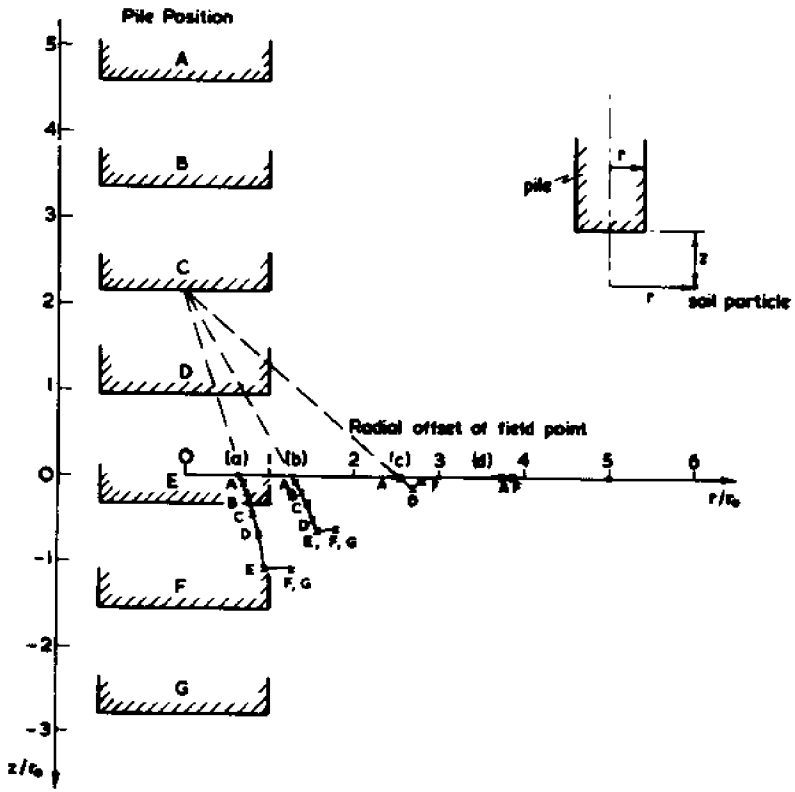

c) displacement paths

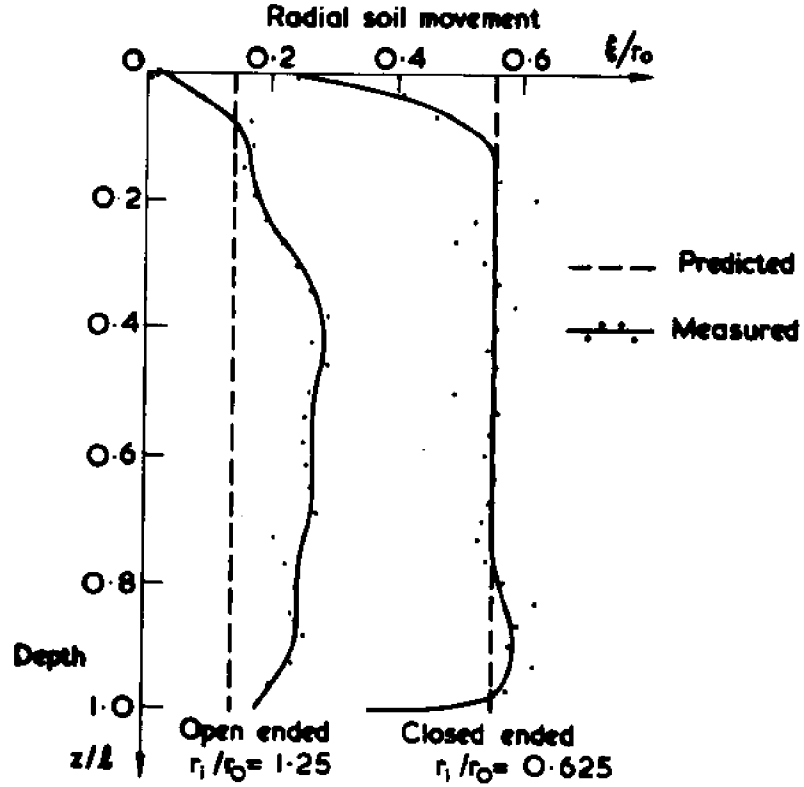

d) radial displacements

Figure 3.8 (continued)

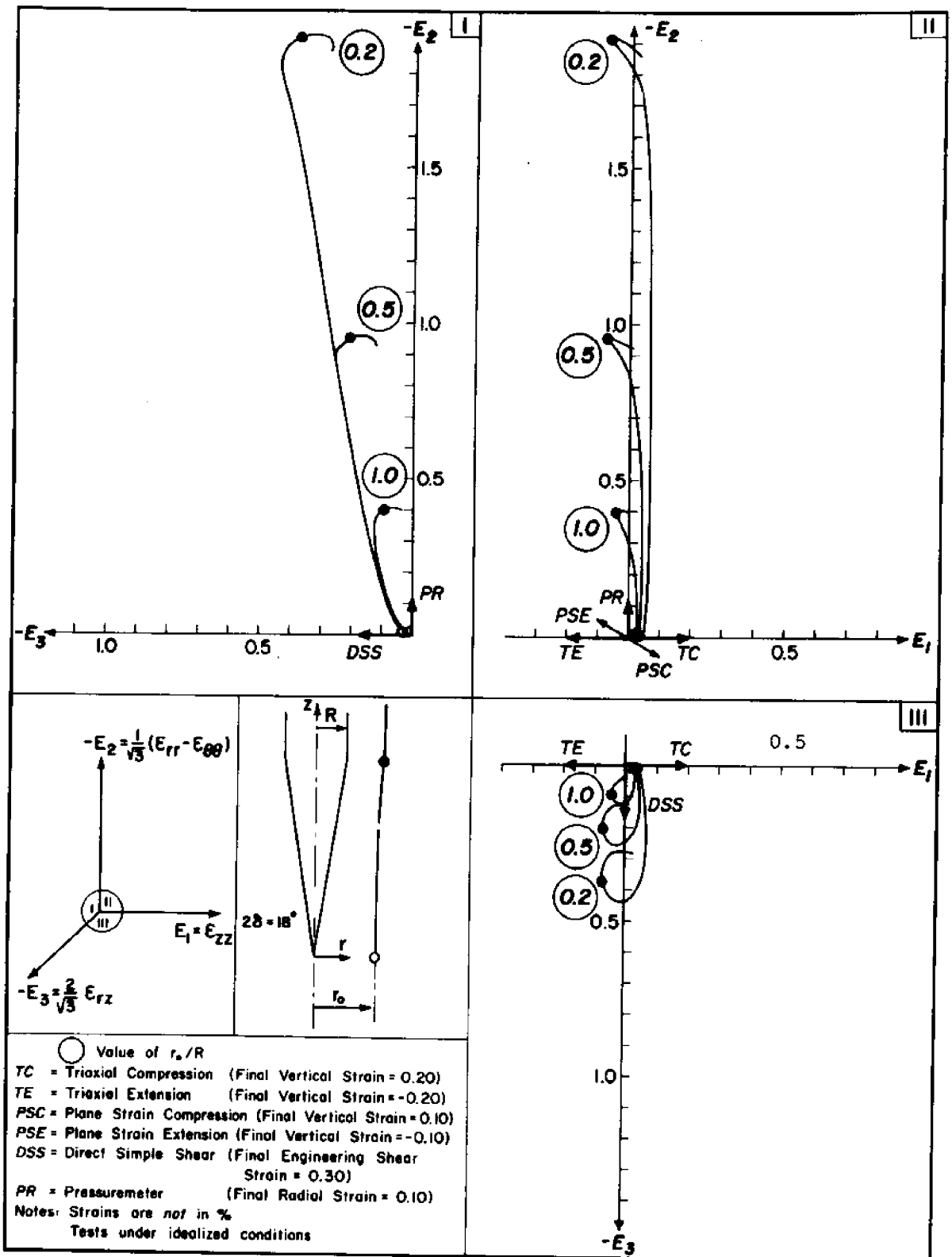

Figure 3.9 Strain paths of selected elements during penetration of an 18° cone

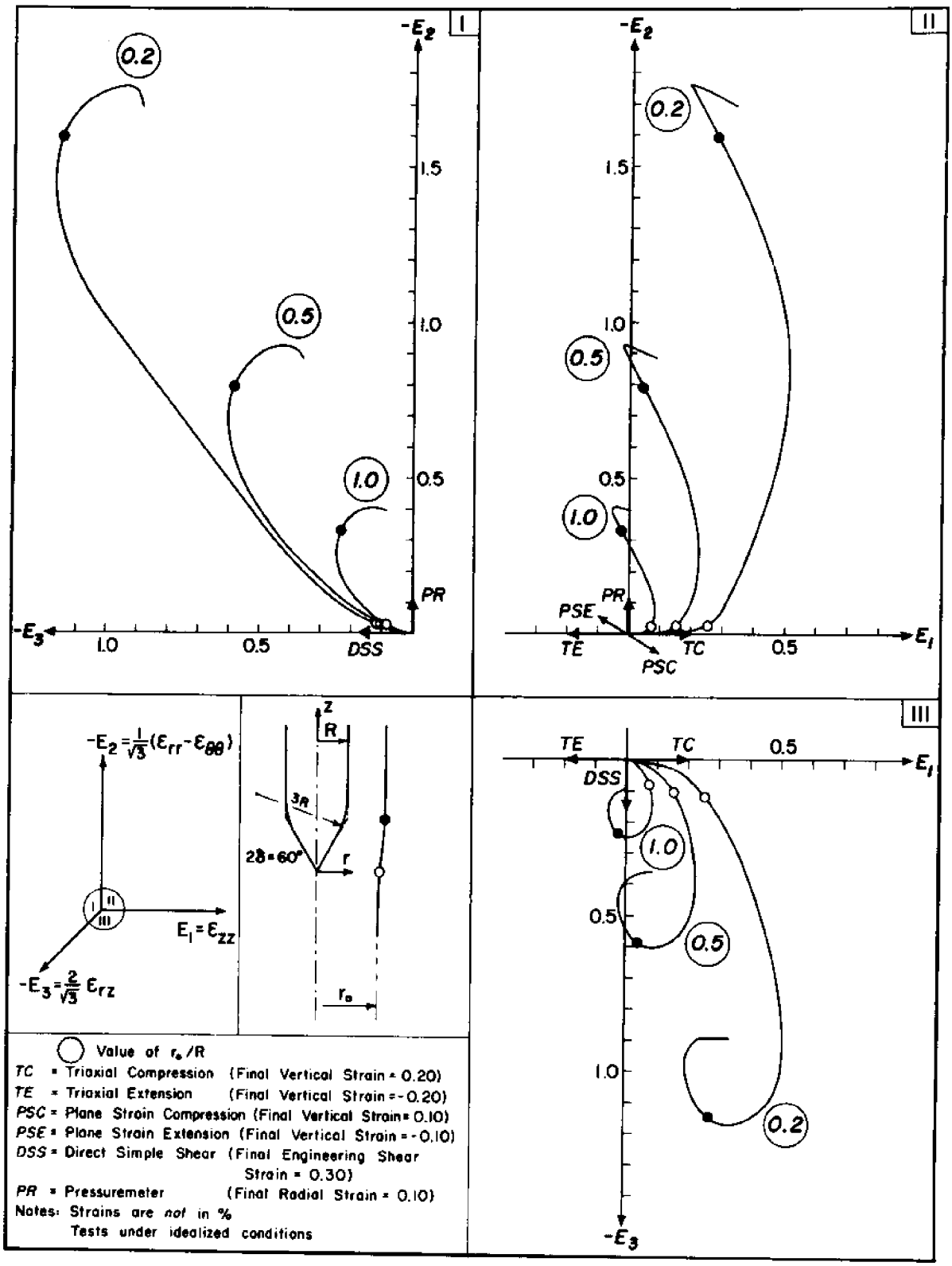

Figure 3.10 Strain paths of selected elements during penetration of a 60° cone

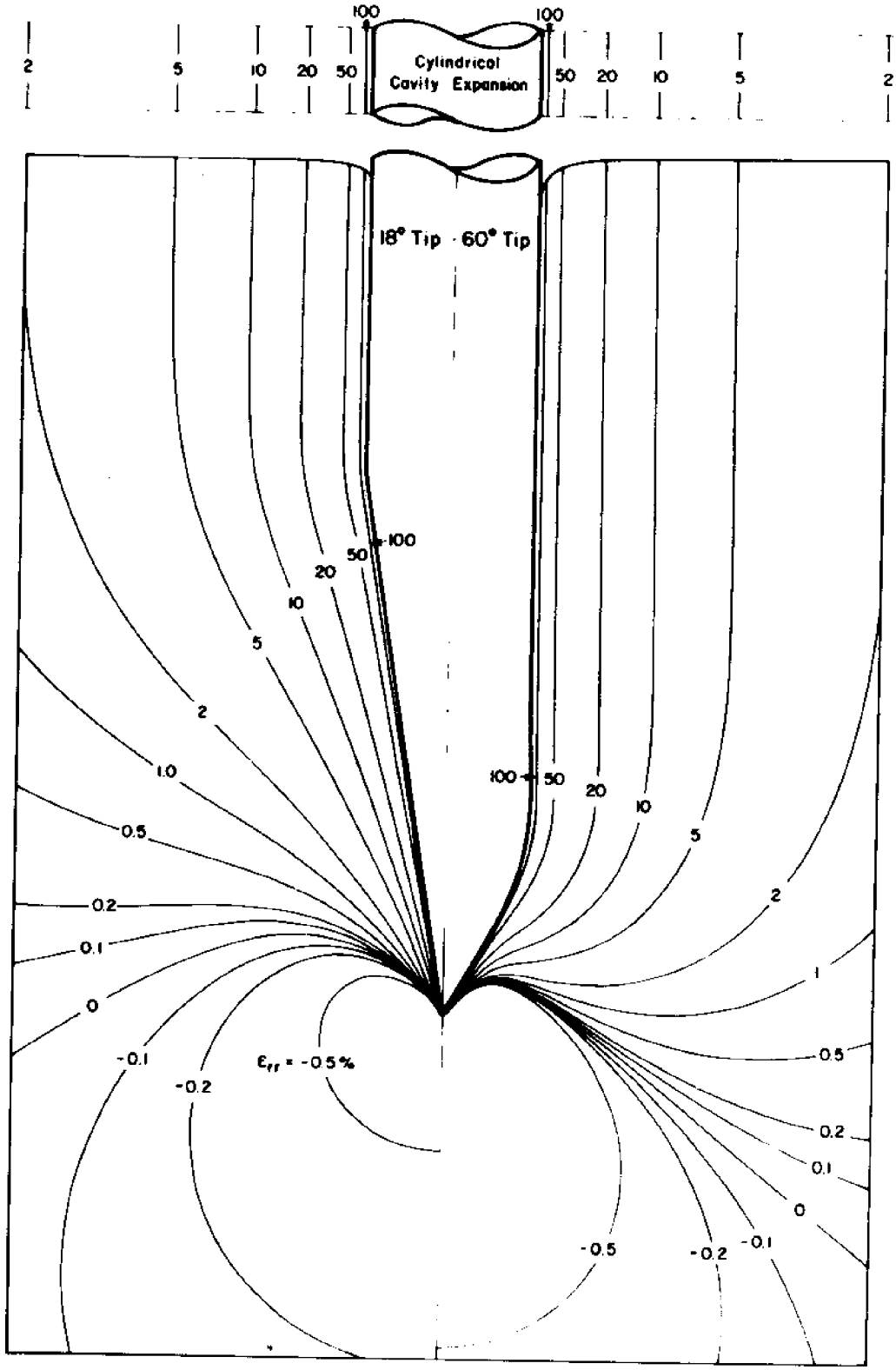

Figure 3.11 Contours of radial normal strain, ε_{rr}

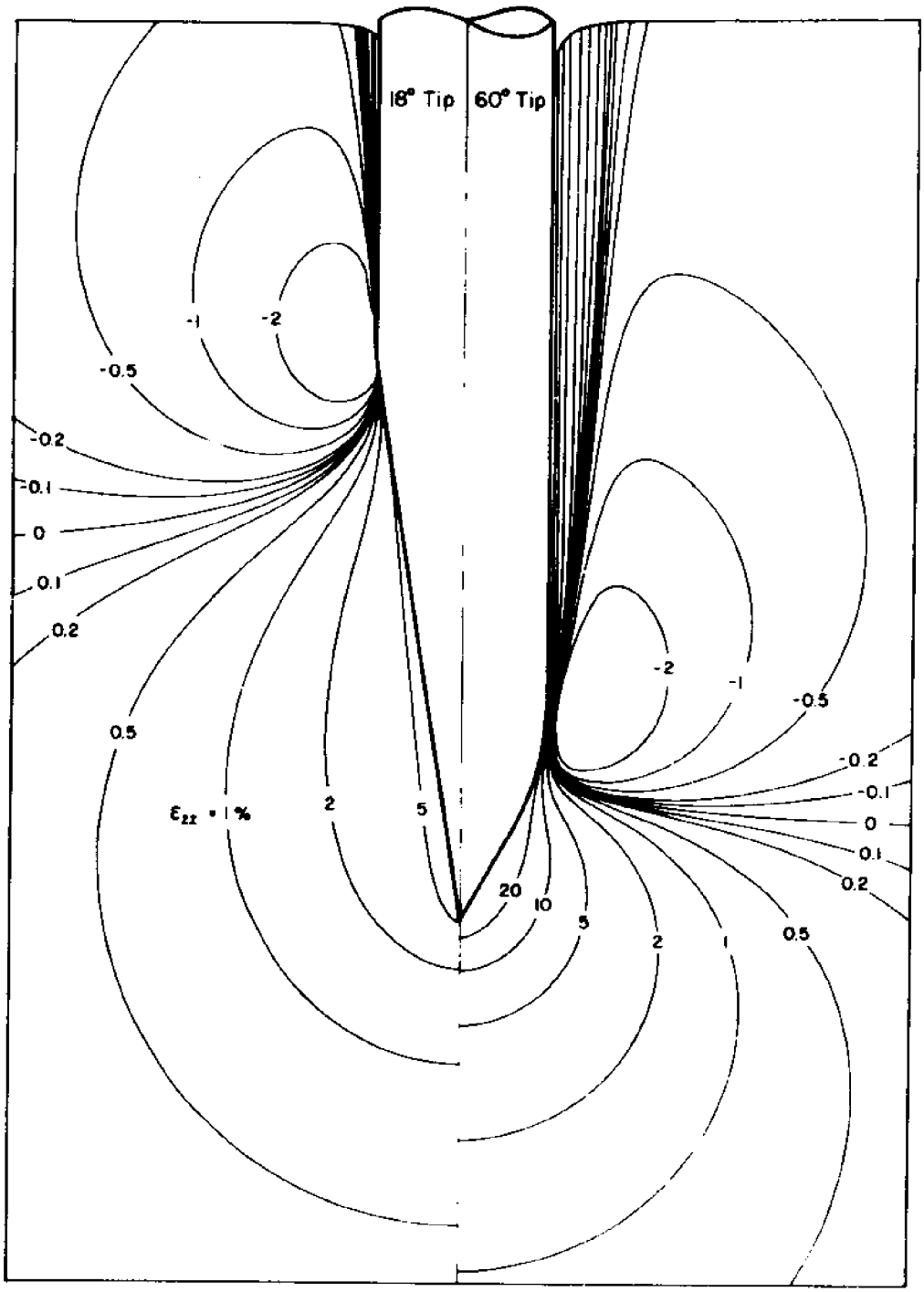

Figure 3.12 Contours of vertical (longitudinal) normal strain, ϵ_{zz}

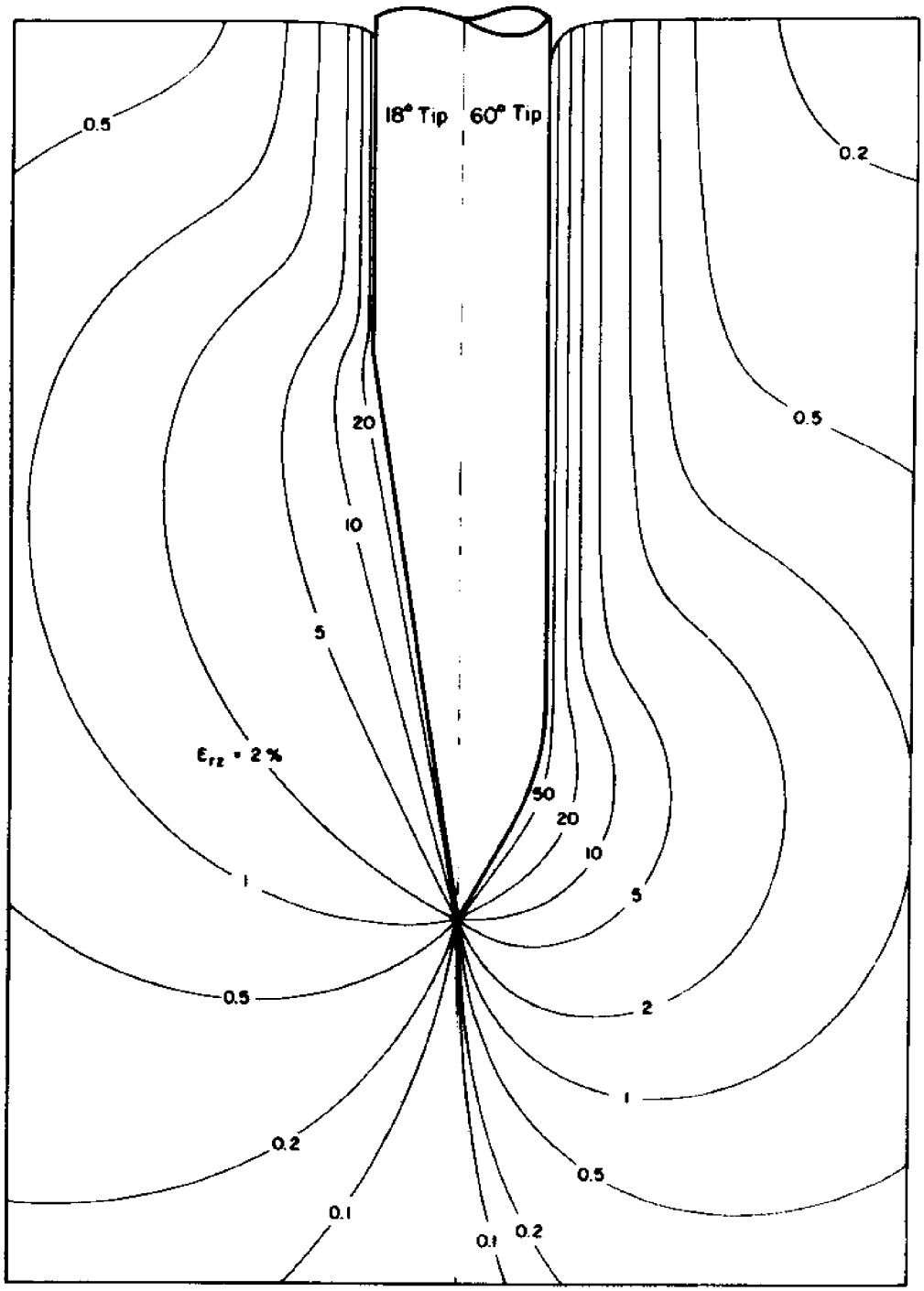

Figure 3.13 Contours of meridional shear strain, ε_{rz}

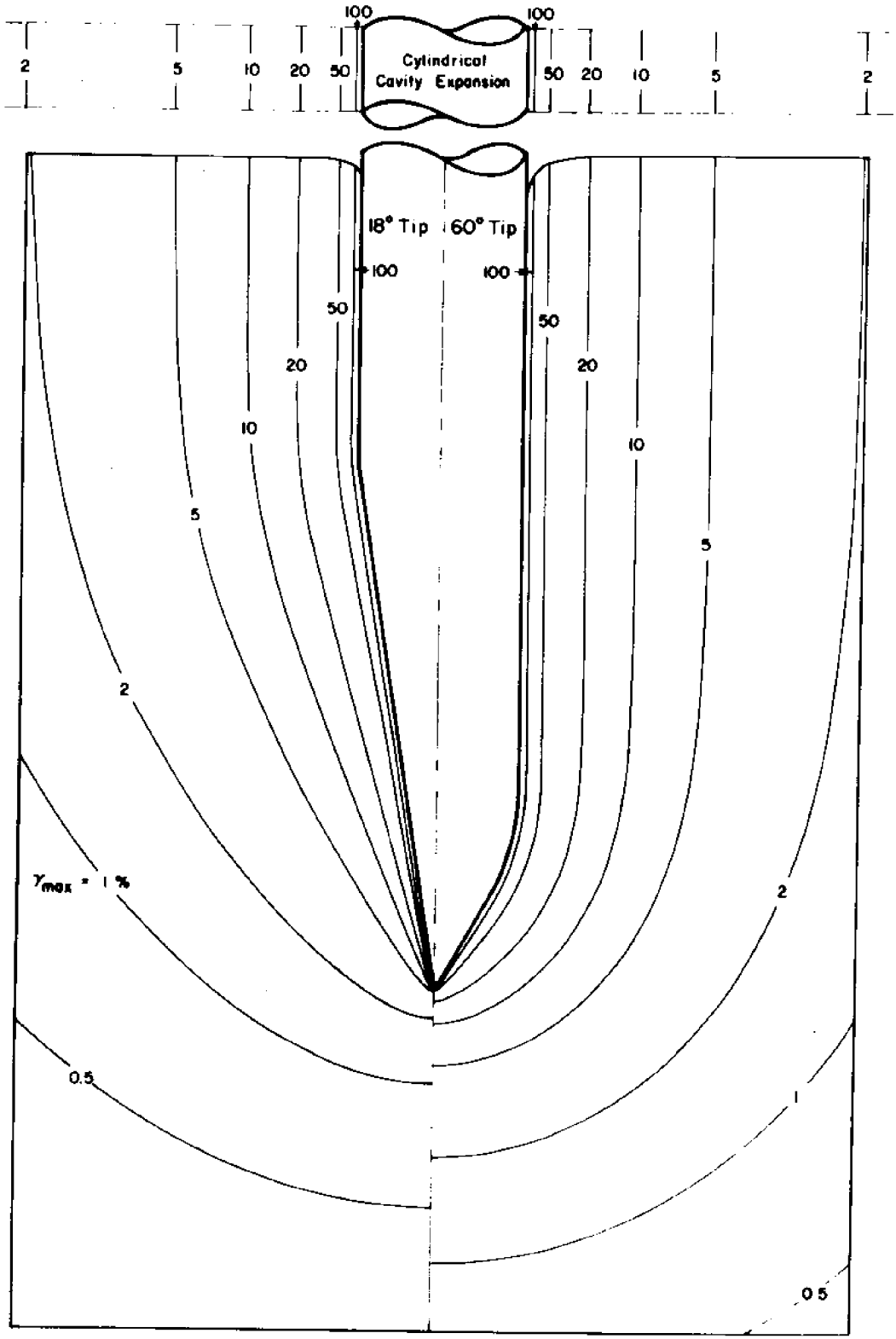

Figure 3.14 Contours of maximum shear strain, $\gamma_{max} = \frac{1}{2}(\varepsilon_1 - \varepsilon_3)$

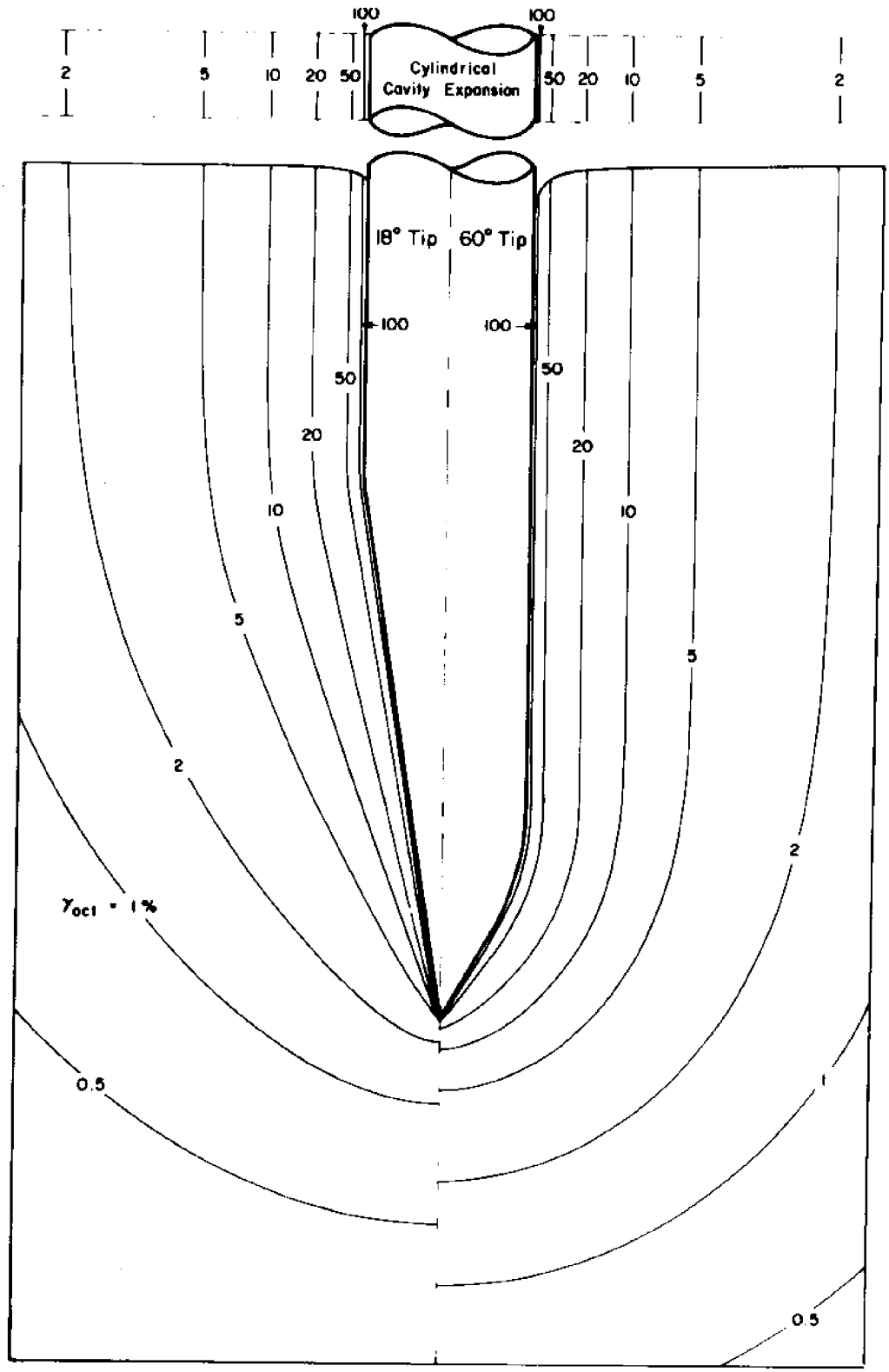

Figure 3.15 Contours of octahedral shear strain, γ_{oct}

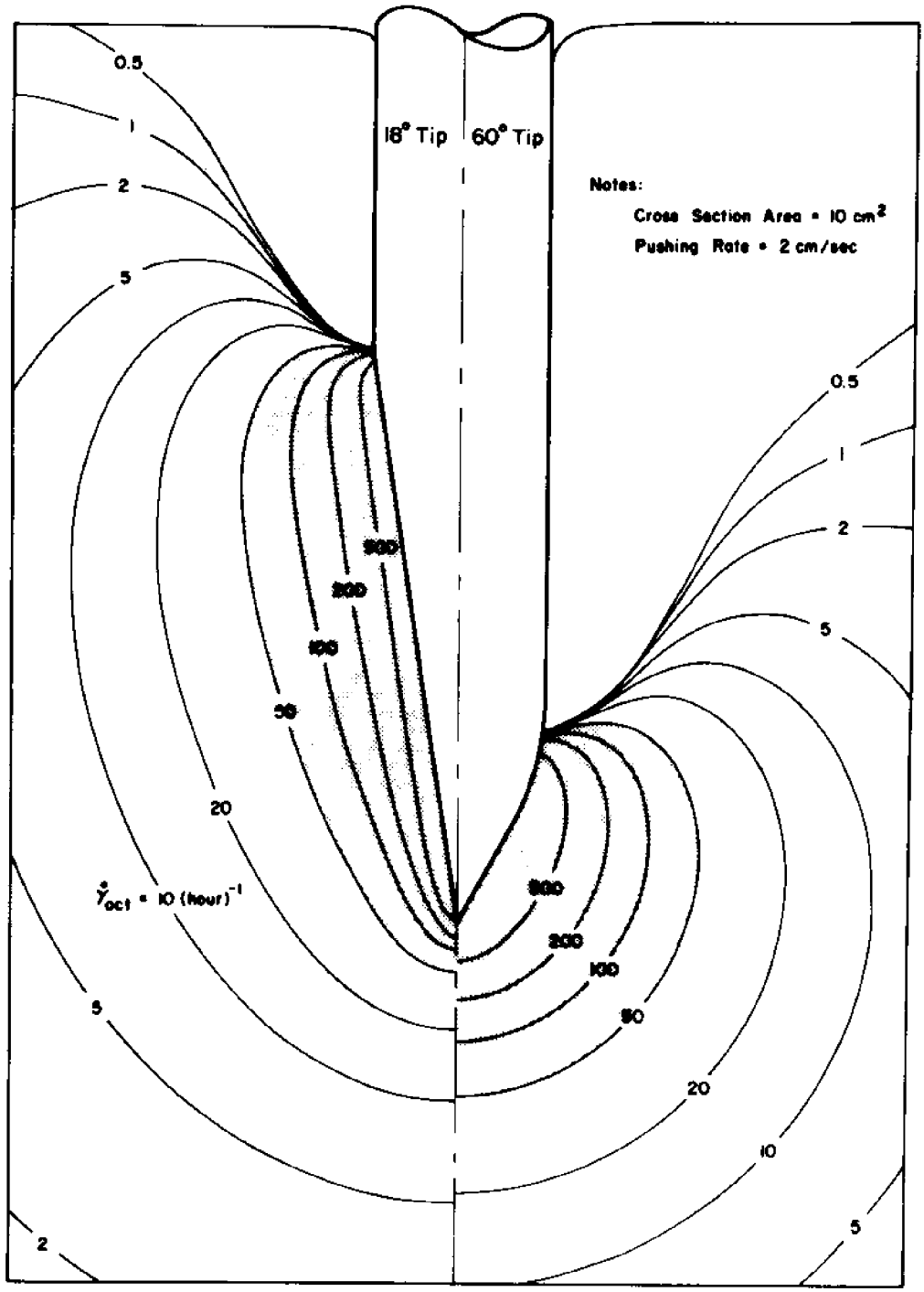

Figure 3.16 Contours of octahedral shear strain rate, $\dot{\gamma}_{oct}$

CHAPTER 4

DEVIATORIC STRESS MODEL

4.1 INTRODUCTION

Chapter 4 provides estimates of the complicated patterns of displacements and strains due to deep steady cone penetration in an incompressible infinite medium. In order to determine the soil stresses caused by these strains and compute the cone penetration resistance in clays, a comprehensive soil model is required to account for the important aspects of soil behavior as related to cone penetration: a) complicated strain paths including strain reversals (i.e., "loading and unloading"), and large non-recoverable strains; b) initial and stress-induced anisotropy; c) post-peak behavior; and, d) time depending deformations (e.g., undrained creep and relaxation). Such a comprehensive model is not available at the present time.

It is widely accepted that effective stresses control soil behavior, and hence, many researchers advocate the use of effective stresses rather than total stresses in predicting soil behavior even in undrained problems (e.g., Schmertmann, 1975; Janbu, 1975). When effective stress approaches are defined in the narrow* sense (as is often the case in geotechnical practice), the above statement can be misleading. Figure 4.1 shows results of

---

*i.e., given the effective stress in the soil at some loading stage, what can be predicted?

$\overline{CK_oU}$ * cyclic triaxial test on Boston Blue Clay (Braathen, 1966) where both the stress difference ($\sigma_v - \sigma_h$) and the mean effective stress $\bar{\sigma}_{oct}$ are plotted vs. the cumulative vertical strain. Results in Fig. 4.1 show that: a) when the loading direction is reversed (points a,b,c, and d in Fig. 4.1), the undrained modulus increases drastically although the mean effective stress has not changed significantly, and b) the points with equal incremental (or tangential) undrained modulus on the stress-strain curves in compression loading and denoted by 1,2, and 3 in Fig. 4.1 are associated with very different effective confinement levels ($\bar{\sigma}_{oct}/\bar{\sigma}_{vc}$ = 0.64, 0.43, and 0.22 at points 1,2, and 3 respectively).

Therefore, for complicated stress (or strain) histories encountered during cone penetration, comprehensive models are required to predict the stress-strain-strength behavior of the soil. For the particular case of undrained shearing of saturated clays, general effective stress models (e.g., the Cam-Clay) provide no clear advantages over the total stress models used subsequently.

---

* $\overline{CK_oU}$ = Anisotropically consolidated (under K_o conditions) test sheared under undrained conditions with pore pressure measurements.

** Where the strain (or stress) history is included.

Iwan (1967) proposes a model for the yielding behavior of materials and structures based on the incremental theory of plasticity (Drucker, 1960; Naghdi, 1960). Given the stress-strain behavior of the material due to monotonic (increasing) loading under simple stress systems as imposed in existing laboratory tests (e.g., triaxial tests) the model can predict: a) the behavior due to complicated (general) stress (or strain) paths (e.g., plane strain tests); and b) the behavior under repeated loading and unloading (e.g., cyclic loading). The attractive aspects of the Iwan model over previous incremental plasticity models are:

1) the complicated material behavior can be interpreted by means of a collection of mechanical elements (spring and slip elements) in parallel and/or series. This provides valuable insight for understanding and using the model appropriately;

2) the ability to introduce stress-induced anisotropy (Bauschinger effects) by means of the simple kinematic hardening proposed by Prager (1955);

3) non-elastic behavior during unloading. This is achieved by using a collection of yield surfaces instead of the usual single surface;

4) flexibility in adapting to more complicated material behavior as encountered in soils, and;

5) easy adaptability to existing numerical computational

methods (e.g., finite element methods).

Independently, Mroz (1967) describes a model which is essentially identical to Iwan's with more emphasis on three-dimensional behavior of materials rather than the one-dimensional cyclic behavior. The valuable additional contributions of Mroz are:

1) more detailed mathematical expressions and introduction of isotropic hardening to improve the performances of the model when applied to complex loading conditions, and;

2) introduction of convenient three-dimensional strain and stress spaces where the loading history can be more easily visualized for plane stress problems.

In order to apply the model for predicting the undrained behavior of clays, Prevost (1977, 1978 and 1979):

1) describes the model in the deviatoric stress space;

2) introduces initial anisotropy by considering yield surfaces initially centered off the origin in the stress space;

3) subdivides the strain increment into elastic and plastic increments so that the flow rule can be inverted;

4) provides three-dimensional strain and stress subspaces that are more convenient for following the loading history in many soil mechanics problems (e.g., plane strain and axisymmetry);

5) presents simple rules to determine the initial

location, size and associated work-hardening moduli of the yield surfaces from laboratory test;

6) proposes simple isotropic hardening rules to model cyclic loading, and;

7) provides all mathematical equations necessary to implement the model into numerical computational methods.

This chapter describes the above soil model and generalizes it to include most of the important factors influencing cone penetration in clays. Predictions of the model are evaluated by means of laboratory test results on a normally consolidated clay of medium sensitivity known as Boston Blue Clay (BBC). Subsequently, the model is used in Chapter 6 to predict stress and pore pressure fields in clays due to steady cone penetration.

4.2 MODEL DESCRIPTION

The proposed analytical model describes the anisotropic, elastoplastic, path-dependent stress-strain-strength properties of inviscid saturated clays under undrained loading conditions.

Strains are divided into elastic and plastic components. Elastic strains are related to stresses assuming linear isotropic elasticity and plastic strains incorporate the nonlinearity and anisotropy of the soil. Soil plasticity is described by means of: (a) a yield condition describing the stress states causing plastic flow; (b) a flow rule relating

the plastic strains* to the stresses, and; (c) hardening (or softening) rules controlling the changes in the yield condition due to plastic flow.

4.2.1 Yield Condition

The undrained shearing behavior of saturated clays is not affected by the octahedral normal total stress, σ_{oct} $(= \frac{\sigma_{ii}}{3})$. Hence, only the deviatoric components of stresses, s_{ij}, affect the yield condition at any level of shearing.

$$s_{ij} = \sigma_{ij} - \delta_{ij} \sigma_{oct} \qquad (4.1)$$

in which σ_{ij} is the total stress tensor and δ_{ij} is the Kronecker delta ($\delta_{ij} = 1$ for $i = j$ and $\delta_{ij} = 0$ for $i \neq j$).

For convenience, yield conditions are depicted by surfaces in the six-dimensional deviatoric stress space. The model considers an arrangement of nested yield surfaces, $f_1, f_2, \ldots f_{p-1}$, externally bound by a failure surface, f_p, which encloses all acceptable stress states. Different shapes of the yield surfaces may be utilized. However, for the sake of simplicity, and in order to reduce the necessary soil parameters to manageable levels, yield surfaces of the Von Mises type are proposed:

$$f_m(s_{ij}) = \{\frac{3}{2}[s_{ij} - \alpha_{ij}^{(m)}]\,[s_{ij} - \alpha_{ij}^{(m)}]\}^{\frac{1}{2}} - k^{(m)} = 0 \qquad \ldots\ldots (4.2)$$

*More precisely, the plastic strain increments.

where $\alpha_{ij}^{(m)}$ and $k^{(m)}$ represent the coordinates of the center and the size of the yield surface f_m, in the stress space, respectively. Each yield surface, f_m, is therefore described by seven parameters: six for its center location $\alpha_{ij}^{(m)}$ and one for its size $k^{(m)}$.

4.2.2 Flow Rule

The flow rule adopted by the model is the associated normality rule of plasticity which states that: for any stress state located on the yield surface (in the stress space), the plastic strain-increment vector lies along the exterior normal to the yield surface. Applying the flow rule to the yield surfaces described by Eq. 4.2, using linearity and isotropy for the elastic response of the soil, and after inversion,* the deviatoric stress increments, ds_{ij} can be obtained in terms of the deviatoric stresses, s_{ij}, and the strain increments, $d\varepsilon_{ij}$:

$$ds_{ij} = 2Gd\varepsilon_{ij} - (2G - H_m)\frac{3}{2}\left(\frac{s_{ij} - \alpha_{ij}^{(m)}}{[k^{(m)}]^2}\right)[s_{k\ell} - \alpha_{k\ell}^{(m)}]\, d\varepsilon_{kl} \quad \ldots.(4.3)$$

in which G is the elastic shear modulus, $H_m = [(H_m')^{-1} + (2G)^{-1}]^{-1}$ is the elasto-plastic modulus and H_m' is the plastic modulus of the soil.

A plastic modulus H_m' is associated with each yield

---

*Inversion of the flow rule is made possible by the presence of the elastic part of the strain increment (Prevost, 1974).

surface. Therefore, by following an incremental procedure one can visualize the regions enclosed by the failure surface, f_p, in stress space as divided into a finite number of subregions where the elasto-plastic modulus, H'_m, is constant (e.g., the stress-strain curve of a triaxial test is subdivided into linear segments where the changes in slope occur when the stress point reaches a new yield surface).

4.2.3 Hardening Rule

Soils harden or soften with shearing. In order to account for strain hardening (or softening) and to incorporate the effects of loading-unloading-reloading,* the model uses a combination of isotropic and kinematic hardening (or softening) rules which depend on the plastic flow undergone by the soil. During the course of plastic flow, the yield surfaces are translated (i.e., $\alpha_{ij}^{(m)}$ changes in the stress space by the stress point, without changing in form) and they consecutively touch and push each other according to hardening rules which prevent them from intersecting.**

---

*The terms "loading" and "unloading" are generalized to three dimensional problems by stating that the soil experiences loading and unloading when the stress point is moving away or toward the center of the current yield surface, respectively.

**Overlapping of the subregions defined by the yield surfaces would create zones of multivalued plastic moduli and hence cause numerical and (more importantly) conceptual difficulties.

The size of the yield surface $k^{(m)}$, and its associated plastic modulus, H'_m are allowed to vary according to stress (or strain) history. The rules governing the translation of the yield surfaces in the stress space are an integral part of the model, whereas, the rules describing changes in $k^{(m)}$ and H'_m have to be adapted to the soil at hand.

4.2.4 Model Limitations

Prior to undrained shearing the initial location and size of each yield surface, which are determined from experimental test results, are only applicable to problems where the soil has experienced the same strain (or stress) history (i.e., same consolidation history). This implies that: a) results of isotropically consolidated undrained test cannot be used to predict the undrained response of a soil element consolidated under K_o-condition (with $K_o \neq 1$); b) soil elements with different stress histories (i.e., different overconsolidation ratios) require separate tests to determine the necessary model parameters, and; c) the behavior of soil elements where principal stress directions vary during consolidation cannot be treated because of the limitations of classical laboratory tests to duplicate the loading history.

4.3 MODEL IMPLEMENTATION

4.3.1 Deviatoric Stress Subspace

In three-dimensional problems, a stress state is described by six independent components. However, since the sum of the deviatoric normal stresses vanishes ($s_{ij} = 0$) it is

sufficient to use five components to identify deviatoric stress states (i.e., use a 5-dimensional space to map deviatoric stress states). In many laboratory and field tests, loading conditions can be reduced to two-dimensional conditions, e.g., axial symmetry or plane strain, in which $\sigma_{\theta z} = \sigma_{r\theta} = 0$ or $\sigma_{xy} = \sigma_{yz} = 0$ (see Fig. 4.2 for definitions). In such simpler cases (including cone penetration), it is possible to map the deviatoric stresses in a 3-dimensional space with coordinates S_i defined as:

$$S_1 = \frac{3}{2} s_z; \quad S_2 = \frac{\sqrt{3}}{2} (s_y - s_x); \quad S_3 = \sqrt{3}\, s_{xz} \tag{4.4}$$

$$S_1 = \frac{3}{2} s_z; \quad S_2 = \frac{\sqrt{3}}{2} (s_\theta - s_r); \quad S_3 = \sqrt{3}\, s_{rz} \tag{4.5}$$

In the S_i-space, the yield surface f_m becomes a sphere with equation;

$$\{\Sigma[S_i - \alpha_i^{(m)}]^2\}^{\frac{1}{2}} - k^{(m)} = 0 \tag{4.6}$$

in which $\alpha_i^{(m)}$ and $k^{(m)}$ are the center coordinates and the radius of the yield surfaces f_m, respectively. The distance from the origin to any point in the S_i-space is proportional to the octahedral shear stress τ_{oct} and, thus provides a good measure of the level of shearing:

$$[S_1^2 + S_2^2 + S_3^2]^{\frac{1}{2}} = \frac{3}{\sqrt{2}} \tau_{oct} \qquad (4.7)$$

$$\tau_{oct} = \frac{1}{3}[(\sigma_{xx} - \sigma_{yy})^2 + (\sigma_{yy} - \sigma_{zz})^2 + (\sigma_{zz} - \sigma_{xx})^2 + 6\sigma_{xz}^2]^{\frac{1}{2}}$$

.....(4.8)

The associated strains E_i (=E_1, E_2 and E_3) are defined such that the rate of work per unit volume of soil is expressed as:

$$dw = s_{ij}\, d\varepsilon_{ij} = \Sigma S_i\, dE_i \qquad (4.9)$$

From Eqs. 4.4, 4.5 and 4.9, the associated strains are respectively given in cartesian and cylindrical coordinates by:

$$E_1 = \varepsilon_{zz}; \quad E_2 = \frac{1}{\sqrt{3}} (\varepsilon_{yy} - \varepsilon_{xx}); \quad E_3 = \frac{2}{\sqrt{3}} \varepsilon_{xz} \qquad (4.10)$$

and

$$E_1 = \varepsilon_{zz}; \quad E_2 = \frac{1}{\sqrt{3}} (\varepsilon_{\theta\theta} - \varepsilon_{rr}); \quad E_3 = \frac{2}{\sqrt{3}} \varepsilon_{rz} \qquad (4.11)$$

The flow rule in Eq. 4.3 becomes:

$$dS_i = 3G dE_i - (3G - \frac{3H_m}{2}) \frac{S_i - \alpha_i^{(m)}}{[k^{(m)}]^2} \sum_{j=1}^{3} [S_j - \alpha_j^{(m)}]\, dE_j \qquad (4.12)$$

4.3.2 Parameters Describing the Initial Yield Surfaces

Prior to undrained shearing, the sizes and locations of the spherical yield surfaces reflect the initial anisotropy of the clay. In most cases of interest, initial anisotropy develops during deposition and subsequent consolidation under one-dimensional straining condition thus leading to symmetry about the vertical z-axis (i.e., cross-anisotropy). The yield surfaces are, therefore, initially centered along the S_1-axis ($\alpha_2^{(m)} = \alpha_3^{(m)} = 0$, for any m, Fig. 4.2.b). In order to determine the model parameters describing the initial yield surfaces, stress-strain curves of K_o-consolidated undrained triaxial compression and extension tests are utilized as illustrated in Fig. 4.3. During triaxial testing, the stress point travels along the S_1-axis and, therefore, the yield surfaces remain centered on the S_1-axis. The elastic shear modulus is obtained from the initial slope of the steeper stress-strain curve (in general that of the compression test) which is equal to 3 G.* The stress-strain curves for compression and extension are then subdivided into a finite number of pairs of linear segments with equal slopes (see Fig. 4.3). The starting points of the m^{th} segments along the compression and extension sides provide the upper and lower intersections of the spherical yield surface f_m with the S_1-axis, respectively. These two points

*Assuming that Poisson's ratio $\nu = 0.5$ for undrained loading.

of intersection completely define the initial location and size of the yield surface f_m (i.e., $\alpha_i^{(m)}$ is equal to the average ordinate and, $k^{(m)}$ is equal to half the distance between the two points). The common slope of the two corresponding segments equals 3/2 H_m^* and hence determines the elasto-plastic modulus H_m associated with f_m.

4.3.3 Pre-Peak Behavior

During undrained shearing, soils develop a "stress-induced" anisotropy which depends on the stress system imposed. In the model, this behavior is accounted for by the translation ($\alpha_i^{(m)}$ change) and the decrease in size ($k^{(m)}$) of the yield surfaces during the process of plastic flow. The rules governing changes in the yield surfaces affect the predicted behavior significantly and, represent a cornerstone of any model.

Figure 4.4 illustrates the translation of yield surfaces during the process of plastic flow as outlined in Section 4.2.3, and provides the equations needed to compute the center displacement vector $d\alpha^{(m)}$ as a function of the stress point displacement vector ds. These equations are similar to those given by Prevost (1978) after assuming that the size of the current yield surface f_m does not change during translation. The simplified equations obtained by neglecting

---

*For triaxial loading, Eq. 4.3 reduces to:

$$d(\sigma_z - \sigma_x) = (3/2) \cdot H_m \cdot d\,\epsilon_z$$

second order terms and given in the above article are not recommended, for they may lead to overlapping of the yield surfaces.

In order to account for the reduction in plastic modulus, H'_m, during the process of plastic flow, the following rule is adopted herein. The plastic modulus H'_m associated with the yield surface f_m is reduced from its initial value H'^{o}_m to a limiting value H'^{ℓ}_m when and only when the current yield surface is outside f_m.* Variation of H'_m between its initial and limiting values is arbitrarily approximated by:

$$H'_m = H'^{o}_m \cdot \exp(-A_m \cdot \lambda_m); \quad H'^{\ell}_m < H'_m < H'^{o}_m \qquad (4.13)$$

in which A_m is an experimental constant and λ_m is the generalized (or equivalent) plastic strain given by:

$$\lambda_m = \int (\frac{2}{3}\, d\varepsilon^p_{ij}\, d\varepsilon^p_{ij})^{\frac{1}{2}} \qquad (4.14)$$

in which $d\,\varepsilon^p_{ij}$ is the plastic strain-increment tensor. Integration in Eq. 4.14 is carried out along the strain path after the stress point has passed the yield surface f_m. The experimental constants H'^{ℓ}_m and A_m in Eq. 4.13 are determined from cyclic laboratory tests in which the plastic modulus H'_m associated with the yield surface f_m is utilized several

---

*This implies that the plastic modulus H'_m associated with the yield surface f_m remains unchanged until the stress point reaches f_{m+1}.

times and where, therefore, its variation can be observed.

4.3.4 A New Model for Post-Peak Behavior

Normally consolidated Boston Blue Clay (BBC), that will be subsequently modelled, exhibits a very pronounced strain-softening behavior when sheared in triaxial (or plane strain) compression under undrained loading, following (one dimensional) K_o-consolidation. To describe this behavior, Prevost (1978) proposes to use an isotropic softening rule where the yield surfaces do not change their position in stress space but all decrease in size simultaneously and by the same amount. However, upon reaching large strains, the strength reduction in the triaxial extension (TE) mode of failure becomes unrealistic (negative strengh!).* Therefore, a more realistic softening rule is introduced herein:

a) the failure surface f_p remains at all times centered on the S_1-axis and, thus, is completely defined by its two intersections with the S_1-axis which are the end points of a diameter of the sphere f_p;

b) the intersection of f_p with the negative S_1-axis remains fixed. This implies that after the peak strength has been reached in a triaxial extension test, plastic flow proceeds at a constant deviatoric stress;

c) the reduction in radius $k^{(p)}$ of the failure surface

---

*Available triaxial extension test results on BBC suggest a perfectly plastic behavior once the peak strength has been reached.

f_p from its initial value $k_o^{(p)}$ to its limiting value $k_\ell^{(p)*}$ is approximated by:

$$k^{(p)}(\lambda_p) = k_\ell^{(p)} + (k_o^{(p)} - k_\ell^{(p)}) \cdot \exp\{-A_p \cdot \lambda_p\} \quad (4.15)$$

in which A_p is an experimental constant and λ_p is the "yielded" generalized (or equivalent) plastic strain given by:

$$\lambda_p = \int (\tfrac{2}{3}\, d\varepsilon_{ij}^p\, d\varepsilon_{ij}^p)^{\frac{1}{2}} \quad (4.16)$$

in which $d\varepsilon_{ij}^p$ is the plastic strain-increment tensor. Integration in Eq. 4.16 is carried out along the strain path if and only if the stress point lies on f_p. Thus, reduction in size of f_p takes place only when the soil has reached the failure state. The experimental constant A_p is determined from the post peak stress-strain curve of a monotonic triaxial compression test;

d) the new location of the stress point, after application of a strain increment $d\varepsilon_{ij}$ is determined according to the associated flow rule; i.e., the stress point moves to the point of the sphere f_p where the inside normal is parallel to and has the same direction as the plastic strain-increment vector $d\varepsilon_{ij}^p$, and;

---

*Note that $k_\ell^{(p)}$ is directly obtained from the strength in the TE mode of failure.

e) together with the radius reduction of the failure surface f_p, all the yield surfaces remain tangent to f_p at the current stress point and decrease in size by the same relative amount. Thus, at any time, the current radius $k^{(m)}$ is given as a function of the initial radius $k_o^{(m)}$ by:

$$\frac{k^{(m)}}{k_o^{(m)}} = \frac{k^{(p)}}{k_o^{(p)}}; \quad m = 1, 2, \ldots, (p - 1) \qquad (4.17)$$

and the coordinates α_i^m $(i = 1, 2, 3)$ of the center of f_m are given as a function of the stress point coordinates S_i $(i = 1, 2, 3)$ by:

$$\frac{S_i - \alpha_i^{(m)}}{k^{(m)}} = \frac{S_i - \alpha_i^{(p)}}{k^{(p)}} \quad ; \quad m = 1, 2, \ldots, (p - 1) \qquad (4.18)$$

4.3.5 Computer Program

The soil model described above was incorporated in a computer program (coded in FORTRAN IV) which is listed and explained for the user in Appendix C. Input data consist of: the initial yield surfaces parameters (Fig. 4.3); the elastic shear modulus G; the parameters describing changes in yield and failure conditions (to be used in Eqs. 4.13 and 4.15); the initial location of the stress point (i.e., initial deviatoric stresses) and; the loading sequence in terms of successive strain increment vectors. For each strain increment vector, the program computes the corresponding deviatoric stress increments, modifies the yield surfaces

and prints the value of updated deviatoric stresses.

4.4 MODEL EVALUATION

This section evaluates the performance of the proposed model by determining the required soil parameters from $\overline{CK_oU}$ triaxial tests, predicting the response in $\overline{CK_oU}$ Plane Strain and Direct Simple Shear tests, and comparing the predictions with measurements obtained from laboratory tests. Results of $\overline{CK_oU}$ cyclic triaxial tests are utilized to determine the parameters describing the reduction in plastic moduli of the soil upon loading reversal. A discussion of the model capability in describing the anisotropic clay behavior under undrained conditions is then presented.

4.4.1 Model Parameters

The soil considered in this section consists of normally consolidated Boston Blue Clay (BBC) which is a fairly sensitive marine illitic clay. Over the last decade, extensive field and laboratory tests were conducted on this clay at MIT. Laboratory tests reported herein were conducted from batches of resedimented BBC which were prepared by consolidating a clay slurry.* The preparation procedure provided a fairly uniform source of clay with strength and consolidation properties similar to those of natural Boston Blue Clay (Ladd et al., 1971). Typical properties from numerous batches that were used over a four year period were:

*Detailed procedures of slurry preparation and consolidation are given in Appendix B of Ladd et al. (1971).

Liquid Limit	= 41 ± 2%
Plastic Limit	= 20 ± 2%
Plasticity Index	= 21 ± 3%

a) Parameters for monotonic loading. Figure 4.5 presents the results of two $\overline{CK_oU}$ triaxial compression tests and four extension tests on samples of resedimented Boston Blue Clay normally consolidated to various levels of vertical consolidation stress $\bar{\sigma}_{vc}$. The stress-strain curves obtained for the two compression tests are virtually identical after the deviator (shear) stresses $(\sigma_v - \sigma_h)$ are divided by $\bar{\sigma}_{vc}$. This indicates that the clay exhibits a normalized behavior and hence enable significant generalizations to be made. Typically, the peak strength is reached at very low strain level ($\epsilon_v \simeq 0.35\%$) and the clay strain-softens significantly such that its shearing resistance at large strain levels (above $\epsilon_v \simeq 10\%$) becomes less than under the initial K_o-consolidation condition.

On the other hand, the results of four triaxial extension tests (Fig. 4.5) exhibit significantly higher scatter than the compression tests. The difficulties in performing and interpreting extension tests might represent one cause of this scatter. Furthermore, no satisfactory explanation could be reached by Ladd and Varallyay (1965) for the unusual observed effect of rate of shearing: fast stress-controlled tests yielded slightly lower strengths than slower strain-controlled tests. In all extension tests, necking of the

samples was observed at vertical strains in the range of 5 to 7%.

The two solid lines in Fig. 4.5 are the idealized stress-strain relationships fitting the experimental data of triaxial compression and extension tests by means of the mathematical expressions of the proposed model. In the subsequent derivations and applications, the normalized stress-strain behavior (with respect to $\bar{\sigma}_{vc}$, the principal vertical effective stress at the end of consolidation) exhibited by normally consolidated Boston Blue Clay will be fully utilized. Normalized properties of clays which is the basis of the SHANSEP* method are presented and discussed by Ladd and Foott (1974) and Ladd et al. (1977).

The initial configuration and associated moduli of the yield surfaces were determined by following the procedure outlined in Fig. 4.3. The parameter A_p in Eq. 4.15, describing the strain-softening behavior was obtained by fitting Eq. 4.15 to the experimental post-peak stress-strain curves from $\overline{CK_oU}$ triaxial compression tests.

b) Parameters for repeated loading. In the laboratory results discussed above, the soil is subjected to monotonic loading and, therefore, the yield surfaces are utilized before any change in their size and associated plastic moduli occurs. Chapter 3 indicates that strain reversals take place during cone penetration. One important

*SHANSEP is an acronym for Stress History And Normalized Soil Engineering Properties.

feature of the proposed model is its ability to predict soil behavior under loading-unloading conditions.

Braathen (1966) performed a series of cyclic $\overline{CK_oU}$ triaxial tests on normally consolidated Boston Blue Clay with highly repeatable results. Figure 4.6 presents the stress-strain curve (open circles) of one of his tests (randomly selected). In this figure, the normalized deviatoric stress, $(\sigma_v - \sigma_h)/\bar{\sigma}_{vc}$, is plotted against the generalized (or equivalent) plastic strain which, in the case of a triaxial test, is the sum of the absolute value of the vertical strain increments, $d\varepsilon_v$.* The solid line in Fig. 4.6 represent the idealized behavior obtained from the model after adjusting by successive trials the parameters A_m and $H_m'^{\ell}$ in Eq. 4.13. In order to reduce the number of parameters, the following simplification was made: the parameter A_m describing the rate of reduction in modulus and the ratio $H_m'^{\ell}/H_m'^{o}$ which represents the maximum amount of softening of the plastic modulus H_m' are common to all yield surfaces (m = 1, 2, ..,p-1). The idealized curve in Fig. 4.6 fits very well the experimental data for the first four loading stages. The agreement is not as good for the remaining loading stages especially during compression loading (stages 5 and 7 in Fig. 4.6).

---

*For practical purposes, $d\varepsilon_{ij}^e$, the elastic part of the total strain increment, can be neglected and, therefore $d\varepsilon_{ij}^p \simeq d\varepsilon_{ij}$

However, the normalized deviatoric stress is very well predicted at the end of any loading stage.

Table 4.1 summarizes the necessary values of the model parameters for predicting the behavior of normally consolidated BBC subjected to various loading paths.

4.4.2 Stress-Strain-Strength Predictions

a) Plane strain tests. Figure 4.7 compares predictions of the model (solid lines) with $\overline{CK_oU}$ plane strain compression and extension test results on normally consolidated resedimented BBC. The predicted strength in the compression mode of failure is approximately 8% too high, but the rate of post-peak strain-softening is very well predicted. In the extension mode, the predicted soil response is too "stiff" up to a vertical strain of 1% and then reaches a lower strength than measured. However, after conducting an extensive program of plane strain tests on resedimented BBC, Ladd et al (1971) conclude that: (a) the plane strain apparatus used to obtain the results in Fig. 4.7 yields reliable data for compression tests, and; (b) stress-strain data in the extension mode are not reliable for vertical strains larger than 3 $\pm$ 1 percent.* In view of test limitations, the predictions of the model in Fig. 4.7 appear quite reasonable.

b) Direct Simple Shear tests. The interpretation of Direct Simple Shear (DSS) test results is very challenging.

*At larger strain, testing errors due to side friction and sample necking lead to measured strength values that are too high.

Ideally, the test should develop a condition of uniform pure shear strain in the sample under conditions of no volume change(i.e., Mohr circle of strain centered at the origin). However, due to possible relative slippage between the clay sample and the upper and lower caps, and the lack of complementary shear stresses on the vertical sides of the specimen, strains and stresses are not uniform throughout the sample. Furthermore, for soils, the strain and deviatoric stress increment vectors are not necessarily coaxial and, thus, a pure shear strain increment will not, in general, produce a pure shear stress increment. Prevost and Hoeg (1976) have investigated stress and strain distributions for an isotropic, elastic material tested in a direct simple shear mode of deformation by extending the work of Roscoe (1953) in considering boundary slippage. They found that relative slippage at the contact between the soil specimen and top and bottom caps (if it occurred), together with the lack of complementary shear stresses on the vertical sides of the sample greatly alter the distributions of shear and normal stresses and prevent the ideal condition of constant volume to take place during the test. To account for the difference between the maximum and the average horizontal shear stresses acting on the sample, Prevost and Hoeg (1976) propose to increase the measured average shear stress value by 10% for estimating the maximum horizontal shear stress.

A more rigorous interpretation of the DSS test requires a three-dimensional drained analysis of the soil specimen together with an anisotropic soil model in terms of effective stresses with adequate modelling of the soil-cap interface slippage. Such a model is not available and is expected to be much more complicated that the one evaluated herein. Therefore, the results of DSS tests presented hereafter must be considered in light of the many uncertainties in interpreting test results.

Stress-strain curves for three $\overline{CK_oU}$-DSS tests performed on normally consolidated resedimented BBC are plotted in Fig. 4.8. In this figure the normalized apparent (or average) horizontal shear stress, $\tau_h/\bar{\sigma}_{vc}$, is plotted against the apparent engineering shear strain γ_h.* The solid line is predicted by the model for a pure shear strain state (and no volume change) after reducing the shear stresses by 10% as recommended by Prevost and Hoeg (1976) to account for stress nonhomogeneities within the sample. Clearly, even after this 10% reduction, the predicted stress strain curve is too stiff at low stress levels and leads to a higher strength (by 20 ± 5%) as compared to the test results.

---

*Note that $\gamma_h = 2\ \varepsilon_{xz}$; where ε_{xz} is the tensorial shear strain which is utilized in the theoretical derivations of this chapter.

4.4.3 Strength Anisotropy

This section evaluates the capabilities of the proposed model in predicting undrained strength anisotropy. Figure 4.9 shows the normalized deviatoric stress path of $\overline{CK_oU}$ triaxial, plane strain and pressuremeter tests* located in the $\{S_1, S_2\}$ plane ($S_3 = 0$). Figure 4.10 offers similar plots for the direct simple shear test* with a stress path located in the $\{S_1, S_3\}$ plane ($S_2 = 0$). It is worth noting that the model predicts that the deviatoric stress path for the ideal pressuremeter test (expansion of a cylindrical cavity) can be deduced directly from that of the ideal direct simple shear by a 90° rotation about the S_1- axis. Also shown in Figs. 4.9 and 4.10 are f_p^o and f_p^r, the peak and residual spherical failure surfaces, repectively, whose sizes are determined from the TC and TE tests.

a) Peak strength. At large straining levels the contribution of elastic strains is small and the plastic strain increments $d\varepsilon_{ij}$ are nearly equal to the total strain increments $d\varepsilon_{ij}$. Consequently, the associated flow rule utilized by the proposed model implies that at failure (peak strength), the total strain increment vector is normal to the failure surface f_p. Therefore, the location of the stress point on the failure surface f_p^o can be directly

---

*Under idealized conditions.

determined when the direction of the line tangent to the strain path at failure is known. Table 4.2 gives the predicted peak strengths of classical tests (for which the idealized strain paths are linear) as a function of the peak strengths in triaxial compression and extension failure modes. Predicted vs. measured peak undrained shear strengths of available laboratory tests on normally consolidated resedimented BBC are summarized in Table 4.3.

In order to further evaluate the capabilities of the proposed model in describing undrained peak strength anisotropy, we consider the class of failure modes under plane strain condition(i.e., $d\varepsilon_{yy} = 0$) with linear strain paths. These failure modes can only be partially investigated in the laboratory with plane strain compression, plane strain extension and direct simple shear tests, until directional shear tests (successfully performed on sands, Arthur et al., 1977) are performed on clays to provide results covering the complete range of plane strain modes of failure. Field applications of such modes of failure are numerous (e.g., bearing capacity of strip footings, stability of embankments and excavations,...).

Failure under plane strain condition ($d\varepsilon_{yy} = 0$) leads to the following equations (Prevost, 1979):

$$\left[\left(\frac{\sigma_z - \sigma_x}{2}\right) - \frac{\alpha_1^{(p)}}{2}\right]^2 + \tau_{xz}^2 = \left[\frac{k^{(p)}}{\sqrt{3}}\right]^2 \qquad (4.19)$$

and $$\sigma_y = \frac{\sigma_z + \sigma_x}{2} - \frac{\alpha_1^{(p)}}{2} \qquad (4.20)$$

The Plane Strain Compression (PSC) and Plane Strain Extension (PSE) peak strengths are related to the radius $k^{(p)}$ and the center coordinate $\alpha_1^{(p)}$ of the failure surface f_p^o by:

$$s_u(PSC) = \frac{\alpha_1^{(p)}}{2} + \frac{k^{(p)}}{\sqrt{3}} \; ; \quad s_u(PSE) = -\frac{\alpha_1^{(p)}}{2} + \frac{k^{(p)}}{\sqrt{3}} \qquad (4.21)$$

Combining Eqs. 4.19 and 4.21:

$$\left[\frac{\sigma_z - s_u(PSC)}{2} - \frac{\sigma_x - s_u(PSE)}{2}\right]^2 + \tau_{xz}^2 = \left[\frac{k^{(p)}}{\sqrt{3}}\right]^2 \qquad (4.22)$$

Davis and Christian (1971) developed one of the most general models to describe the undrained strength anisotropy of clays. At (peak) failure the in-plane stresses satisfy:

$$\left[\frac{\sigma_z - s_u(PSC)}{2} - \frac{\sigma_x - s_u(PSE)}{2}\right]^2 + \frac{a^2}{b^2}\,\tau_{xz}^2 = a^2 \qquad (4.23)$$

in which a and b are two experimental constants given by:

$$a = \frac{s_u(PSC) + s_u(PSE)}{2} \quad \text{and} \quad \frac{b}{a} = \frac{s_u(45)}{[s_u(PSC) \cdot s_u(PSE)]^{1/2}} \qquad (4.24)$$

in which $s_u(45)$ is the measured undrained shear strength with the major principal stress at failure inclined 45° with the vertical (z-axis). Comparing Eqs. 4.22 and 4.23 it becomes clear that the description of undrained strength anisotropy implied by the proposed model is equivalent to

that of Davis and Christian when:

$$a = b = \frac{k^{(p)}}{\sqrt{3}} \tag{4.25}$$

The strength anisotropy described by the proposed model is, therefore, less general than Davis and Christian's strength model simply because the former utilizes two strength values (s_u(PSC) and s_u(PSE)) whereas the latter utilizes three (s_u(PSC), s_u(PSE) and s_u(45)).

Using Eq. 4.22 together with the stress transformation laws, the following equation is obtained:

$$s_{u\theta} = \frac{k^{(p)}}{\sqrt{3}} \left\{\frac{\sqrt{3}}{2} \frac{\alpha_1^{(p)}}{k^{(p)}} \cos 2\theta + \left[1 - \frac{3}{4}\left(\frac{\alpha_1^{(p)}}{k^{(p)}} \sin 2\theta\right)^2\right]^{\frac{1}{2}}\right\} \tag{4.26}$$

in which $s_{u\theta} = \frac{1}{2}(\sigma_{1f} - \sigma_{3f})$ is the undrained shear strength for plane strain loading ($d\varepsilon_{yy} = 0$) and θ the angle between the major principal stress at failure (σ_{1f}) and the vertical (z-axis). Substituting the values corresponding to f_p in Table 4.1 into Eq. 4.26, the variation of $s_{u\theta}/\bar{\sigma}_{1c}$ as a function of θ for normally consolidated BBC is obtained and represented by the solid line in Fig. 4.11. Also shown in Fig. 4.11 (dashed line) is the variation of $(\tau_{xz})_f/\bar{\sigma}_{1c}$ where $(\tau_{xz})_f$ is the shear stress acting on the horizontal plane at (peak) failure. The common point of the two curves corresponds to a state of pure shear in terms of stresses ($\tau_{xz} = \tau_{max}$), whereas the extremum of the horizontal stress curve ($\theta = 34.74°$) corresponds to a state of pure shear

in terms of strains. The latter situation would be reproduced in a DSS test with perfect boundary conditions imposing complementary shear stresses along the vertical sides and allowing no slippage at the specimen-cap interface. The strength in case of pure shear in terms of strains (maximum shear stress at failure) is slightly higher than the horizontal shear stress measured during the test. In order to compare strength anisotropy predicted by the proposed model and the Davis and Christian model, strength plots are presented in Fig. 4.12. These strength plots consist of a polar representation where the radius is equal to $s_{u\theta}/\bar{\sigma}_{1c}$ and the angle with the horizontal axis is equal to 2θ. The outer circle (dashed line) describes the strength variation predicted by the proposed model and the dotted area covers a range predicted by Davis and Christian model depending on two limiting assumptions for interpreting the DSS test. In the first assumption, the measured horizontal shear stress at failure during a DSS test equals the maximum shear stress acting on the soil specimen (i.e., pure shear in terms of stresses) and consequently $\theta = 45°$, whereas in the second assumption $\theta = 30°$ corresponding to $\bar{\phi} = 30°$ for BBC (Azzouz, 1977). Results in Fig. 4.12 indicate that the peak undrained shear strength predicted by the proposed model for plane strain modes of failure ($d\varepsilon_{yy} = 0$) between PSC and PSE is generally higher than that prediced by Davis and Christian.

b) Residual strength. The residual strength of the soil after significant shearing is believed to be important in penetrations problems which cause very large straining levels in the soil (see Chapter 3). Unfortunately, classical laboratory tests impose limited deformations (and, therefore, limited strains) and, hence, can provide little reliable information regarding residual strength. However, the post-peak behavior in triaxial tests appears to support the proposed hypotheses that the residual strength is identical for any mode of failure (i.e., isotropic) and equal to the strength in the triaxial extension test.

4.5 SUMMARY AND CONCLUSIONS

This chapter describes the soil model proposed by Iwan, Mroz and Prevost and evaluates the model by comparing predictions with laboratroy tests on mormally consolidated resedimented Boston Blue Clay under various undrained shear conditions. For plane strain conditions, the model predicts the same peak strengths obtained by the Davis and Christian (1971) elliptical model in the special case when the ellipse degenerates into a circle.

The model is extended herein by means of a strain-softening rule to describe the post peak behavior of clays. The rule is based on the assumption that, in the triaxial extension mode of loading, the clay behaves as a perfectly plastic material once failure has occurred. The stress-strain

behavior of the clay subjected to monotonic loading is modelled by a hardening rule which reduces the plastic moduli associated with each yield surface as a function of the magnitude of plastic flow, and the necessary parameters are evaluated by means of cyclic triaxial test.

Based on comparisons between predicted and measured stress-strain-strength behavior of normally consolidated resedimented Boston Blue Clay, the following conclusions are reached:

1) the model predictions for plane strain compression and extension tests are reasonably good, especially in describing the post-peak behavior;

2) the simple softening law to model repeated loading leads to good simulation of cyclic triaxial tests, and;

3) the model lacks flexibility to describe accurately intermediate modes of failure (e.g., Direct Simple Shear, cylindrical cavity expansion, etc., ...). Although the DSS test is difficult to interpret and results of "true" triaxial test simulating cylindrical cavity expansion (e.g., Kirby and Esrig, 1979) are scarce, it is apparent that the model overestimates the strength for these two modes of failure.

Improvements in the strength prediction capabilities of the model could be easily achieved by considering yield surfaces of more general shapes (e.g., ellipsoids or spheroids).

However, this requires reliable stress-strain curves for general loading conditions that are not presently available* and hence, the additional complications arising from a more sophisticated model do not appear justifiable at the present time.

*Directional shear and true triaxial tests on clay are presently being conducted at M.I.T.

1. Elastic Shear Modulus

$G/\bar{\sigma}_{vc} = 182.479$

2. Initial Yield Surfaces (Spheres)

Yield Surface Number m	Center Location $\alpha_1^{(m)}/\bar{\sigma}_{vc}$	Radius $k^{(m)}/\bar{\sigma}_{vc}$	Elasto-Plastic Modulus $H_m/\bar{\sigma}_{vc}$
1	0.4874	0.0244	239.649
2	0.4429	0.0942	166.263
3	0.3999	0.1630	110.842
4	0.3625	0.2218	73.895
5	0.3338	0.2675	49.263
6	0.3087	0.3066	32.842
7	0.2895	0.3370	21.895
8	0.2726	0.3629	14.596
9	0.2595	0.3830	9.731
10	0.2480	0.3999	6.487
11	0.2388	0.4127	4.325
12	0.2304	0.4234	2.883
13	0.2237	0.4313	1.922
14	0.2177	0.4379	1.281
15	0.2129	0.4429	0.854
16	0.2088	0.4471	0.570
17	0.2056	0.4503	0.380
18	0.2030	0.4530	0.253
19	0.2010	0.4550	0.169
20	0.1995	0.4565	0.113
21	0.1987	0.4573	0.050
22	0.1980	0.4580	0.000

3. Change in Plastic Modulus (Eq. 4.13).

Rate of Decrease in Plastic Modulus $A_m = 25.0$

Limiting (Minimum) Plastic Modulus $H_m'^{\ell}/H_m'^{0} = 0.10$ } $m=1,2,..,22$

4. Strain Softening; Post-Peak (Eq. 4.15)

Rate of Decrease in Radius $A_p = 10.55$

Initial Radius $k_o^{(p)}/\bar{\sigma}_{vc} = 0.458$

Limiting (Minimum) Radius $k_{\ell}^{(p)}/\bar{\sigma}_{vc} = 0.260$

Table 4.1 Numerical Values of the Model Parameters for Normally Consolidated Resedimented Boston Blue Clay ($K_o = 0.537$)

Test	Predicted Peak Strength
Triaxial Compression	$s_u(TC) = \frac{\sigma_v - \sigma_h}{2}$
Triaxial Extension	$s_u(TE) = \frac{\lvert\sigma_v - \sigma_h\rvert}{2}$
Plane Strain Compression	$s_u(PSC) = \frac{\sigma_v - \sigma_h}{2} = \frac{\sqrt{3}}{3}[s_u(TC) + s_u(TE)] + \frac{1}{2}[s_u(TC) - s_u(TE)]$
Plane Strain Extension	$s_u(PSE) = \frac{\lvert\sigma_v - \sigma_h\rvert}{2} = \frac{\sqrt{3}}{3}[s_u(TC) + s_u(TE)] - \frac{1}{2}[s_u(TC) - s_u(TE)]$
Direct Simple Shear	$s_u(DSS) = \tau_h = \frac{1}{\sqrt{3}}[s_u(TC) + s_u(TE)]$
Pressuremeter	$s_u(PR) = \frac{\sigma_r - \sigma_\theta}{2} = \frac{1}{\sqrt{3}}[s_u(TC) + s_u(TE)]$

Note: All tests are $\overline{CK_oU}$ tests;
$s_u(DSS)$ = apparent strength.

Table 4.2 Peak Strength Prediction for Different Modes of Failure, as a Function of the Strengths for Triaxial Compression and Extension Tests.

Test	Normalized Strength	Predicted	Measured
Triaxial compression	$\frac{\sigma_v - \sigma_h}{2\,\bar{\sigma}_{vc}}$	--[1]	0.328
Triaxial extension	$\frac{\sigma_h - \sigma_v}{2\,\bar{\sigma}_{vc}}$	--[1]	0.130
Plane strain compression	$\frac{\sigma_v - \sigma_h}{2\,\bar{\sigma}_{vc}}$	0.363	0.335
Plane strain extension	$\frac{\sigma_h - \sigma_v}{2\,\bar{\sigma}_{vc}}$	0.165	0.175
Direct simple shear	$\frac{\tau_h}{\bar{\sigma}_{vc}}$ [4]	0.238[2]	0.200
Cylindrical cavity expansion	$\frac{\sigma_r - \sigma_\theta}{2\,\bar{\sigma}_{vc}}$	0.264	0.210[3]

(1) Test used for obtaining model parameters. Therefore, the prediction exactly matches the measured value.

(2) After a 10% reduction to account for non-homogeneity of stresses during the test (Prevost and Hoeg, 1976).

(3) Value from true triaxial test quoted by Kirby and Esrig, 1979. Complete testing information not available.

(4) Apparent strength.

Table 4.3 Predicted vs. Measured Undrained Shear Strength of Laboratory Tests on Normally Consolidated Resedimented Boston Blue Clay.

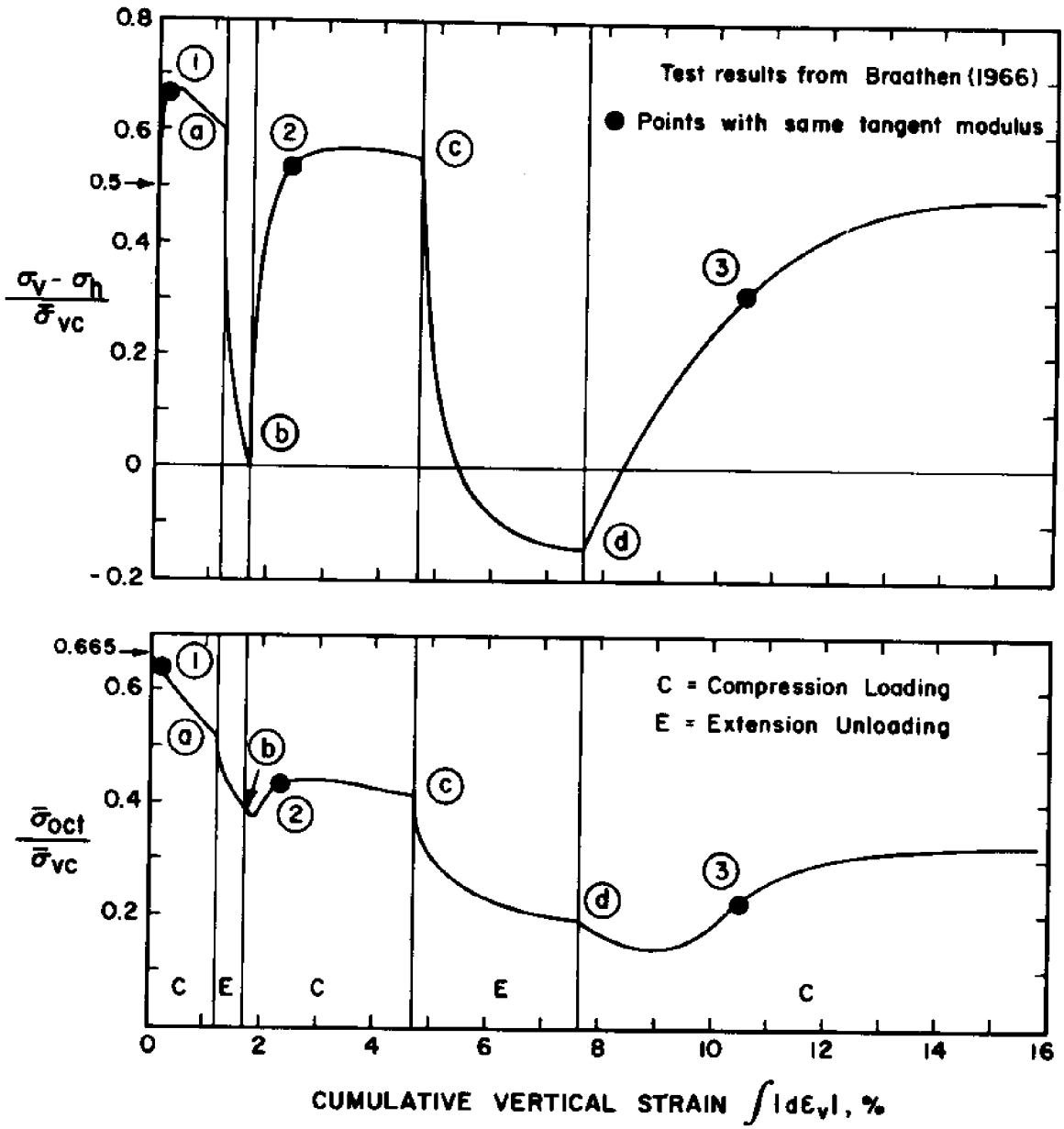

Figure 4.1. Principal stress difference and mean effective stress vs cumulative vertical strain during $\overline{CK_oU}$ triaxial test on normally consolidated Boston Blue Clay.

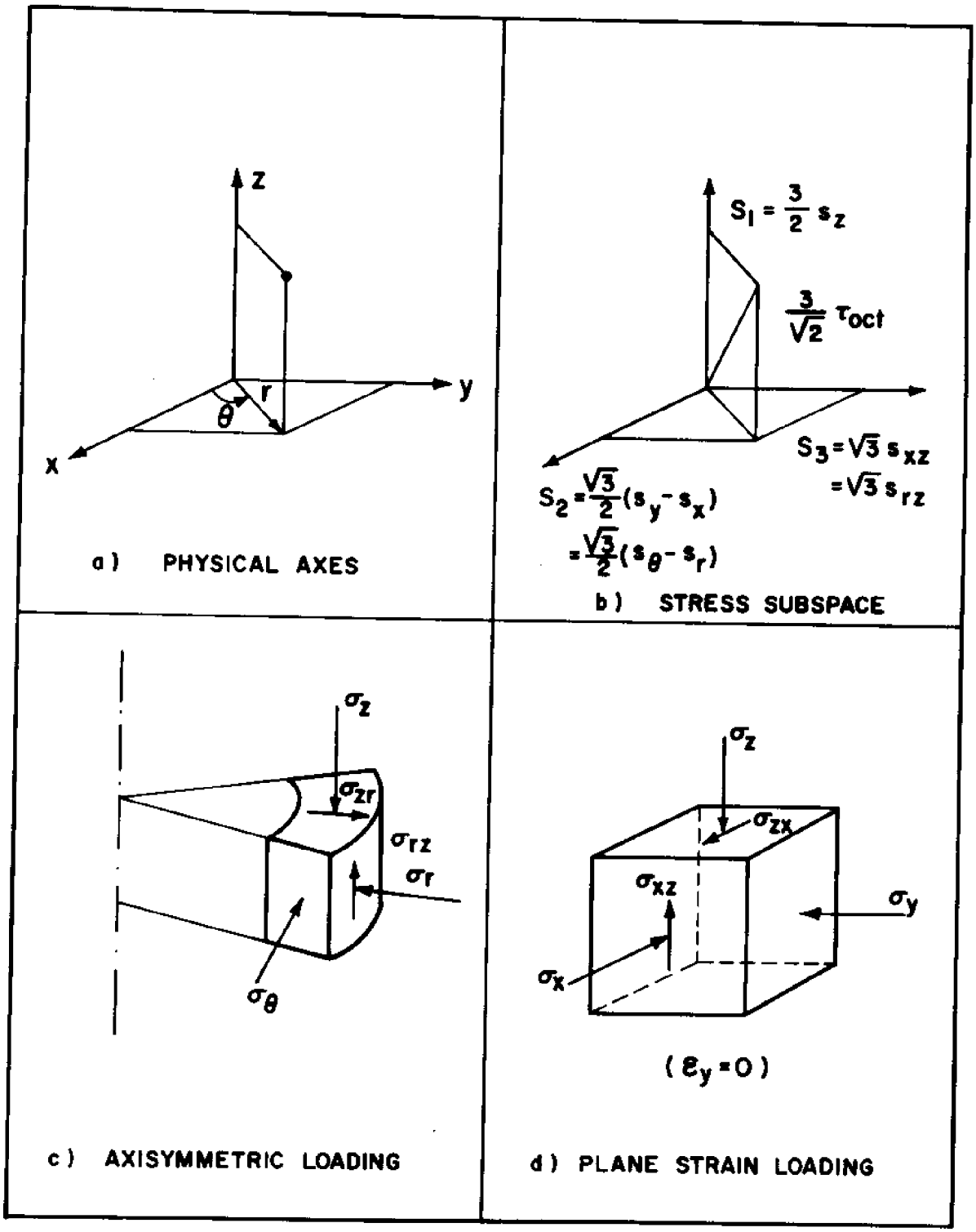

Figure 4.2 Notations and definitions.

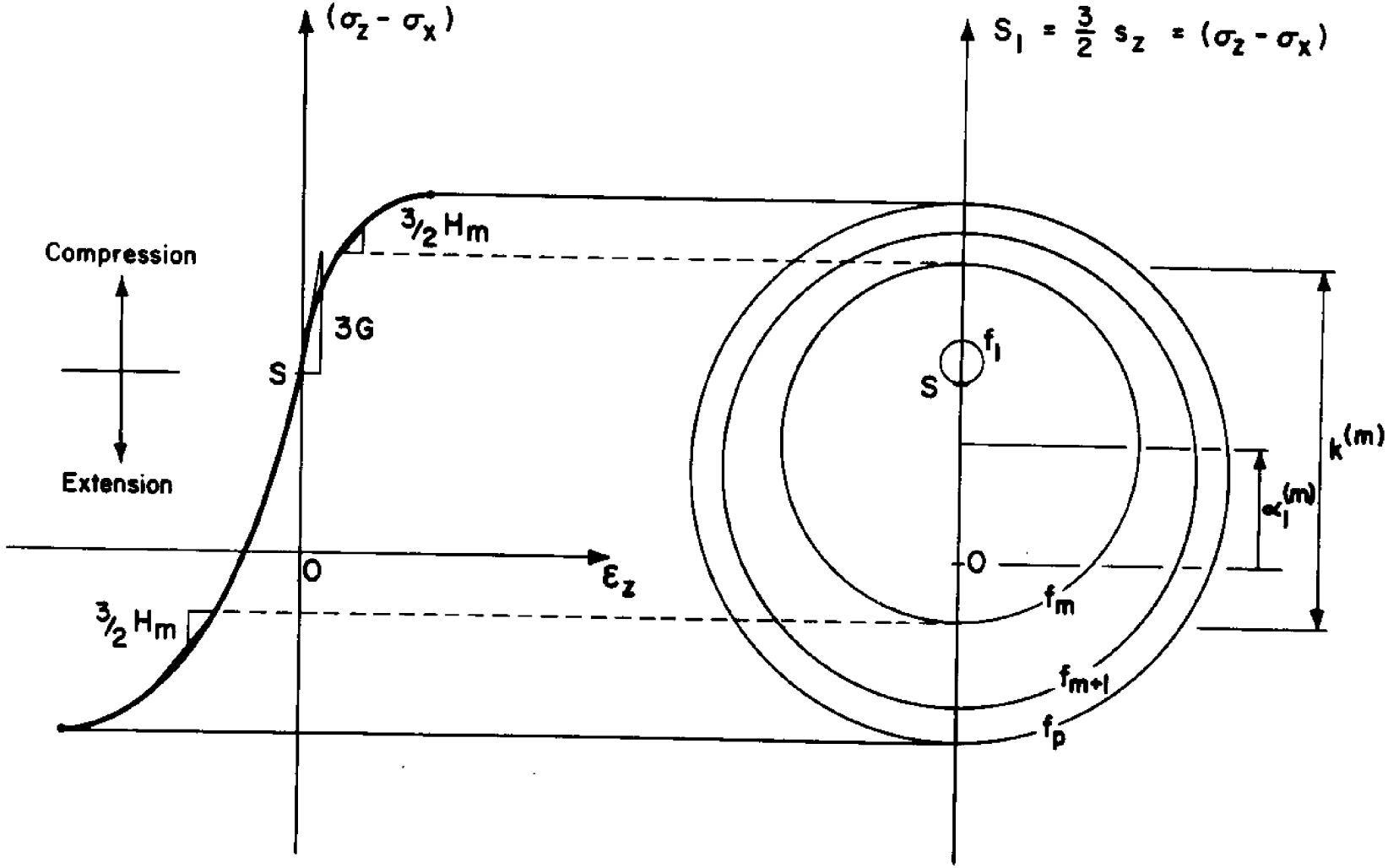

Figure 4.3 Determination of initial model parameters.

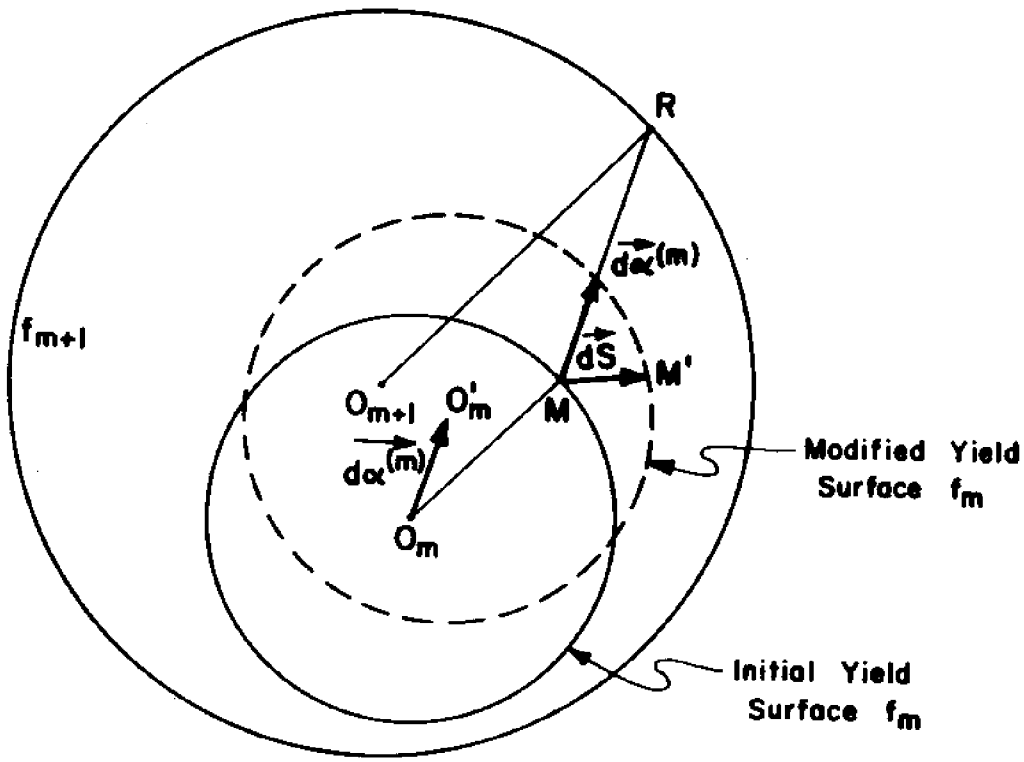

Translation of f_m

$$d\alpha_i^{(m)} = \mu_i \cdot d\mu$$

where

$$\mu_i = \frac{k^{(m+1)}}{k^{(m)}}(S_i - \alpha_i^{(m)}) - (S_i - \alpha_i^{(m+1)});$$

$$d\mu = -\frac{1}{A}(B + \sqrt{B^2 - AC});$$

$$A = \mu_i^2;$$

$$B = \mu_i \cdot (\alpha_i - S_i - dS_i); \text{ and}$$

$$C = 2\,dS_i \cdot (S_i - \alpha_i) + dS_i^2$$

Translation of f_j, $j = 1, \ldots, (m-1)$

$$\frac{S_i - \alpha_i^{(1)}}{k^{(1)}} = \cdots\cdots = \frac{S_i - \alpha_i^{(j)}}{k^{(j)}} = \cdots\cdots = \frac{S_i - \alpha_i^{(m)}}{k^{(m)}}$$

Figure 4.4 Translation of yield surfaces.

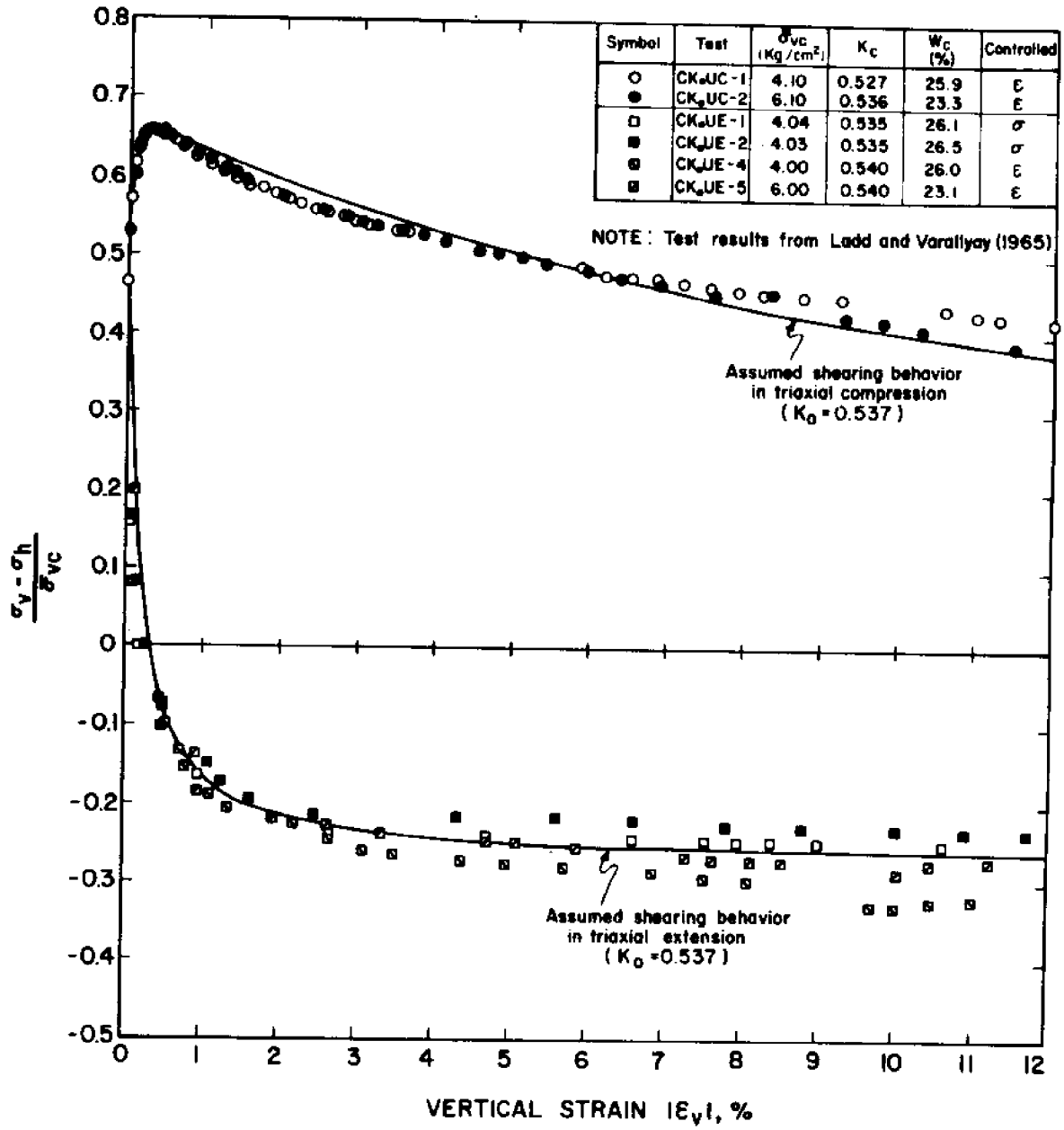

Figure 4.5 Measured stress-strain curves in undrained triaxial tests on normally consolidated resedimented Boston Blue Clay.

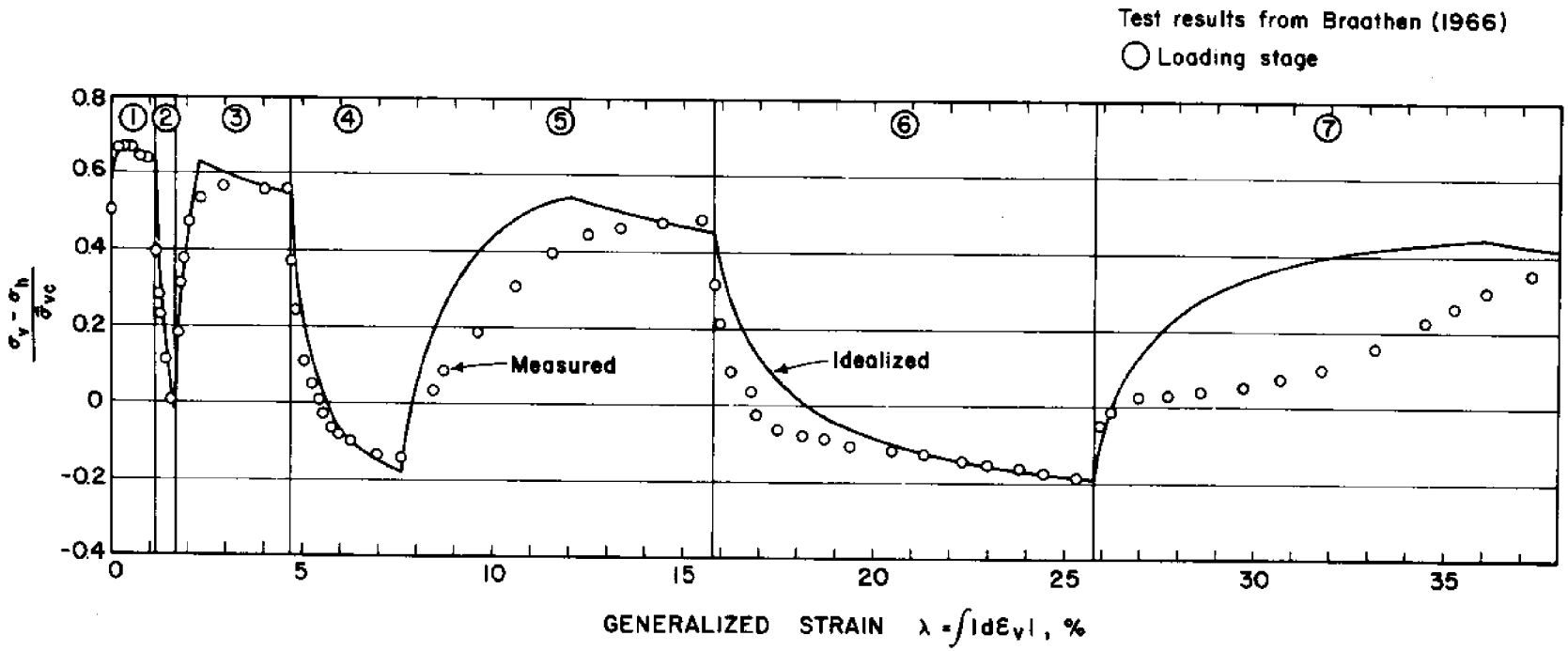

Figure 4.6 Measured and idealized stress-strain curves for an undrained cyclic triaxial test on normally consolidated resedimented Boston Blue Clay.

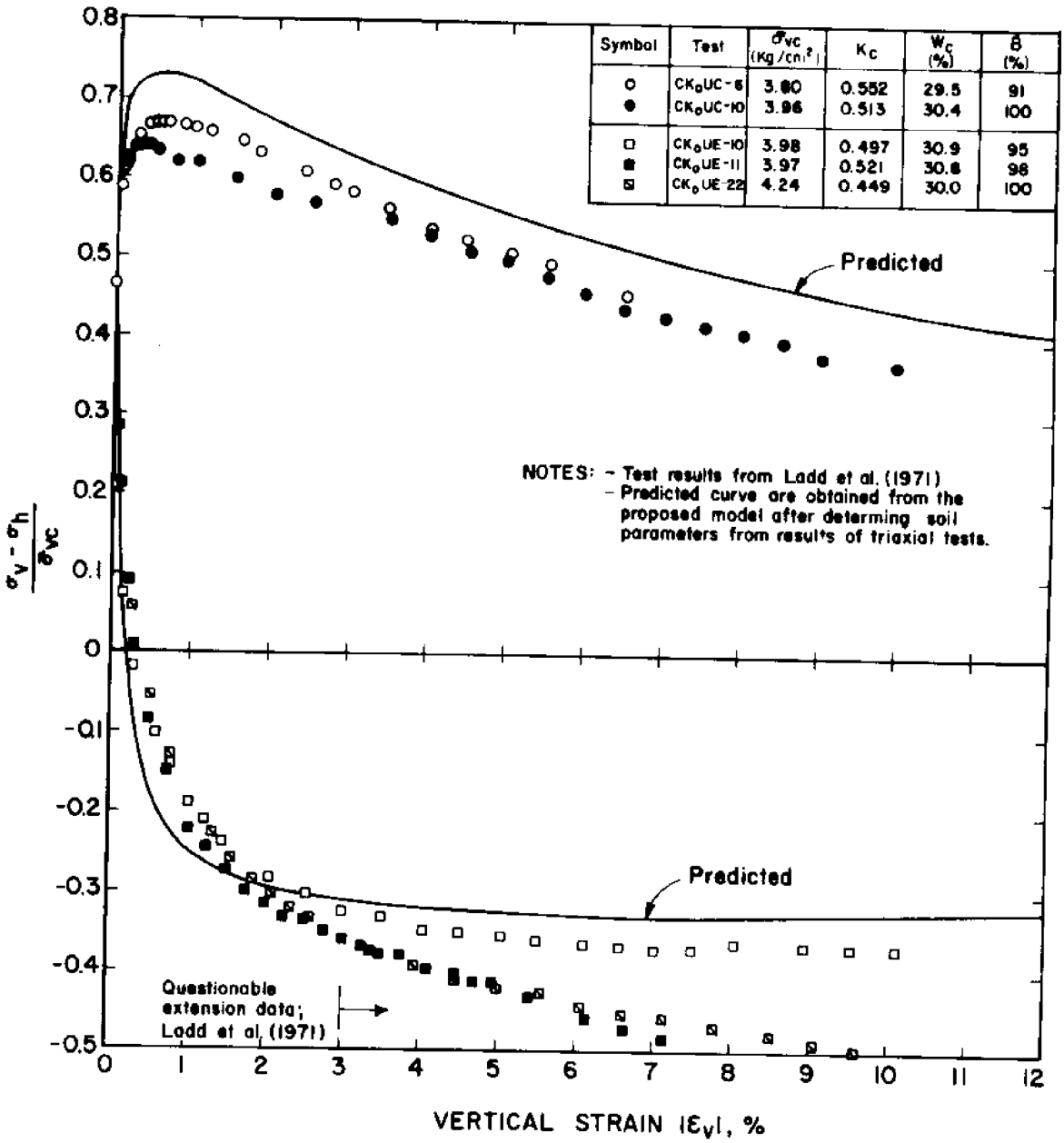

Figure 4.7 Predicted and measured stress-strain curves for undrained plane strain tests on normally consolidated resedimented Boston Blue Clay.

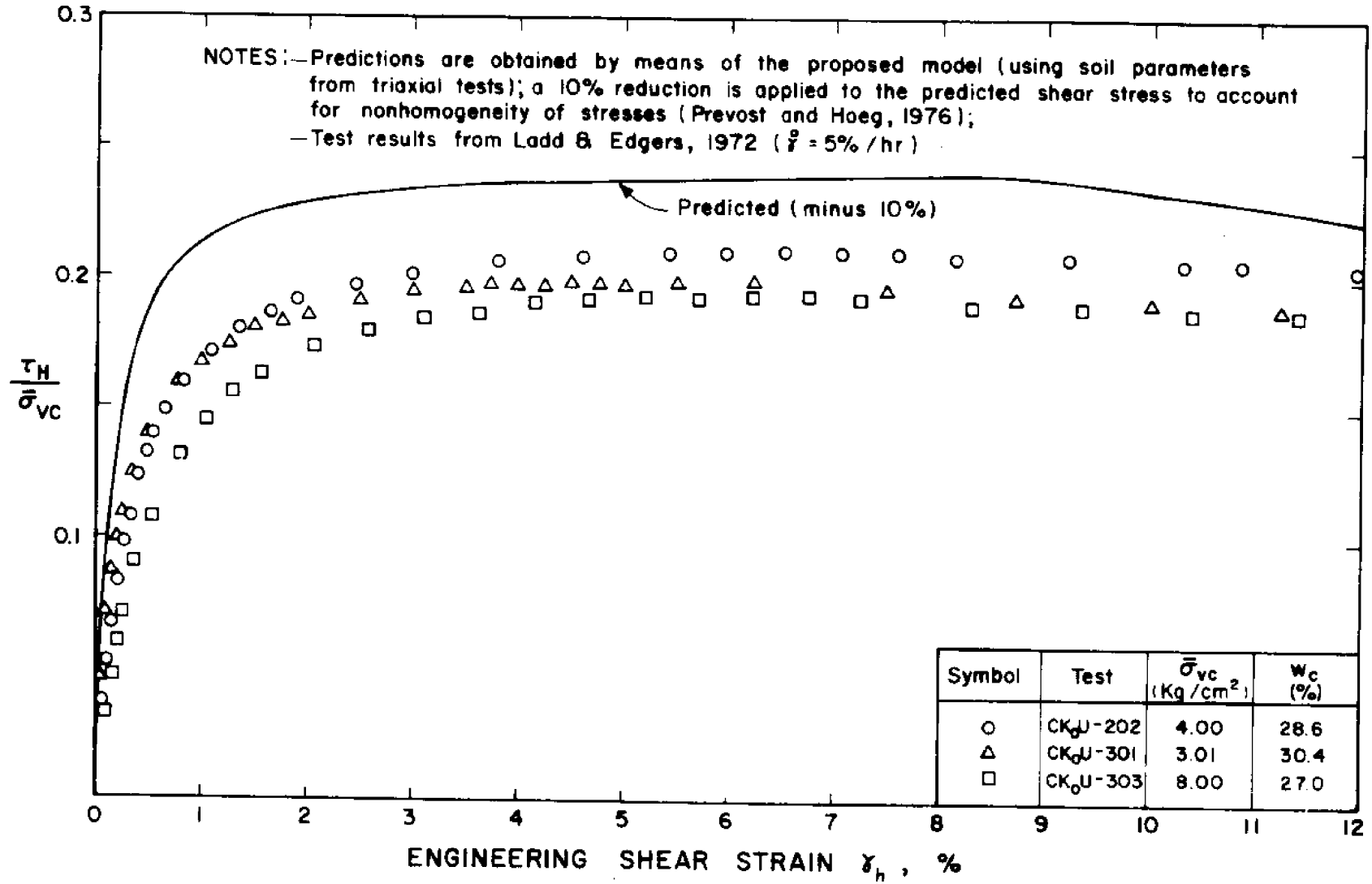

Figure 4.8 Predicted and measured stress-strain curves for undrained Direct Simple Shear tests on normally consolidated resedimented Boston Blue Clay.

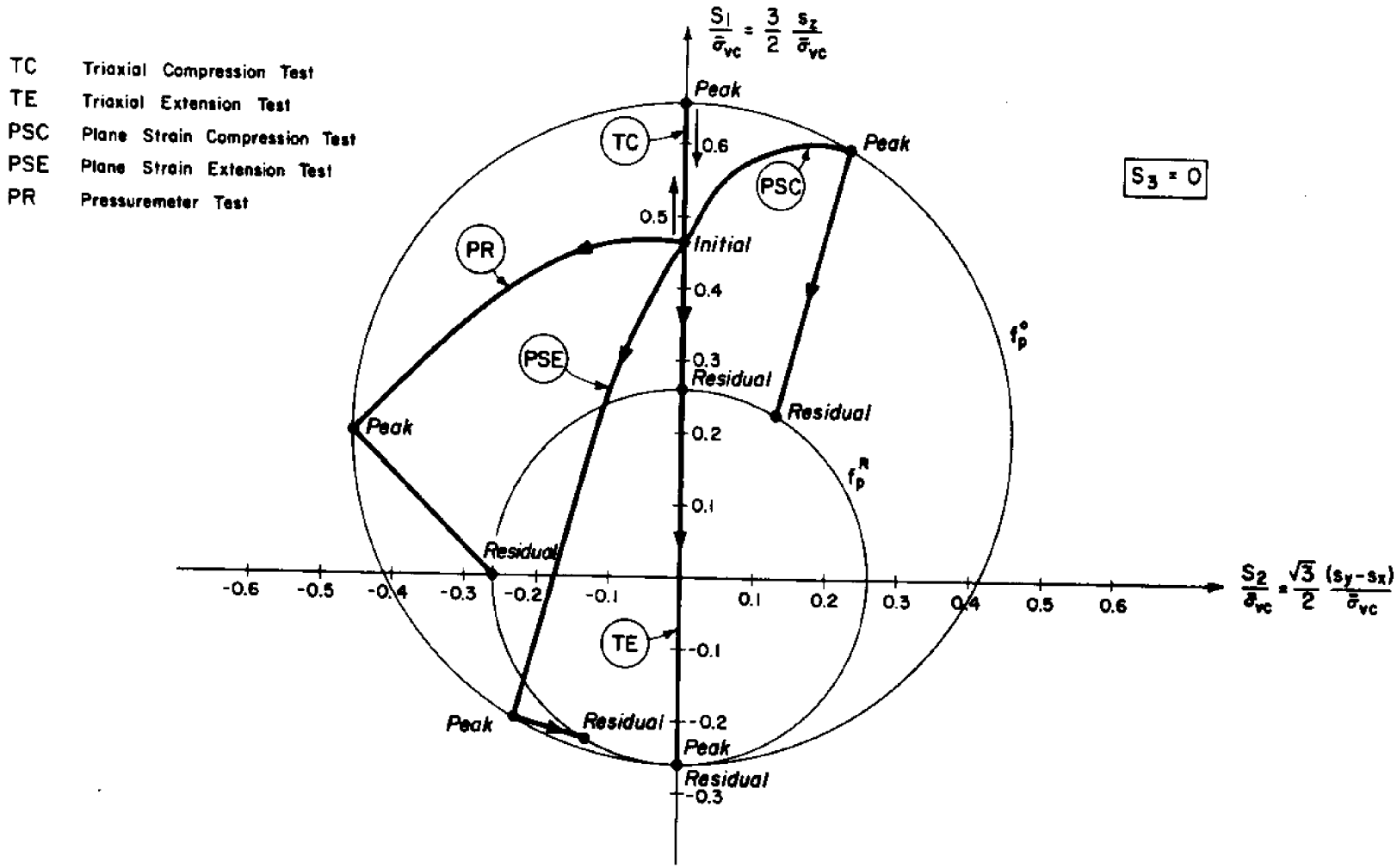

Figure 4.9 Predicted deviatoric stress paths in the (S_1, S_2) plane for undrained tests on normally consolidated resedimented Boston Blue Clay.

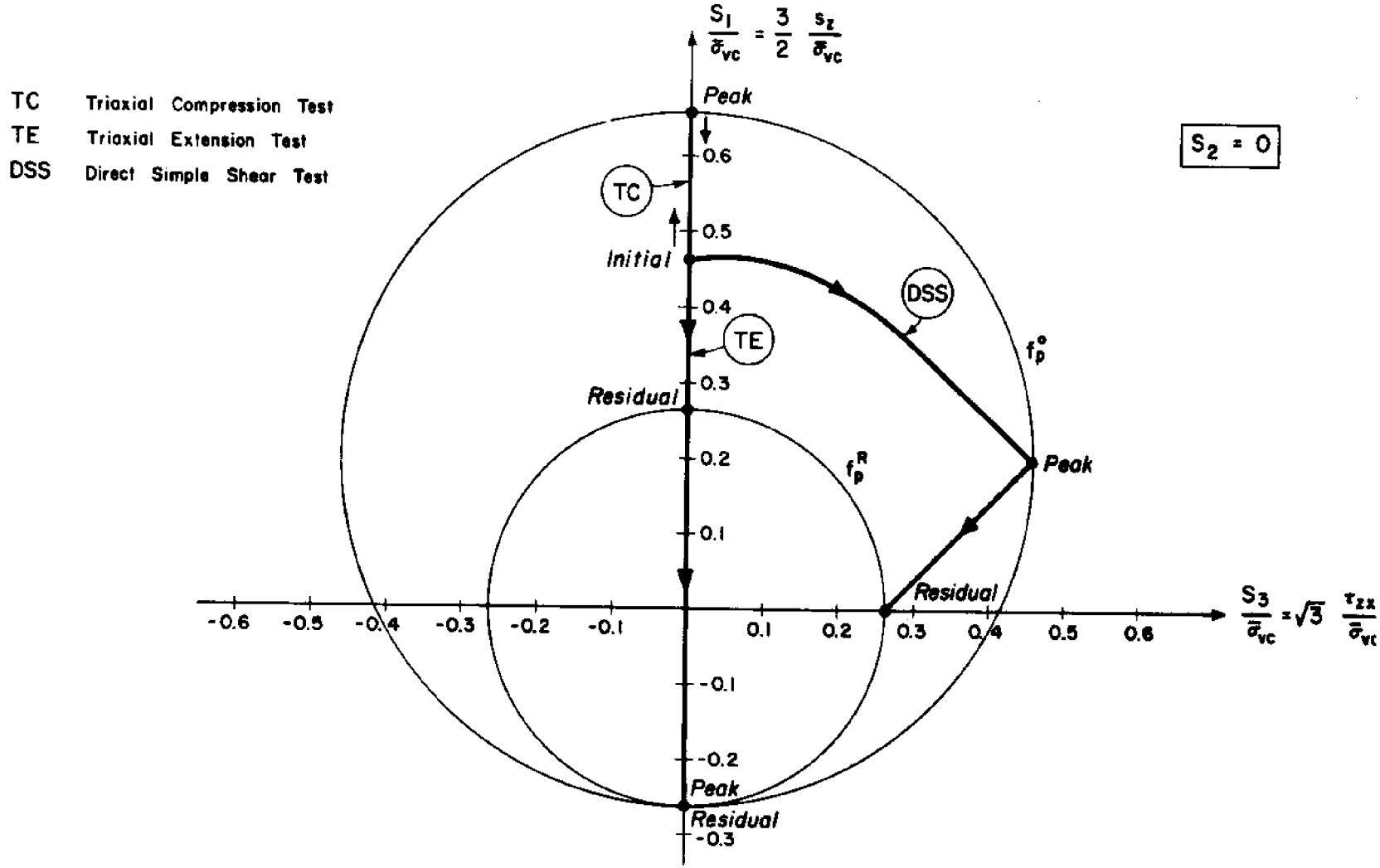

Figure 4.10 Predicted deviatoric stress paths in the (S_1, S_3) plane for undrained tests on normally consolidated resedimented Boston Blue Clay.

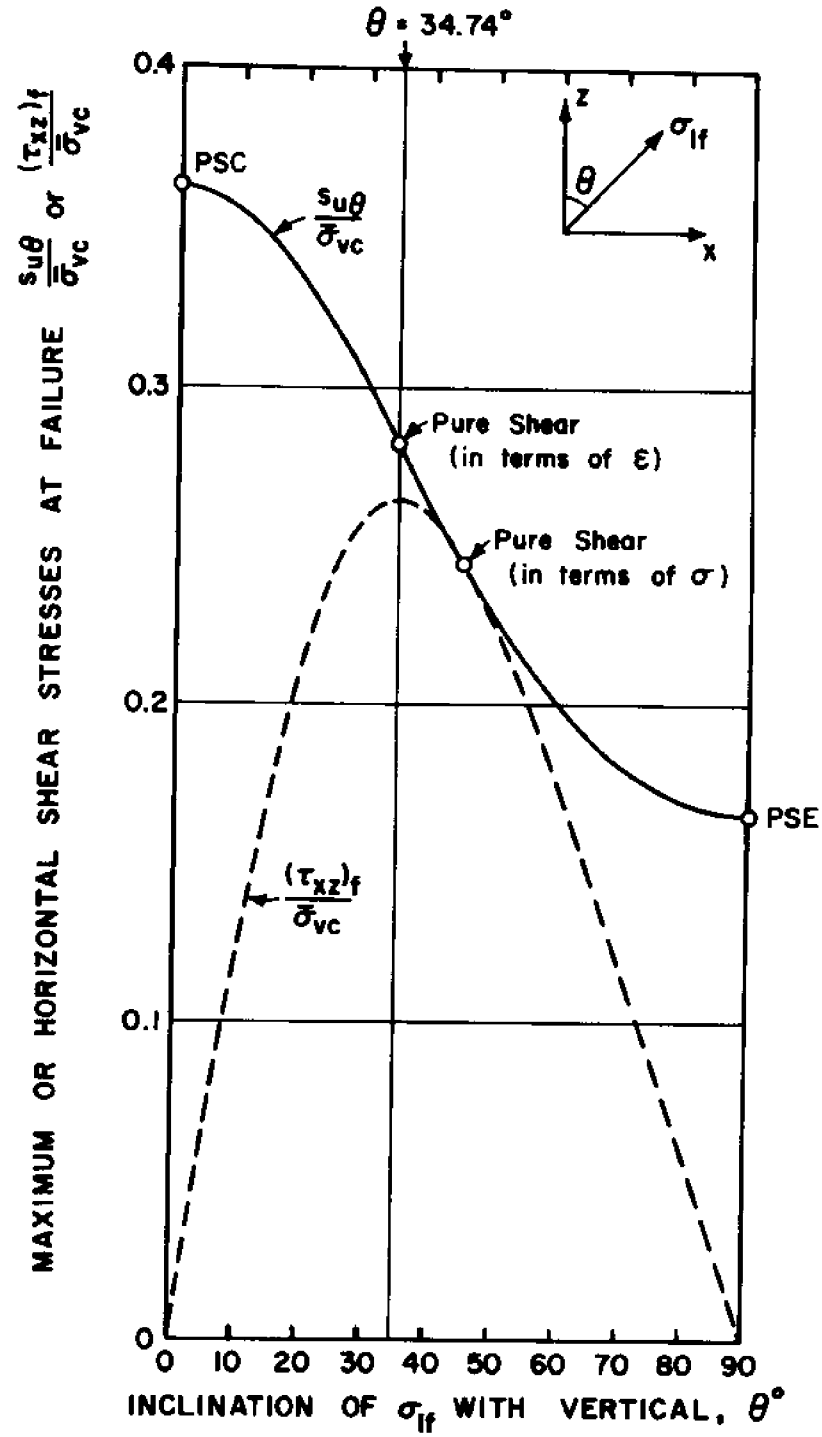

Figure 4.11 Predicted strength anisotropy for plane strain loading.

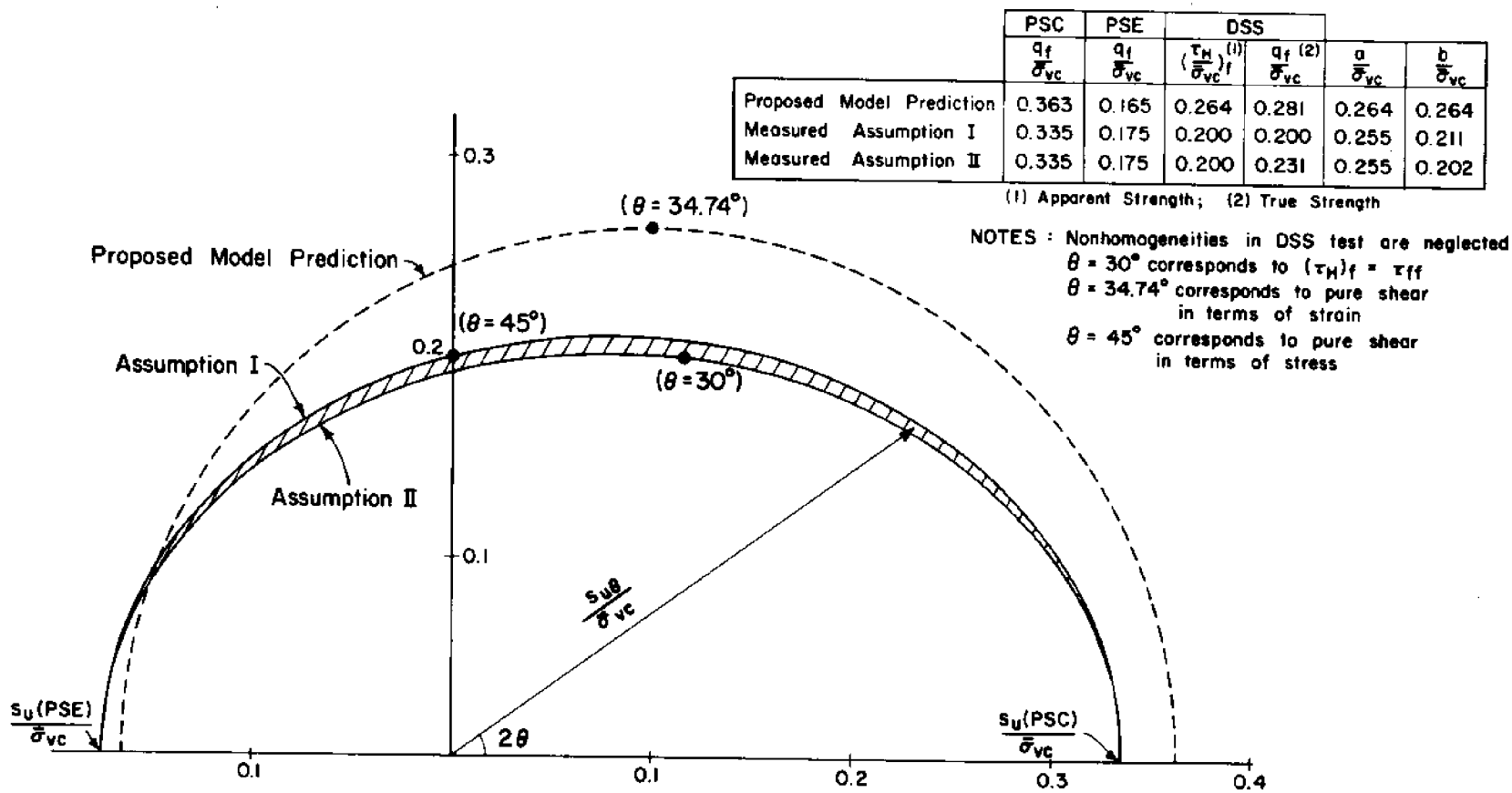

Figure 4.12 Plane strain strength anisotropy predicted by different models.

CHAPTER 5

PORE PRESSURE MODEL

This chapter reviews methods for predicting the excess pore pressures generated by undrained shearing of saturated clays. A new analytical model to estimate the pore pressures during undrained straining of clays (e.g., during pile or cone penetration) is proposed and evaluated by comparing predictions with laboratory test results.

5.1 REVIEW OF PORE PRESSURE PREDICTION METHODS

5.1.1 Stress Theories

In order to predict the excess pore pressure, Δu, during undrained loading of soils, Skempton (1954) proposes an expression for Δu in terms of the changes in principal stresses $\Delta\sigma_1$ and $\Delta\sigma_3$:

$$\Delta u = B[\Delta\sigma_3 + A(\Delta\sigma_1 - \Delta\sigma_3)] \qquad (5.1)$$

where A and B are pore pressure parameters.

The B parameter relates the increase in pore pressure to an all around (isotropic) increase in total stress. For saturated clays, where the skeleton compressibility is very large compared to the water compressibility, the B parameter equals

unity and Eq. 5.1 reduces to:

$$\Delta u = \Delta\sigma_3 + A(\Delta\sigma_1 - \Delta\sigma_3) \qquad (5.2)$$

The A parameter relates the increase in pore pressure to an increase in the stress deviator (or principal stress difference), $\Delta(\sigma_1 - \sigma_3)$. For a linearly elastic isotropic material, loaded in triaxial compression, A = 1/3, and in triaxial extension, A = 2/3. The variation of A with vertical strain, ε_v, during a $\overline{CK_oU}$ triaxial compression test on normally consolidated resedimented Boston Blue Clay (BBC) is shown in the lower part of Fig. 5.1*. The A parameter, initially equals 1/3, reaches a value $A_f \simeq 0.50$ at peak strength and then increases indefinitely as the stress deviator approaches its consolidation value (i.e., $\Delta(\sigma_1 - \sigma_3) = 0$). Figure 5.1 clearly indicates that, for saturated clays, the A parameter expressed by Eq. 5.2 cannot be used without difficulty in predictions involving strain softening of the soil. In addition, the A parameter, for a given soil type, is very sensitive to the initial and the applied stress systems. Despite these shortcomings, and perhaps because of simplicity in concept and computation, A is the pore pressure parameter most widely used.

Henkel and Wade (1966) recognized that Eq. 5.2 does not adequately separate the contribution of isotropic and deviatoric stress increments to the excess pore pressure during undrained shear

---

*See Chapter 4 for information on resedimented BBC.

of saturated clays, and expressed Δu in terms of increments of stress invariants*:

$$\Delta u = \Delta\sigma_{oct} + a\ \Delta\tau_{oct} \qquad (5.3)^{**}$$

where:

$$\sigma_{oct} = \frac{1}{3}\ (\sigma_1 + \sigma_2 + \sigma_3) \qquad (5.4);$$

$$\tau_{oct} = \frac{1}{3}\ [(\sigma_1 - \sigma_2)^2 + (\sigma_2 - \sigma_3)^2 + (\sigma_1 - \sigma_3)^2]^{\frac{1}{2}} \qquad .....(5.5);$$

and Δ denotes the difference between the present and initial (at end of consolidation) values. The major advantage of the pore pressure parameter "a" in Eq. 5.3 is that it equals zero for a linearly elastic isotropic material subjected to any kind of loading and, hence, describes the tendency of the soil to change in volume (if drained) when subjected to a pure shear (deviatoric) loading condition. Furthermore, a is much less sensitive than Skempton A parameter to the applied stress system for soils. However, as illustrated in Fig. 5.1, a initially equal to zero, reaches a value $a_f \simeq 0.35$ at peak

---

*In an earlier publication (1960), Henkel expressed Δu in terms of invariants of stress increments but later, based on experimental evidence, abandoned this approach.

**Henkel and Wade (1966) define the octahedral shear stress as 3 $\Delta\tau_{oct}$ in Eq. 5.5 and, therefore, write a/3 $\Delta\tau_{oct}$ instead of a $\Delta\tau_{oct}$ in Eq. 5.3.

strength and then increases indefinitely as the octahedral shear stress approaches its consolidation value (i.e., $\Delta\tau_{oct} = 0$). This indicates that, for saturated clays, similarly to Skempton A parameter, the a parameter expressed by Eq. 5.3 cannot be readily used in predictions involving strain softening of the soil.

Henkel equation (Eq. 5.3) is, therefore, better suited for estimating excess pore pressures in stress-controlled problems where soil elements are subjected to general loading conditions but, only up to a strain level where no significant softening has occurred.

5.1.2 Strain Theory

Vaid and Campanella (1974) performed a comprehensive program of triaxial and plane strain undrained tests with pore pressure measurements on normally K_o - consolidated Haney clay* specimens trimmed from block samples. For both triaxial and plane strain conditions, they investigate four total stress paths: compression loading ($\Delta\sigma_1 > 0$, $\Delta\sigma_3 = 0$), compression unloading ($\Delta\sigma_1 = 0$, $\Delta\sigma_3 < 0$), extension loading ($\Delta\sigma_1 = 0$, $\Delta\sigma_3 > 0$) and extension unloading ($\Delta\sigma_1 < 0$ $\Delta\sigma_3 = 0$). In order to make a valid comparison between triaxial and plane strain results, all specimens were initially normally consolidated under K_o conditions to the same vertical effective stress,

---

*Canadian clay with PI = 18% and sensitivity = 6-10.

$\bar{\sigma}_{vc}$ = 6 kg/cm^2. Figure 5.2.a compares the pore pressure change, Δu, versus axial strain during triaxial and plane strain shear and, illustrates the importance of the total stress system on Δu. On the other hand, when the change in octahedral (or mean) normal stress, $\Delta\sigma_{oct}$, is eliminated and the pore pressure change due to shear alone, Δu_s, is plotted, Fig. 5.2.b, much more consistent results are obtained.

$$\Delta u_s = \Delta u - \Delta\sigma_{oct} \tag{5.6}$$

Figure 5.3.b indicates that:

(1) For a given type of test (triaxial or plane strain) and a given mode of shearing (compression or extension) Δu_s is independent of the total stress path (loading or unloading); i.e., the shear induced pore pressure, Δu_s, is only a function of the stress path. This important result indicates that for a saturated clay sheared under undrained conditions, Δu_s can be predicted in terms of strains independently of the mean (or octahedral normal) stress level;

(2) in the compression mode, Δu_s is virtually the same for triaxial and plane strain tests*. In the extension mode, Δu_s is slightly larger ($\simeq$ 10%) for plane strain than for triaxial test and, finally;

(3) in extension tests, Δu_s develops earlier (at a faster

---

*Vaid and Campanella (1974) do not mention how $\Delta\sigma_2$ (total stress increment normal to the no displacement plane) was obtained in order to evaluate $\Delta\sigma_{oct}$ (in Eq. .6). However, it is probable that $\Delta\sigma_2$ was measured by means of a total stress cell as in the MIT plane strain device.

rate with strain) than in compression tests, but the limiting values are approximately equal ($\frac{\Delta u_s}{\bar{\sigma}_{vc}} = 0.33 - 0.37$).

5.2 EFFECT OF LOADING REVERSAL ON PORE PRESSURES

Lo (1961) performed undrained stress-controlled cyclic tests on normally isotropically consolidated Fornebu clay* where the vertical stress was increased (or decreased) in steps. Sufficient time was allowed between steps for the deviator stress and the pore pressure to reach equilibrium values. Therefore, each test consisted of a series of undrained incremental creep tests performed at various stress levels. Figure 5.3 shows the principal stress difference (or deviator stress) and pore pressure vs. axial strain; and pore pressure vs. principal stress difference for one of Lo's tests (Test number 2).

Comparing Figs. 5.3.b and 5.3.c, it is clear that the pore pressure is better correlated to strain than to principal stress difference during these repeated loading tests. In fact, the pore pressure appears to be uniquely related to strain when the applied stresses are maintained for a long period of time after each load increment (or for very slow rate of loading). Unfortunately, strain controlled cyclic test results on Boston Blue Clay presented subsequently do not confirm this

---

*Norwegian clay with PI = 34 ± 6, Sensitivity = 2-4.

unique relationship between pore pressure and strain in strain-controlled cyclic tests. Furthermore, changes in octahedral normal stress, $\Delta\sigma_{oct}$, associated to changes in principal stress difference, $\Delta(\sigma_1 - \sigma_1)$, vary for different loading conditions and, thus, similar relationship for other applied stress systems is not warranted.

Figure 5.4.b shows the excess pore pressure Δu vs. vertical strain, ε_v, during a $\overline{CK_oU}$ cyclic test* on normally consolidated resedimented Boston Blue Clay (Braathen, 1966) and indicates that in contrast to the results reported by Lo (1961) Δu is very sensitive to strain (or stress) history and exhibits a very complicated behavior. Variation in the shear induced pore pressure, Δu_s, with vertical strain (Fig. 5.4.c) exhibits a somewhat simpler behavior and indicates that:

a) When the shearing direction is changed from compression to extension (a,c and e in Fig. 5.4.c), the rate of shear induced pore pressure generation increases drastically;

b) When the shearing direction is changed from extension to compression (b and d in Fig. 5.4.c), the shear induced pore pressure, Δu_s, first decreases and then increases to reach, asymptotically, the curve corresponding to a monotonic (compression) loading (dashed line in Fig. 5.4.b and c), and;

---

*This is the same test described in Chapter 4 (see Figs. 4.1 and 4.6); the loading history during the test is illustrated by means of total and effective stress paths (Fig. 5.4.a).

c) The curves of Δu_s vs. vertical strain during extension shearing (ab, cd and ef in Fig. 5.4.c) appear to tend toward a common asymptotic value, $(\Delta u_s)_{max}$.

Results of triaxial compression tests, subjected to straining reversal, reported by Bishop and Henkel (1953) are presented in Fig. 5.5. Although they plot the total excess pore pressure, Δu, comparison of Figs. 5.4.a and 5.5.a qualitatively confirms the above remarks on Δu_s

In summary, a review of existing methods for predicting the increments in pore pressure, Δu, that develop in saturated clays due to undrained shearing, indicates that Δu should be divided into two components (Henkel, 1960, Henkel and Wade, 1966): the increment in the mean total stress, $\Delta\sigma_{oct}$, which is controlled by equilibrium considerations in each particular problem; and the shear induced pore pressure, Δu_s, caused by the soil tendancy to dilate (or contract) upon shearing.

The prediction of Δu_s depends on the type of problem at hand:

(a) in stress-controlled problems (e.g., flexible footing on top of a half-space) where the stress increments can be estimated reliably, Δu_s can be determined knowing Henkel "a" parameter and the octahedral shear stress τ_{oct} (Eq. 5.5); and

(b) in strain controlled problems (e.g., cone penetration, pile driving) where strains in the soil can be estimated more reliably than stress-increments, Δu_s should be

predicted by means of a model relating Δu_s to the strain history. Such a model is described below.

5.3 PROPOSED PORE PRESSURE PREDICTION MODEL

This section presents a new analytical model for predicting the shear induced excess pore pressure, Δu_s (Eq. 5.6), generated in a normally consolidated saturated clay by undrained shearing. The model is incremental and anisotropic and, can predict Δu_s for general strain paths (various shearing modes as well as loading - unloading).

5.3.1 General Description

The incremental shear induced excess pore pressure, $d(\Delta u_s)$, is expressed as a function of the octahedral shear strain increment, $d\gamma_{oct}$, by the expression

$$d\Delta(u_s) = \sqrt{2} \cdot I(\varepsilon_{ij}) \cdot |d\gamma_{oct}| \qquad (5.7)$$

where the scalar function I, which controls the rate of shear induced pore pressure, depends on strain history and, the octahedral shear strain, γ_{oct}, given by

$$\gamma_{oct} = \frac{1}{3}[(\varepsilon_1 - \varepsilon_2)^2 + (\varepsilon_2 - \varepsilon_3)^2 + (\varepsilon_3 - \varepsilon_1)^2]^{\frac{1}{2}} \qquad (5.8)$$

Therefore, Δu_s can be estimated by integrating Eq. 5.7 along the strain path once the function I is determined. In order to describe the funtion I, the strain space (ε_{ij}) is divided into a finite number of regions where I is constant. These

regions are limited by surfaces g_m corresponding to a rate of shear induced pore pressure generation I_m. For simplicity, the surfaces g_m are described in the ε_{ij} space by the equation:

$$(\varepsilon_{ij} - \beta_{ij}^{(m)})(\varepsilon_{ij} - \beta_{ij}^{(m)}) = \rho_m^2 \qquad (5.9)$$

where $\beta_{ij}^{(m)}$ and ρ_m are the center coordinates and the size of the surface g_m, respectively.

During loading, the surfaces g_m which are reached by the strain point (traveling along the strain path) are translated remaining tangent to each other at the strain point. The rules governing the translation of the surfaces g_m are identical to those presented in Chapter 4 so that the surfaces do not change in size and never intersect each other (see Fig. 5.6). The rate of shear induced pore pressure generation, I_m, associated to the surface g_m is independent of the relative magnitude of the strain increment components (i.e., independent of the direction of the strain increment vector) and, of the strain history when the soil had been only subjected to monotonic loading. Upon loading reversal* (unloading), all I_m are reduced from their initial value I_m to an updated value I_m° described from the expression:

---

*By definition, loading reversal occurs when the strain increment vector is pointing towards the interior of the current surface.

$$I_m = \left(\frac{(\Delta u_s)_{max} - \Delta u_s}{(\Delta u_s)_{max}}\right) I_m^\circ \qquad (5.10)$$

in which $(\Delta u_s)^*_{max}$ and Δu_s are the maximum and current shear induced pore pressures, respectively. Since the model will only be applied to strain paths involving at most one loading reversal (cone penetration problem), the variation of Δu_s for more general cyclic straining is not needed herein.

Application of the model, therefore, requires knowledge of the initial location and size of the surface ($\beta_{ij}^{(m)}$ and ρ_m) and of the maximum shear induced pore pressure, $(\Delta u_s)_{max}$, which are determined experimentally as explained later.

5.3.2 Model Implementation

Although the model can readily be applied to general strain paths where the six strain components, ε_{ij}, vary, the following derivations are limited to the 3-dimensional E_i - space described in detail in Chapters 3 and 4. The E_i - space is very convenient for visualizing the strain paths of classical laboratory tests (triaxial, plane strain and direct simple shear) and field tests (pressuremeter, cone penetration) under idealized conditions. The strains E_i (= E_1, E_2 and E_3) are respectively given in cartesian and cylindrical coordinates by:

---

* $(\Delta u_s)_{max}$ which is the asymptotical value of Δu_s, after strain reversal, will be defined later in this chapter.

$$E_1 = \varepsilon_{zz};\quad E_2 = \frac{1}{\sqrt{3}}(\varepsilon_{yy} - \varepsilon_{xx});\quad E_3 = \frac{2}{\sqrt{3}}\ \varepsilon_{xz} \qquad (5.11)$$

and

$$E_1 = \varepsilon_{zz};\quad E_2 = \frac{1}{\sqrt{3}}(\varepsilon_{\theta\theta} - \varepsilon_{rr});\quad E_3 = \frac{2}{\sqrt{3}}\ \varepsilon_{rz} \qquad (5.12)$$

In the E_i - space, the proposed surfaces g_m are spheres described by the equation:

$$\sum_i [E_i - \beta_i^{(m)}]^2 - \rho_m^2 = 0 \qquad (5.13)$$

in which $\beta_i^{(m)}$ and ρ_m are the center coordinates and the radius of the sphere g_m, respectively. The octahedral shear strain, γ_{oct}, is equal to:

$$\gamma_{oct} = \frac{1}{3}\left[(\varepsilon_{xx} - \varepsilon_{yy})^2 + (\varepsilon_{yy} - \varepsilon_{zz})^2 + (\varepsilon_{zz} - \varepsilon_{xx})^2 + 6\,\varepsilon_{xz}^2\right]^{\frac{1}{2}} \qquad \ldots.(5.14)$$

After substituting Eqs. 5.11 into Eq. 5.14

$$\gamma_{oct} = \frac{1}{\sqrt{2}}\left[E_1^2 + E_2^2 + E_3^2\right]^{\frac{1}{2}} \qquad (5.15)$$

and Eq. 5.7 becomes:

$$d(\Delta u_s) = I_m \cdot \left|d\left[E_1^2 + E_2^2 + E_3^2\right]\right| \qquad (5.16)$$

Prior to undrained shearing, the sizes and locations of the spheres g_m reflect the initial anisotropic behavior of the clay. In most cases of interest, initial anisotropy develops during deposition and subsequent consolidation under one-dimensional straining conditions, thus, leading to symmetry about the

vertical z-axis (i.e., cross-anisotropy). The surfaces g_m are, therefore, initially centered along the E_1 -axis ($\beta_2^{(m)} = \beta_3^{(m)} = 0$, for any m).

In order to determine the model parameters describing the initial spheres g_m, curves of $(\Delta u_s/\bar{\sigma}_{vc})$ vs. axial strain from K_o-consolidated undrained triaxial compression and extension tests are utilized as illustrated in Fig. 5.7. During triaxial testing the strain point moves along the E_1-axis and, therefore, the spheres g_m remain centered on the E_1-axis; furthermore, Eq. 5.16 simplifies to:

$$d(\Delta u_s) = I_m \, |dE_1| = I_m \, |d\,\epsilon_{zz}| \qquad (5.17)$$

The two curves for compression and extension are then subdivided into a finite number of pairs of linear segments with slope of opposite sign and the same absolute value. The starting points of the m^{th} segments along the compression and extension sides provide the upper and lower intersections of the sphere g_m with the E_1-axis, respectively. These two points of intersection completely define the initial location and size of the sphere g_m (i.e., $\beta_1^{(m)}$ is equal to the average ordinate and ρ_m is equal to half the distance between the two points). The common absolute value of the slope of the two corresponding segments equals $\frac{1}{I_m}$ and, hence, determines the rate of pore pressure generation I_m associated to g_m. The value of $\frac{(\Delta u_s)_{max}}{\bar{\sigma}_{vc}}$ is obtained from results of cyclic triaxial tests as illustrated in Section 5.4.

5.3.3 Computer Program

The pore pressure model described above was incorporated in a computer program (coded in FORTRAN IV) which is listed and explained for the user in Appendix D. Input data consists of the initial spheres radii ρ_m, ordinates, $\beta_1^{(m)}$, and associated rate of pore pressure generation, I_m and of the parameters $(\Delta u_s)_{max}/\bar{\sigma}_{vc}$ to predict unloading (if any). The strain path to be followed is input by means of successive strain increment vectors. For each strain increment vector, the program computes the corresponding deviatoric pore pressure increment, modifies the sphere configuration and prints the value of the updated deviatoric pore pressure.

5.4 EVALUATION OF THE PORE PRESSURE MODEL

5.4.1 Model Parameters

The soil considered in this section consists of normally consolidated Boston Blue Clay (BBC) described earlier in section 4.4.1.

Figure 5.8 shows results of $\overline{CK_oU}$ triaxial compression and extension tests performed on normally consolidated BBC with different vertical consolidation stresses. These results exhibit little scatter (less than 12%), thus confirming that Δu_s can be normalized with the vertical consolidation effective stress $\bar{\sigma}_{vc}$. In order to facilitate the determination of the model parameters (as outlined in Fig. 5.7), each set of experimental data points is fitted with an hyperbola. The hyperbolae

for compression and extension yield the same asymptotic value $(\frac{\Delta u_s}{\bar{\sigma}_{vc}})_{lim} = 0.43$. This means that at large strains, the clay develops the same shear induced pore pressure in triaxial compression and extension.

The maximum value of the shear induced excess pore pressure, $(\Delta u_s)_{max}$, developed after straining reversal, is evaluated from the results of cyclic triaxial tests presented in Fig. 5.4.c. For BBC, $\frac{(\Delta u_s)_{max}}{\bar{\sigma}_{vc}} = 0.54$ proved to be a reasonable value in the three cyclic triaxial tests with similar stress paths reported by Braathen (1966).

Numerical values of the model parameters for normally consolidated resedimented BBC are tabulated in Table 5.1. The equations necessary for computing Δu_s in classical laboratory tests are given in Table 5.2.

5.4.2 Pore Pressure Predictions

Plane Strain Tests

Figure 5.9 compares predictions of the model (solid lines) with results of $\overline{CK_oU}$ plane strain compression and extension tests on normally consolidated resedimented BBC. Changes in the octahedral total normal stress, $\Delta\sigma_{oct}$ during these tests are evaluated from the measured values of the three normal total stresses as tabulated by Ladd et al (1971).

In compression tests, the predicted shear induced pore pressure Δu_s, (Fig. 5.9.a) is approximately 10% higher than measured, whereas, in extension tests, Δu_s (Fig. 5.9.b) is

mostly within the scatter of experimental data.

Direct Simple Shear Tests

In order to compare the predicted and measured pore pressures, Δu($= \Delta\sigma_{oct} + \Delta u_s$), in a DSS test, two problems arise: (1) the change in the octahedral total normal stress, $\Delta\sigma_{oct}$, in the experiment cannot be determined from measurements and; (2) the stresses and strains are not uniform throughout the sample. Therefore, simplifying assumptions are required.

Based on the detailed discussion of the DSS test in Chapter 4, Δu is predicted in the following manner:

(1) Stresses and strains are assumed to be uniform within the soil sample which is sheared in a pure shear mode in terms of strains (idealized testing conditions);

(2) Δu_s is predicted with the proposed model by following a strain path located along the E_3-axis (i.e., $d\varepsilon_{zz} = d\varepsilon_{xx} = d\varepsilon_{yy} = 0$, $d\varepsilon_{xz} \neq 0$); and,

(3) $\Delta\sigma_{oct}^{*}$ is evaluated by means of the deviatoric stress model of Chapter 4.

Figure 5.10 shows the predicted and measured values of Δu vs. the engineering shear strain, γ. Predictions compare reasonably well with measurements up to $\gamma = 8\%$ but are lower at higher strains ($\approx$25% at $\gamma = 30\%$). Such accuracy is considered reasonable in view of the uncertainties associated with interpretation of the experimental results.

---

*During a DSS test $\Delta\sigma_{zz} = \Delta s_{zz} + \Delta\sigma_{oct} = 0$; i.e., $\Delta\sigma_{oct} = -\Delta s_{zz}$ (Δs_{zz} = deviatoric strain increment).

Cyclic Triaxial Tests

Figure 5.11 compares the predicted shear induced pore pressures to measurements obtained in a $\overline{CK_oU}$ cyclic triaxial test on normally consolidated BBC (described earlier, Fig. 5.4). Since the model can predict one unloading branch only, predictions are evaluated for the unloading performed at vertical strain levels ε_v= 1.2%, 3.6% and 8.3%, in Figs. 5.11.a, b and c, respectively.

Predictions of Δu_s during unloading for ε_v = 1.2 and 3.6% (Figs. 5.11.a and b) are virtually identical to the measured values. Furthermore, Δu_s during the last unloading (Fig. 5.11c) is slightly underpredicted (≃15%) at first but the agreement is very good after the sample has been subjected to significant extension strain.

5.5 SUMMARY AND CONCLUSIONS

A review of existing methods for predicting the excess pore pressure, Δu , generated during undrained shearing of clays indicates the need for a new method to predict Δu caused by the very complicated strains associated with cone penetration (variable principal strain directions with large strains and strain reversals). A method is proposed to predict Δu in strain controlled problems. Following Henkel's approach, Δu is divided into two components: a) $\Delta\sigma_{oct}$ due to changes in confinement and b) Δu_s caused by the tendency of the soil to

to dilate (or contract) due to pure shear loading. The first component, $\Delta\sigma_{oct}$, is obtained from equilibrium considerations and, the second component, Δu_s, is evaluated by means of a new analytical model.

The model can predict Δu_s for anisotropic clays subjected to general straining conditions (with rotation of principal strain direction) and one unloading. For monotonic loading, all model parameters can be obtained from results of $\overline{CK_oU}$ triaxial compression and extension tests. For unloading, the model requires an estimate of the maximum (or limiting) Δu_s which can be obtained from results of laborabory tests including straining reversal.

A comparison between the predicted and measured pore pressures during plane strain compression and extension and in direct simple shear tests indicates good agreement in spite of the difficulty in evaluating $\Delta\sigma_{oct}$ during these tests. Furthermore, the predicted pore pressures during unloading are very close to measurements obtained from $\overline{CK_oU}$ cyclic triaxial tests.

Sphere #	Center Location	Radius	Rate of Pore Pressure Generation
m	$\beta_1^{(m)}$	ρ_m	I_m°
1	0.0	0.0	55.0
2	-0.0006421	0.0006421	43.37736
3	-0.0008770	0.0008770	38.24489
4	-0.0011675	0.0011675	33.09526
5	-0.0015227	0.0015227	28.11354
6	-0.0019544	0.0019544	23.44749
7	-0.0024771	0.0024771	19.20351
8	-0.0031096	0.0031096	15.44683
9	-0.0025968	0.0051542	12.20514
10	-0.0014419	0.0081677	9.47457
11	-0.0006395	0.0112320	7.22698
12	0.0010294	0.0156636	5.41752
13	0.0022827	0.0203056	3.99169
14	0.0047507	0.0269504	2.89127
15	0.0067247	0.0340986	2.05902
16	0.0104657	0.0442845	1.44189
17	0.0136211	0.0555129	0.99303
18	0.0194399	0.0715036	0.67270
19	0.0245783	0.0895362	0.44828
20	0.0338714	0.1152752	0.29392
21	0.0424176	0.1449294	0.18962
22	0.0576643	0.1874405	0.12040
23	0.0722062	0.2374262	0.07524
24	0.0979093	0.3095063	0.04628
25	0.1232521	0.3959293	0.02803
26	0.1677816	0.5214342	0.01671
27	0.2130503	0.6747632	0.00981
28	0.2923348	0.8992079	0.00568
29	0.3752503	1.1784196	0.00323
30	0.5203211	1.5906991	0.00181
31	0.6761177	2.1126571	0.00100
32	0.9488651	2.8904875	0.00055
33	1.2492010	3.8922077	0.00029
34	1.7760948	5.3994725	0.00016
35	2.3702142	7.3729410	0.00008
36	3.4153561	10.3719029	0.00004
37	4.6213929	14.3636664	0.00002
38	6.7513929	20.4918094	0.00001

Maximum Normalized Shear Induced Pore Pressure (Eq. 5.10) :

$$\frac{(\Delta u_s)_{max}}{\sigma_{vc}} = 0.54$$

Table 5.1 Numerical values of the model parameters for normally consolidated resedimented Boston Blue Clay.

TEST	APPLIED STRESS SYSTEM		Δu_s
Triaxial compression loading	$\Delta\sigma_v > 0$	$\Delta\sigma_h = 0$	$\Delta u = \frac{1}{3}\Delta\sigma_v$
Triaxial extension unloading	$\Delta\sigma_v < 0$	$\Delta\sigma_h = 0$	
Triaxial compression unloading	$\Delta\sigma_v = 0$	$\Delta\sigma_h < 0$	$\Delta u = \frac{2}{3}\Delta\sigma_h$
Triaxial extension loading	$\Delta\sigma_v = 0$	$\Delta\sigma_h > 0$	
Plane strain compression loading	$\Delta\sigma_v > 0$	$\Delta\sigma_h = 0$	$\Delta u = \frac{1}{3}(\Delta\sigma_v + \Delta\sigma_2^{(1)})$
Plane strain extension unloading	$\Delta\sigma_v < 0$	$\Delta\sigma_h = 0$	
Plane strain compression unloading	$\Delta\sigma_v = 0$	$\Delta\sigma_h < 0$	$\Delta u = \frac{1}{3}(\Delta\sigma_h + \Delta\sigma_2^{(1)})$
Plane strain extension loading	$\Delta\sigma_v = 0$	$\Delta\sigma_h > 0$	
Direct simple shear	$\Delta\sigma_v = 0$	$\Delta\tau_h > 0$	$\Delta u^{(2)} = \frac{2}{3}\Delta\sigma_h^{(3)}$

Note: Tests under idealized conditions;

(1) $\Delta\sigma_2$ = change in the intermediate principal total stress (normal to the fixed planes);

(2) During a DSS test, it is assumed that $\Delta u = -\Delta\bar{\sigma}_v$, where $\bar{\sigma}_v$ is the applied vertical pressure;

(3) In general $\Delta\sigma_h$ is unknown; measurements of $\Delta\sigma_h$ require a specially equipped membrane.

Table 5.2 Computation of the shear induced pore pressure during undrained shear of clays in classical laboratory tests.

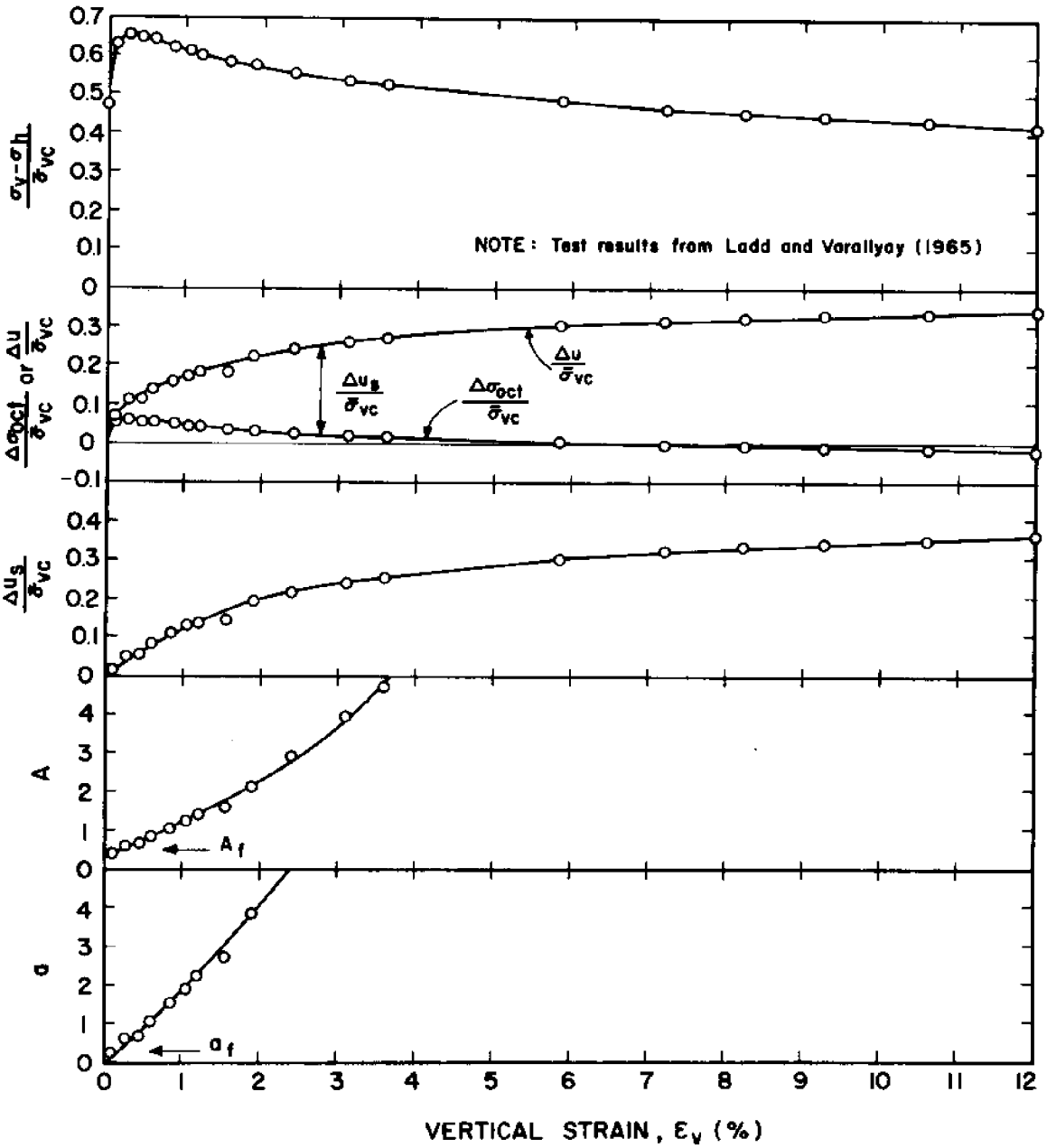

Figure 5.1 Pore pressure behavior during $\overline{CK_oU}$ triaxial test on normally consolidated resedimented Boston Blue Clay.

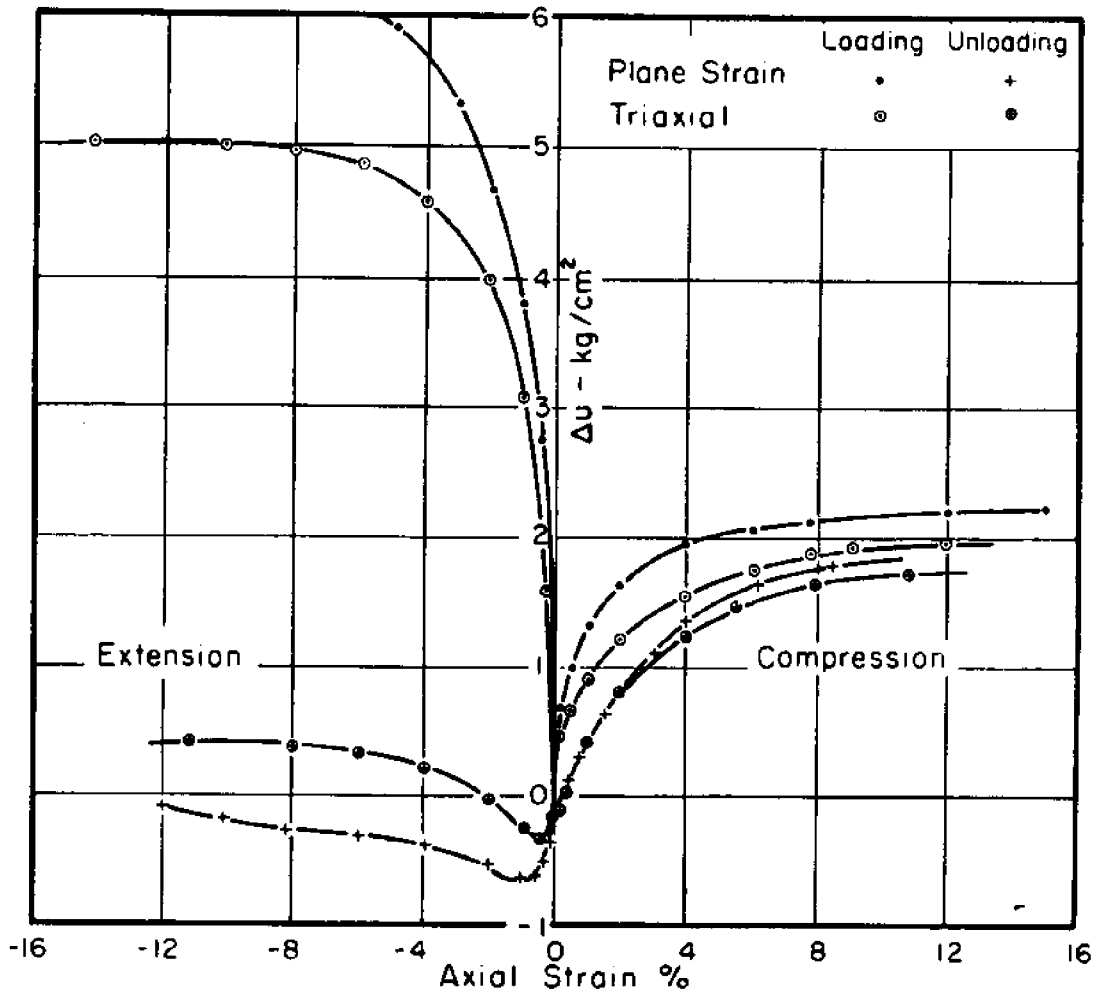

(a) PORE PRESSURE CHANGE VS. AXIAL STRAIN

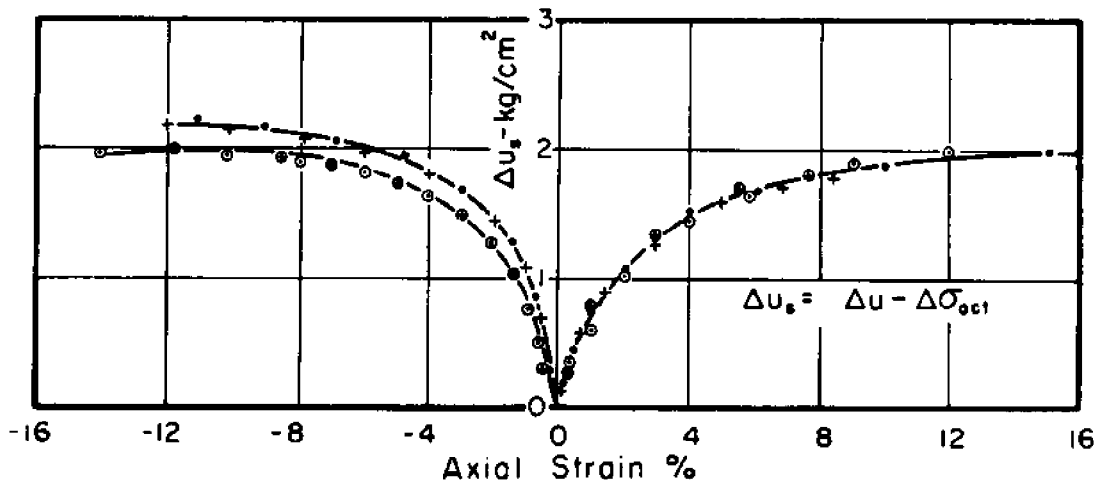

(b) SHEAR INDUCED PORE PRESSURE VS. AXIAL STRAIN

Figure 5.2 Comparison of undrained pore pressure vs axial strain relations in triaxial and plane strain tests on normally consolidated undisturbed Haney clay (after Vaid and Campanella, 1974).

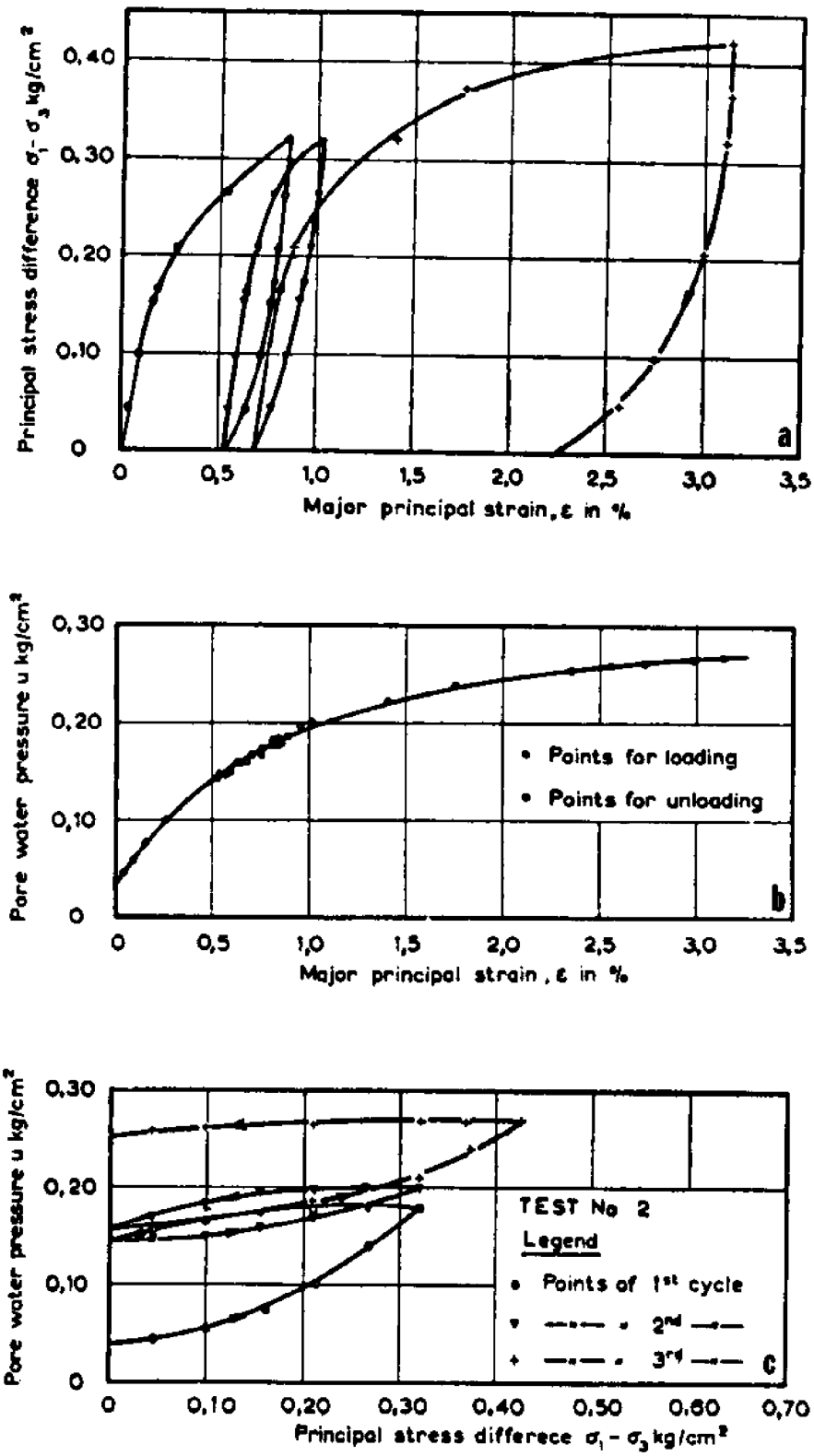

Figure 5.3 Results of a cyclic triaxial test on an undisturbed sample of Fornebu Clay (after Lo, 1961).

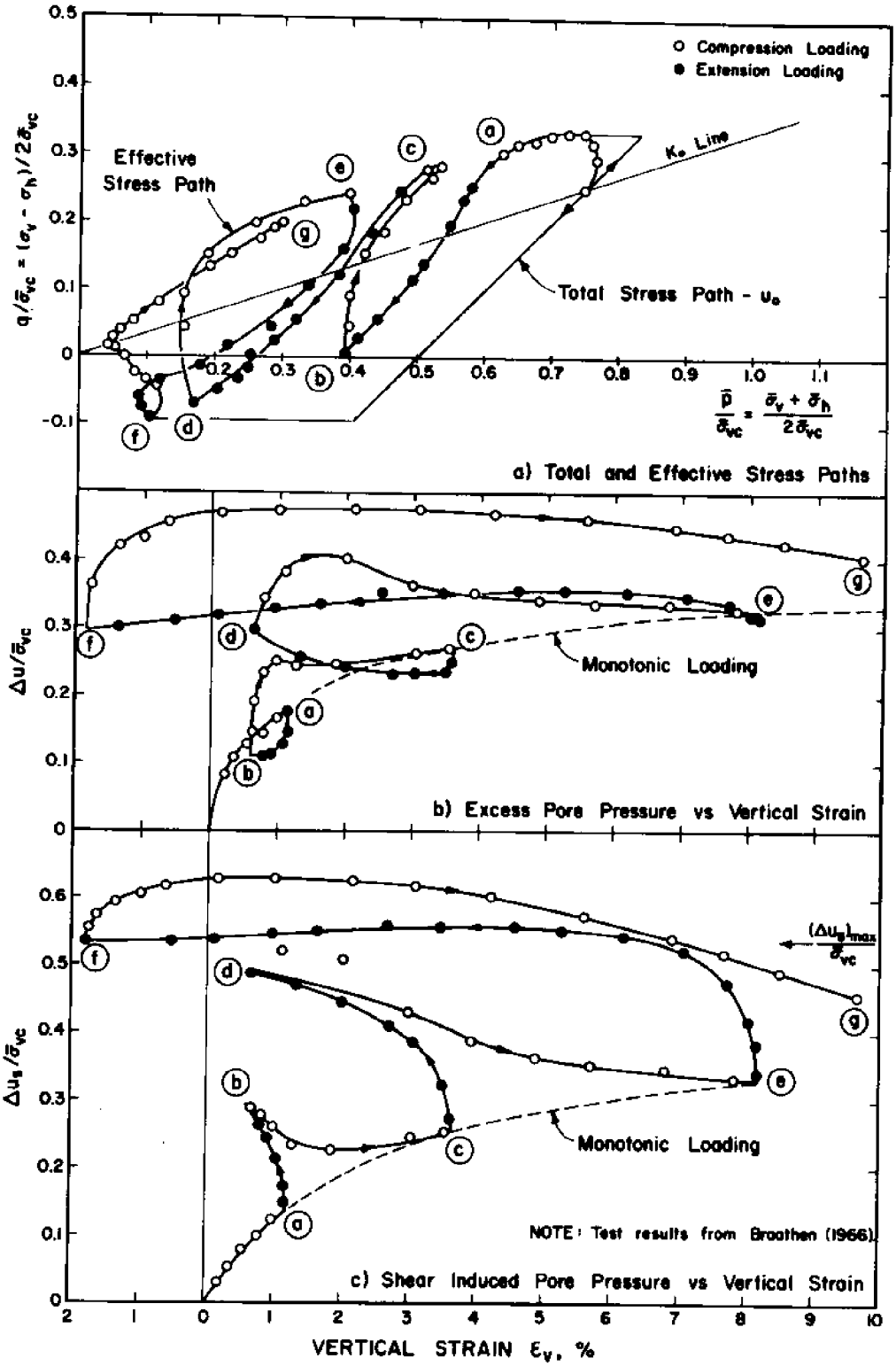

Figure 5.4 Stress path and pore pressure vs vertical strain in $\overline{CK_oU}$ cyclic triaxial test on normally consolidated resedimented Boston Blue Clay.

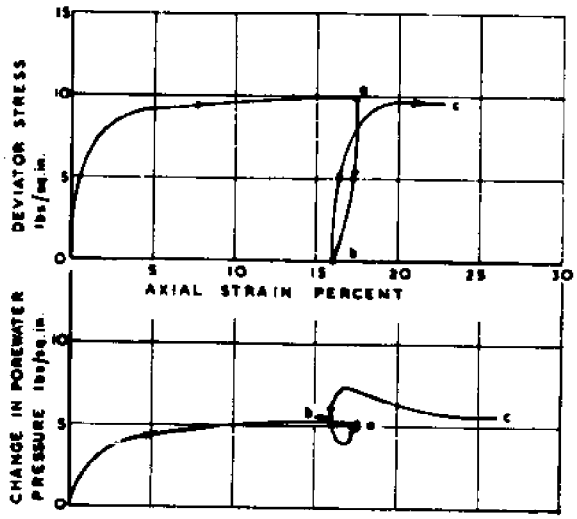

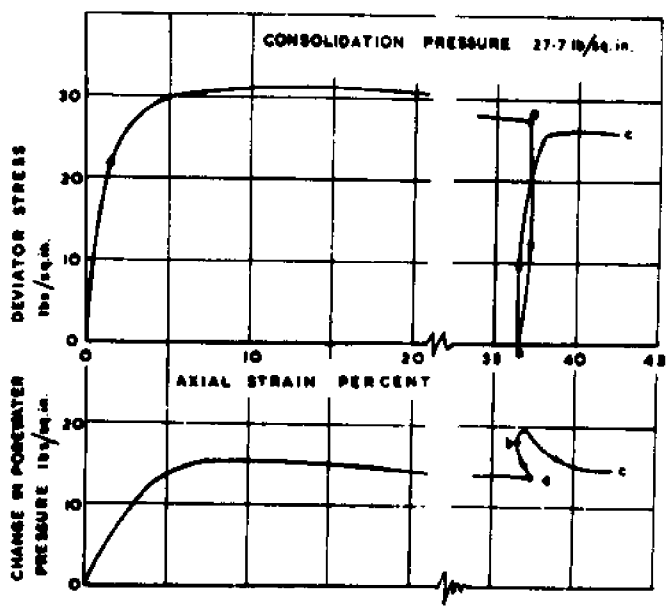

Figure 5 .5 Relation between deviator stress, pore water pressure and axial strain (after Bishop and Henkel, 1953).

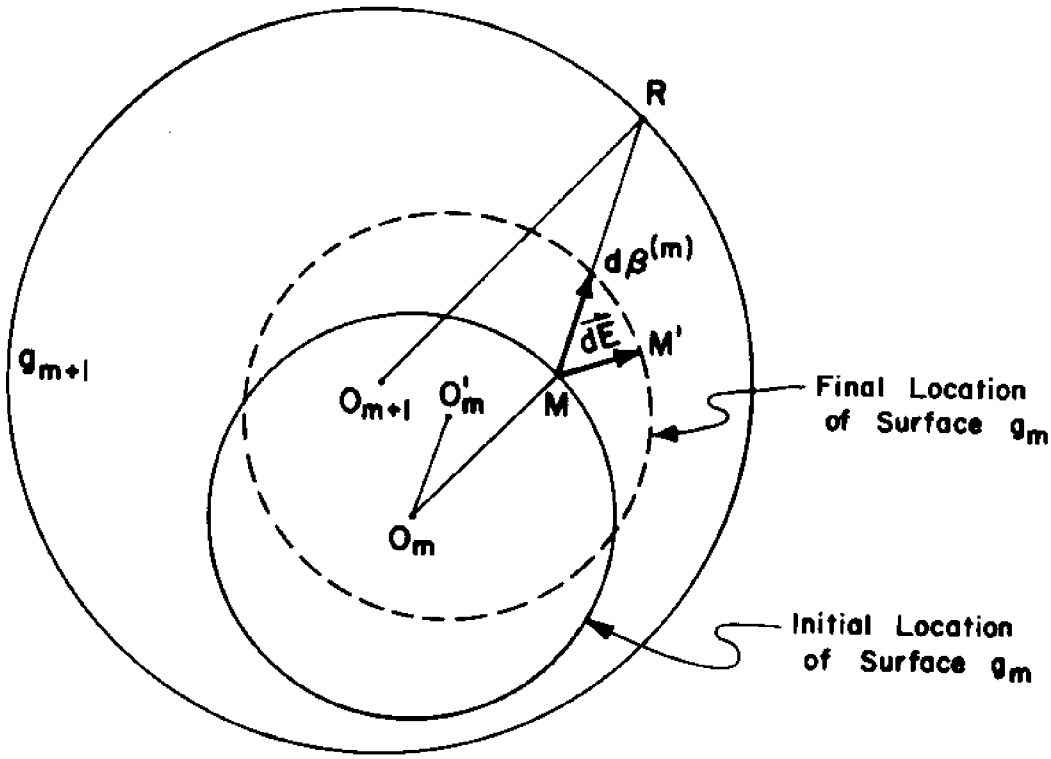

Translation of g_m

$$d\beta_i^{(m)} = \mu_i d\mu$$

where

$$\mu_i = \frac{\rho_{m+1}}{\rho_m}(E_i - \beta_i^{(m)}) - (E_i - \beta_i^{(m)});$$

$$d\mu = -\frac{1}{A}(B + \sqrt{B^2 - AC});$$

$$A = \mu_i^2;$$

$$B = \mu_i(\beta_i^{(m)} - E_i - dE_i); \text{ and}$$

$$C = 2dE_i(E_i - \beta_i) + dE_i^2$$

Translation of g_j, $j = 1, \ldots, (m-1)$

$$\frac{E_i - \beta_i^{(1)}}{\rho_i} = \ldots = \frac{E_i - \beta_i^{(j)}}{\rho_j} = \ldots = \frac{E_i - \beta_i^{(m)}}{\rho_m}$$

Figure 5.6 Surfaces translation.

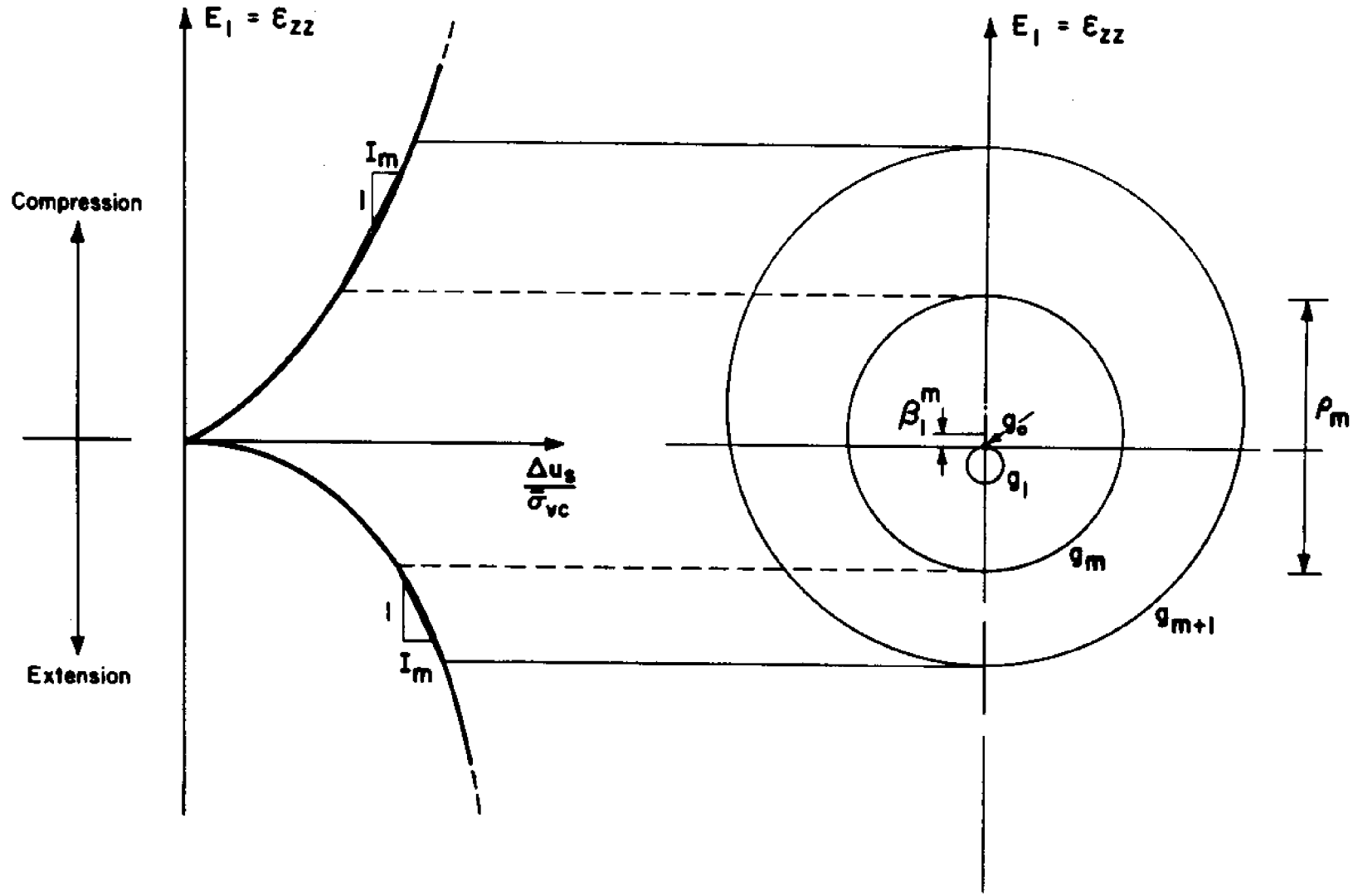

Figure 5.7 Determination of initial model parameters.

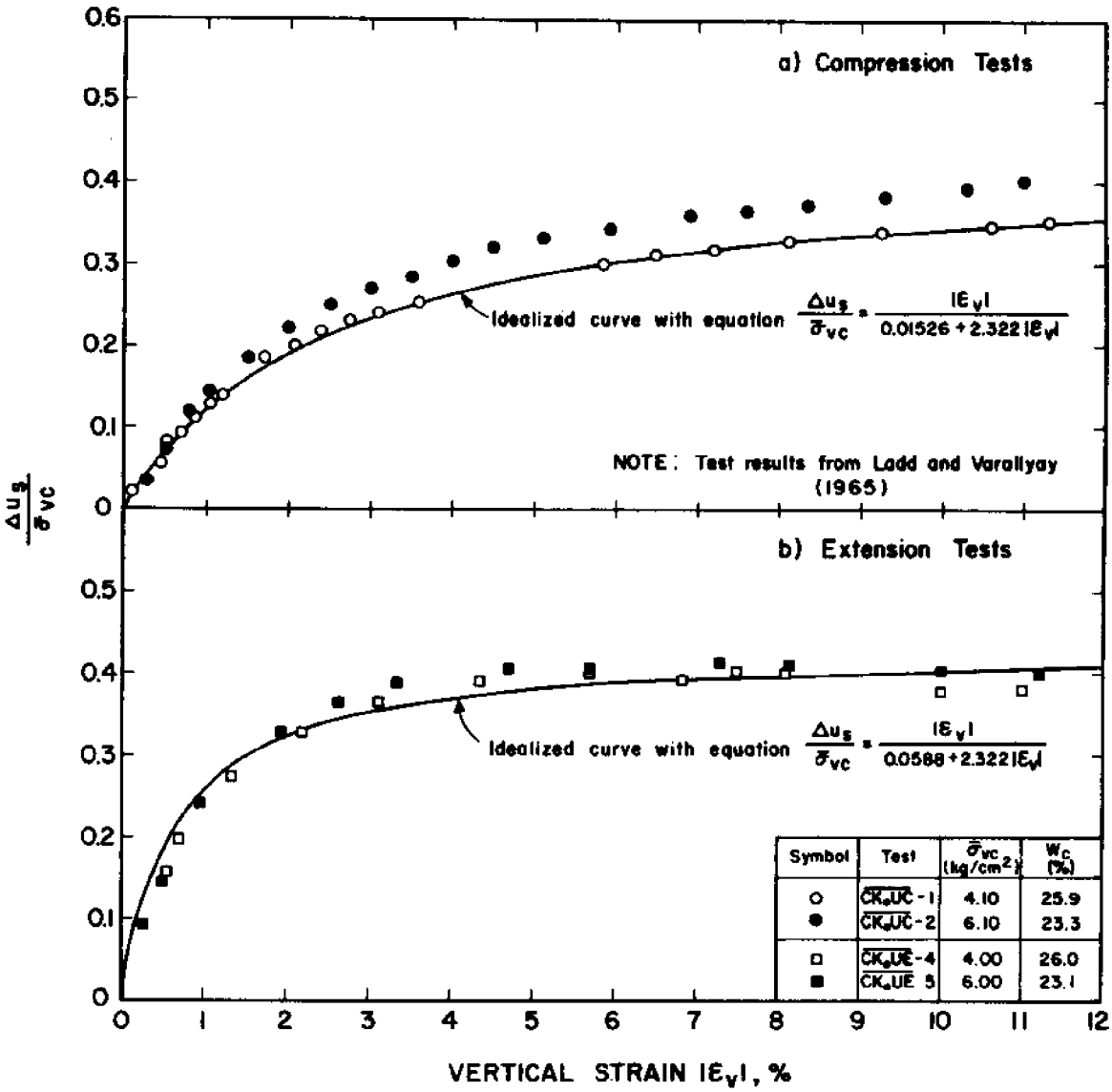

Figure 5.8 Measured shear induced pore pressures vs vertical strain in $\overline{CK_oU}$ triaxial tests on normally consolidated resedimented Boston Blue Clay.

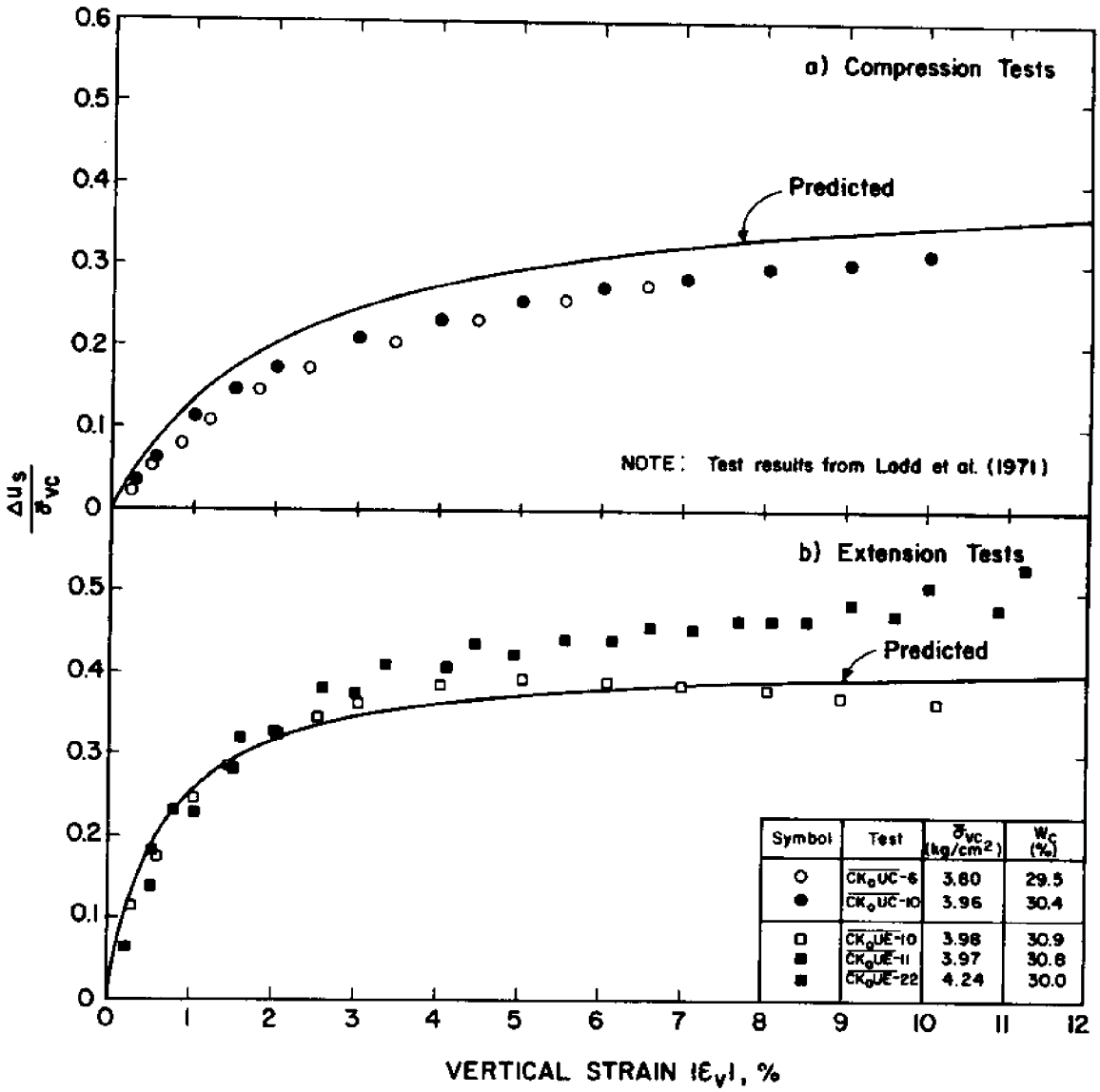

Figure 5.9 Predicted and measured shear induced pore pressures vs vertical strain in $\overline{CK_oU}$ plane strain tests on normally consolidated resedimented Boston Blue Clay.

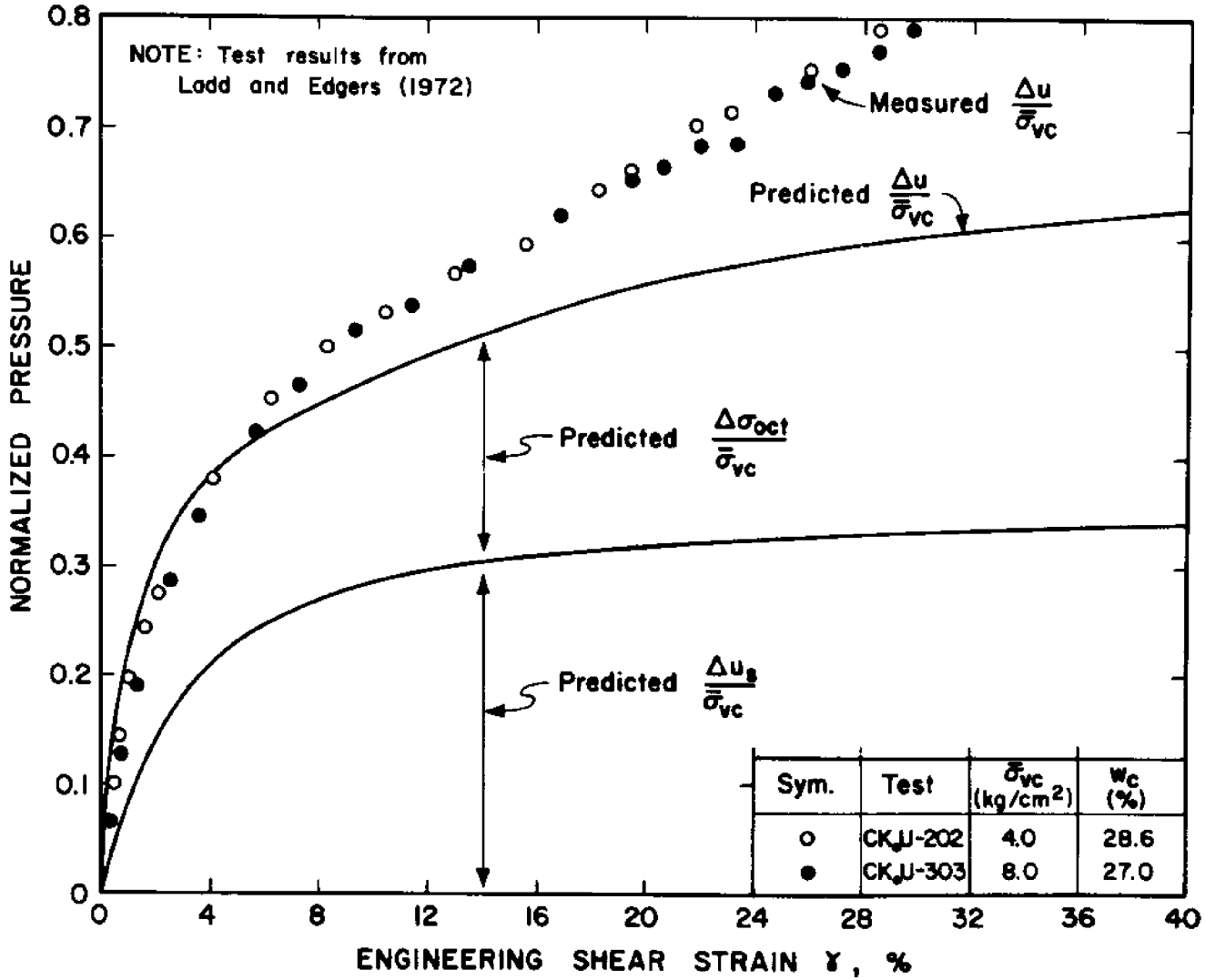

Figure 5.10 Predicted and measured pore pressures vs engineering shear strain in $\overline{CK_oU}$ Direct Simple Shear tests on normally consolidated resedimented Boston Blue Clay.

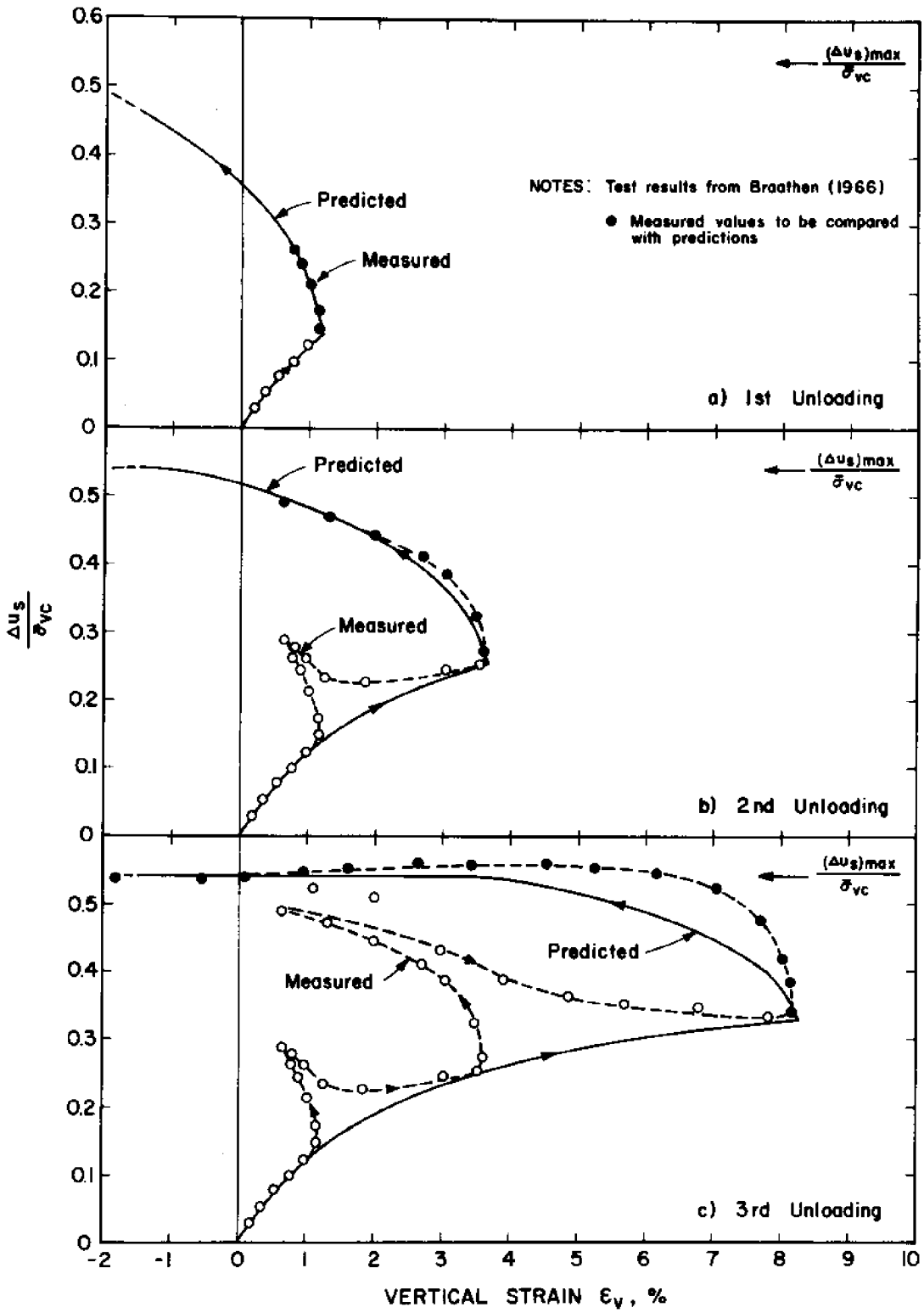

Figure 5.11 Measured and predicted shear induced pore pressure in $\overline{CK_oU}$ triaxial tests with strain reversal.

CHAPTER 6

PENETRATION PORE PRESSURES IN BOSTON BLUE CLAY

6.1 INTRODUCTION

The primary objective of this chapter is to estimate the pore water pressures in the soil during cone penetration because they are essential for the rational interpretation of the consolidation that takes place after penetration stops. Reliable estimates of penetration pore pressures are difficult to achieve because of two major factors:

1) Uncertainties in the mathematical model simulating soil behavior and, in particular, the parameters describing the in situ properties of a given soil. Chapters 4 and 5 present the proposed models to predict stresses and pore pressures during undrained shearing of clays, provide the parameters describing normally consolidated Boston Blue Clay and show that the models lead to reasonable predictions of selected laboratory test results, and;

2) Uncertainties in the method of analysis. Due to the complexity of the mechanism of steady cone penetration, only approximate solutions can be obtained by the strain path method described in Chapter 2.

In view of these uncertainties and with the ultimate objective of interpreting the decay of pore pressures in Boston Blue Clay (BBC), the chapter treats the following subjects:

1) The pressuremeter test in a soft BBC are compared to predictions of the proposed models in normally consolidated BBC are compared to predictions of other models and to experiemntal results of self-boring pressuremeter tests. Since the analysis of pressuremeter tests involve much fewer uncertainties than the more difficult penetration process, these comparisons thus focus on the adequacy of the soil models used and the importance of the model parameters selected to perform field predictions in BBC; and

2) cone penetration in the same BBC deposit. The strain path method (Chapter 2) is used to predict stresses and pore pressures during steady quasi-static penetration of 18° and 60° conical tips in normally consolidated BBC. For these predictions, strains during penetration are approximated by the fields corresponding to a perfect fluid (Chapter 3) and soil behavior is described by the soil models in Chapters 4 and 6. The predicted cone

resistance, q_c, and pore pressures at different locations on the cone are then compared to experimental results and limitations of the strain path method are discussed.

6.2 EXPANSION OF CYLINDRICAL CAVITIES AND THE PRESSUREMETER TEST

This section presents a detailed treatment of the pressuremeter test to check the adequacy of: a) the proposed soil behavior models, and; b) the parameters selected on the basis of laboratory test results on resedimented Boston Blue Clay in predicting the field performance in the soft BBC deposit at the Saugus, Massachusetts site (Baligh et al., 1978, 1980).

Predictions are made for the idealized conditions associated with the undrained expansion of a (vertical) cylindrical cavity from a finite radius, in an incompressible soil.

6.2.1 Proposed Solution

a) Stress-Strain Curves

In order to predict the undrained expansion curve*

---

*The expansion curve of a pressuremeter test relates the internal cavity pressure (i.e., σ_r) to the dimensionless volumetric expansion of the cavity, $\Delta V/V_o$; where ΔV = increase in volume and V_o = initial volume of the cavity.

of an idealized pressuremeter test in clay, the following are required:

1) The initial horizontal stress:

$\sigma_{ho} = K_o \bar{\sigma}_{vo} + u_o$ before expansion, and;

2) The shear stress $(\frac{\sigma_r - \sigma_\theta}{2})$ at various strain levels when the soil is deformed under plane strain conditions, i.e., $d\varepsilon_z = 0$ and $d\varepsilon_r = - d\varepsilon_\theta$

This will enable the determination of σ_r and σ_θ in the soil during cavity expansion. However, the prediction of pore pressures requires that, in addition, the shear induced pore pressures, the initial vertical stress $\sigma_{vo} (= \bar{\sigma}_{vo} + u_o)$ and its variation, $\Delta\sigma_z$, during expansion be estimated. This could be achieved by knowing

1) the shear induced pore pressure $\Delta u_s (= \Delta u - \Delta\sigma_{oct})$ and;

2) the deviatoric vertical stress $s_z [= \sigma_z - \sigma_{oct}; \sigma_{oct} = \frac{1}{3}(\sigma_r + \sigma_\theta + \sigma_z)]$ at various strain levels when the soil is sheared under plane strain conditions $(d\varepsilon_z = 0)$.

Therefore, comprehensive predictions including stresses and pore pressures during cavity expansion require three stress-strain relationships:

a) $(\sigma_r - \sigma_\theta)/2$; b) s_z, and; c) Δu_s.

The solid lines (labelled #1) in Fig. 6.1 present these three relationships for normally consolidated BBC

assuming normalized behavior with respect to the vertical consolidation stress, $\bar{\sigma}_{vc}$. The dependence of the normalized shear stress $(\sigma_r - \sigma_\theta)/2\bar{\sigma}_{vc}$ and the normalized vertical deviatoric stress, $s_z/\bar{\sigma}_{vc}$ on the radial strain $\varepsilon_r (= -\varepsilon_\theta)$ are derived from the deviatoric stress model in Chapter 4 using the parameters in Table 4.1 derived from laboratory tests on normally consolidated resedimented BBC. The relationship between the normalized shear induced pore pressure, $\Delta u_s/\bar{\sigma}_{vc}$, and ε_r is obtained form the pore pressure model of Chapter 5 using the parameters in Table 5.1 also based on laboratory tests on normally consolidated resedimented BBC.

For normally consolidated resedimented Boston Blue Clay, Fig. 6.1 indicates that the soil model in Chapter 4 predicts that:

1) The shear stress-strain relationship of the soil in a pressuremeter mode is the same as in a direct simple shear mode of shearing (Fig. 4.8). The peak undrained shear strength, $s_u/\bar{\sigma}_{vc}$ [$= (\sigma_r - \sigma_\theta)/2\bar{\sigma}_{vc}$ at failure], equals 0.26 at a radial strain $\varepsilon_r = 4.4\%$ before significant strain softening takes place;

2) the "residual" undrained shear strength, $(s_u/\bar{\sigma}_{vc})_{residual}$ equals 0.15 and is asymptotically reached at "large" strains (in excess of $\varepsilon_r = 20\%$); and;

3) the vertical deviatoric stress, $s_z/\bar{\sigma}_{vc}$, initially equal to 0.31 (corresponding to $K_o = 0.537$), decreases during undrained shear to 0.13 at the peak

undrained shear strength (ε_r = 4.4%) and eventually vanishes at large strains. When s_z = 0, the vertical stress, σ_z, equals the octahedral stress, σ_{oct}, which equals the average of σ_r and σ_θ i.e., $\sigma_z = \sigma_{oct} = (\sigma_r + \sigma_\theta)/2$.

b) Predictions in normally consolidated Boston Blue Clay

Predictions of stresses and pore pressures during cylindrical cavity expansion are determined numerically (Levadoux, 1980). Integration of the radial equilibrium equation begins at a radius equal to 200 times the initial radius of the cavity ($r = 200R_o$) where conditions at infinity are imposed: $\sigma_z = \bar{\sigma}_{vo} + u_o$; and $\sigma_r = \sigma_\theta = K_o\bar{\sigma}_{v_o} + u_o$. Using approximately 105 intervals (i.e., 106 nodal points), the interval length equals $10R_o$ at $r = 200R_o$ and decreases with $1/(r-R_o)$ to provide better resolution in zones of hggh stress gradients near the cavity wall. At each nodal point, the natural radial strain, ε_r, is calculated and the corresponding values of $(\sigma_r - \sigma_\theta)/2$, s_z and Δu_s are evaluated by means of the curves labelled #1 in Fig. 6.1. The solution accuracy is checked by increasing both the outer boundary radius and the number of intervals. Parametric studies show a maximum discrepancy of 0.1% between the computed stresses, and therefore, the grid described above is considered adequate.

Figure 6.2 presents predictions of radial and vertical total stress and excess pore pressure distributions in the soil (normally consolidated BBC) surrounding a pressuremeter at different levels of expansion, $\frac{\Delta V}{V_o}$ (= 0.5, 2, 10 and 100%). Results in Fig. 6.2 illustrate the progressive shearing of the soil during a pressuremeter test. When the volumetric strain of the cavity, $\frac{\Delta V}{V_o}$, reaches high levels, stresses and pore pressures approach values predicted for the expansion from zero radius (Azzouz et al., 1980). The solid lines in Fig. 6.3 show the predicted radial stress, σ_r, and excess pore pressure, Δu, at the cavity wall versus the volume increase of the cavity $\frac{\Delta V}{V_o}$.

6.2.2 Existing Solutions

Carter et al. (1978) employ the finite element technique to analyze the expansion of a cylindrical cavity from an initial radius R_o using the "modified Cam-Clay" model for soil behavior (Roscoe and Burland, 1968; Schofield and Wroth, 1968). Table 6.1 presents the model parameters selected by Carter et al. to simulate a soil with "properties similar to those of Boston Blue Clay" (λ, κ, e_{cs}, M). Based on these parameters, and the modified Cam-Clay model described by Roscoe and Burland (1968), Kavvadas (1979) computed: 1) the equivalent input parameters obtained from more conventional oedometer and triaxial tests [CR, RR, $\bar{\phi}$(TC) and $\bar{\phi}$(TE)], and; 2) the predictions of K_o and s_u shown in the first column of Table 6.1 assuming a Mohr-Coulomb failure envelope.

The modified Cam-Clay model generally overpredicts K_o. Accordingly, Carter et al. use a more realistic value of $K_o = 0.55$ for normally consolidated BBC in their analyses. The second column in Table 6.1 presents the equivalent parameters and the predictions of the model used by Carter et al. (1978) as determined by Kavvadas (1979) assuming an extended Von Mises failure envelope.

Comparing the soil parameters selected by Carter et al. (1978) with measured values for normally consolidated BBC in different laboratory tests (third column in Table 6.1) we note that:

1) the compression ratio CR (or alternatively λ) is underestimated by 20 to 50%;
2) the recompression ratio is within the range of variation of experimental results and is therefore reasonable;
3) the friction angle in triaxial compression, $\bar{\phi}$(TC) is underestimated by 3° (i.e., M is low). This is probably necessary in order to predict reasonable strengths at large strains because the modified Cam-Clay model cannot simulate the observed strain softening behavior.
4) the friction angle in plane strain compression, $\bar{\phi}$(PSC), is grossly overestimated by about 10°. The Mohr-Coulomb criterion predicting $\bar{\phi}$(PSC) = $\bar{\phi}$(TC) = 30° (see first column in Table 6.1) therefore appears more reasonable than the

extended Von Mises failure criterion.

5) the undrained shear strength for K_o consolidated triaxial compression and extension tests are identical and equal to $0.295\ \bar{\sigma}_{vc}$. Although this value only slightly underestimates the measured strength in the compression mode (by 10%), it greatly overestimates that in the extension mode (by 127%);

6) the undrained shear strength for K_o-consolidated plane strain test is independent of the loading direction and equals $0.34\ \bar{\sigma}_{vc}$. This provides a very reasonable estimate of the measured strength in plane strain compression test but much too high estimated strengths for plane strain extension (94% too high), direct simple shear (70% too high) and pressuremeter loading mode (62% too high) tests.

The stress-strain curves pertinent to cylindrical cavity expansion in normally consolidated BBC and predicted by Carter et al. (1978)* are plotted in Fig. 6.1 (curves #2). For illustration, the stress strain curves of an idealized elastic ($G/\bar{\sigma}_{vc} = 25$, $\nu = 0.5$) perfectly-plastic ($s_u/\bar{\sigma}_{vc} = 0.34$) material are also plotted in Fig. 6.1 (curves #3). A comparison of curves number 2 and 3 in Fig. 6.1 indicates the very

*These curves are backfigured from the predicted stress distributions predicted by Carter et al. (1978) for the expansion of a cylindrical cavity from zero radius.

small difference in soil behavior (during expansion of a cylindrical cavity) predicted by the modified Cam-Clay and the very simplistic elastic perfectly-plastic models.

When compared to the proposed models (curves #1) the modified Cam-Clay predicts:

1) higher value of $s_u/\bar{\sigma}_{vc}$ (0.34 vs. 0.26) and no strain softening;
2) a softer response at small strain levels;
3) a faster decrease in s_z with strains such that $s_z = 0$ [i.e., $\sigma_z = \frac{1}{2}(\sigma_r + \sigma_\theta)$] at about $\varepsilon_r = 3\%$, and;
4) smaller values of the shear induced pore pressure Δu_s when $\varepsilon_r > 2\%$.

Finally, the radial stress, σ_r, and the excess pore pressure, Δu, at the cavity wall predicted by Carter et al. are shown by the dashed lines in Fig. 6.3. Compared to the proposed model, the Cam-Clay predicts:

1) a softer response [$(\sigma_r - u_o)/\bar{\sigma}_{vo}$ vs. $\frac{\Delta V}{V_o}$] at low expansion levels caused by the lower stiffness at small strains (see Fig. 6.1);
2) a very similar limiting pressure. The limiting pressure reached at high $\frac{\Delta V}{V_o}$ is identical to the radial stress at the wall of a cavity expanded from zero radius. Azzouz et al., 1980, show that Cam-Clay and the proposed model predict similar radial stresses at the cavity wall because the compensating effects of

i) the lower stiffness at small strain levels and

ii) the higher strength predicted by Cam-Clay, and;

3) lower excess pore pressures (approximately half when $\frac{\Delta V}{V_o} = 10\%$) because of the lower predicted shear induced pore pressures (see Fig. 6.1).

In summary, the comparison of expansion curves predicted by the proposed and Cam-Clay models in Fig. 6.3 clearly indicate that even though the two models predict significantly different stress-strain curves in the pressuremeter mode of deformation (Fig. 6.1) the resulting expansion curves exhibit very little difference. This emphasizes the difficulty of back figuring the "material stress-strain curve" from experimental expansion curves: small experimental errors can cause large errors in the back figured stress-strain curve.

6.2.3 Evaluation of Predictions

Ladd et al. (1979) present results of an extensive pressuremeter testing program conducted in Boston Blue Clay at Saugus, Massachusetts. Results of two tests performed with the French self-boring pressuremeter PAFSOR at depths 83.2 and 103.2 feet are plotted in Fig. 6.4. The expansion curves for the two tests are very close even though one of the tests (closed circles) was conducted after a full loading-unloading cycle had been preformed.* The expansion curve predicted by the

---

* The loading-unloading cycle consisted of increasing $\frac{\Delta V}{V_o}$ to 2.8% and then decreasing it back to 0.

proposed model (in 6.2.1) is represented by the solid line in Fig. 6.4. The prediction considers a loading stage up to $\frac{\Delta V}{V_o}$ = 16.2% followed by an unloading stage until $\sigma_r - u_o = 0$. The large discrepancy between predicted and measured pressuremeter results is obvious. A fair agreement can be reached if the shear resistance $(\sigma_r - \sigma_\theta)/2$ in Fig. 6.1 is multiplied by a factor of 2.08 at all (ε_r) strain levels.

A number of investigators have noted that the pressuremeter test overestimates the undrained shear strength of clays compared to laboratory tests (Baguelin, et al., 1978; Ladd et al., 1979). Ladd et al. (1979) provide a number of possible causes for this important problem resulting from differences between the actual test and the idealized conditions assumed in the theoretical analyses. These assumptions are:

(1) The surrounding soil is homogeneous and saturated.

(2) The stress-strain relationship for the soil is not affected by variations in strain rate.

(3) Insertion of the probe is accomplished without disturbing the soil.

(4) The test is performed under undrained conditions; i.e., expansion occurs at a sufficiently rapid rate to preclude any drainage.

(5) The length to diameter ratio of the cell is sufficiently large to satisfy the plane strain condition (i.e., no vertical strain).

The poor agreement between the predicted and measured expansion curves in Fig. 6.4 is probably due to a combination of all these assumptions and possibly, the estimated stress strain curve (Fig. 6.1) as well. However, the most significant causes for discrepancies are believed to consist of four categories: 1) non-cylindrical expansion; 2) partial drainage; 3) rate effects, and; 4) slight overconsolidation of the clay.

1) Non-cylindrical expansion

For practical reasons, pressuremeter tests are conducted by expanding a cylinder of finite length whereas predictions assume an infinite cylinder length. Guard cells are sometimes used to minimize the undesirable end effects in the test but, additional complications have limited their application in practice. End effects can be crudely assessed by assuming the experimental expansion curve to be bounded by the expansion pressures for cylindrical and spherical cavities. In an elastic perfectly-plastic material subjected to an initial isotropic stress, σ_o, the incremental spherical cavity pressure (above σ_o) is 33% higher than that of a cylindrical cavity. For more realistic conditions (K_o initial stresses, anisotropic soil), the spherical expansion pressure is difficult to estimate because the problem becomes two dimensional (i.e., strains and stresses do not exhibit spherical symmetry).

Laier et al. (1975) investigate the influence of length

to diameter ratio (L/d)* in laboratory pressuremeter tests performed on dry sand. Results of 32 tests on samples prepared at two relative densities (D_R = 55 and 95%) and six confining pressures indicate that: a) the L/d ratio has no significant effect on the measurement of the pseudo-elastic modulus, E, and; b) the L/d ratio has a marked effect on measured limit pressure, p_L. Laier et al., (1975) propose a correction curve to account for the finite pressuremeter length. This curve which is independent of relative density and overconsolidation ratio indicates that the limit pressure, p_L, obtained from a pressuremeter with L/d = 7.5 is twice that predicted with $L/d \to \infty$.** However, the validity of these results for undrained cavity expansion in clay is doubtful.

Recently, Ghionna et al., (1979), conducted in situ pressuremeter tests in normally consolidated Porto Tolle clay for L/d ratios of 2 and 4. Their results show that the undrained shear strength, s_u, back figured from tests with L/d=2 (as in PAFSOR tests) is approximately 50% higher than that back figured with L/d = 4. However, Ladd et al.(1979)

---

*Laier et al., utilized pressuremeters with two guard cells with lengths equal to that of the measuring cell; i.e., L = 3 ℓ where ℓ = measuring cell length.

**Typical L/d used in pressuremeter tests are 2 in PAFSOR and 6 in CAMKOMETER equipments.

present results of CAMKOMETER (L/d = 6) and PAFSOR (L/d = 2) pressuremeter tests in Boston Blue Clay which show no noticeable difference in limiting pressures. Furthermore, results they obtain in the upper overconsolidated BBC with the same PAFSOR equipment (L/d = 2) show less discrepancy between the extimated and measured strengths of the soil.

2) Partial Drainage

Pressuremeter tests are typically performed at a strain rate $\dot{\epsilon}$ = 1.0%/min* and thus require 10 to 20 minutes to perform. During expansion, pore pressures develop due to the increase in isotropic compression and due to the shearing of the soil. However, pore pressures also dissipate as soon as gradients take place, i.e., immediately after expansion starts. Dissipation of excess pore pressures represents partial drainage which tends to increase the shearing resistance of soft clays. Faster dissipation takes place when gradients are high (near the cavity wall) and when the soil is pervious and stiff (high drained bulk modulus).

Clarke et al.(1979) present results of a regular pressuremeter in soft silty clay with pore pressure measurements (at the cavity wall) followed by a holding test where the volume of the cavity is held constant. Expansion required approximately 14 minutes and stopped at ϵ = 10% when the

---

*The strain ϵ represents the ratio of the radial movement of the pressuremeter membrane to its initial radius; $\epsilon \simeq \frac{1}{2}\frac{\Delta V}{V_o}$

excess pore pressure $\Delta u \simeq 100$ kN/m^2. Fourteen minutes later, Δu decreased to 40 kN/m^2 . This clearly indicates that significant pore pressure dissipation must have already occurred at the end of the expansion stage.

The effects of pore pressure dissipation on the expansion curve are difficult to assess because the increase in strength and the rate of dissipation depend on the effective stresses during consolidation. Prediction of these effective stresses require very complicated soil models beyond present capabilities.

3) Strain-Rate Effects

The stress-strain relationship for clays sheared under undrained conditions is strain-rate dependent. Laboratory tests performed by Taylor (1943) on Boston Blue Clay and reported by Bishop and Henkel (1962) show an 11% increase in s_u when the strain rate is increased from 0.0083 %/min (= 0.5%/hour) to 0.5%/min, i.e., about 60 times.

Although comprehensive experimental data on strain-rate effects are not available, it is generally believed that an increase in strain rate leads to an increase in undrained shear resistance of the soil at all strain level (Ladd et al., 1977). However, results recently obtained by Hight et al. (1979) show that the effects of strain-rate on the shearing behavior of a sandy clay can exhibit opposite trends, depending on the overconsolidation ratio (OCR) of the material: at low OCR (< 4), the undrained shear

resistance increases with increasing strain rates whereas, at high OCR (> 4) the inverse is true. Nevertheless, in the slightly overconsolidated BBC where the pressuremeter tests plotted in Fig. 6.4 were conducted, little doubt exists that an increase in strain-rate causes an increase in the undrained shear resistance.

The strain rate in the soil during a pressuremeter test varies inversely with the square of the radial distance to the cavity axis. Therefore, even if expansion takes place at a constant rate, the strain-rates in the soil vary significantly. A soil element near the cavity wall will typically be subjected to a strain-rate two orders of magnitude larger than in $\overline{CK_oU}$ triaxial tests ($\dot{\varepsilon}_v \simeq 0.5\%$/hour) but an element at a radius 10 times larger will be subjected to the same strain-rate.

Prevost (1976) proposed a simplified formula to describe the undrained stress-strain-time behavior of clays under axisymmetric loading conditions. He then showed that strain rate effects can greatly influence the stress-strain curve backfigured from the expansion curve of a pressuremeter test. In particular, even if the clay is strain-hardening, the stress-strain curve derived from constant strain-rate pressuremeter tests conducted at conventional testing rates can exhibit strain-softening behavior because of strain rate effects.

In summary, strain rate effects complicate the

interpretation of the expansion curve obtained from undrained pressuremeter tests. However, in normally consolidated BBC, they are not believed to have a dominant influence on the expansion curve (especially the limiting pressure).

4) Overconsolidation of the Clay

Because of availability of laboratory tests results on normally consolidated BBC, the predictions in Fig. 6.4 are obtained for an overconsolidation ratio (OCR) of unity. Recent consolidation test results on high quality samples (Ladd, et al., 1979) indicate that at depths 83.2 and 103.2 feet where the pressuremeter tests in Fig. 6.4 were conducted, the overconsolidation ratio of the clay is in the range: OCR = 1.25 - 1.35. Possible causes of overconsolidation in the deep clay include erosion, lowering of water table elevation, desiccation during clay deposition, or aging, i.e., quasi-consolidation or precompression as defined by Leonards and Altschaeffl (1964) and Bjerrum (1967), respectively.

The increase in undrained shear strength due to overconsolidation can be estimated from results of $\overline{CK_oU}$ direct simple shear tests on Boston Blue Clay given by Ladd et al., 1977. At OCR = 1.3, s_u increases by 25% compared to OCR = 1.

6.2.4 Summary and Discussion of Pressuremeter Studies

Bearing in mind that the primary objective of this chapter is to estimate pore pressures during cone penetration in Boston Blue Clay (BBC), the pressuremeter studies presented above were conducted in order to: 1) check the proposed soil behavior models to be used in analyzing the more complicated problem of cone penetration, and; 2) evaluate the adequacy of the soil parameters obtained from laboratory tests on normally consolidated BBC to predict field performance.

Results of these studies indicate that:

1) Predictions of cylindrical cavity expansion curves obtained by the proposed model described in Chapter 4 are fairly close to predictions determined by Carter et al., (1978) using the Cam-Clay model (see Fig. 6.3) even though the relevant stress-strain behavior of the two models differ significantly (see upper diagram in Fig. 6.1). This is due to the compensating effects of the lower moduli at small strains and the higher strength exhibited by the Cam-Clay as compared to the proposed model.

2) The proposed models in Chapter 4 and 5 predict much higher pore pressures during cavity expansion than the Cam-Clay model (see Fig. 6.3). This difference is basically due to the shear induced pore pressure Δu_s which is underestimated by Carter et al., (see lower diagram in Fig. 6.1).

3) The proposed model* significantly underpredicts the self-boring pressuremeter expansion pressures performed at depths 83.2 and 103.2 ft when the model parameters are determined from laboratory test results on resedimented normally consolidated BBC. Matching of field measurements can be obtained by approximately doubling the estimated in situ shearing resistance of the soil (e.g., increasing $s_u/\bar{\sigma}_{vo}$ from 0.264 to 0.549, Fig. 6.4). Consolidation tests on high quality samples indicate that the clay at that depth is slightly overconsolidated (OCR ≈ 1.3) which justifies a 25% increase in the selected strength for field predictions. The remaining discrepancy (75% of the estimated strength) might be explained by:

a) inadequacies of the predictive model based on laboratory test results on normally consolidated BBC. These inadequacies can be due to:

- the OCR of the clay is actually higher than 1.3 and hence the in situ strength is higher than estimated. This would, however, leave the field vane strengths inexplicably low.
- The in situ clay has a significantly different behavior from the resedimented BBC used to determine the model parameters. In particular,

*To be used in the analysis of cone penetration.

the in situ clay has very high peak shear strength and/or initial stiffness that affect pressuremeter (and cone penetration) results but is not detected by the field vane test. This proposition is supported by the more sensitive behavior of the in situ clay (as detected by consolidation tests and suggested by the low salt concentration in the pore water) but is hard to evaluate or even prove satisfactorily.

- Strain rate effects which tend to underestimate the field strength measured by pressuremeter (or cone penetration) tests performed at higher rates than laboratory tests.

b) differences between the actual pressuremeter test and the idealized conditions assumed in theoretical analyses. The most significant differences in the BBC tests shown in Fig. 6.4 are believed to be:

- the limited length to diameter ratio (L/d =2 in PAFSOR equipment used) which might introduce important end effects (i.e., deviations from idealized one dimensional cavity expansion solutions) and hence increase the measured expansion pressures.
- Partial drainage associated with local

consolidation and strengthening of the clay during expansion.

6.3 STRAIN PATH PREDICTIONS DURING CONE PENETRATION

The strain path method described in Chapter 2 is now applied to predict stresses and pore pressures during deep steady cone penetration in normally consolidated Boston Blue Clay.

6.3.1 Problem Geometry and Solution Technique

The problem of cone penetration in a cross-anisotropic material exhibits axial-symmetry about the vertical axis of the cone. It is, therefore, sufficient to determine solutions (stresses and pore pressures) in a meridional plane; i.e., any vertical plane containing the vertical axis.

Figure 6.5 illustrates the geometry adopted to solve the cone penetration problem by means of the strain path method. Stresses and pore pressures are determined at selected soil elements (15594 locations) as they move along streamlines around the cone following the strain paths described in Chapter 3. Streamlines are identified by their radial location far ahead of the cone, r_o. Analyses are performed using 46 streamlines to cover the soil mass between r_o = 0.01 R and r_o = 150 R in the radial direction and, z = - 200 R and z = 15 R in the vertical direction (R is the radius of the shaft). Chapter 3 describes the procedures followed to determine the streamlines and the locations of soil elements by integrating the assumed velocities. For a

steady cone penetration velocity V_o, the time increment, Δt, for integration equals $10(R/V_o)$ at $z = -200$ R, decreases with $1/z$ and, reaches $0.1(R/V_o)$ at $z \geq -10$ R. Table 6.2 describes the streamlines (r_o) and the boundary conditions used in the analyses.

6.3.2 Deviatoric Stress Paths

Following the strain path imposed by cone penetration (Chapter 3), the deviatoric stress path of each soil element is computed by means of the soil model in Chapter 4. The deviatoric stress space $\{S_1, S_2, S_3\}$ described in Chapter 4 provides a convenient illustration of the type and degree of shearing to which soil elements are subjected.

Figure 6.6 shows the deviatoric stress path of an element of normally consolidated BBC initially at a radial distance $r_o = 25$ R from the axis of a 60° cone. For comparison, the deviatoric stress paths corresponding to the idealized Direct Simple Shear (DSS) and Pressuremeter (PR) modes of shearing* are also drawn in Fig. 6.6; they are located in the planes $S_2 = 0$ and, $S_3 = 0$, respectively. Figure 6.6 indicates that cone penetration subjects the soil to a very complicated mode of shearing which consists of a combination of Triaxial Compression (along S_1 - axis), DSS and PR modes. However, the end point of the deviatoric stress path in Fig. 6.6 (representing the state of stress of the element

---

*According to the model in Chapter 4.

far behind the tip) is close to the deviatoric stress path of the pressuremeter test.

Figures 6.7 and 6.8 show the projections in the $\{S_1, S_2, S_3\}$ space of the deviatoric stress paths of two elements, initially located at $r_o = R$ and $r_o = 25\ R$, due to penetration of 18° and 60° cones, respectively. Comparing results in Figs. 6.7 and 6.8 we note that:

a) the deviatoric stress path of a soil element at some distance from the cone axis ($r_o = 25\ R$) is virtually independent of the cone angle, and;

b) an element near the axis ($r_o = R$) is initially sheared in a triaxial compression mode. Its deviatoric stress path then follows a trajectory that is significantly dependent on the cone angle. However, the final deviatoric stress state shows little effect of cone angle.

6.3.3 Extent of Failure

Figure 6.9 presents the predicted contours of the octahedral shear stress*, τ_{oct}, and the extent of failure** during

---

* τ_{oct} is a good measure of the level of shearing in soil (see Chapter 4).

** A soil element is said to have reached failure when its associated stress point in the deviatoric stress space lies on the failure surface, f_p (see Chapter 4).

steady penetration of 18° and 60° cones in normally consolidated BBC. For comparison, predictions during expansion of a cylindrical cavity (from zero radius) using the same soil model are also shown at the top of Fig. 6.9. The cavity expansion solution is extensively used to study the shaft resistance of piles (e.g. Esrig et al., 1977) and corresponds to the limiting stresses at very large expansion levels in a pressuremeter test under idealized conditions.

Figure 6.9 shows that:

1) cone penetration causes shearing over a much larger volume of soil than cavity expansion in spite of the strong similarities between the strain path of soil elements in the two problems (see Figs. 3.9 and 3.10);

2) the size of the failure zone behind the cone is relatively independent of the cone angle and is significantly larger than predicted by cavity expansion (6.5 R compared to 3.4 R);

3) the strain softening behavior incorporated in the soil model causes a) the boundary of the failure zone (represented by the dotted line) to pass through points where τ_{oct} contours change sharply in direction and, b) the peak values of τ_{oct} are located at some distance

from the cone or the shaft behind it, and;

4) the extent of failure ahead of the blunt cone tip (where the soil is subjected to a triaxial compression mode of shearing) is larger than ahead of the sharp tip (7.1 R vs. 4.8 R). However, the results of 18° and 60° cones exhibit strong similarities outside the failure zone, especially if the origin of z-coordinate is located at mid-height of the cone instead of the tip.

This is illustrated by Fig. 6.10 showing the contours of the shear stress τ_{rz} obtained for 18° and 60° cone angles. The dashed line represents the contours of γ_{oct}* = 2% and approximately defines two zones: an inner zone where soil elements are subjected to intense shearing and an outer zone where shearing is more moderate. We note in Fig. 6.10 that: a) outside the dashed line, the cone angle has little effect on the results; b) ahead of the cone, negative** shearing takes place because soil elements near the axis (small r) are pushed downwards with respect to the outer elements (large r). On the other hand, behind the cone tip, shearing is reversed because conservation of volume requires elements near the

---

* $\gamma_{oct} = \frac{1}{3}\left[(\varepsilon_r - \varepsilon_\theta)^2 + (\varepsilon_\theta - \varepsilon_z)^2 + (\varepsilon_z - \varepsilon_r)^2 + 6\varepsilon_{rz}^2\right]^{\frac{1}{2}}$

** See sign convention in Fig. 6.10.

cone to be pushed upwards with respect to the outer elements, and; c) the shear stress τ_{rz} vanishes behind the cone. This is a reminder that the strain rates used in determining the deviatoric stresses correspond to an ideal fluid for which $\dot{\gamma}_{rz}$ vanishes along the shaft (frictionless boundary).

6.3.4 Isotropic (Octahedral) Total Stresses

The deviatoric stresses presented above were directly obtained by means of the deviatoric soil model described in Chapter 4 for the estimated strain paths corresponding to an ideal fluid (Chapter 3). Since the soil treated herein is incompressible, octahedral (isotropic) stresses, σ_{oct}, cannot be estimated from soil behavior models but must be determined from equilibrium considerations. Values of σ_{oct} are necessary to estimate the pore pressures during cone penetration.

In the axisymmetric cone penetration problems, equilibrium in the radial (r) and vertical (z) directions can be written in the form (see Appendix A):

$$\frac{\partial \sigma_{oct}}{\partial r} = f_r(r,z);\ f_r(r,z) = -\frac{\partial s_r}{\partial r} - \frac{\partial s_{rz}}{\partial z} - \frac{s_r - s_\theta}{r} \qquad (6.1.a)$$

$$\frac{\partial \sigma_{oct}}{\partial z} = f_z(r,z);\ f_z(r,z) = -\frac{\partial s_{rz}}{\partial r} - \frac{\partial s_z}{\partial z} - \frac{s_{rz}}{r} \qquad (6.1.b)$$

The functions $f_r(r,z)$ and $f_z(r,z)$ are known once the

deviatoric stresses are determined. Hence, integration of Eq. 6.1.a (or Eq. 6.1.b) satisfies equilibrium in the r-direction (or z-direction) and σ_{oct} can be determined for every soil element. However, the value of σ_{oct} depends on the integration path unless

$$\frac{\partial}{\partial z}\{f_r(r,z))\} = \frac{\partial}{\partial r}\{f_z(r,z)\} \qquad (6.2)$$

This condition can only be satisfied if the strain paths are compatible with the model used to determine the deviatoric stresses; i.e., the strains are determined from "exact" solutions (given a soil model) rather than the approximate strains corresponding to an ideal fluid.

a) Influence of Integration Path

In order to assess the effect of integration paths on σ_{oct} and thus evaluate the approximations caused by the simplified strain paths, the equilibrium equations were integrated along two paths described in detail in Appendix E. These paths are believed to provide reasonable bounds on σ_{oct}. In the first path, integration is carried out along isochronic lines* which are predominantly horizontal (i.e., close to the r-direction). In the second path, integration is carried out along streamlines which are predominantly vertical (i.e., close to the z-direction).

---

* Isochronic lines are the (initially) horizontal lines after deformation caused by cone penetration (see Figs. 3.3 and 3.4).

Figures 6.11 and 6.12 show the octahedral (isotropic) stresses, σ_{oct}, obtained by means of the two integration paths for different soil elements (initially located at various radii, r_o/R, from the axis) due to penetration by 18^o and 60^o cones, respectively. Results in Figs. 6.11 and 6.12 indicate that:

1) The two integration paths give the same general trends at most locations ahead of the cone base (or $z < -5R$, say). In this zone, streamline integration (dotted lines) overpredicts $(\sigma_{oct} - u_o)/\bar{\sigma}_{vo}$ by 15 to 60% for the sharp 18^o cone and 15 to 35% for the blunt 60^o cone;

2) behind the cone base (or $z > 5R$, say), streamline integration predicts unrealistic drops in σ_{oct} at some radii ($r_o = 0.1R$ and $r_o = 5R$ in Figs. 6.11 and 6.12), and;

3) using the same integration path, the cone angle has little effect on σ_{oct} in the soil located at some distance from the cone ($r_o > 5R$, say), provided the origin of coordinates in taken at midheight of the two cones.

b) Choice of an Integration Path

The results in Figs. 6.11 and 6.12 clearly show that the approximations in the strain path method lead to deviatoric stresses that, upon integration, yield an isotropic stress field significantly dependent upon the

integration path. It is thus appropriate to identify the deviatoric stress mostly responsible for the path dependency of integration and, select an integration path minimizing its effects.

The shearing strains corresponding to an ideal fluid (and used in these predictions) are believed to generally overestimate the shear strains, γ_{rz}, during cone penetration in clay. This is because of the lack of shearing resistance in a perfect fluid. Furthermore, in the deviatoric model, the predicted variations in shearing stresses, τ_{rz}, are controlled by the variations in γ_{rz} (or, more precisely in $\dot{\gamma}_{rz}$) and can, therefore, be unrealistic. This can be seen by the contours of τ_{rz} in Fig. 6.10. Consequently, the meridional shear stresses, τ_{rz} (especially behind the cone base),are believed to be the main cause for the integration path dependency observed in Figs. 6.11 and 6.12.

Furthermore, an examination of the equilibrium equations (Eqs. 6.1.a and 6.1.b) and Fig. 6.10 indicates that:

a) when integration is conducted along isochronic lines little variation in the z-coordinate takes place (except at small distances from the cone axis), $\frac{\partial s_{rz}}{\partial z}$ is generally small (except in the immediate vicinity of the tip) and hence the effect of $\tau_{rz} (= s_{rz})$ on the octahedral stresses, σ_{oct}, is small and;

b) when integration is conducted along streamlines, σ_{oct} is dominated by τ_{rz} because (1) streamlines are nearly vertical and hence σ_{oct} is determined (except at elevations close to that of the tip), principally by f_z, Eq. 6.1.b and (2), the function f_z depends on both s_{rz} and $\frac{\partial s_{rz}}{\partial r}$ that, according to Fig. 6.10, can be large.

In summary, predictions of the meridional shear stresses, τ_{rz} based on strains corresponding to an ideal fluid can involve significant errors and are believed to be the main cause for the path dependency of the octahedral normal total stress, σ_{oct}. However, when integration is carried out along isochronic lines (which are predominantly horizontal) the effect of τ_{rz} on σ_{oct} is minimized and hence more reliable estimates of σ_{oct} are obtained.

Accordingly, predictions of total stresses and pore pressures presented subsequently are determined by means of isochronic integration.

6.3.5 Total Stresses

Based on the isochronic integration path, the predicted contours of radial and vertical total stresses, σ_r and σ_z, during steady cone penetration in normally consolidated BBC are given in Figs. 6.13 and 6.14, respectively. The dashed line represents the contour of $\gamma_{oct} = 2\%$. For comparison, the results obtained for the expansion of a cylindrical cavity (from zero radius) using the same soil model are shown in the upper diagrams. Figures 6.13 and 6.14

indicate that:

1) outside the dashed line, which has a typical size of 4.5R, the cone angle has little effect on the results. In this outer zone; (a) soil elements located near the axis ahead of the cone are subjected to an increase in both σ_z and σ_r (with $\Delta\sigma_z > \Delta\sigma_r$) following a triaxial compression mode of shearing ($\Delta\sigma_r \simeq \Delta\sigma_\theta$), and; (b) far behind the cone, a steady condition is approached where σ_r and σ_z are slightly higher than predicted by the cavity expansion solution;

2) inside the dashed line the effect of cone angle is more pronounced. In this inner zone: (a) soil elements located close to the 60^o cone face are subjected to higher values of σ_r and σ_z than the 18^o cone, and; b) far behind the cone base and near the shaft, σ_r and σ_z are smaller than predicted by cavity expansion.

The variations in total stresses, σ_r, σ_θ and σ_z along a streamline initially located at a radial distance $r_o = 0.01R$ (i.e., practically on the centerline), are shown in Figs. 6.15 and 6.16 for 18^o and 60^o cones, respectively. In the outer zone, the effect of cone angle is negligible but a significant gradual increase in all three stresses takes place as the cone is approached. In the inner zone, the stresses go through three distinct phases:

1) Ahead of the tip, stresses increase sharply but

remain in the same order, $\sigma_z > (\sigma_r \simeq \sigma_\theta)$.

2) Along the cone face, the stresses are more or less uniform and: (a) change their relative order to become $\sigma_r > \sigma_z > \sigma_\theta$ as predicted by cavity expansion; (b) the difference between the stresses is small, i.e., the state of stress is close to isotropic with little deviatoric component and; (c) the magnitude of the stresses is higher than predicted by cavity expansion; and depends on the cone angle; stresses are higher for the blunt (60^o) than for the sharp (18^o) cone.

3) Behind the cone base, the stresses decrease sharply within a distance of 5R and reverse their relative order to become $\sigma_z > \sigma_\theta > \sigma_r$. A steady state appears to be approached 10 to 15R behind the cone base where the stresses are less than those predicted for the expansion of a cylindrical cavity.

The dashed lines (curves d) in Figs. 6.15 and 6.16 represent the variation of the octahedral shear stress, τ_{oct}, for a soil element near the axis. As the cone tip is approached, the shearing strains become very large and the shearing resistance of the soil drops sharply to its residual strength (i.e., minimum strength) at about 0.5R ahead of the cone tip.

6.3.6 Pore Pressures

The pore pressures generated in the clay due to steady cone penetration, Δu, are the sum of two components: (a) the increase in octahedral normal total stress, $\Delta\sigma_{oct}$, and; (b) the shear induced pore pressure, Δu_s.

Figure 6.17 presents the predicted contours of Δu_s for steady penetration of 18^o and 60^o cones based on the model in Chapter 5. These contours show that:

1) Δu_s is relatively small (compared to the changes in isotropic stress $\Delta\sigma_{oct}$), and;

2) behind the cone base, predictions of Δu_s are very close to cylindrical cavity solutions (upper diagram in Fig. 6.17) even at small distances from the shaft. The cone angle has some effect on Δu_s in the immediate vicinity of the shaft (about 2 radii).

Figure 6.18 shows the predicted contours of the excess pore pressure, Δu (= $\Delta u_s + \Delta\sigma_{oct}$), during steady penetration of 18^o and 60^o cones in normally consolidated BBC. The results in Fig. 6.18 show that:

1) The excess pore pressures, Δu, are significant even at large distances from the cone.

2) In the outer zone ($\gamma_{oct} < 2\%$), we note that:
   a) the cone angle has little effect on Δu, and;
   b) far behind the cone base, Δu is higher than predicted by the cavity expansion solution.

3) In the inner zone ($\gamma_{oct} > 2\%$) we note that:

a) in the vicinity of the cone face, the contours are nearly spherical (especially for the 60^{o} cone) and are affected by the cone angle. The 60^{o} cone gives higher values of Δu ($\Delta u/\bar{\sigma}_{vo}$ slightly higher than 2), and;

b) behind the cone base, Δu decreases sharply and reaches values that are not strongly affected by the cone angle and are lower than predicted by cavity expansion.

6.3.7 Effective Stresses and Hydraulic Fracturing

Hydrofracture takes place in a soil when the pore pressures become large enough to cause negative effective stresses. Cracking can then take place and hence increase the effective permeability of the soil. Hydrofracture due to cone penetration must therefore be considered if the pore pressure decay (after penetration stops) is to be used in estimating the consolidation properties of the soil.

The effective stresses, σ_{ij} in any soil element can be written as:

$$\bar{\sigma}_{ij} = \bar{\sigma}^{o}_{ij} + \Delta\sigma_{ij} - \Delta u\ \delta_{ij} \qquad (6.3)$$

Using Eq. 6.3 requires separate estimates of $\Delta\sigma_{ij}$ and Δu which are relatively large compared to $\bar{\sigma}_{ij}$. Small errors in these quantities can lead to negative effective stresses and thus predict that hydrofracture takes place (Massarch & Broms, 1977). However, Eq. 6.3 can also be

written as:

$$\bar{\sigma}_{ij} = \bar{\sigma}^{o}_{ij} + \Delta s_{ij} - \Delta u_s \, \delta_{ij} \qquad (6.4)$$

in which

$$\Delta s_{ij} = \Delta \sigma_{ij} - \Delta \sigma_{oct} \, \delta_{ij}$$

This equation avoids the aforementioned problem and in fact predicts the effective stresses during cone penetration without requiring the determination of σ_{oct} (which depends on the integration path; see Section 6.3.4).

The predicted contours of radial and circumferential effective stresses, $\bar{\sigma}_r$ and $\bar{\sigma}_\theta$ are presented in Figs. 6.19 and 6.20, respectively. We note in these figures that $\bar{\sigma}_r$ and $\bar{\sigma}_\theta$ remain positive everywhere in the field. The radial effective stress, $\bar{\sigma}_r$, is, however, greatly reduced along the cone shaft. This implies that measurements of pore pressures and lateral stresses along the shaft of driven pile whould yield very close values. On the other hand, the circumferential effective stresses, $\bar{\sigma}_\theta$, vary very little ($0.25\ \bar{\sigma}_{vo} < \bar{\sigma}_\theta < 0.50\ \bar{\sigma}_{vo}$ in most of the field, Fig. 6.20).

In order to investigate hydrofracture, it is necessary to evaluate the minor principal effective stress, $\bar{\sigma}_3$, in the soil. Results indicate that $\bar{\sigma}_3$ reaches a minimum value of 0.15 and 0.12 $\bar{\sigma}_{vo}$ along the shaft and at approximately 8R behind the base of 18^o and 60^o cones, respectively. This means that the strain path method predicts (with a substantial safety margin) no hydrofracture during cone penetration (or pile driving) in normally consolidated BBC.

6.4 COMPARISON WITH FIELD MEASUREMENTS

In this section, the predicted normalized excess pore pressures (needed for linear consolidation studies) are checked by means of field measurements. In addition, predictions of cone resistance, q_c, and pore pressures, u, are compared to in situ test results obtained in the BBC deposit at Saugus, Mass.

6.4.1 Field Measurements

Figure 6.21 shows the soil profile at Saugus, Mass. as determined by conventional laboratory tests. The clay between depths 25 and 75 feet is clearly overconsolidated with an OCR decreasing from 7 to 1.4. Below 75 ft the clay is reasonably uniform with an OCR = 1.3 $\pm$0.1.

Figure 6.22 shows the undrained shear strength of the clay obtained by different methods. Because of sample disturbance, results of unconfined (U) and unconsolidated-undrained (UU) tests exhibit significant scatter (s_u = 0.4 $\pm$ 0.2 kg/cm^2), without a clear trend with depth. The peak SHANSEP strengths are based on results of laboratory tests on resedimented BBC and on the OCR profile in Fig. 6.21. The field strength for embankment stability was backfigured from an induced embankment failure extending to a depth of 75 ft using the SHANSEP profiles (Azzouz and Baligh, 1978). The field vane strength from four holes exhibits less scatter and shows a variation

with depth which is consistent with the OCR profile (and hence the SHANSEP strengths and the field strength profiles).

Baligh et al. (1978) present extensive cone penetration results at the same site, including q_c and u measurements for cones with different geometries. Figure 6.23 shows typical profiles of q_c for a 60° cone and u at the tip of an 18° cone. This figure combines the results of 3 tests for both q_c and u and illustrates the good repeatability of the measurements. Figures 6.24 and 6.25 present the penetration pore pressures obtained at different locations along 18° and 60° cones, respectively, after eliminating the scatter in the results caused by the natural variability of the soil.

Figure 6.26 compares penetration pore pressures measured on the shaft behind an 18° cone with those measured behind enlarged 18° and 60° cones. Results in Fig. 6.26 indicate that:

1) after a distance of about 5 diameters behind the cone base, the pore pressures on the shaft of the regular (unenlarged) 18° cone appear to reach a constant value $(u)_{sh}$, Fig. 6.26.a;

2) the pore pressures behind the enlarged 18° cone, Fig. 6.26.b, are practically equal to $(u)_{sh}$ below a depth of 60 ft and slightly less in the upper stiff deposit, and;

3) the pore pressures behind the enlarged 60° cone, Fig. 6.26.c, are slightly higher than the enlarged 18° cone and closer to $(u)_{sh}$.

6.4.2 Normalized Excess Pore Pressure Distributions

The primary objective of this report is to estimate pore pressures in the soil during cone penetration as they represent the initial conditions for the consolidation that takes place after penetration stops.

Linear consolidation analyses require estimates of the relative (or normalized) distribution of excess pore pressure, $\Delta u (= u - u_o)$, in the soil rather than the absolute values of Δu which are more difficult to predict. This section compares the predicted and measured excess pore pressure fields in the soil when normalized with respect to the excess pore pressure on the shaft, $(\Delta u)_{sh}$, at a sufficiently large distance behind the cone $[(\Delta u)_{sh} = (u)_{sh} - u_o]$.

Figure 6.26a presents measured values of $(u)_{sh}$ behind an unenlarged 18° cone. Unfortunately, similar measurements behind a 60° cone are not available. However, Figs. 6.26b and c strongly suggest that $(u)_{sh}$ is not very sensitive to the cone angle. Therefore, in order to normalize experimental results, $(u)_{sh}$ behind the 60° cones were assumed to be the same as the 18° cone in Fig. 6.26a. This assumption tends to underestimate $(u)_{sh}$ behind 60° cones.

The solid lines in Fig. 6.27 show predictions of

$\Delta u/(\Delta u)_{sh}$ in a soil element initially located very close to the axis of 18° and 60° cones according to the strain path method and based on properties of resedimented normally consolidated BBC (OCR = 1). Values of Δu are the same as in Fig. 6.18 and the excess pore pressure on the shaft, $(\Delta u)_{sh}$ is taken as the predicted value of Δu at a distance 14R behind the cone tips. Figure 6.27 also shows the measured values of $\Delta u/(\Delta u)_{sh}$ at the Saugus site obtained at depths 45 ± 5, 60 ± 5 and 85 ± 5 ft which correspond to approximate overconsolidation ratios OCR = 3 ± 0.4, 2 ± 0.3 and 1.3 ± 0.1, respectively. Values of Δu are directly obtained from the results in Figs. 6.24 and 6.25. The uncertainty band of experimental results represents the range of $\Delta u/(\Delta u)_{sh}$ within a 10 ft layer centered at the required depth after neglecting "small scale" variability in Δu and $(\Delta u)_{sh}$. A more accurate band of uncertainty in $\Delta u/(\Delta u)_{sh}$ should include all the scatter in Δu and $(\Delta u)_{sh}$ due to inherent soil variability. Figure 6.23 presents the scatter in u due to soil variability when the porous stone is located at the tip of an 18° probe. If included in Fig. 6.27, this scatter would be represented by a band in the $\Delta u/(\Delta u)_{sh}$ plot equal to ± 0.31, 0.25 and 0.18, about the same mean, at depths 45, 60 and 85 ft, respectively.*

*Assuming that $(\Delta u)_{sh}$ has no scatter.

Figure 6.27 indicates that:

1) the measured values of the normalized excess pore pressure $\Delta u/(\Delta u)_{sh}$ vary very slightly with overconsolidation ratio ($1.3 < OCR < 3$), and;

2) the predicted distributions of $\Delta u/(\Delta u)_{sh}$ based on properties of resedimented normally consolidated BBC (OCR = 1) are very close to the measurements. This important result means that consolidation analyses based on the predicted distributions of $\Delta u/(\Delta u)_{sh}$ <u>can</u> be used to interpret dissipation records obtained in the BBC deposit at Saugus, Mass., below a depth of 45 ft (OCR < 3).

Attempts to extend this result to the upper stiff deposit above a depth of 40 ft was not successful because of the large scatter in measurements of u (due to inherent soil variability, see Fig. 6.23) as compared to the small average values of u in this layer. When Δu ($= u - u_o$) and $(\Delta u)_{sh}$ are small, scatter makes the measured values of $\Delta u/(\Delta u)_{sh}$ quite unreliable.

In order to check the predicted penetration pore pressures at some distance from the cone, measurements of u in the soil around the cone are required. Such measurements are very difficult to obtain in situ because of: a) the interference between the measuring device and soil deformations, and; b) the uncertainties in alignments which can

introduce significant errors in the estimated radial distances. Attempts to perform such measurements in BBC by means of two piezometers were unsuccessful, Baligh & Levadoux, 1980. Therefore, using the analogy between cone penetration and pile installation, predictions of $\Delta u/(\Delta u)_{sh}$ in the soil are compared with measurements conducted around a cylindrical pile (21.9 cm in diameter) jacked into Champlain Clay (Roy et al., 1979).

The measurements are quite consistent and reliable and, because of the small size of the piezometers (Geonor M-600) compared to the pile,* are hopefully less sensitive to the errors mentioned above (piezometer-soil interaction and alignment). Furthermore, the excess pore pressure measured along the shaft of the pile $(\Delta u)_{sh} \simeq 2\bar{\sigma}_{vo}$ is very close to that measured in BBC behind piezometers ($\simeq 2.1\ \bar{\sigma}_{vo}$, see Fig. 6.26).

Figure 6.28 compares the predicted radial distribution of excess pore pressure at a sufficiently large distance ($r \simeq 14R$) behind 18° and 60° cones during penetration in normally consolidated BBC to measurements in Champlain Clay. Results in Fig. 6.28 show that:

1) the predicted radial distributions of pore pressures behind 18° and 60° are almost identical;

2) the agreement between predictions and measurements is remarkable, in view of (a) the approximations in the

---

*the pile diameter is about 6.5 times that of the piezometer.

strain path method, (b) the uncertainties in the field measurements (in particular at small radii) and especially, (c) the difference in behavior between BBC (OCR = 1) used for predictions and the Champlain Clay (OCR ≈ 2) where measurements are made.

Results in Fig. 6.28 are very encouraging since they suggest that the normalized excess pore pressure distribution during pile driving is not very sensitive to soil type or stress history (OCR). This is further supported by the results in Fig. 6.29 showing that measurements in Champlain Clay are not unique but are similar to other clays of different types and stress histories. The properties of the different clays are described in more detail in Table 6.3

In summary, the two-dimensional (axisymmetric) normalized excess pore pressure distribution around cones (or piles) predicted by the strain path method compares very well with field measurements (a) at different locations along the cone for a wide range of overconsolidation ratios ($1.3 < OCR < 3$) and (b) in the radial direction far behind the tip. These distributions appear, therefore, sufficiently accurate to perform dissipation analyses which will hopefully be applicable for a wide variety of clays with $OCR < 3$.

6.4.3 Cone Resistance and Pore Pressures

a) Cone Resistance

The cone resistance, q_c is the force per unit area required to push the cone and is related to the total stresses (tractions) acting on the cone face by the expression:

$$q_c = \frac{1}{\pi R^2} \int_A (s_t \cos \delta + s_n \sin \delta)\, dA \qquad (6.5)$$

where s_n and s_t are the normal and tangential components of the surface traction vector on the cone face; 2δ is the cone angle; A is the surface area of the cone ($A = \pi R^2/\sin \delta$) and; R is the radius of the cone base (and of the shaft).

In the strain path solutions presented earlier, the strain rates were determined assuming the soil to behave as an ideal fluid with no shearing resistance. This, together with the soil model (described in Chapter 4) obeying the normality rule of plasticity, leads to negligible values of s_t on the cone face.* Therefore, predictions of q_c obtained by integrating the total stresses derived from the strain path method represent "smooth" cone solutions. In order to introduce the effects of shear stresses on the cone face and predict q_c for "rough" cones,

---

*and along the shaft behind; see Fig. 6.10.

we note that when the surface tractions s_t and s_n are uniform on the cone face and equal to τ and σ, respectively, Eq. 6.5 becomes:

$$q_c = \frac{\tau}{\tan \delta} + \sigma \qquad (6.6)$$

and hence the shearing stresses on the cone face increases the cone resistance by $\tau/\tan \delta$. Predictions of q_c for "smooth" and "rough" cones can, therefore, be estimated as follows:

1. Smooth cone:

   Integrate the total normal stress on the cone face obtained from the strain path solutions (see Figs. 6.13 and 6.14).

2. Rough cone:

$$(q_c)_{rough} = (q_c)_{smooth} + \frac{\tau}{\tan \delta} \qquad (6.7)$$

where τ = average shear stress acting on the cone face

$\simeq$ residual undrained shear strength of the soil

$\simeq 0.15\ \bar{\sigma}_{vo}$ for the model in Chapter 4.

Rigorously speaking, the predicted stress fields apply to normally consolidated resedimented Boston Blue Clay (Table 4.1) and hence q_c (and u) can only be estimated for this type of clay. Unfortunately, the BBC at the Saugus site, Fig. 6.21, is nowhere normally consolidated.

Between depths 25 and 75 ft, the OCR decreases from 7 to 1.3 and below 75 ft OCR ≈ 1.3. Consequently, comparisons with measurements at the Saugus site require extrapolation of q_c (and u) predictions to different values of OCR. An approximate method is described below.

Using the classical bearing capacity expression for deep foundations (Terzaghi, 1943; Skempton, 1951) we write the cone resistance:

$$q_c = N_c \, s_u + \sigma_{vo} \tag{6.8}$$

Noting that $\sigma_{vo} = \bar{\sigma}_{vo} + u_o$ and setting $\alpha = s_u/\bar{\sigma}_{vo}$, Eq. 6.8 becomes:

$$\frac{q_c - u_o}{\bar{\sigma}_{vo}} = \alpha N_c + 1 \tag{6.9}$$

Table 6.4 presents values of α obtained from laboratory tests on resedimented normally consolidated BBC and indicates that, depending on the mode of consolidation and undrained shearing, α_{NC} can vary between 0.155 and 0.34. This illustrates the difficulty of defining and estimating a cone factor N_c, Eq. 6.9. However, the existence of an N_c factor which is independent of the overconsolidation* of the clay allows interesting extrapolations

---

*If N_c is significantly dependent on OCR, the usefulness of Eq. 6.8 becomes highly questionable.

to various OCR to be made. Assuming N_c to be independent* of OCR, Eq. 6.9 enables estimates of the normalized cone resistance in the overconsolidated clays $\left(\frac{q_c - u_o}{\bar{\sigma}_{vo}}\right)_{OC}$ to be made from the predicted values $\left(\frac{q_c - u_o}{\bar{\sigma}_{vo}}\right)_{NC}$

$$\left(\frac{q_c - u_o}{\bar{\sigma}_{vo}}\right)_{OC} = \frac{\alpha_{OC}}{\alpha_{NC}} \left[\left(\frac{q_c - u_o}{\bar{\sigma}_{vo}}\right)_{NC} - 1\right] + 1 \qquad (6.10)$$

Table 6.4 presents values of α_{OC}/α_{NC} for BBC at different OCR's. For OCR < 4 the effect of the mode of shearing on α_{OC}/α_{NC} is not very significant** and values are close to the approximate expression proposed by Ladd et al., (1977) based on results of direct simple shear tests on clays***

$$\frac{\alpha_{OC}}{\alpha_{NC}} = (OCR)^{0.8} \qquad (6.11)$$

Using the ratios α_{OC}/α_{NC} obtained from direct simple shear tests as a reasonable average for different modes of shearing, Table 6.5 presents predictions of $(q_c - u_o)/\bar{\sigma}_{vo}$ for "smooth" and "rough" cones (2δ = 18° and 60°) at different OCR (= 1, 1.3, 2, and 3) according to Eqs. 6.7 and 6.10. Figure 6.30 compares predictions with the estimated

---

*Baligh and Vivatrat (1979) show that the variation of N_c for a 60° cone between depths 40 and 100 ft (OCR = 3.5 to 1.3) at the Saugus site using the "field" strength is relatively small ($N_c = 10 \pm 2$). The "field" strength is backfigured from an embankment failure together with the SHANSEP strength profile.

**As compared to its effect on α_{NC}, say.

***Including BBC.

range of measured values reported by Baligh et al. (1978). The estimated ranges (dashed areas in Fig. 6.30) are obtained by drawing the envelopes representing the average ± one standard deviation* of the measured values for 18°, 30° and 60° cones over a 10 ft layer. Results in Fig. 6.30 indicate that:

1) the "smooth" cone solutions give reasonable estimates of q_c for the 60° cone but are too low for the 18° cone. More importantly, "smooth cone" predictions contradict measurement trends regarding the effect of cone angle, and;

2) the "rough" cone solutions give reasonable estimates of q_c for 18° and 60° cones at low OCR but underpredict $q_c(18°)$ and overpredict $q_c(60°)$ at OCR = 3 ± 0.4. This suggests that "rough" cone solutions are more realistic and that extrapolations to high OCR's is not possible.**

The predicted resistance of 18° and 60° "rough" cones is plotted versus depth in Fig. 6.30. This figure provides a better assessment of predictions by showing the scatter in measurements. The overall agreement

---

*Due to scatter caused by inherent soil variability.

**Most probably due to the assumptions that N_c is independent of OCR and/or that friction on the cone face is also independent of OCR.

between predictions and measurements is good. In particular, predicted and measured values are virtually identical at depths 70 ± 10 and 115 ± 10 feet. The changes in $[q_c(18°) - q_c(60°)]$ below a depth of 75 feet, where the clay is generally classified as "uniform" (OCR = 1.3 ± 0.1), illustrate the sensitivity of q_c to local soil variations which cannot be accounted for by predictions.

b) Pore pressures

Section 6.4.2 shows that the distribution of the normalized pore pressures, $\Delta u/(\Delta u)_{sh}$ along the cone and the shaft behind it are well predicted by the strain path solutions (Fig. 6.27). It is therefore, sufficient to compare predicted and measured excess pore pressure along the shaft,* $(\Delta u)_{sh}$.

Solutions obtained for resedimented normally consolidated BBC (OCR = 1) yield $(\Delta u)_{sh}/\bar{\sigma}_{vo} = 1.0 \pm 0.05$ for both 18° and 60° cones. On the other hand, field measurements in the soft clay (below depth 75', OCR = 1.3 ± 0.1) give $(\Delta u)_{sh}/\bar{\sigma}_{vo} = 2.0 \pm 0.1$ i.e., about 100% higher than predicted. Interestingly, pressuremeter results discussed earlier (Sec. 6.2.4) were also underpredicted by the same soil model by roughly the same degree. Had the in situ OCR of the clay been used (OCR ≃ 1.3), prediction of Δu_{sh}

*Or at any other location on the cone.

would increase by about 25%. The remaining discrepancy can be due to: 1) the difference in behavior between resedimented BBC and the in situ clay. This includes the shear strength and the undrained stiffness (especially) at low strains and, 2) strain rate effects discussed earlier in Sec. 6.2.3. However, it is important to note that changes in soil parameters to improve predictions of pore pressures will increase the predicted cone resistance, q_c, and hence upset the good predictions in Figs. 6.30 and 6.31 by overpredicting q_c in the soft deposit below 75 ft (OCR ≈ 1.3), especially for the 60° cone.

A more complete analysis of pore pressures during penetration in the stiff upper deposit (OCR > 2) is expected to encounter less difficulty in simultaneously predicting cone resistance and pore pressure measurements. In this upper deposit, the pore pressures are not as high compared to the cone resistance [see u(tip) in Figs. 6.25 and q_c in Fig. 6.23 for 60° cones].

6.5 SUMMARY AND CONCLUSIONS

This chapter consists of 3 parts:

In Part 1 pressuremeter studies are conducted to check the soil behavior models (Chapters 4 and 5) and the adequacy of soil parameters estimated from laboratory tests on resedimented BBC. The predicted expansion curves are close to Cam-Clay results (determined by others for BBC) even though the stress-strain curves of the two models

differ significantly. This is due to the compensating effects of the shear modulus at low strains and the shear strength of the clay.

Comparison of the predicted expansion curves with pressuremeter tests results in the soft BBC (depths 83.2 and 103.2 ft at the Saugus site) show that matching of field measurements requires doubling of the estimated shear resistance of the soil. Part of this discrepancy (about 25%) is due to overconsolidation of the in situ clay (OCR ≈ 1.3) neglected in predictions. The remaining discrepancy (75%) can be due to: 1) simplifications made in theoretical analyses and/or the formulation of the soil model (e.g., end effects, partial drainage, strain rate effects,...etc.) and/or; 2) inadequacies in soil model parameters as described by the shear strength and/or shear modulus at small strain levels. The latter is very difficult to estimate reliably from conventional laboratory tests and is believed to represent a major reason for underpredicting field measurements (Azzouz et al., 1980).

In Part 2 of this chapter, the same soil model, with appropriate parameters for normally consolidated BBC, is incorporated in the strain path method (Chapter 2) to predict the normalized excess pore pressures in the soil during deep steady penetration of 18° and 60° cones. In spite of uncertainties resulting from the simplified nature of strain path

resulting from the simplified nature of strain path analyses, comparisons of predictions with extensive field measurements of pore pressures at different locations on the cone and the shaft behind it shows excellent agreement for both the 18° and 60° cones and, surprisingly, in the overconsolidated BBC as well (OCR $\leq$ 3). Further comparisons with pore pressure measurements obtained by others in the soil surrounding a jacked pile in Champlain Clay also show surprisingly close agreement. Since the measurements in Champlain Clay exhibit strong similarities with other clays, this suggests that predictions of the normalized excess pore pressure distribution in the soil is not very sensitive to the clay type or its overconsolidation ratio (for OCR $\leq$ 3). This hypothesis is important because, if true, it enables valuable generalizations to be made. In particular, results of linear consolidation analyses based on this normalized excess pore pressure distribution can be applied to a wide variety of clay deposits to estimate their coefficient of consolidation.

In Part 3 of this chapter predictions of cone resistance, q_c, and penetration pore pressures, u, based on the same solutions in Part 2 are compared with field measurements in BBC. Good agreement of q_c is achieved for 18° and 60° cones for OCR < 3 provided that the overconsolidation of the clay and the friction at the cone-soil

interface are accounted for. On the other hand, predictions of u are significantly underestimated in the soft BBC deposit below 75 ft (OCR ≃ 1.3) as in the case of the pressuremeter test data obtained in this clay.

	Roscoe and Burland (1968) (1)		Carter et al. (1978), Randolph et al. (1978) (2)			
input parameters	elastic strains neglected	elastic strains included	elastic strains neglected	elastic strains included	laboratory tests on remoulded RBC	comments
λ	0.15	0.15	0.15	0.15	-	slope of the virgin, e vs. lnp
κ	0.00	0.03	0.00	0.03	-	slope of rebound, e vs. lnp
M	-	-	1.20	1.20	-	see note (3)
$\bar{\phi}$	30°	30°	-	-	-	see definitions
k_o (4)	0.55	0.55	0.55	0.55	-	value used in analyses; see note (5)
e_o	1.16	1.16	1.16	1.16	-	equivalent to using critical state void ratio e_{cs}
$\frac{G}{K}$ (6)	-	2.17	-	2.17	-	
equivalent input parameters						
CR (5)	0.160	0.160	0.160	0.160	0.17 ± 0.03	compression ratio CR $=\Delta\varepsilon/(\Delta\log\bar{\sigma}_{vc})$ (at e_o=1.16)
RR (5)	0.000	0.032	0.000	0.032	0.025 - 0.05	recompression ratio RR $=\Delta\varepsilon/(\Delta\log\bar{\sigma}_{vc})$ (at e_o=1.16)
$\bar{\phi}_{TC}$	30°	30°	30°	30°	33° (12)	at max obliquity
predictions						
k_o (5)	0.671	0.627	0.671	0.627	0.50 - 0.55	normally consolidated clay
$\bar{\phi}$(TE)	30°	30°	48.5° (6)	48.5° (6)	35° - 40° (12)	at max obliquity (from $\overline{CK_oU}$ tests)
$\bar{\phi}$(PSC)	30°	30°	43.8° (7)	43.8° (9)	34° (12)	
$\bar{\phi}$(PSE)	30°	30°	43.8° (7)	43.8° (9)	≤40° (12)	
$Su/\bar{\sigma}_{vo}$(TC)	0.270	0.295 (9)	0.270	0.295 (9)	0.328 (11)	$\overline{CK_oU}$ triaxial compression peak strength
$Su/\bar{\sigma}_{vo}$(TE)	0.256	0.264 (9)	0.270	0.295 (9)	0.130 (11)	$\overline{CK_oU}$ triaxial extension peak strength
$Su/\bar{\sigma}_{vo}$(PSC)	0.296 (8)	0.310 (9)	0.312	0.340 (9)	0.335 (11)	$\overline{CK_oU}$ plane strain compression peak strength
$Su/\bar{\sigma}_{vo}$(PSE)	0.296 (8)	0.310 (9)	0.312	0.340 (9)	0.175 (11)	$\overline{CK_oU}$ plane strain extension peak strength
$Su/\bar{\sigma}_{vo}$(PM)	0.296 (8)	0.223 (9,10)	0.312	0.340 (9)	0.210 (11)	$\overline{CK_oU}$ pressuremeter " "
$Su/\bar{\sigma}_{vo}$(DSS)	0.296 (8)	0.310 (9)	0.312	0.340 (9)	0.200 (11)	$\overline{CK_oU}$ direct simple shear " "

Table 6.1 Model parameters and predictions of the Cam-Clay model (after Kavadas, 1979)

Table 6.1 (cont.)

DEFINITIONS

(1) $q = \frac{1}{\sqrt{2}} \{(\bar{\sigma}_1-\bar{\sigma}_2)^2 + (\bar{\sigma}_2-\bar{\sigma}_3)^2 + (\bar{\sigma}_3-\bar{\sigma}_1)^2\}^{1/2}$; $q \geq 0$

(2) $p = \frac{1}{3}(\bar{\sigma}_1 + \bar{\sigma}_2 + \bar{\sigma}_3)$; $\bar{\sigma}_1$, $\bar{\sigma}_2$, $\bar{\sigma}_3$ are major intermediate and minor principal effective stresses ($\bar{\sigma}_1 \geq \bar{\sigma}_2 \geq \bar{\sigma}_3$)

(3) $\bar{\phi} = \arcsin\left(\frac{\bar{\sigma}_{1f}-\bar{\sigma}_{3f}}{\bar{\sigma}_{1f}+\bar{\sigma}_{3f}}\right)$ or $\frac{\bar{\sigma}_{1f}}{\bar{\sigma}_{3f}} = \frac{1+\sin\bar{\phi}}{1-\sin\bar{\phi}} = N_\phi$; subscript f refers to failure (according to a failure criterion)

(4) $S_u = \frac{\bar{\sigma}_{1f}-\bar{\sigma}_{3f}}{2}$

NOTES

(1) Assuming Mohr-Coulomb failure criterion:

- $\bar{\phi}$ is independent of failure mode
- The yield surface is an ellipse with an associated flow rule, but, at failure, violates incompressibility requirement

(2) Assuming Extended Mises criterion:

- $M = \frac{q_f}{p_f}$
- M is evaluated from triaxial compression test ($\bar{\sigma}_2=\bar{\sigma}_3$)
  $\bar{\phi}_{(TC)} = \arcsin(\frac{3M}{6+M})$
- The yield surface is an ellipse with an associated flow role; therefore, in plane strain failures $\bar{\sigma}_{2f} = \frac{1}{2}(\bar{\sigma}_{1f}+\bar{\sigma}_{2f})$

(3) For M = 1.2 we have:

- neglecting elastic strains: $k_o = 0.671$
- without neglecting elastic strains: $k_o = 0.627$

(4) K is the bulk elastic modulus: $K = \frac{p(1+e)}{k}$

We assume $\frac{K}{G} = \frac{2(1+\bar{\nu})}{3(1-2\bar{\nu})}$ and $\bar{\nu} = 0.3$

Table 6.1 (cont.)

(5) $CR = \frac{2.3\lambda}{(1+e)}$; $RR = \frac{2.3\kappa}{(1+e)}$

(6) $\bar{\phi}_{(TE)} = \arcsin(\frac{3M}{6-M})$

(7) $\bar{\phi}_{(PSC)} = \bar{\phi}_{(PSE)} = \arcsin(\frac{M}{\sqrt{3}})$

(8) Assuming $\bar{\sigma}_{2f} = \frac{1}{2}(\bar{\sigma}_{1f}+\bar{\sigma}_{3f})$

(9) Numerically evaluated

(10) Numerical computation of $\bar{\sigma}_{1f}$, $\bar{\sigma}_{2f}$, $\bar{\sigma}_{3f}$, yielded that $\bar{\sigma}_{2f} \neq \frac{1}{2}(\bar{\sigma}_{1f}+\bar{\sigma}_{3f})$

(11) Table 4.3

(12) After Ladd et al. (1971)

Streamlines

r_o/R *	
0.01	3.30
0.1	3.60
0.2	4.0
0.3	4.5
0.4	5.0
0.5	5.75
0.6	6.5
0.7	7.5
0.8	8.5
0.9	9.5
1.0	11.0
1.1	12.5
1.2	14.0
1.3	16.0
1.4	18.0
1.5	20.0
1.65	25.0
1.8	30.0
2.0	40.0
2.25	50.0
2.5	70.0
2.75	100.0
3.0	150.0

* r_o = initial radial distance of the streamline from the axis
R = shaft radius

Boundary Stresses

- Total stresses - u_o = effective stresses

$\bar{\sigma}_z = \bar{\sigma}_{vc}$ $\bar{\sigma}_r = \bar{\sigma}_\theta = K_o \bar{\sigma}_{vc}$; $K_o = 0.537$

- Deviatoric stresses

$s_z = 0.309\ \bar{\sigma}_{vc}$; $s_r = s_\theta = -0.154\ \bar{\sigma}_{vc}$

Table 6.2 Streamlines and boundary stresses used in the analyses.

Case	a	b	c	d	e	f	g	h
Reference	Bjerrum and Johannessen (1960)	Lo and Stermac (1965)	Koizumi and Ito (1967)	Roy et al (1979)	Raligh et al (1978)	Airhart et al (1969)	Immel and Klym (1979)	Soderman and Milligan (1961)
1) Site	Southern Norway	Walleceburg Ontario, Canada	Otemachi Tokyo, Japan	Saint Alban Quebec, Canada	Saugus Massachusetts, USA	Beaumont Texas, USA	Pickering Ontario, Canada	Big Pic River Canada
2) Soil								
2-a Type and description	Soft Marine clay	Soft to firm silty clay	Very sensitive slightly organic silty clay	Very sensitive Marine soft silty Champlain Clay	Marine illitic Boston Blue Clay	Highly over-consolidated	Firm clayey-sandy silt	Medium to stiff varved silty clay
2-b Plasticity Index (PI)	25	20	60	20	20	40	10	37 clay, 7 silt
2-c Overconsolidation ratio (OCR)	≈ 1	≈ 1	≈ 2.5 [5]	2 to 2.4	1.2 to 4	OCR = 7 [5]	High sand content	OCR = 3 [5]
2-d Undrained Strength (s_u)	2 to 2.5 TSM [1]	2 to 2.5 TSM [1]	3 to 3.5 TSM [2]	1 to 2 [1]	3.5 to 5.5 TSM [1]	11 TSM [3]	No OCR & s_u meas.	2.5 to 4.5 TSM
2-e Sensitivity (S_t)	6 to 8 [1]	4 to 6 [1]	v. high	16	6			
3) Pile: 3-a type	Steel Hollow Box	Steel pipe	Steel pipe	Steel pipe	Steel cylinder	Steel pipe	H-pile	H-pile
3-b Cross section	20 x 20 cm	ϕ = 8.9 cm	ϕ = 30 cm	ϕ = 21.9 cm	ϕ = 3.8 cm	ϕ = 40.7 cm	12"x 53 lb.	12" x 53 lb.
3-c Length	≈ 20 m	15 m	5.5 m	7.5 m	Variable	16.2 m	7.6 m	16.8 to 50.6 m
3-d Installation	Driving	Driving	Jacking	Jacking	Jacking	Driving	Driving	Driving
4) Pore Pressures Measurements								
4-a Device	MGI piezometer	not reported	Cells on piles and piezometers	Gloetzl cell on pile & Geonor electric piezometer in soil	Electric Transducer	Pressure Transducer	Gage at surface for pressure on pile and geonor piezometer in soil	Casagrande open tube
4-b Quality	Good		Fair	Very Good	Very Good	Fair	Fair	Questionable
5) Notes	No measurements of u_i close to pile	Significant scatter. Pore pressures still rising after 1 hr when second pile was driven	Significant scatter. Comprehensive study [4]	Very repeatable	Very repeatable	Pore pressure still rising after 8 hours. No data on G.W. level.		

(1) Field Vane Test
(2) Dutch Cone Test
(3) Unconfined Test
(4) Important uncertainty in $\bar{\sigma}_{vo}$ due to 1.5m excavation. We assume wide excavation and pore pressure equalization. Otherwise $\bar{\sigma}_{vo}$ doubles at depth = 5m.
(5) Estimated

Table 6.3 Data on clays where pore pressure measurements were obtained during pile installation.

Test	α_{NC} (OCR = 1)	α_{OC}/α_{NC} [1]			$s_u = \alpha\bar{\sigma}_{vc}$	Reference
		OCR = 2	OCR = 3	OCR = 4		
K_o-Consolidated Direct Simple Shear ($\overline{CK_oUDSS}$)	0.2	1.85	2.5	3.1	$(\tau_h)_{max}$	Ladd & Edgers (1972)
K_o-Consolidated Triaxial Compression ($\overline{CK_oUC}$)	0.33	---	---	---	$(\frac{\sigma_1 - \sigma_3}{2})_{max}$	Ladd & Varallyay (1965)
K_o-Consolidated Triaxial Extension ($\overline{CK_oUE}$)	0.130	---	---	---	$(\frac{\sigma_1 - \sigma_3}{2})_{max}$	Ladd & Varallyay (1965)
K_o-Consolidated Plane Strain Compression ($\overline{CK_oUPSC}$)	0.34	1.7	2.15	2.8	$(\frac{\sigma_1 - \sigma_3}{2})_{max}$	Ladd et al. (1971)
K_o-Consolidated Plane Strain Extension ($\overline{CK_oUPSE}$)	0.175	2	2.7	3.3	$(\frac{\sigma_1 - \sigma_3}{2})_{max}$	Ladd et al. (1971)
Isotropically Consolidated Triaxial Compression ($\overline{CIUC}$)	0.3	1.6	2.2	2.6	$(\frac{\sigma_1 - \sigma_3}{2})_{max}$	Ladd & Varallyay (1965)
Isotropically Consolidated Triaxial Extension ($\overline{CIUE}$)	0.245	---	---	---	$(\frac{\sigma_1 - \sigma_3}{2})_{max}$	Ladd & Varallyay (1965)
	$(OCR)^{0.8}$	1.74	2.41	3.03		

(1) From Ladd and Edgers (1972)

Table 6.4 Undrained shear strengths of resedimented Boston Blue Clay from laboratory tests.

OCR	1		1.3		2		3	
$\frac{\alpha^{(1)}}{\alpha_{NC}}$	1.0		1.25		1.85		2.5	
	Smooth	Rough	Smooth	Rough	Smooth	Rough	Smooth	Rough
$2\delta^{(2)} = 18°$	2.70[3]	3.65	3.13	4.31	4.15	5.9	5.25	7.63
$2\delta = 60°$	2.95[3]	3.21	3.44	3.76	4.61	5.09	5.88	6.53

(1) Value from Direct Simple Shear tests, Ladd et al. (1977); $\alpha_{NC} = 0.2$

(2) 2δ = cone angle

(3) Value predicted by strain path analyses for a smooth cone and OCR = 1

Table 6.5 Prediction of $(q_c - u_o)/\bar{\sigma}_{vo}$ for different OCR.

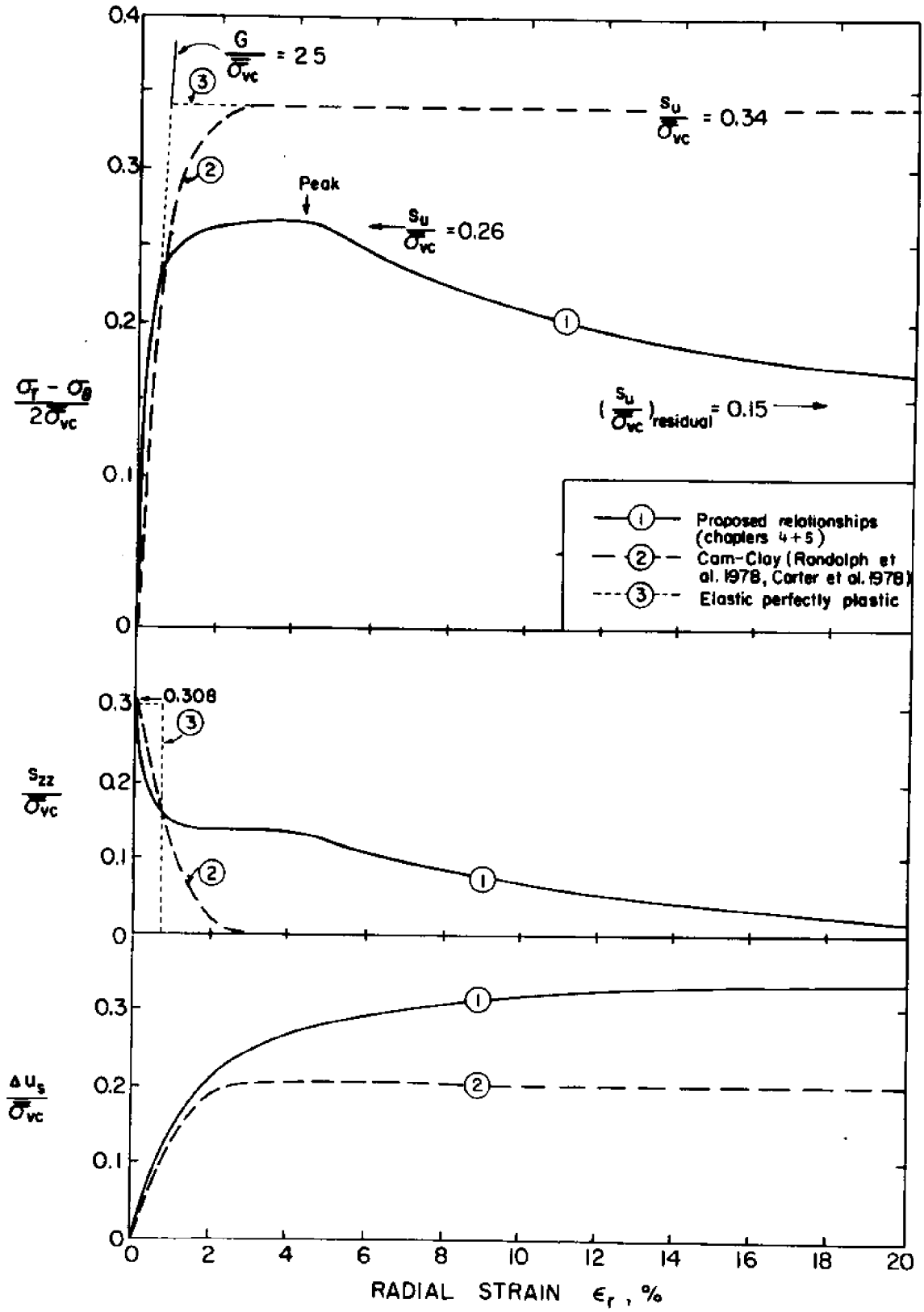

Figure 6.1 Comparison of predicted stress-strain curves for $\overline{CK_oU}$ undrained expansion of a cylindrical cavity in normally consolidated Boston Blue Clay.

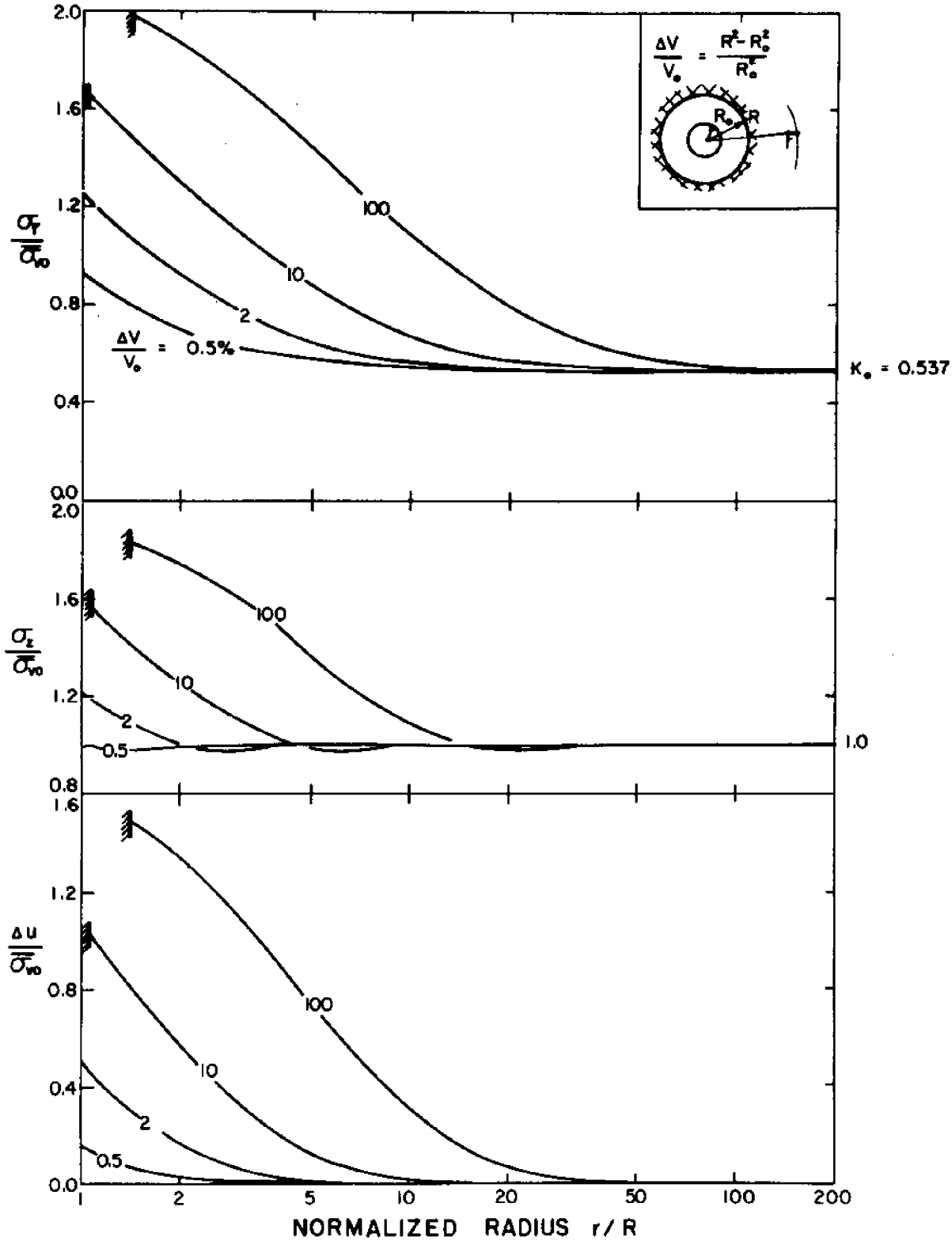

Figure 6.2 Prediction of stress and pore pressure distributions at different levels of expansion during a pressuremeter test in normally consolidated Boston Blue Clay.

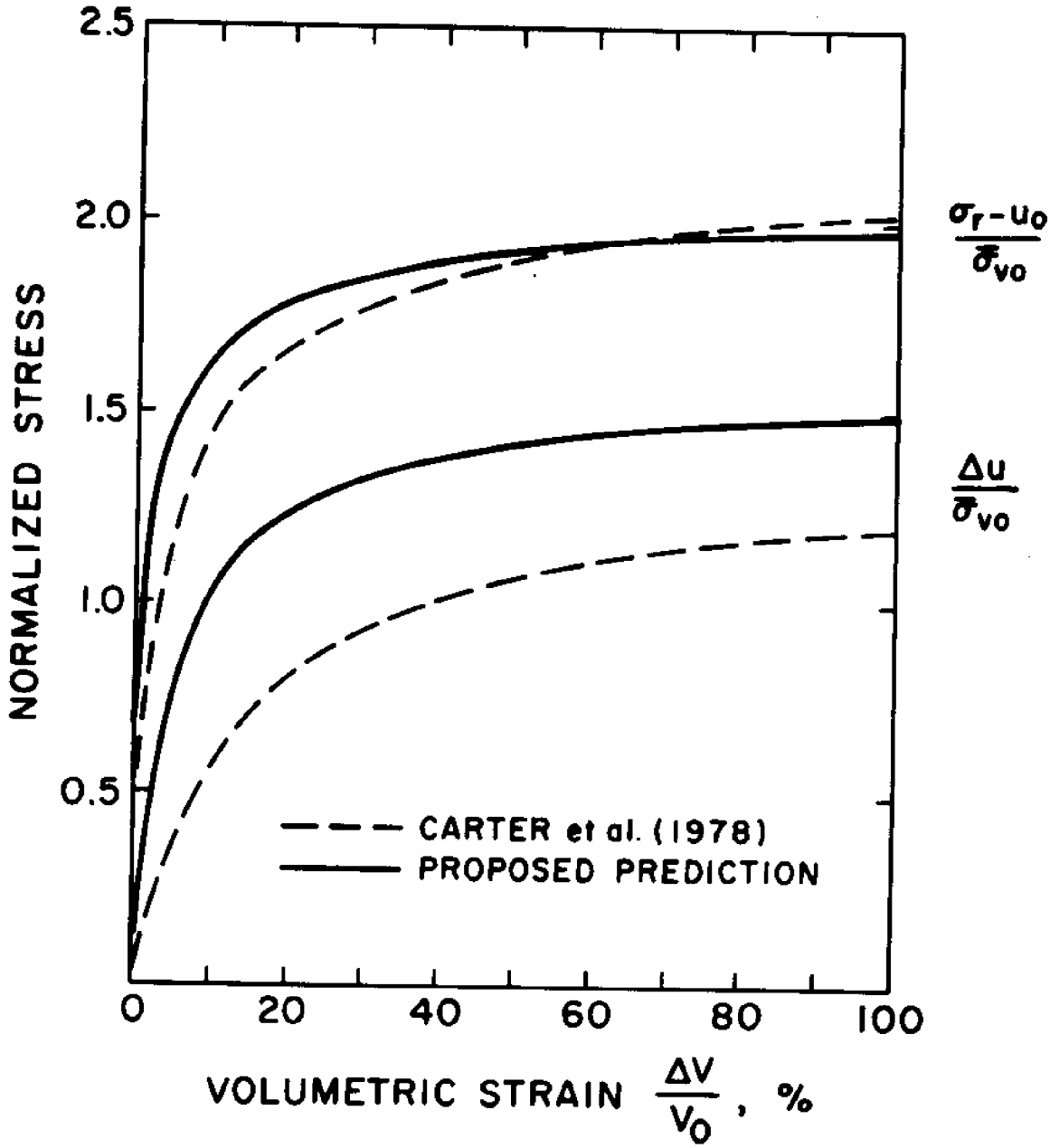

Figure 6.3 Comparison of predicted pressuremeter expansion curves in normally consolidated Boston Blue Clay.

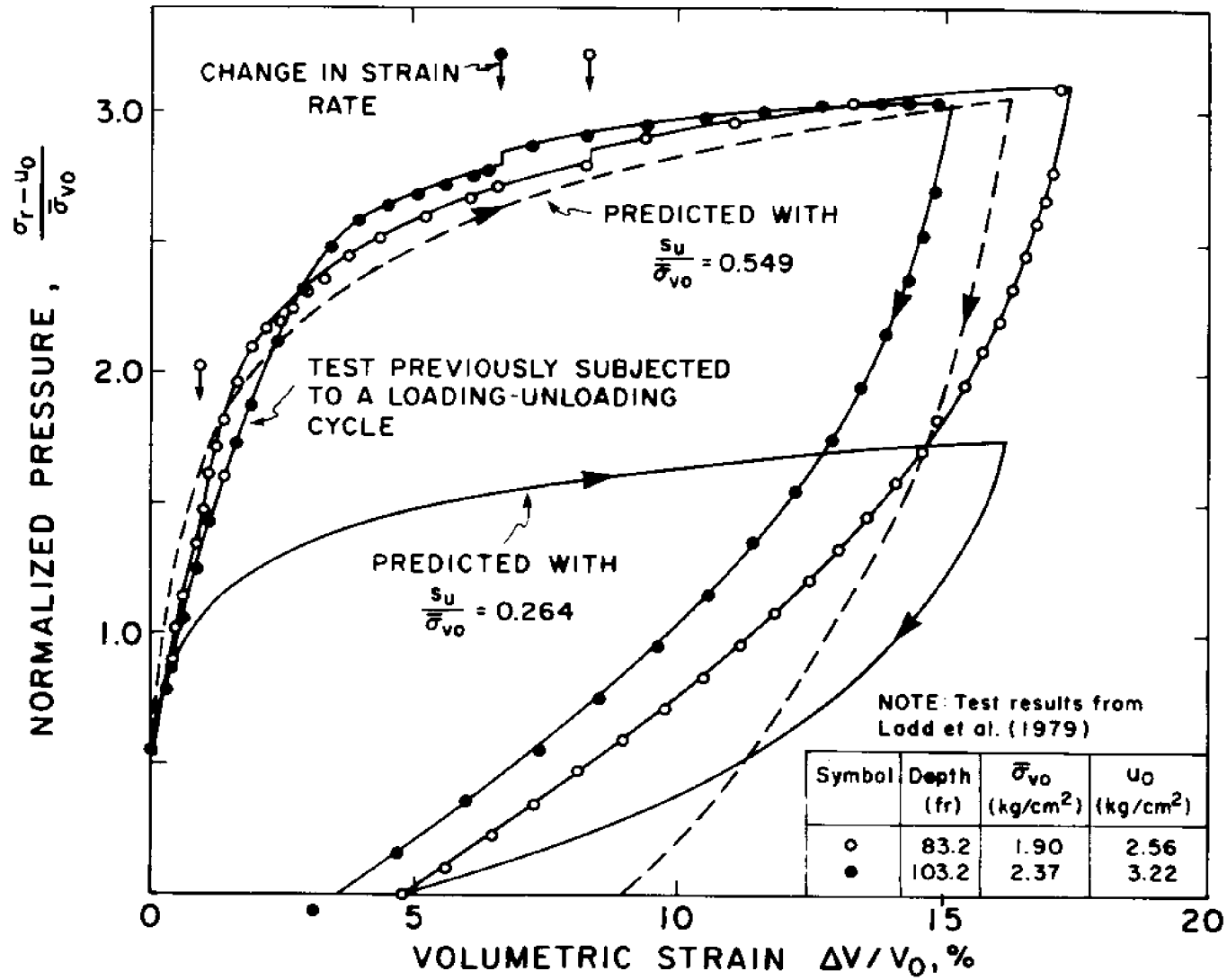

Figure 6.4 Predicted vs. measured expansion curves for pressuremeter tests in normally consolidated Boston Blue Clay.

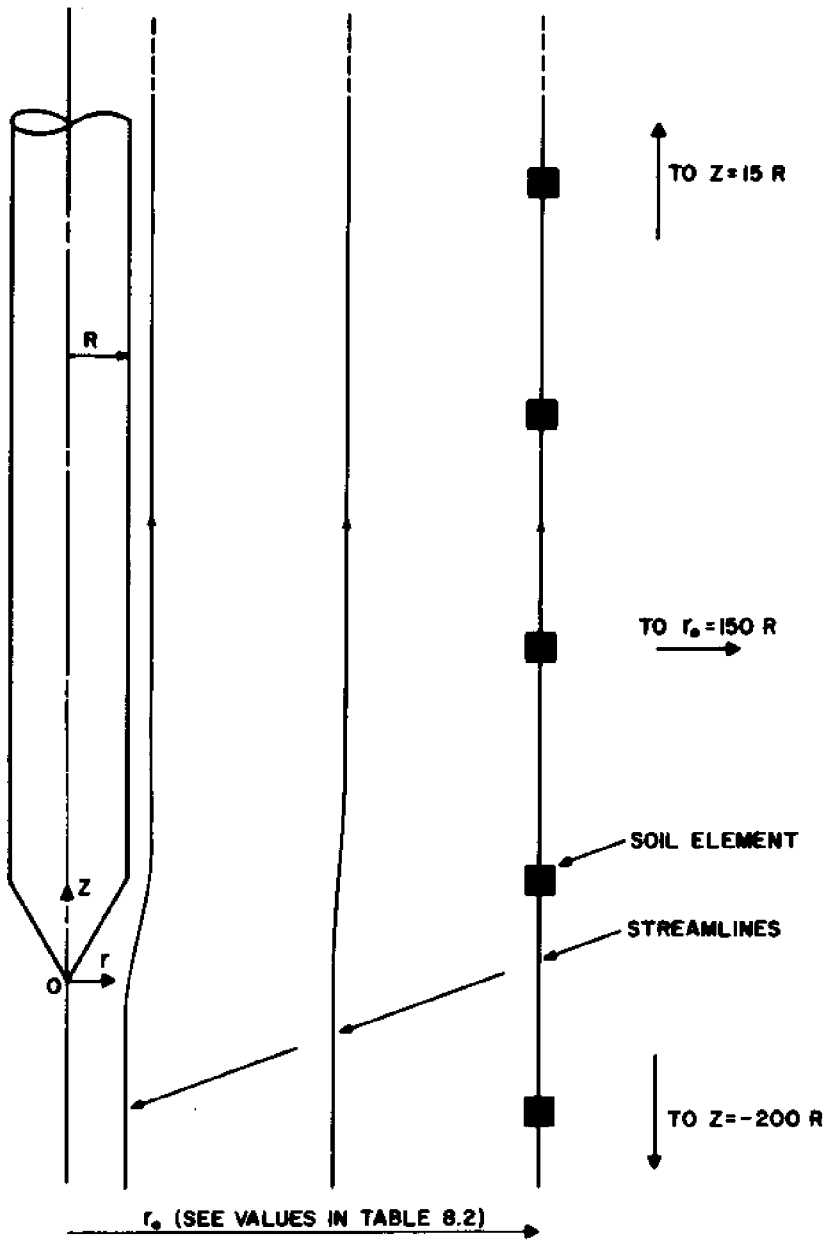

Figure 6.5 Solution to cone penetration in clay: problem geometry.

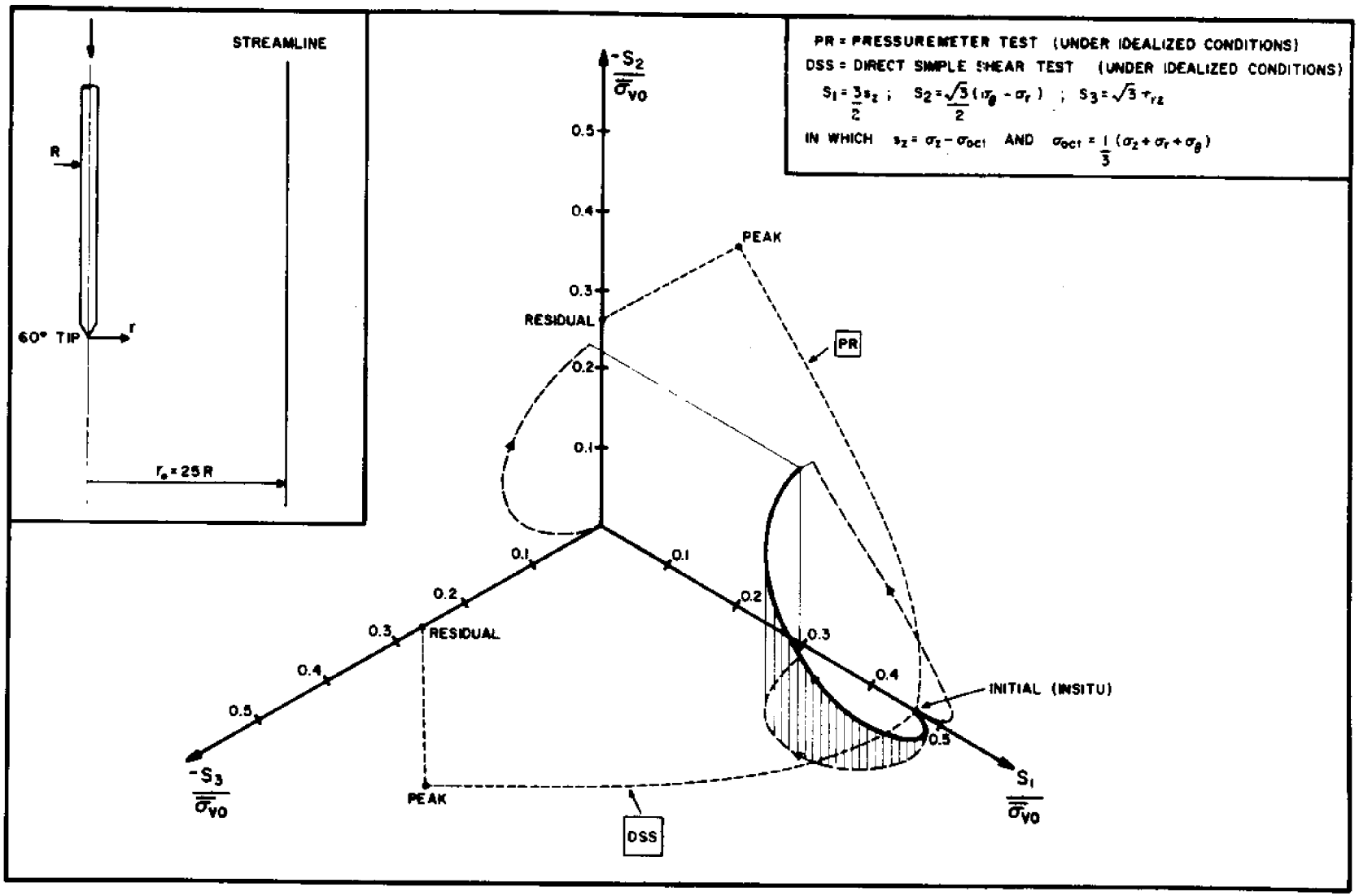

Figure 6.6 Predicted three-dimensional deviatoric stress path during steady penetration of a 60° cone in normally consolidated Boston Blue Clay.

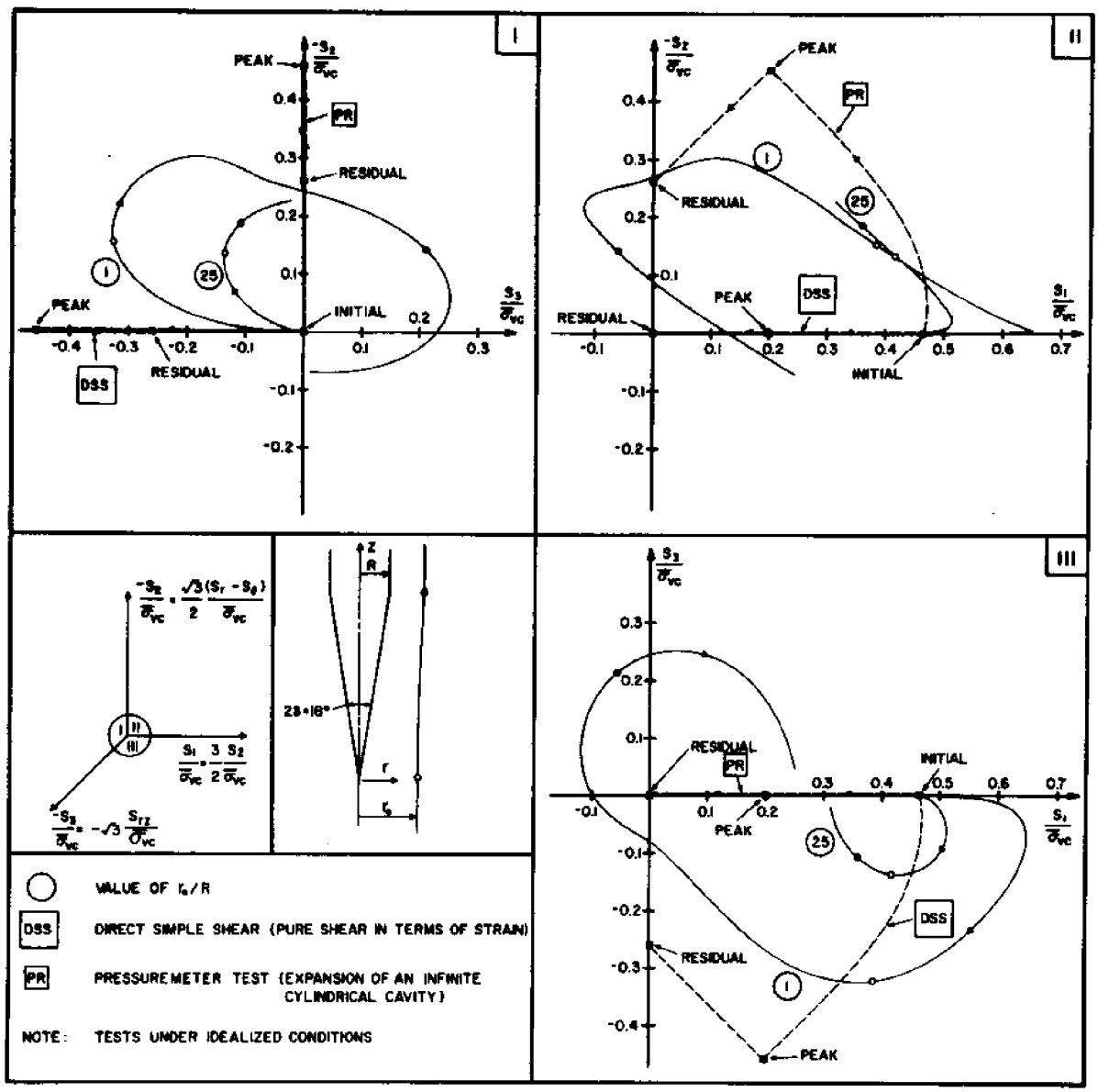

Figure 6.7 Predicted deviatoric stress paths along two streamlines during steady penetration of an 18° cone in normally consolidated Boston Blue Clay.

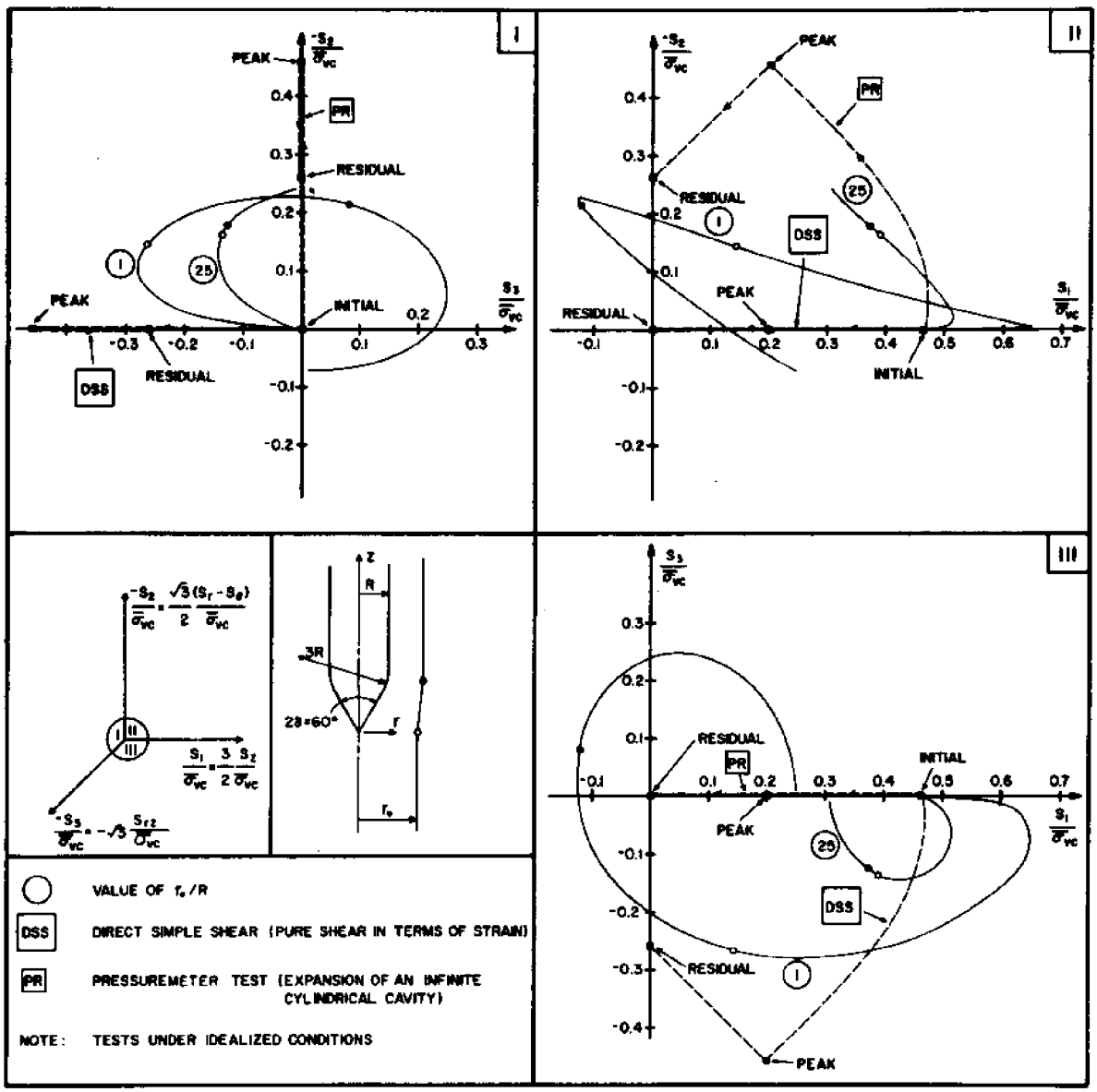

Figure 6.8 Predicted deviatoric stress paths along two streamlines during steady penetration of a 60° cone in normally consolidated Boston Blue Clay.

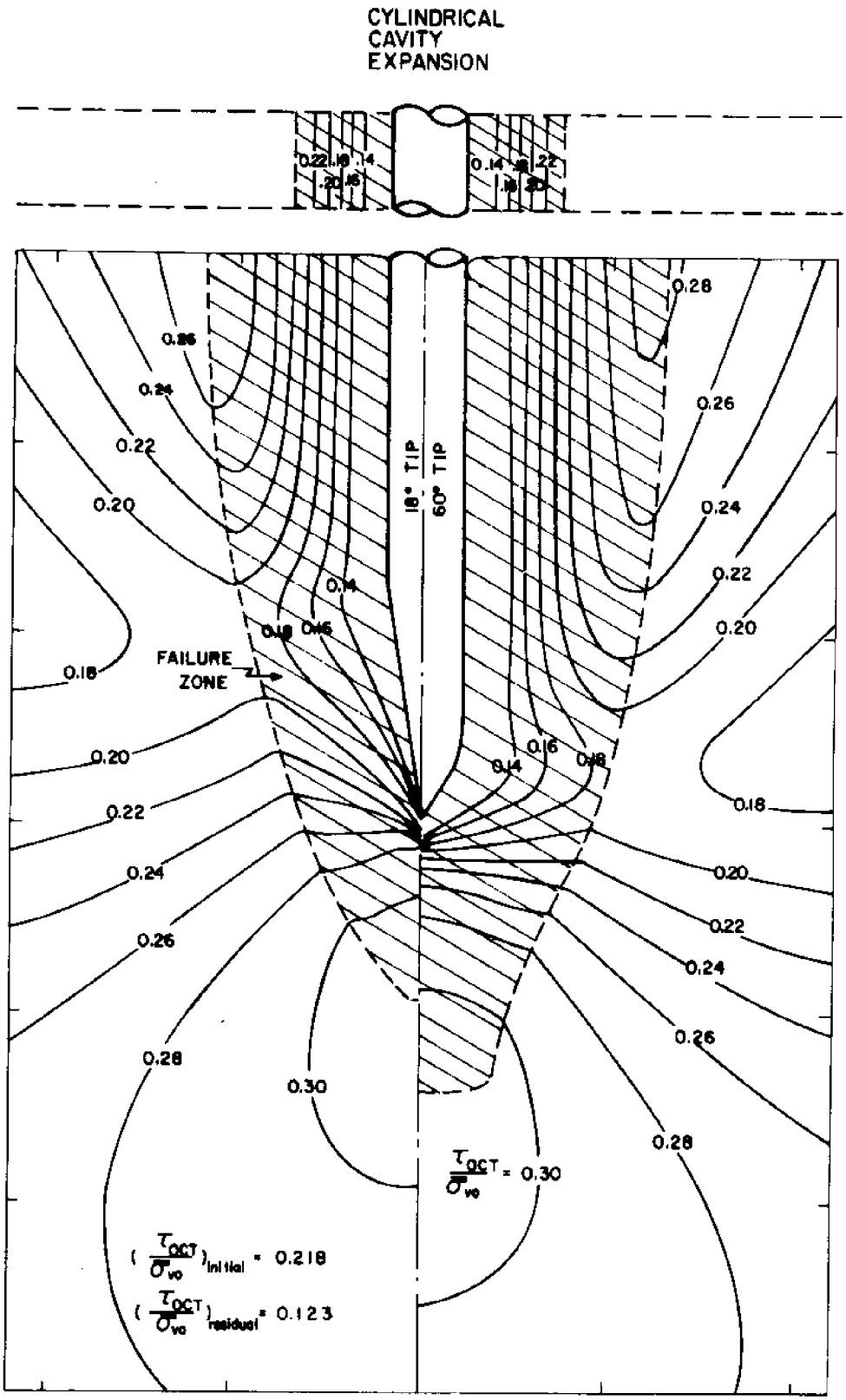

Figure 6.9 Predicted contours of normalized octahedral shear stress, τ_{oct}, and extent of failure during steady cone penetration in normally consolidated Boston Blue Clay (18° and 60° tips).

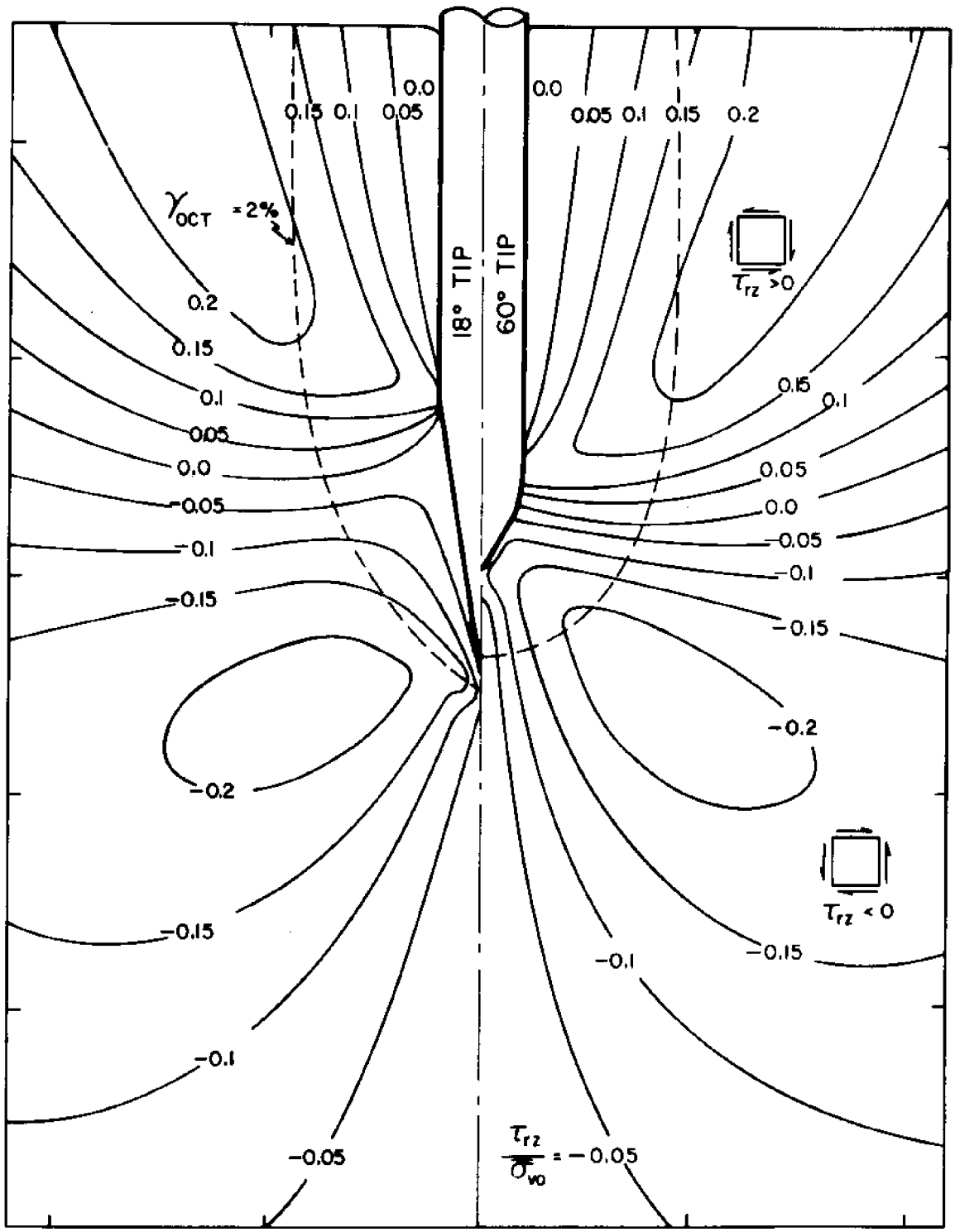

Figure 6.10 Predicted contours of normalized shear stress, τ_{rz}, during steady cone penetration in normally consolidated Boston Blue Clay (18° and 60° tips).

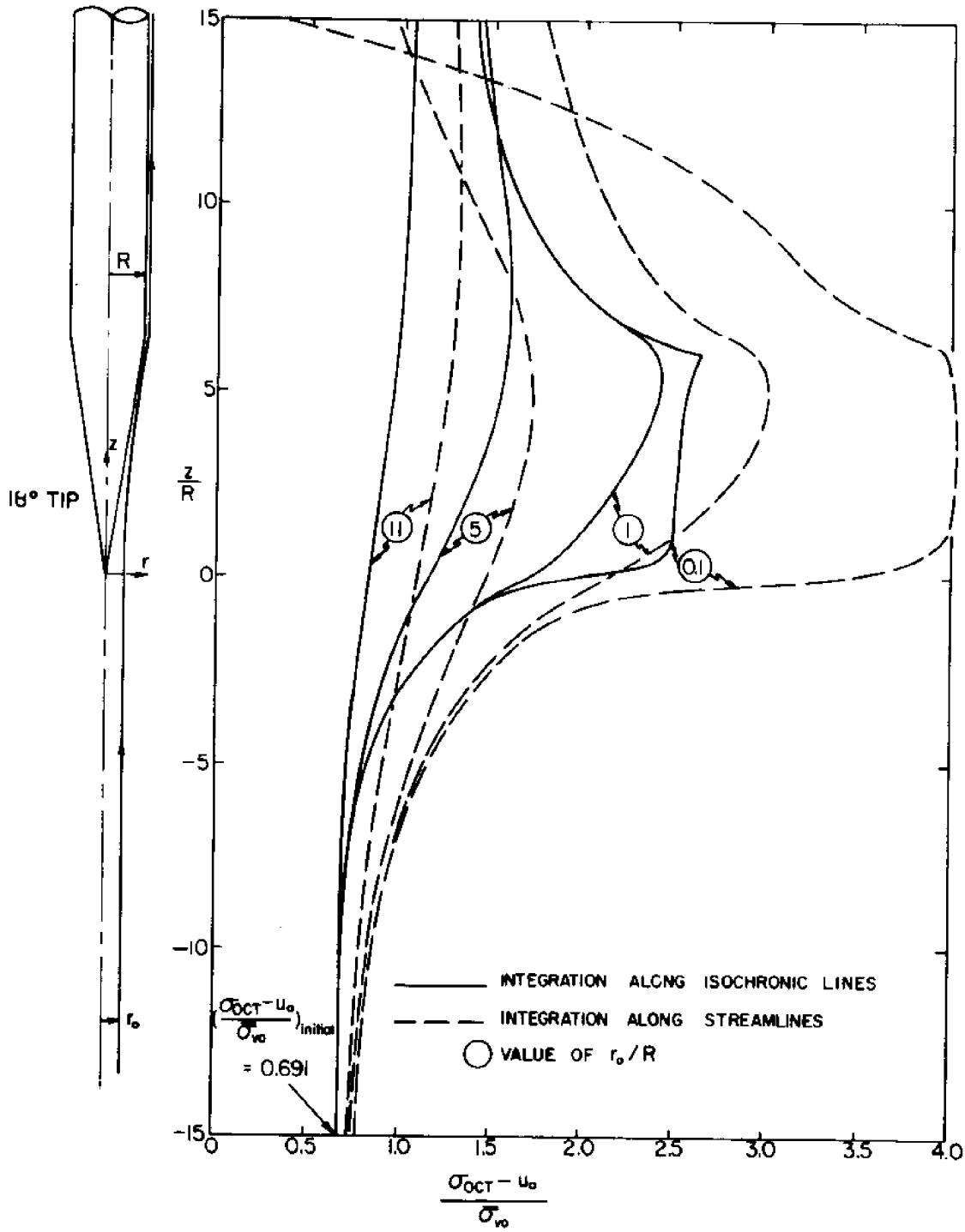

Figure 6.11 Comparison between two methods of integration (18° cone).

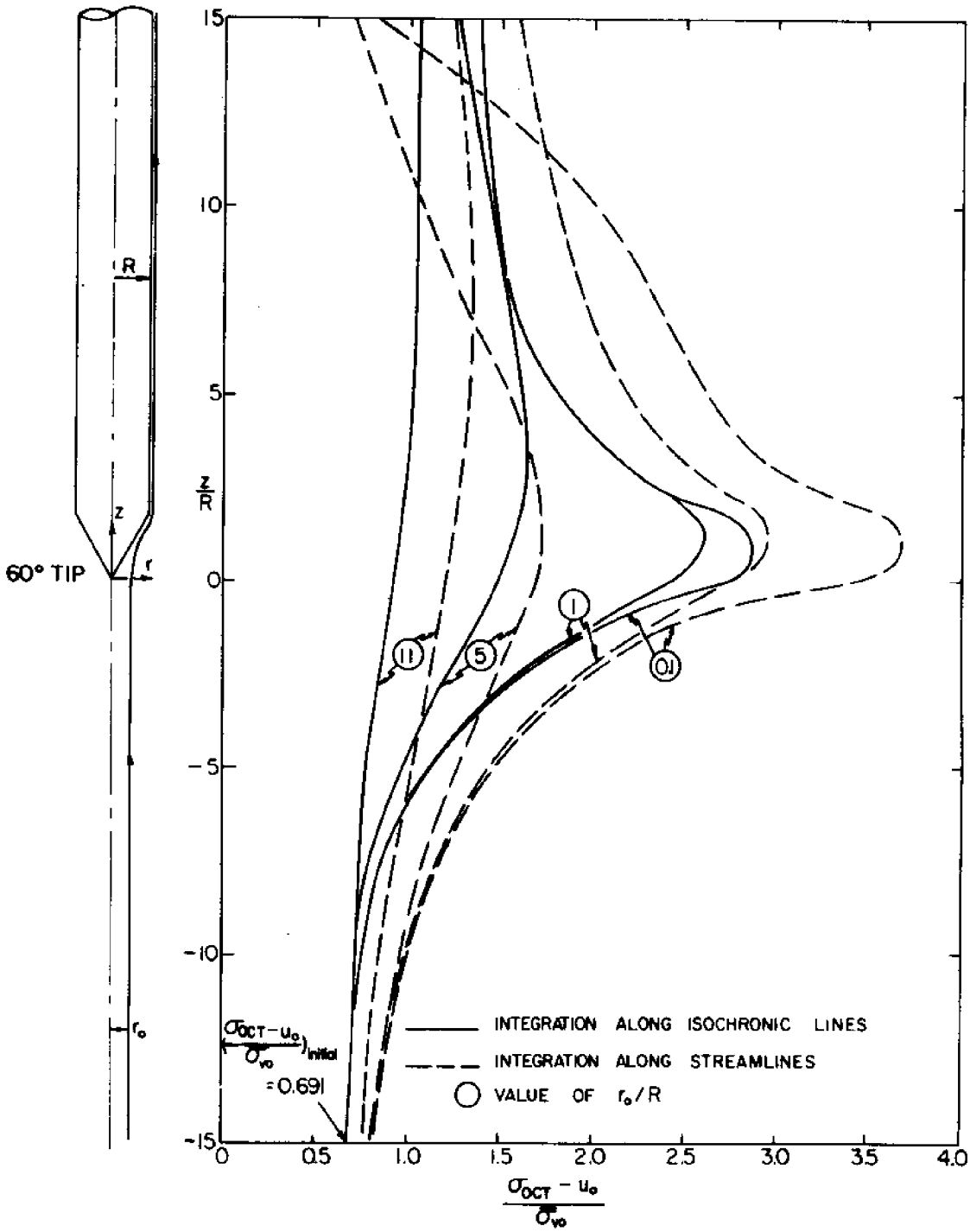

Figure 6.12 Comparison between two methods of integration (60° cone).

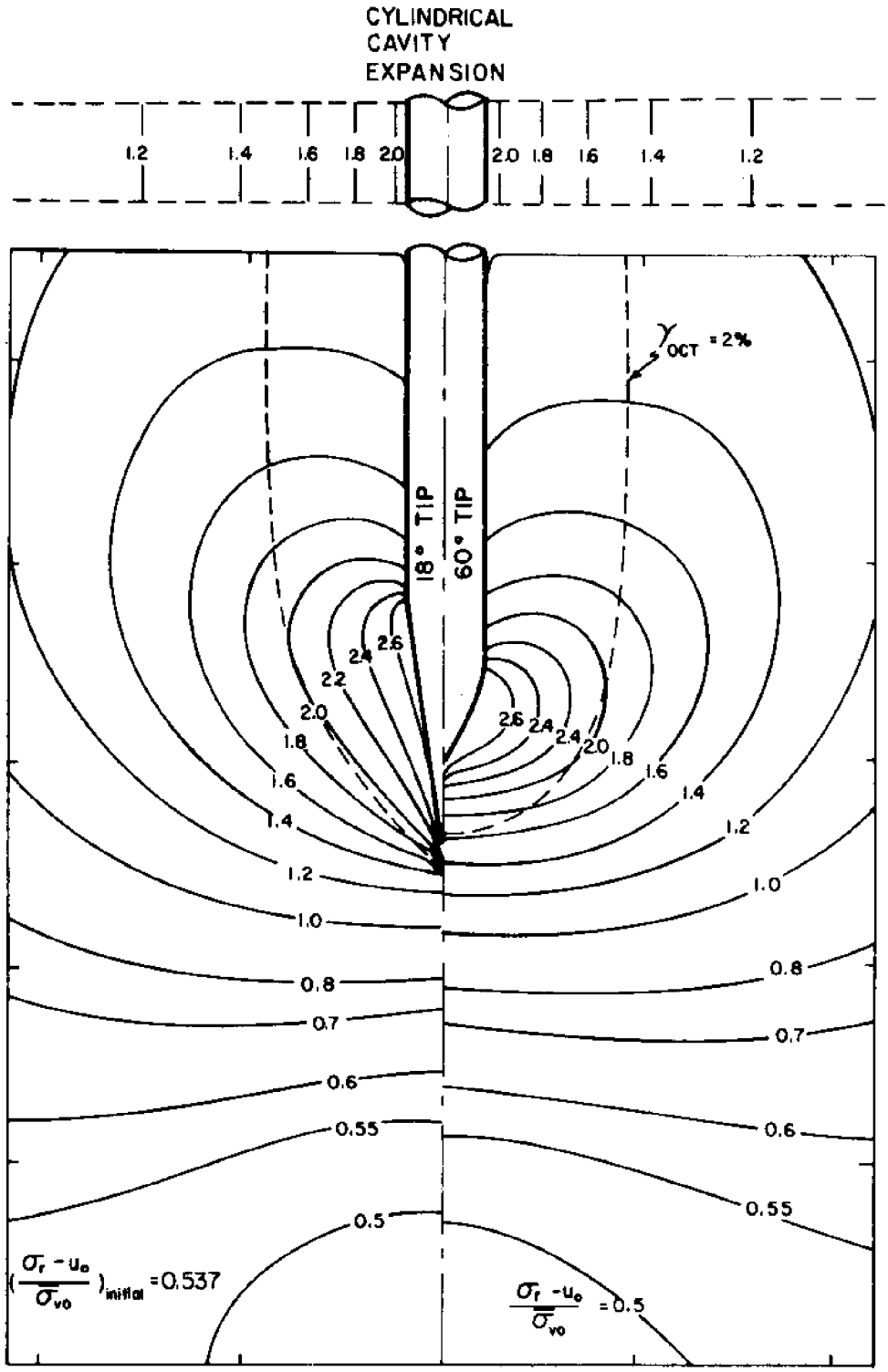

Figure 6.13 Predicted contours of normalized radial total stress, σ_r, during steady cone penetration in normally consolidated Boston Blue Clay (18° and 60° tips).

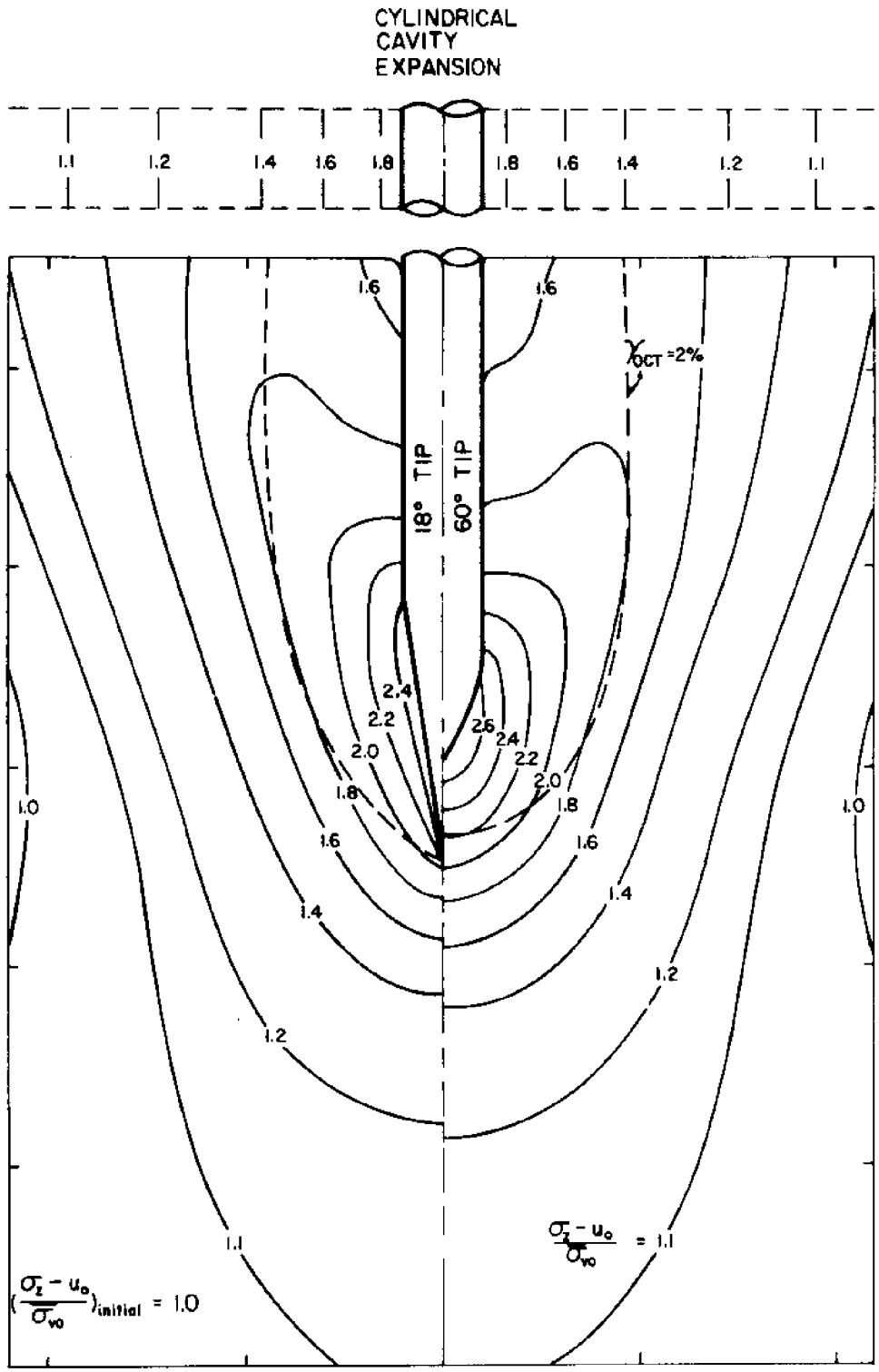

Figure 6.14 Predicted contours of normalized vertical total stress, σ_z, during steady cone penetration in normally consolidated Boston Blue Clay (18° and 60° tips).

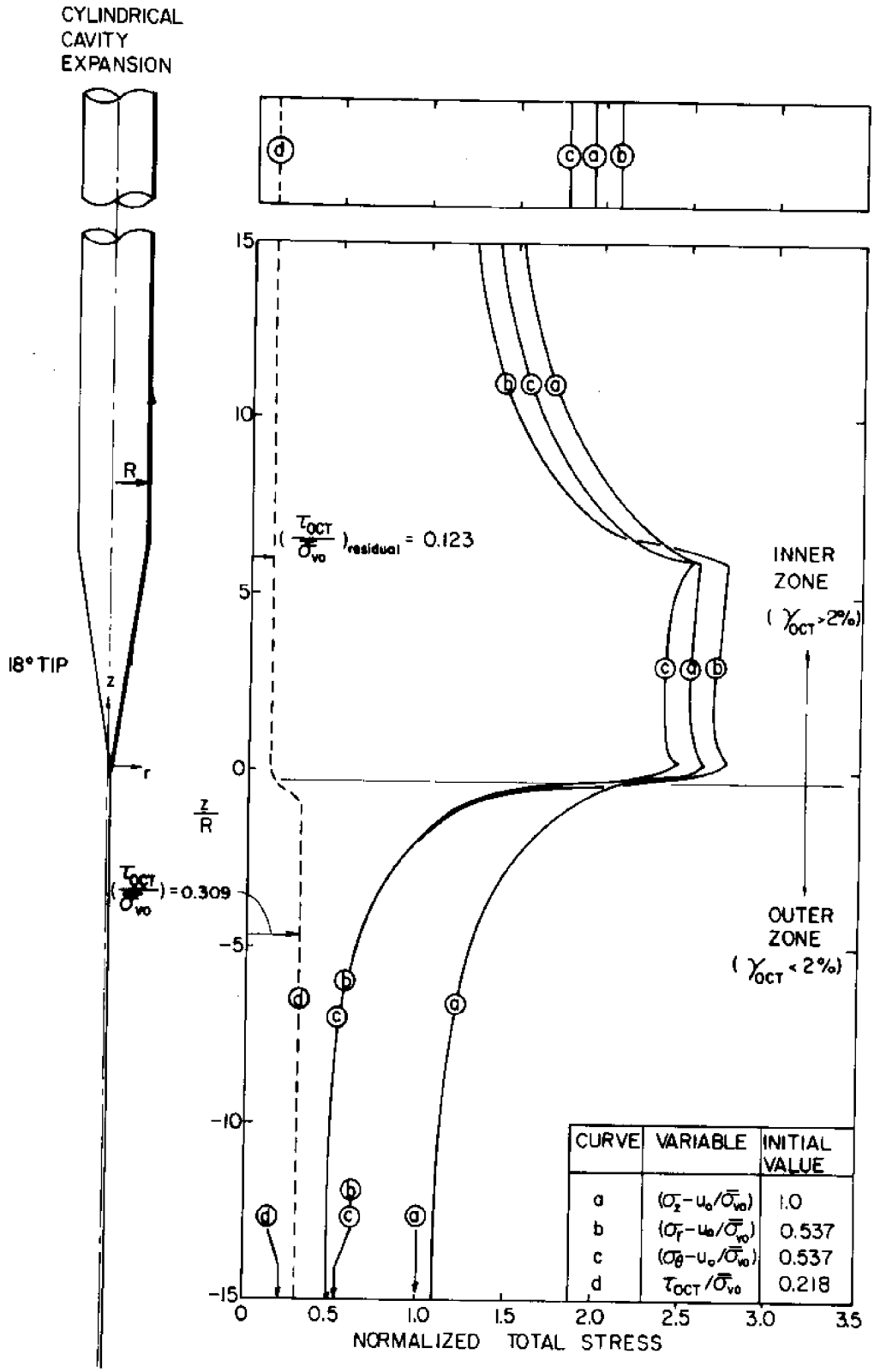

Figure 6.15 Total stress variation along the streamline initially located at the centerline (18° tip).

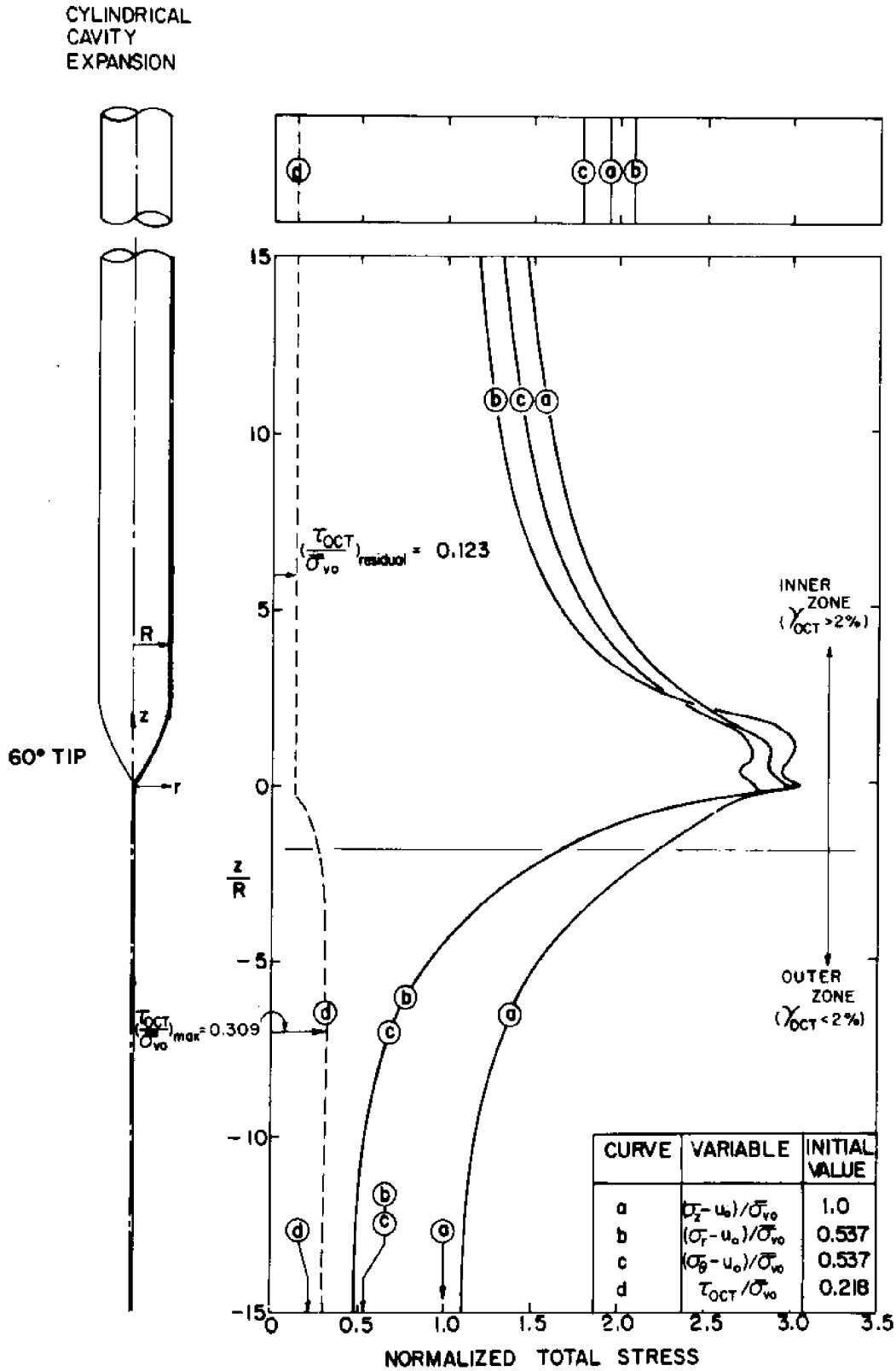

Figure 6.16 Total stress variation along the streamline initially located at the centerline (60° tip).

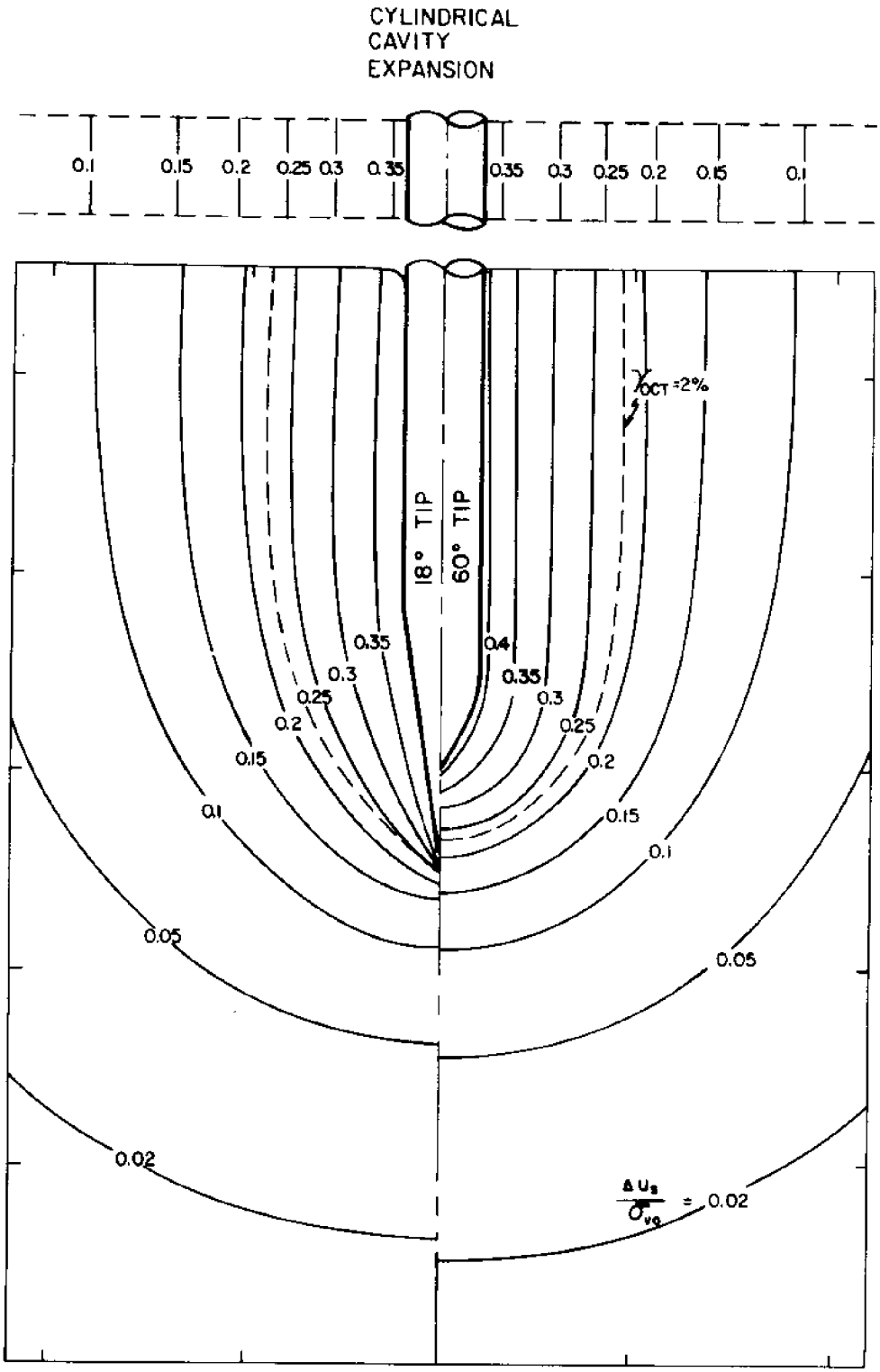

Figure 6.17 Predicted contours of normalized shear induced pore pressure, Δu_s, during steady cone penetration in normally consolidated Boston Blue Clay (18° and 60° tips).

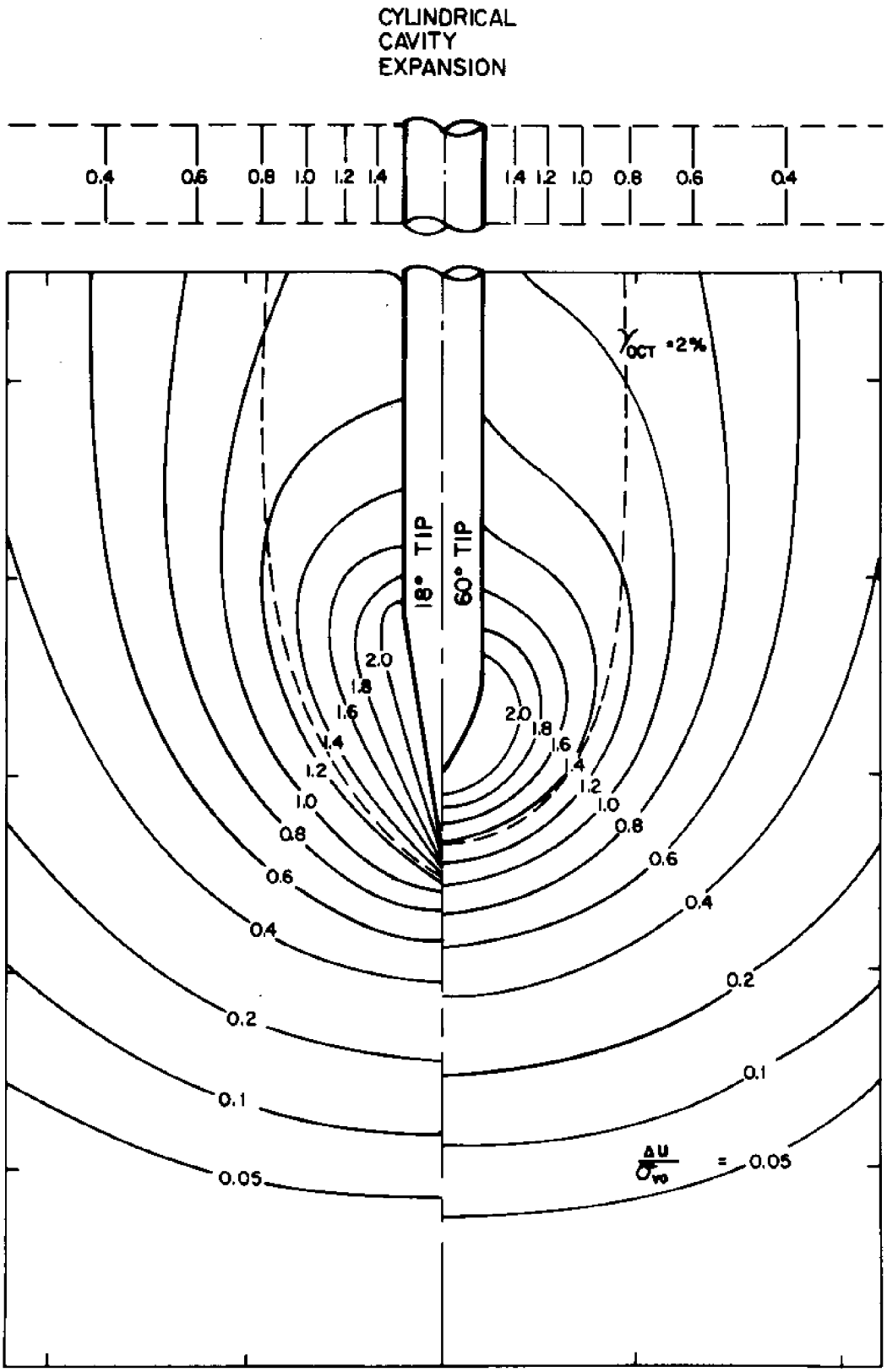

Figure 6.18 Predicted contours of normalized excess pore pressure, Δu, during steady cone penetration in normally consolidated Boston Blue Clay (18° and 60° tips).

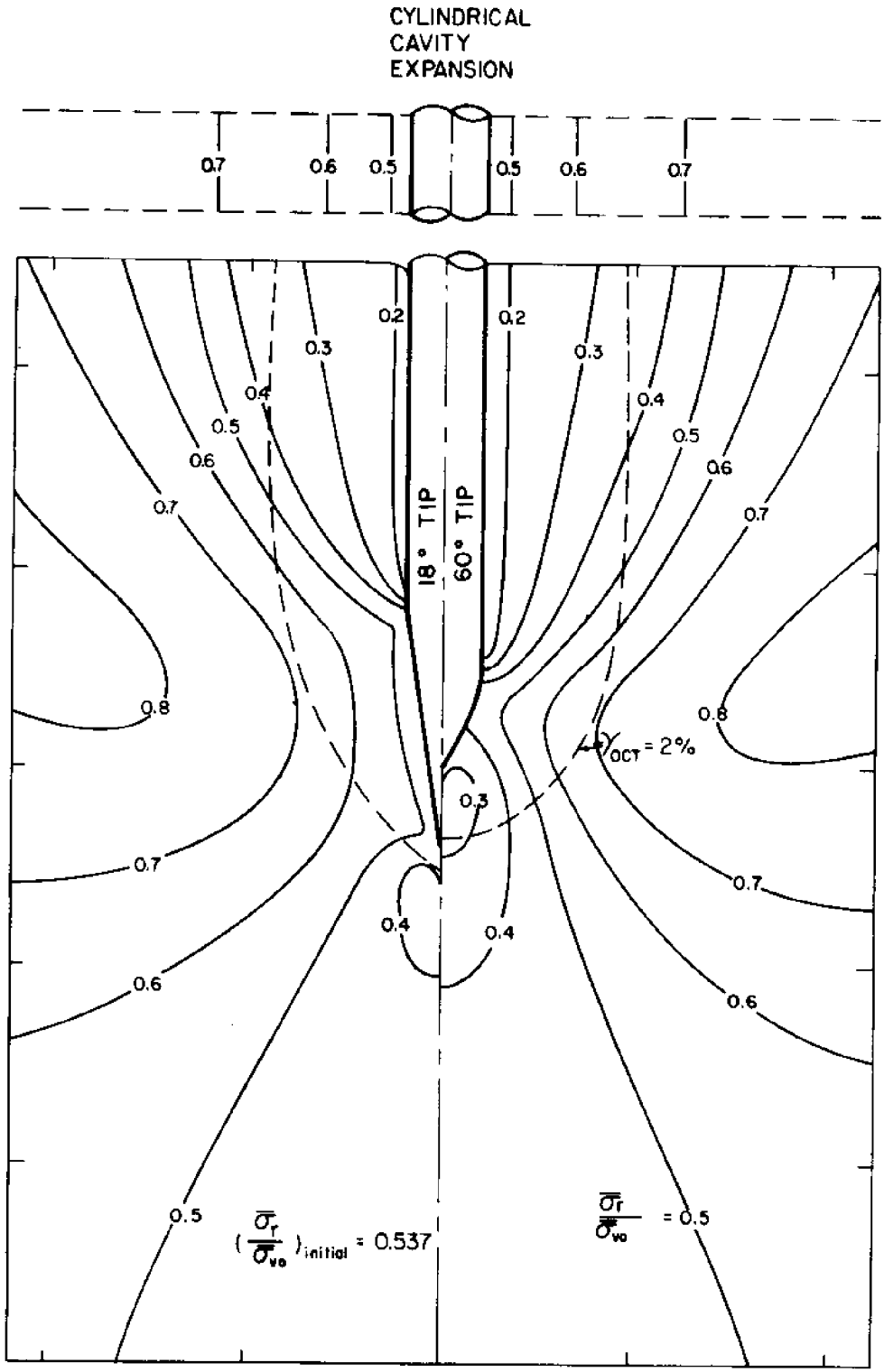

Figure 6.19 Predicted contours of normalized radial effective stress, $\overline{\sigma}_r$, during steady cone penetration in normally consolidated Boston Blue Clay (18° and 60° tips).

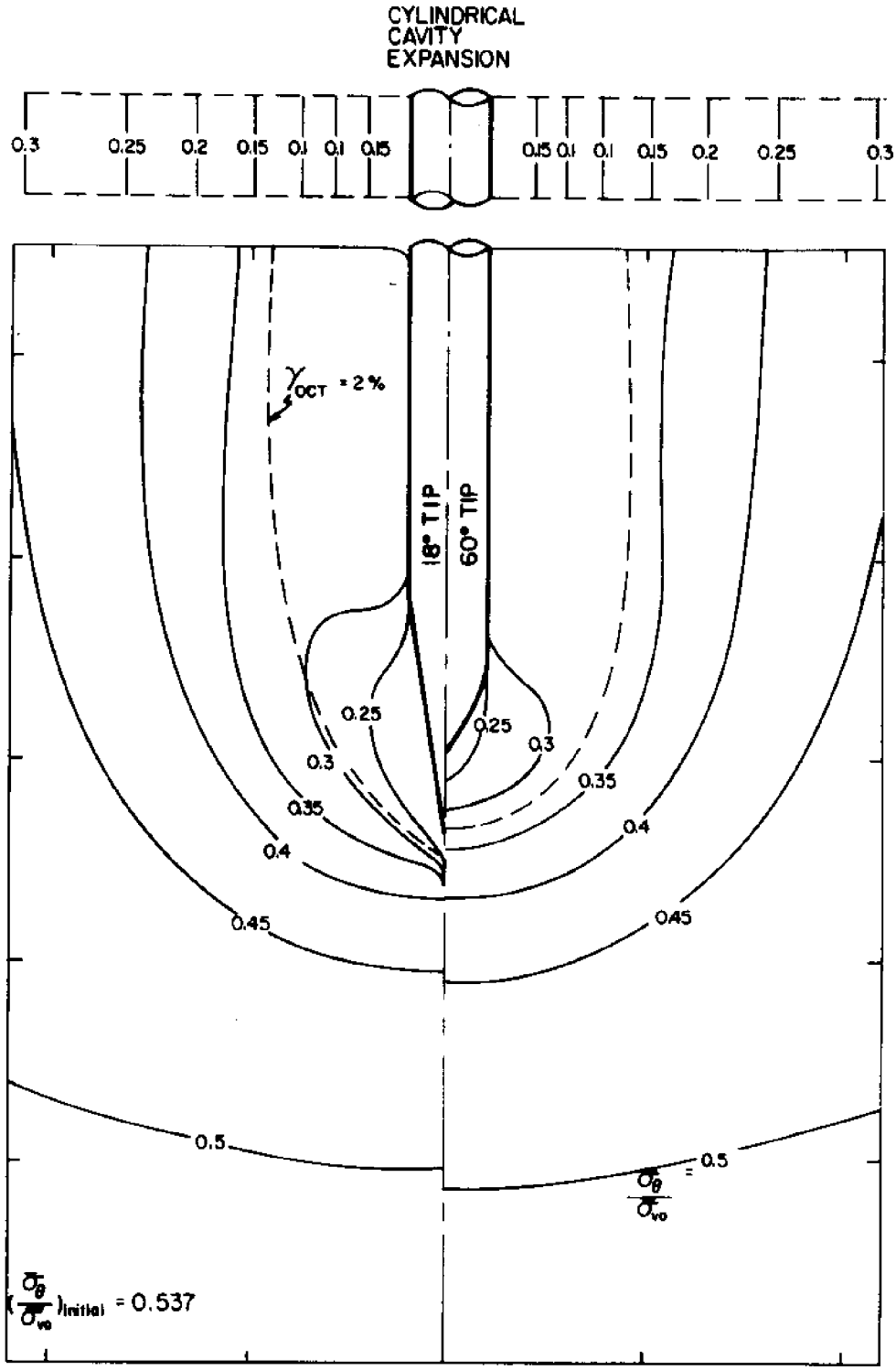

Figure 6.20 Predicted contours of normalized circumferential effective stress, $\bar{\sigma}_\theta$, during steady cone penetration in normally consolidated Boston Blue Clay (18° and 60° tips).

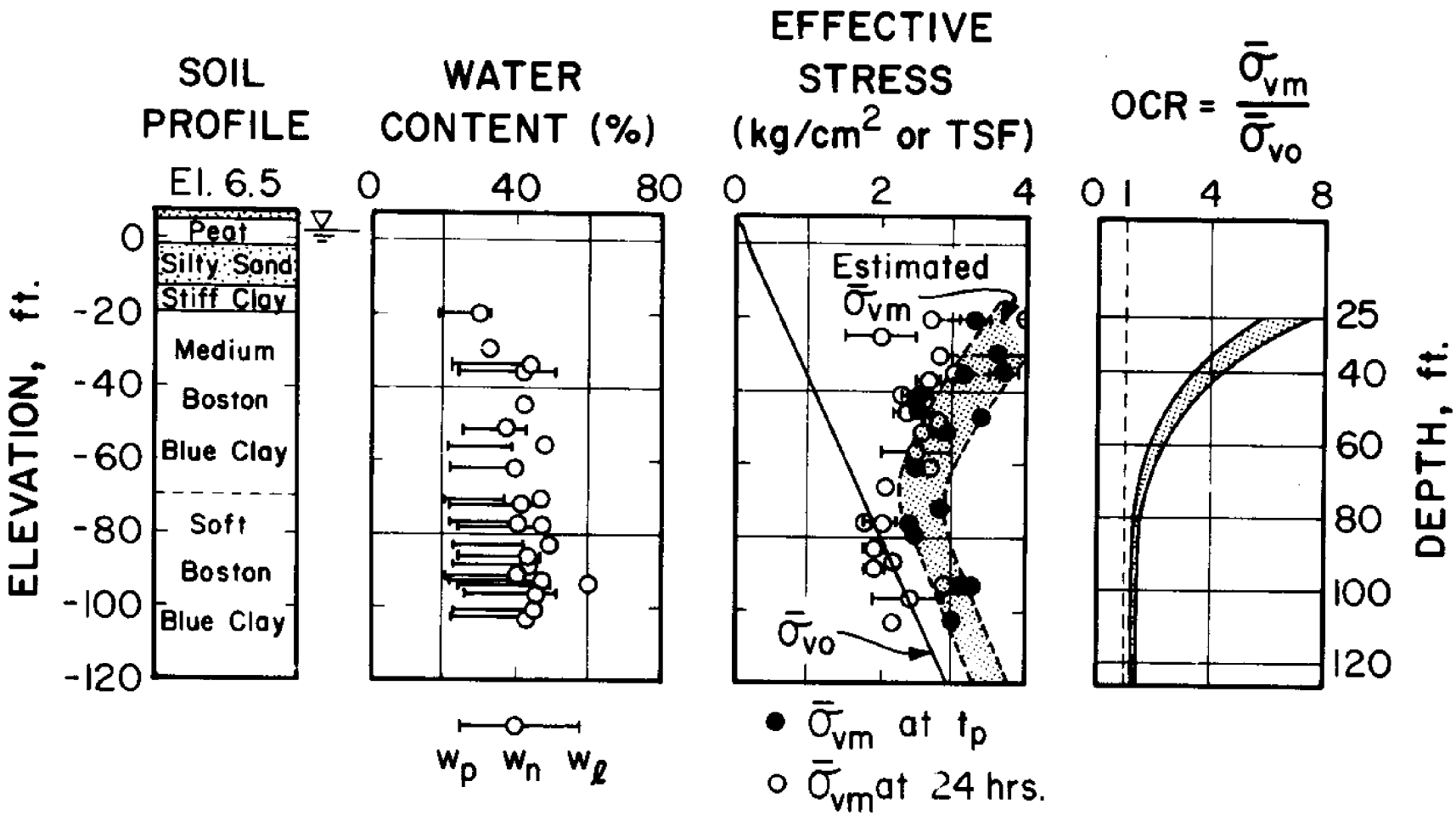

Figure 6.21 Soil profile at the test site as determined by conventional laboratory tests (from Baligh and Vivatrat, 1979).

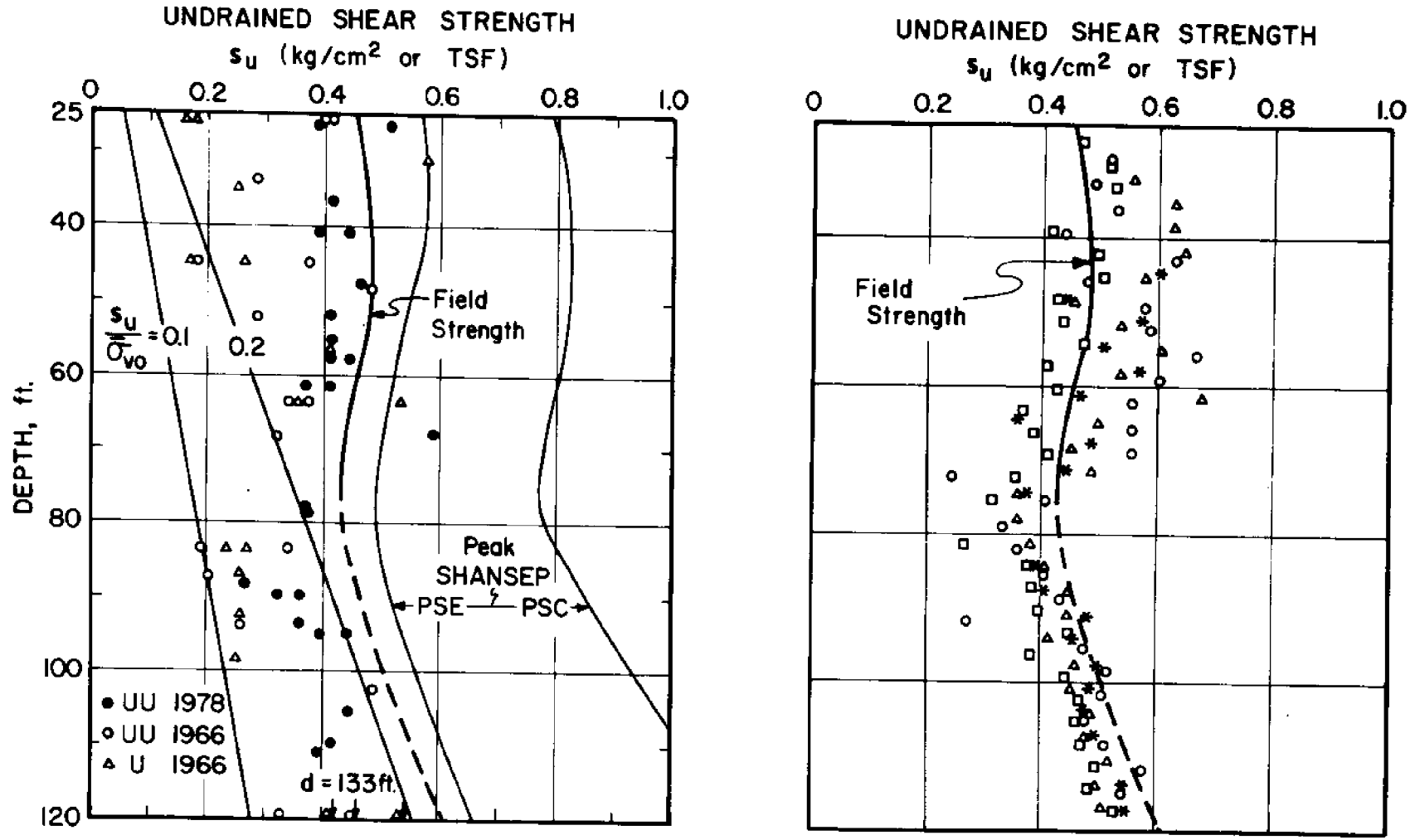

Figure 6.22 Laboratory and field vane undrained shear strength at the test site (from Baligh and Vivatrat, 1979).

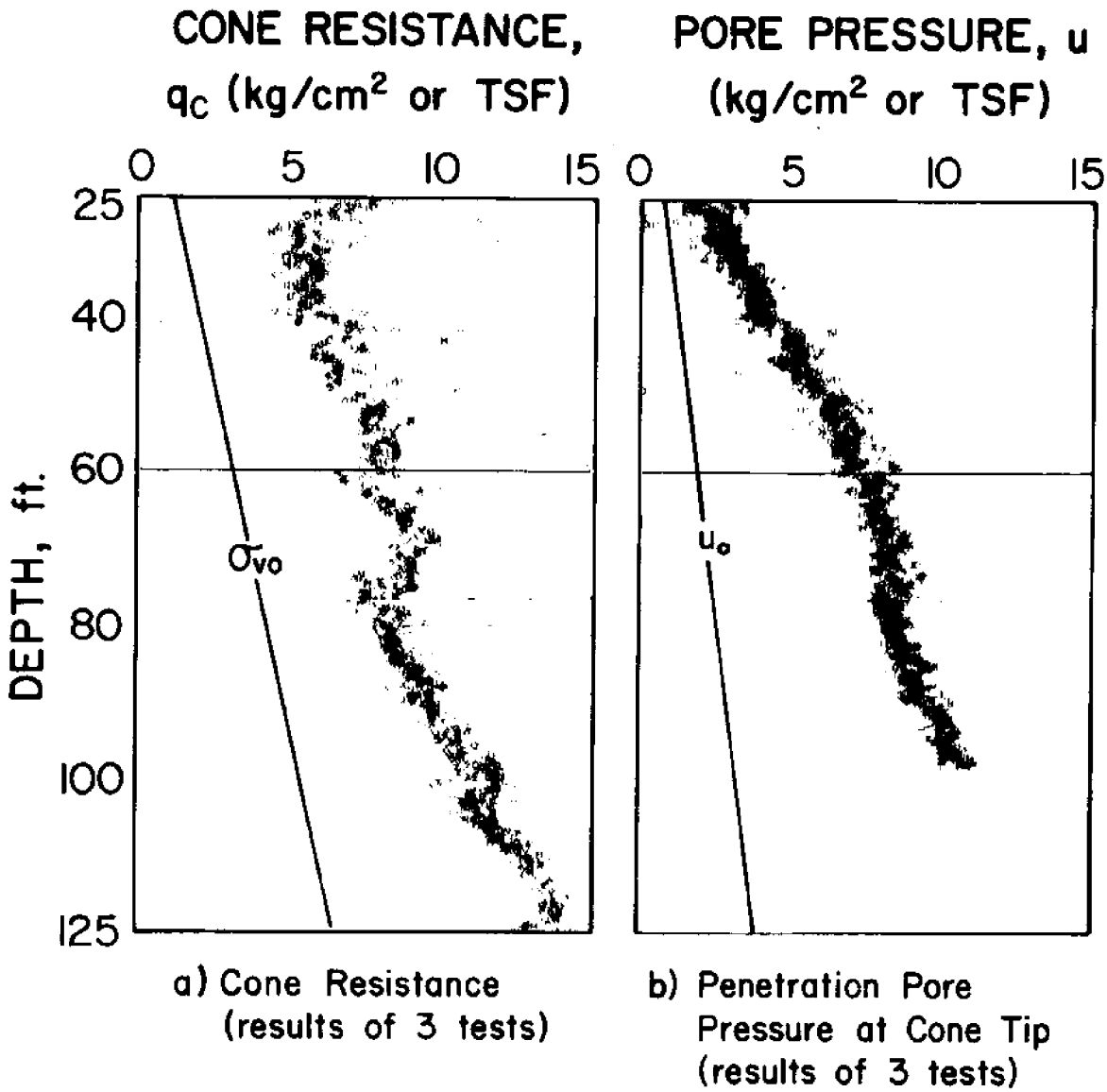

Figure 6.23 Cone resistance and pore pressure during penetration (from Baligh and Vivatrat, 1979).

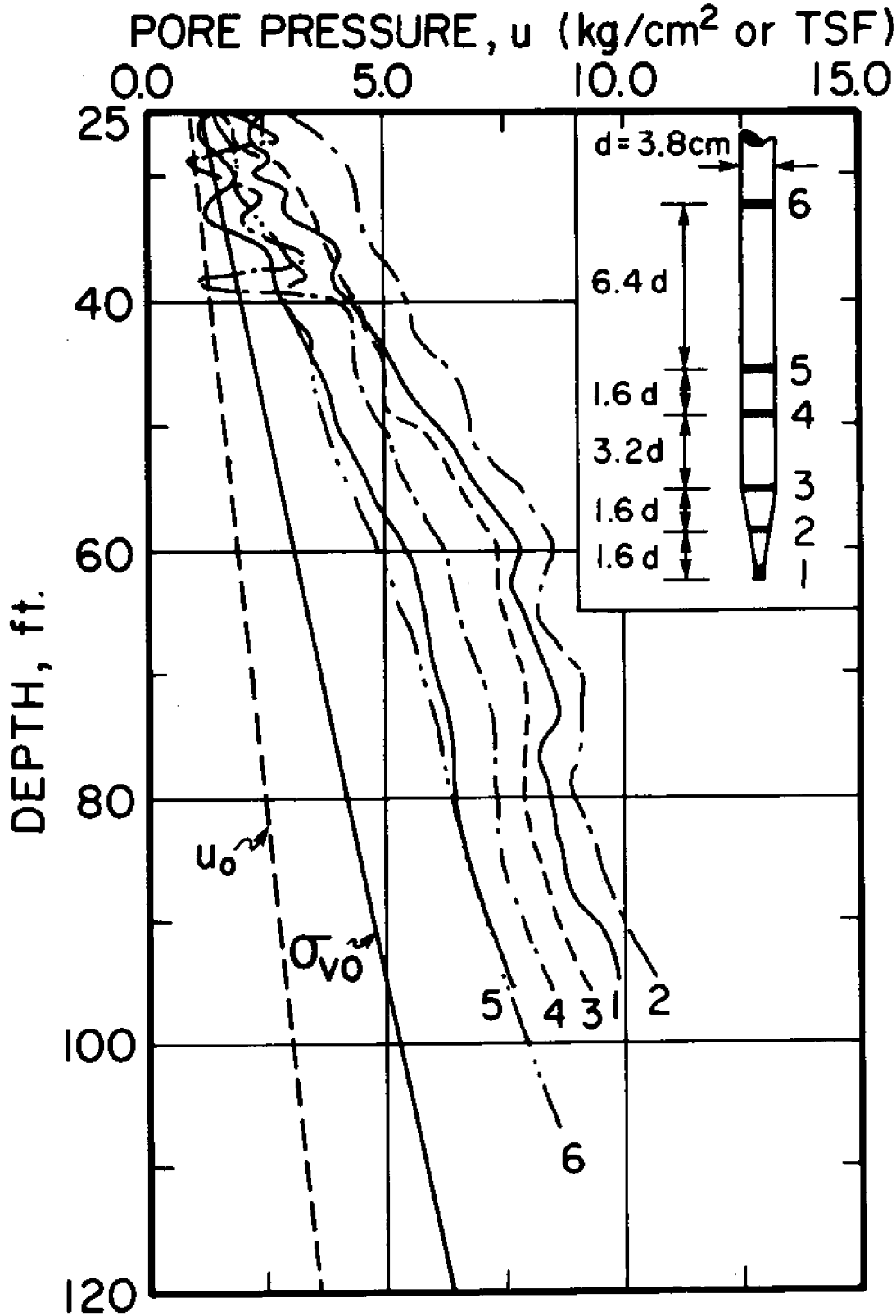

Figure 6.24 Penetration pore pressures at different locations on an 18° conical tip (from Baligh et al., 1978).

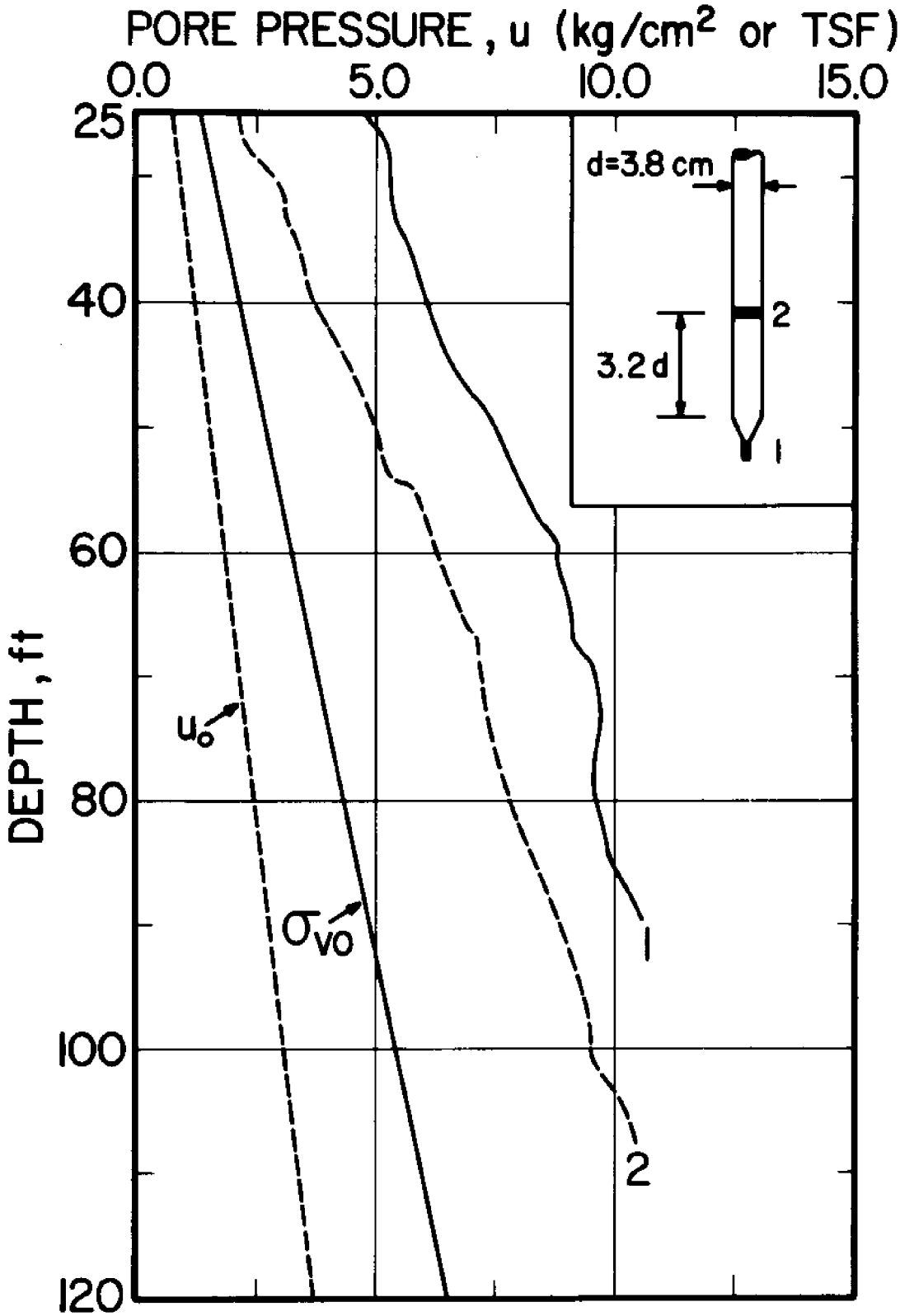

Figure 6.25 Penetration pore pressures at different locations on a 60° conical tip (from Baligh et al., 1978).

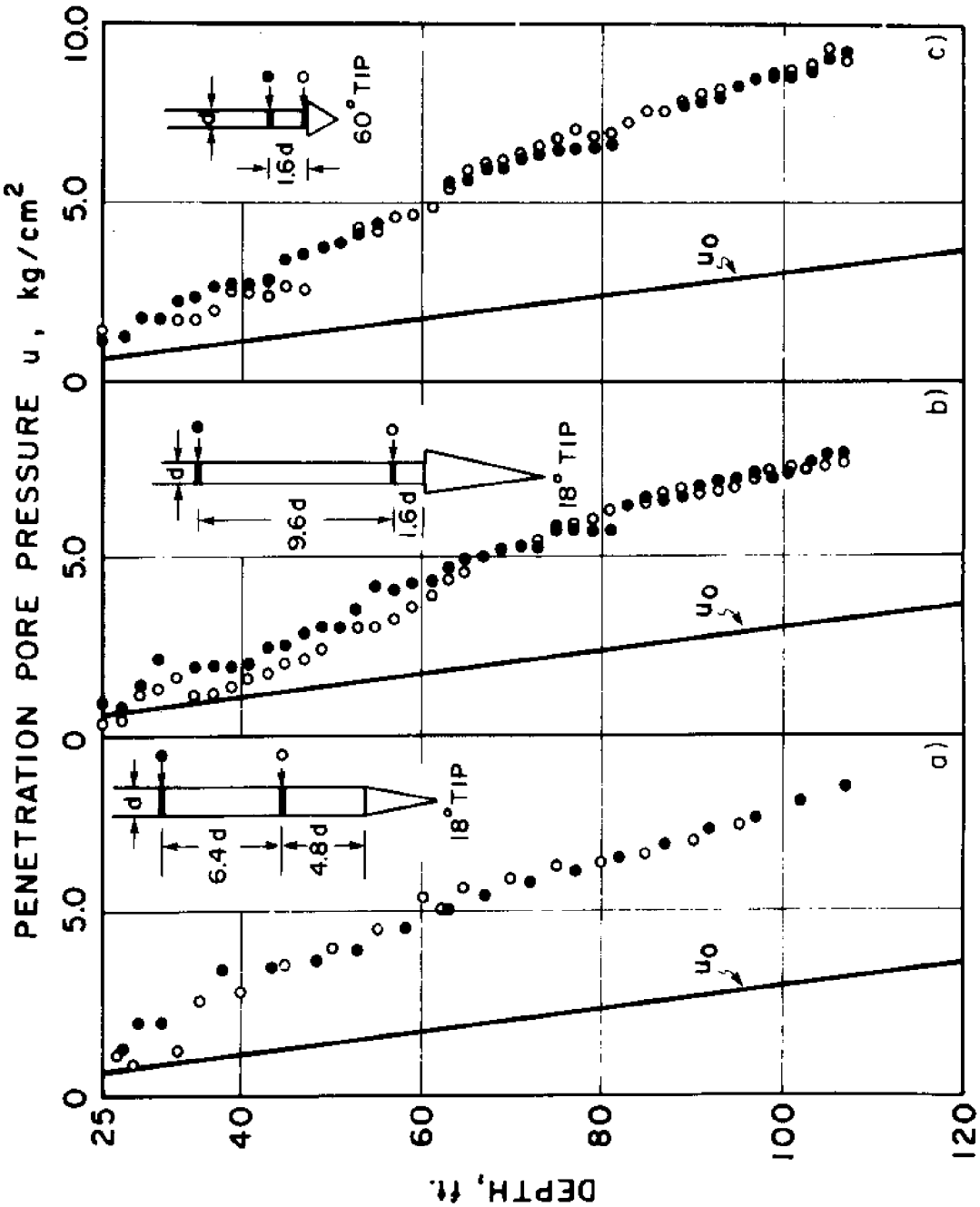

Figure 6.26 Penetration pore pressures behind cones with different geometries (from Baligh et al., 1978).

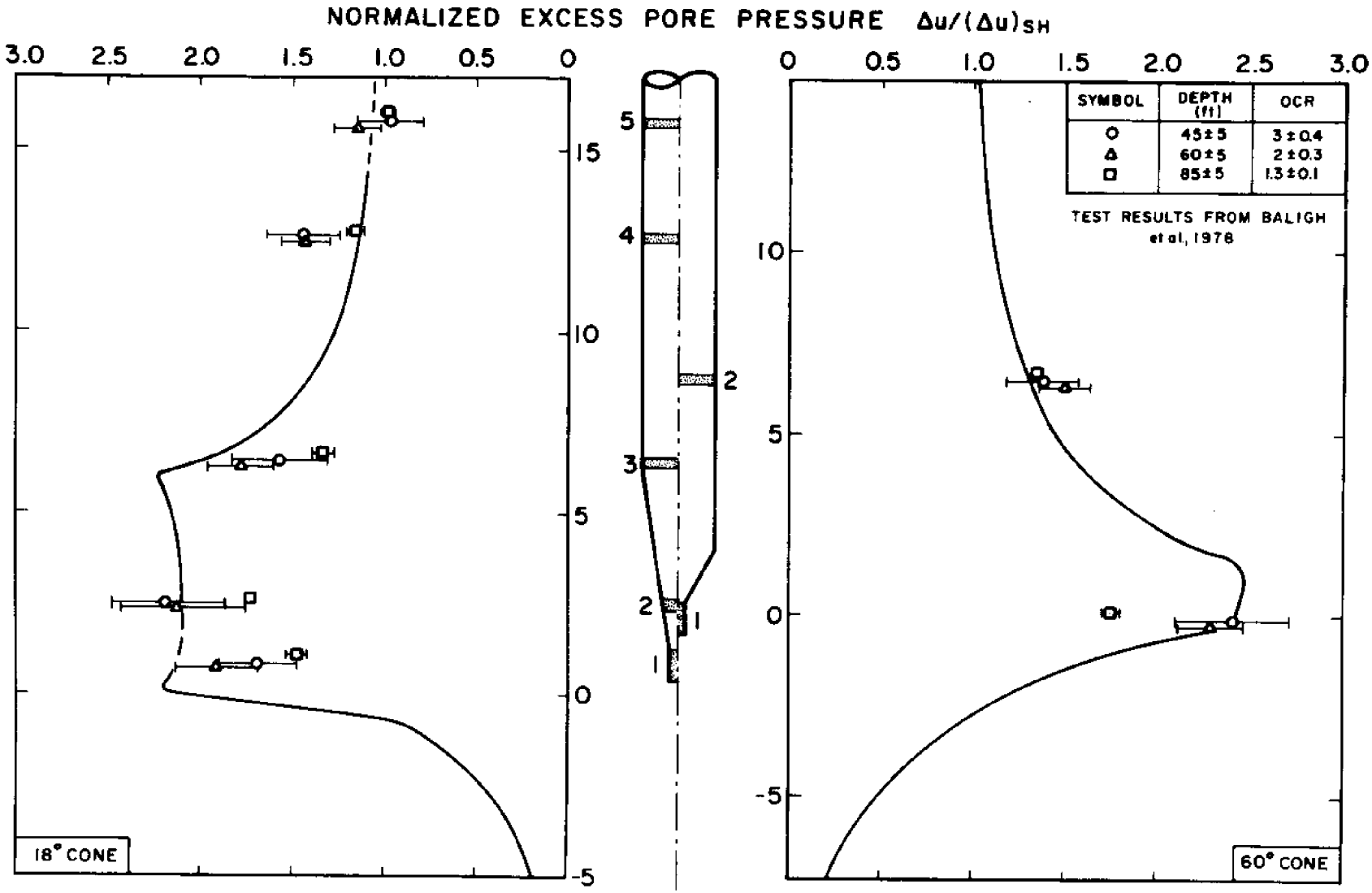

Figure 6.27 Predicted vs. measured longitudinal distributions of normalized excess pore pressures along 18° and 60° cones during steady penetration in Boston Blue Clay.

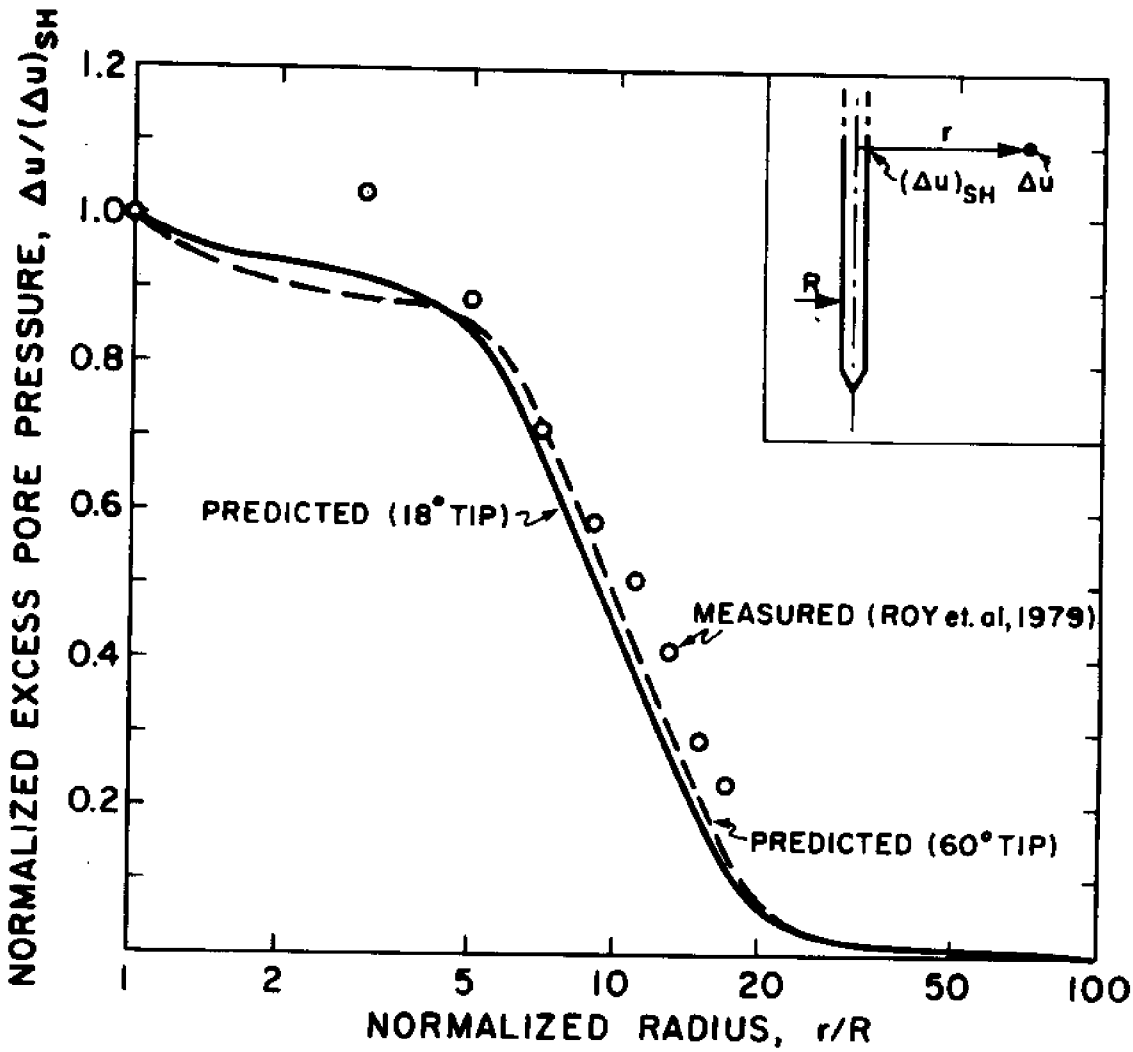

Figure 6.28 Predicted vs. measured radial distribution of normalized excess pore pressure during steady cone penetration in clay.

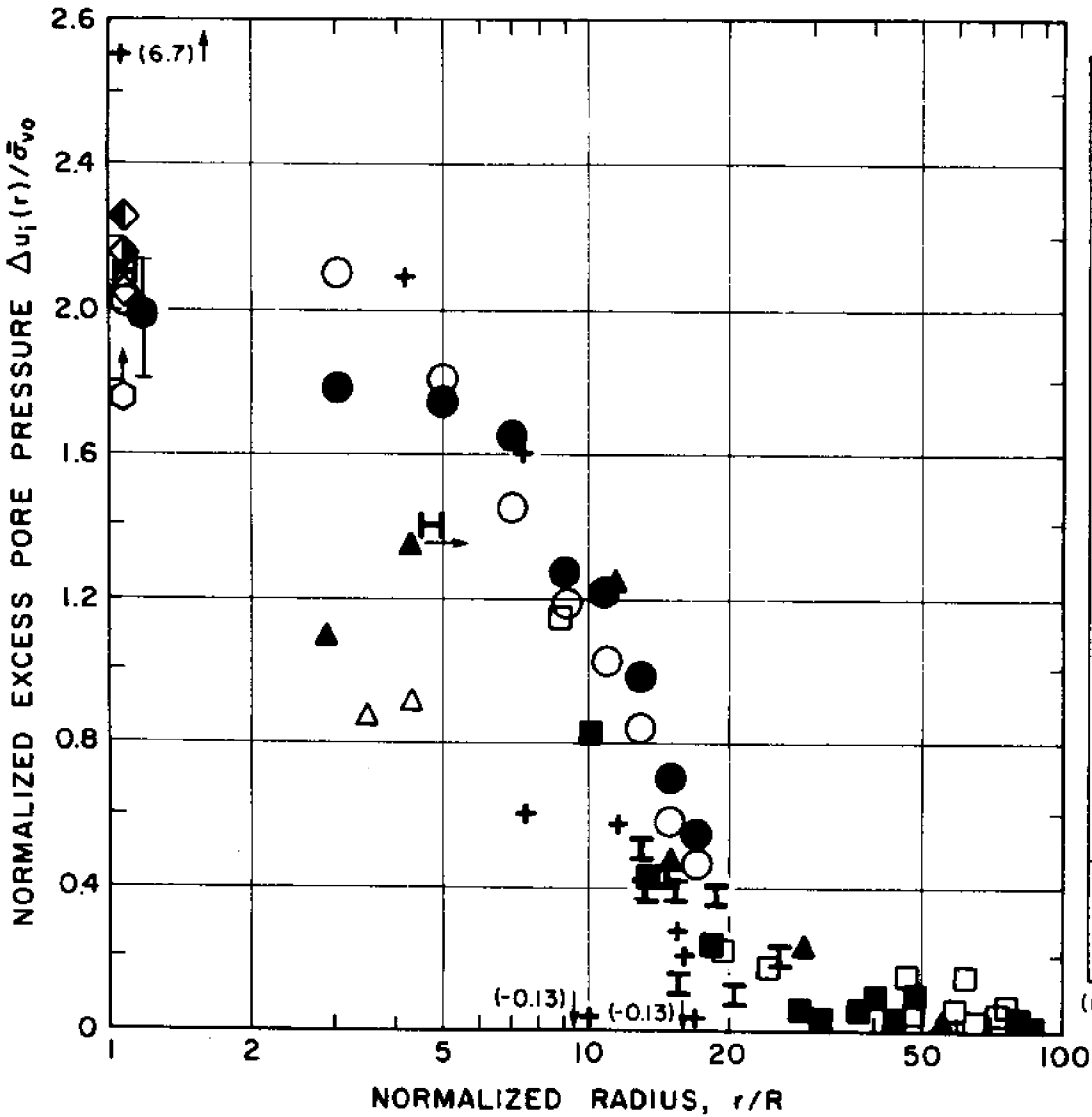

	Case	Symbol	Piezometer Depth (m)	OCR	S_u (TSM)	PI	S_t
DISPLACEMENT PILES (Δu_i in soil)	a	□	7.5	≃1	2 (1) to 2.5	25	6 (1) to 8
		■	10				
	b	△	7.6	≃1	2 (1) to 2.5	20	4 to 6
		▲	10.7				
	c	+	5	2.5?	3 to 3.5 (2)	60	very high
	d	●	3	2.3	1.3 (1)	20	16
		○	6	2.3	2.0 (1)		
DISPLACEMENT PILES (Δu_i on shaft)	e	◆	11.5	4	5.5 (1)	20	6
		◆	14	3	5 (1)		
		◇	24 to 30	1.2	3.5 to 4.5 (1)		
	f	⬡	12.2	7?	11 (3)	40	
H-piles	g	H	5.8			10	
	h	I	6 to 9	3?	2.5 to 4.5	37 clay 7 silt	

(1) Field Vane (2) Dutch Cone (3) Unconfined

Fig. 6.29 $\Delta u/\bar{\sigma}_{vo}$ for different clays due to pile driving

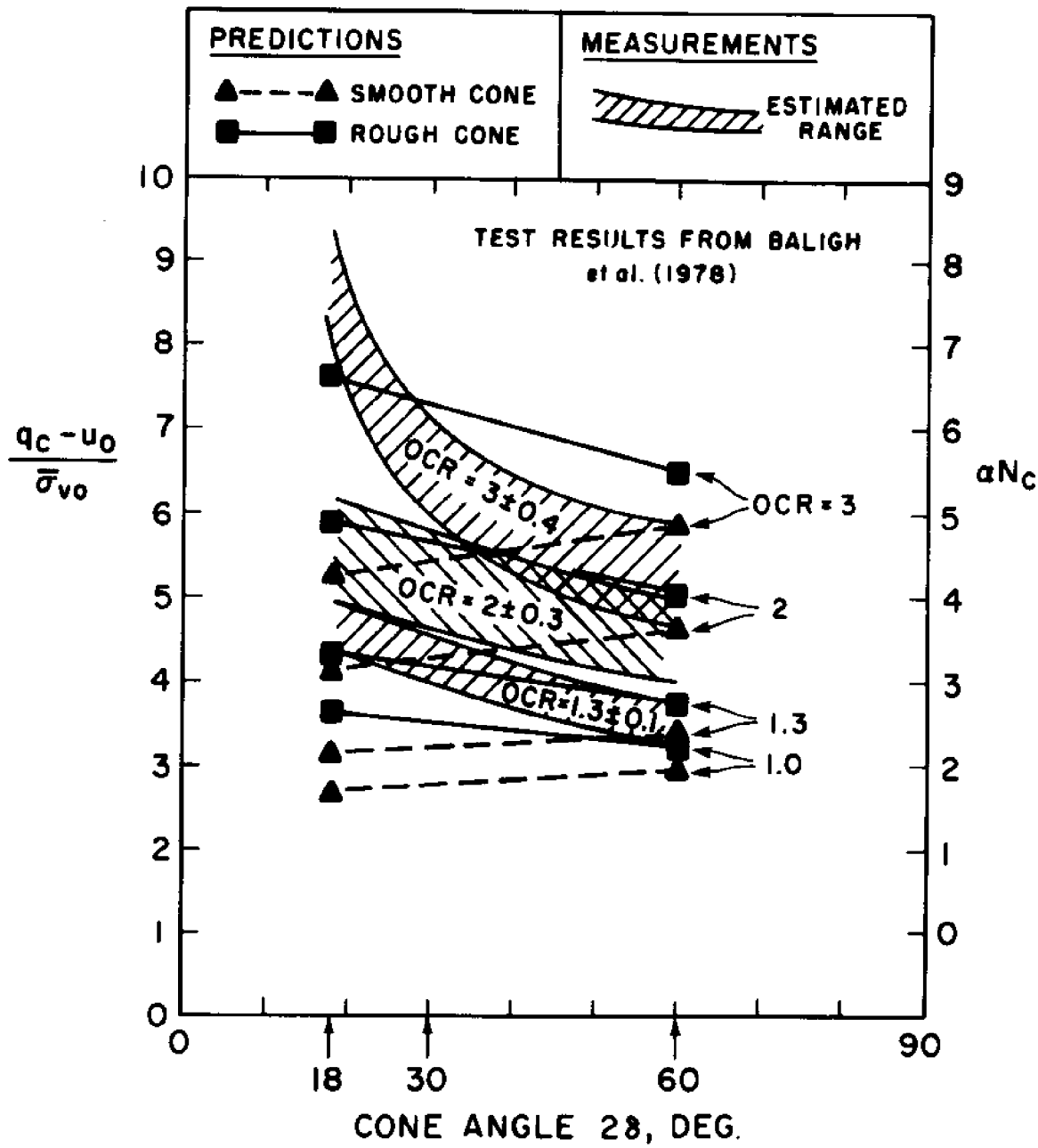

Figure 6.30 Comparison of predicted and measured cone resistances in Boston Blue Clay.

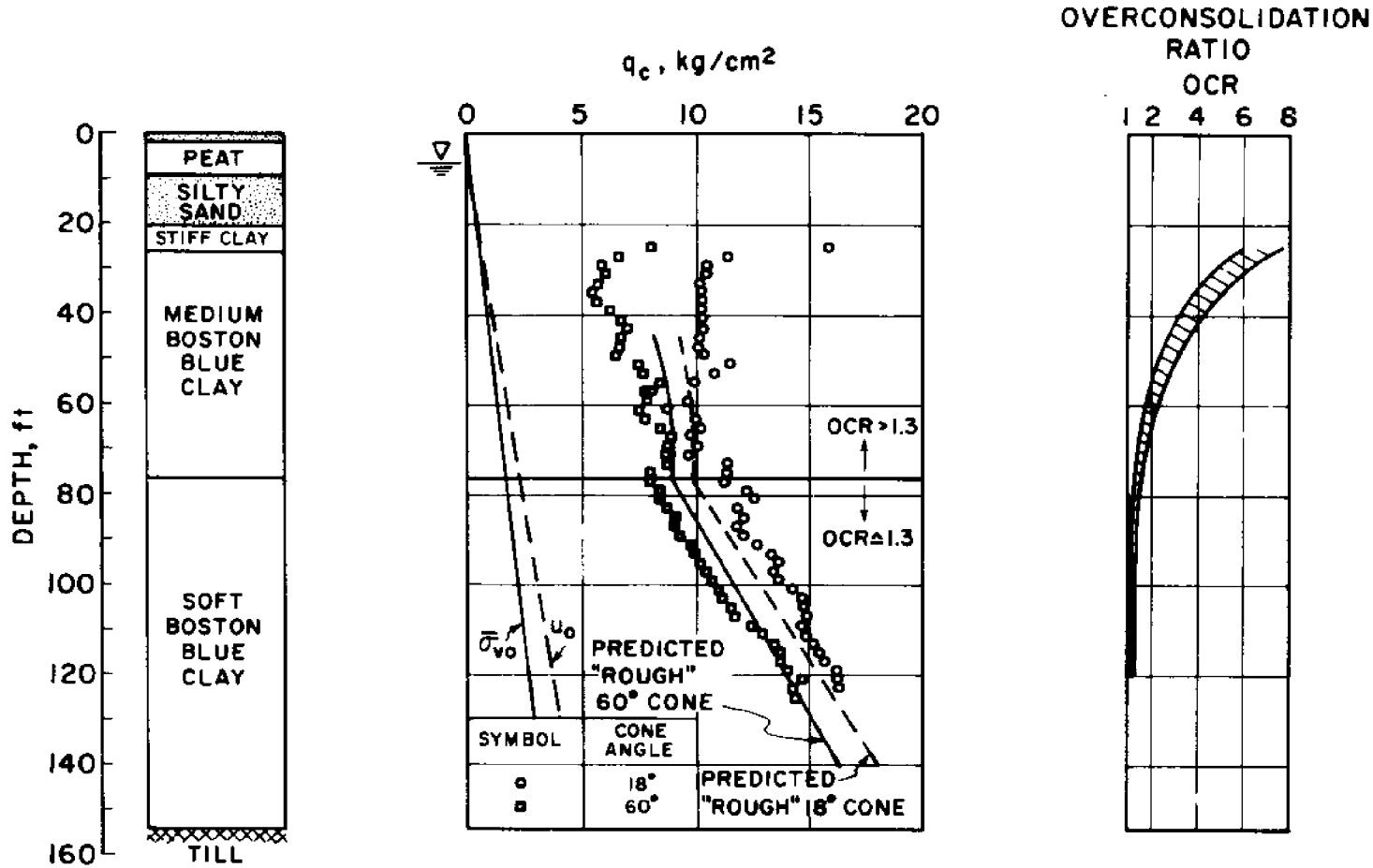

Notes: The measured values of q_c are obtained by filtering and averaging digitized data over 2 ft layers (See Baligh et al., 1978)

Stress history from Ladd et al. (1979)

Predicted values obtained from fig. 6.29.

Figure 6.31 Predicted and measured point resistance in Boston Blue Clay (18° and 60° tips) at Station 246, Saugus, Massachusetts.

CHAPTER 7

SUMMARY AND CONCLUSIONS

(1) Cone penetration testing provides a superior soil exploration technique to establish stratification, determine variability, and perform soil identification; especially if pore pressures generated by cone pentration are measured in addition to cone resistance (Baligh et al. 1980).

(2) Due to the complicated nature of cone penetration, research is needed to interpret test results and hence estimate engineering properties of the soils for predicting foundation performance and conducting foundation designs. Past research at MIT concentrated on estimating the undrained shear strength of clays (Baligh et al. 1978). This report is primarily aimed at estimating the pore pressures during cone penetration.

(3) Additional interesting aspects of this study include: a) the applicability of cavity expansion approaches to deep penetration and pile installation problems; b) the likelihood of soil hydrofracture due to pile installation; c) the generalization of a deviatoric stress model and the evaluation of its capabilities in predicting the undrained behavior of Boston Blue Clay in various laboratory shearing tests; d) the development and evaluation of a shear induced pore pressure model for clays subjected to undrained loading along general strain paths; and, e) a comparison between predicted and measured results of self-boring pressuremeter tests in Boston Blue Clay to compare laboratory vs. field behavior of clays.

(4) The pore pressures, u, generated in the soil by steady cone penetration are important because a) they represent the initial conditions for the dissipation that takes place when penetration is interrupted, and b) they provide insight into the mechanism of cone penetration and hence enable better interpretation of the test results.

(5) Penetration pore pressures, u, are difficult to predict because of the complicated behavior of soils; the large strains and the complicated strain paths to which the soil is subjected; and, the boundary conditions at the cone-soil interface.

(6) Deep cone penetration in clays is an axisymmetric two-dimensional steady state problem which is essentially strain-controlled, i.e., strains and deformations in the soil are primarily imposed by kinematic requirements. For this type of problem, Baligh (1975) proposes an approximate method of solution called the "strain path method" consisting of four basic steps: a) estimate the initial stresses; b) estimate an approximate strain field satisfying conservation of volume, compatibility and boundary velocity requirements; c) evaluate

the deviatoric stresses at a selected number of elements by performing laboratory tests on samples subjected to the same strain paths or, alternatively, by using an appropriate soil behavioral model, and; d) estimate the octahedral (isotropic) stresses by integrating the equilibrium equations.

Chapter 2 describes the application of the strain path method to deep steady cone penetration in clays and indicates the need to develop: a) A method for estimating approximate velocity fields and hence compute deformations and strain paths of the soil during cone penetration; b) Appropriate models to determine the deviatoric stresses and the shear induced pore pressures corresponding to these strain paths c) A method to estimate octahedral stresses by integrating the equilibrium equations and hence determine cone resistance and penetration pore pressures (See Figure 4.3).

(7) Predictions of velocities, strains and deformations in saturated clays due to steady cone penetration are conducted in Chapter 3, assuming that the soil offers no shearing resistance (i.e., behaving like an ideal fluid) utilizing the method of "sources and sinks" of potential theory. The principal advantage of this prediction method is to provide analytic expressions for the strain rates, everywhere in the soil, which

can be accurately integrated to obtain strains and deformations. This avoids the important errors associated with the more obvious method of differentiating measured displacement fields to obtain the strains.

Results obtained for 18° and 60° cones indicate that: a) Strain paths caused by cone penetration are very complicated and cannot be imposed by any one of the existing laboratory tests; b) Cone penetration shears the soil at much higher rates and to much higher levels of strains than common laboratory tests; and c) Significant strain reversals take place behind the cone base. This, together with shearing strains neglected by (one-dimensional) expansion theories (ϵ_{rz} and ϵ_{zz}) raises serious questions regarding the applicability of cavity expansion solutions to penetration problems (cones and piles).

Finally, Chapter 3 shows reasonable agreement between the predicted soil deformations and model test results. More accurate experimental results are, however, needed.

(8) In order to determine the shear (deviatoric) stresses in the soil, a comprehensive model is required to account for the important aspects of soil behavior as related to cone penetration: a) complicated strain paths including strain reversals (i.e., "loading" and "unloading"), and large non-recoverable strains; b) initial and stress-induced anisotropy c) post-peak behavior, and; d) time-dependent deformations

e.g., undrained creep and relaxation).

At the present time such a model is not available. However, the deviatoric stress model introduced by Iwan (1967) and Morz (1967); and applied to soils by Prevost (1977), accounts for most of the above factors except for the time-dependent (viscous) behavior of clays. The model is described in Chapter 4 and is extended by means of a new strain-softening rule describing post-peak stress-strain behavior in order to predict a more realistic behavior. Furthermore, based on theoretical considerations, the model is shown to predict, under plane strain conditions, the same peak strengths obtained by the Davis and Christian (1971) elliptical model in the special case when the ellipse degenerates into a circle.

Using soil parameters from triaxial tests on normally consolidated resedimented Boston Blue Clay (BBC), the model predictions are evaluated in Chapter 4 by comparisons with other laboratory test results.

These comparisons show that:

a) Reasonably good predictions are obtained in plane strain compression and extension tests, especially in describing the post-peak behavior;

b) The simple softening law describing repeated loading leads to good agreement with results of cyclic triaxial tests, and;

c) The model lacks the necessary flexibility to accurately describe intermediate modes of failure, e.g., Direct Simple Shear (DSS), cylindrical cavity expansion, etc., ... Although the DSS test is difficult to interpret and results of "true" triaxial test simulating cylindrical cavity expansion (e.g., Kirby and Esrig, 1979) are scarce, it is apparent that the model slightly overestimates the strength for these two modes of failure.

Improvements in the strength prediction capabilities of the model could be easily achieved by considering yield surfaces of more general shapes (e.g., ellipsoids or spheroids). However, this requires reliable stress-strain curves for general loading conditions that are not presently available and hence, the additional complications arising from a more sophisticated model do not appear justifiable at the present time.

(9) A review of existing methods for predicting the excess pore pressure, Δu, generated during undrained shearing of clays indicates the need for a new method to predict Δu caused by the very complicated strains associated with cone penetration (variable principal strain directions with large strains and strain reversals). A method is proposed in Chapter 5 to predict Δu in strain-controlled problems. Following Henkel's approach, Δu is divided into two components: a) $\Delta\sigma_{oct}$ due to changes in confinement and b) Δu_s caused by the tendency of the soil to dilate (or contract) due to pure shear loading. The first component, $\Delta\sigma_{oct}$, is controlled by equilibrium considerations and, the second component, Δu_s, is evaluated by means of a new analytical model.

The model can predict Δu_s for anisotropic clays subjected to general straining conditions (with rotation of principal strain direction) and <u>one</u> unloading. For monotonic loading, all model parameters can be obtained from triaxial tests. For unloading, the model requires an estimate of the maximum (or limiting) Δu_s which can be obtained from results of laboratory tests including straining reversal.

A comparison between the predicted and measured pore pressures during plane strain compression and extension and in direct simple shear tests indicates good agreement in spite of the difficulty in evaluating $\Delta\sigma_{oct}$ during these tests.

Furthermore, the predicted pore pressures during unloading are very close to measurements obtained from cyclic triaxial tests.

(10) Chapter 6 conducts cylindrical cavity expansion studies to evaluate the adequacy of the deviatoric stress model (Chapter 4), the shear-induced pore pressure model (Chapter 5) and the soil parameters estimated from laboratory tests on resedimented BBC by comparisons with other models and in situ measurements during pressuremeter tests.

The predicted expansion curves are close to Cam-Clay results (determined by others for BBC) even though the stress-strain curves of the two models differ significantly. This is due to the compensating effects of the shear modulus at low strains and the shear strength of the clay. Additional results show that, for cavity expansion problems, simple soil models (e.g., the bilinear or the hyperbolic models) can provide as reliable predictions as the sophisticated models (e.g., the Cam-Clay and the proposed models) provided appropriate soil parameters are selected.

Comparison of the predicted expansion curves with pressuremeter tests results in the soft BBC (depths 83.2 and 103.2 ft. at the Saugus site) show that matching of field measurements requires doubling of the estimated shear resistance of the soil. Part of this discrepancy (about 25%) is due to overconsolidation of the in situ clay (OCR $\simeq$ 1.3) neglected in predictions. The remaining discrepancy (75%) can be due to: 1) simplifications

made in theoretical analyses and/or the formulation of the soil model (e.g., end effects neglected in pressuremeter analyses, partial drainage, strain rate effects, ...etc.) and/or; 2) inadequacies in soil model parameters as described by the shear strength and/or shear modulus at small strain levels. The latter is very difficult to estimate reliably from conventional laboratory tests and is believed to represent a major reason for underpredicting field measurements.

(11) Based on the strain path method, the strain paths estimated in Chapter 3, the deviatoric stress model in Chapter 4, the shear-induced pore pressure model in Chapter 5, and the soil parameters obtained from laboratory tests on normally consolidated resedimented BBC, Chapter 6 predicts the normalized excess pore pressures in the soil during deep steady penetration of 18° and 60° cones.

In spite of uncertainties resulting from the simplified nature of strain path analyses, comparisons of predictions with extensive field measurements of pore pressures at different locations on the cone and the shaft behind it shows excellent agreement for both the 18° and 60° cones and, surprisingly, in the overconsolidated BBC as well (OCR $\leq$ 3). Further comparisons with pore pressure measurements obtained by others in the soil surrounding a jacked pile in Champlain Clay also show surprisingly close agreement. Since the measurements in Champlain Clay exhibit strong similarities with other clays

(see Fig. 6.29), this suggests that predictions of the normalized excess pore pressure distribution in the soil is not very sensitive to the clay type or its overconsolidation ratio (for OCR $\leq$ 3). This hypothesis is important because, if true, it enables valuable generalizations to be made. In particular, results of linear consolidation analyses (performed on the basis of this normalized excess pore pressure distribution) can be applied to a wide variety of clay deposits to estimate their coefficient of consolidation.

(14) Predictions of cone resistance, q_c, and penetration pore pressures, u, based on the strain path method are compared in Chapter 6 with field measurements in BBC. Good agreement of q_c is achieved for 18° and 60° cones for OCR < 3 provided that the overconsolidation of the clay and the friction at the cone-soil interface are accounted for. On the other hand, predictions of u are significantly underestimated in the soft BBC deposit below 75 ft (OCR ≈ 1.3) as was the case of the pressuremeter test data obtained in this clay.

REFERENCES

Arthur, J.R.F., Chua, K.S., and Dunstan, T., "Induced Anisotropy in a Sand," Geotechnique, London, Vol. 27, No. 1, 1977, pp. 13-36.

Arthur, J.R.F. and Phillips, A.B., "Homogeneous and Layered Sand in Triaxial Compression," Geotechnique, London, Vol. 25, No. 4., 1975, pp. 799-815.

Azzouz, A.S., "Three-Dimensional Analysis of Slopes," Ph.D. thesis, Department of Civil Engineering, MIT, Cambridge, Mass., 1977.

Azzouz, A.S. and Baligh, M.M., "Three-Dimensional Stability of Slopes," Publication No. R78-8, Order No. 595, Department of Civil Engineering, MIT, Cambridge, Mass., June 1978.

Azzouz, A.S., Levadoux, J.N., and Baligh, M.M., "Cavity Expansion Approaches in Deep Foundations," Research Report, Department of Civil Engineering, MIT, Cambridge, Mass., 1980 (in preparation).

Baguelin, F., Jezequel, J.F., and Shield, D.H., The Pressuremeter and Foundation Engineering, Trans. Tech. Publ., Germany, 1978.

Baligh, M.M., "Theory of Deep Site Static Cone Penetration Resistance," Publication No. R75-56, Order No. 517, Department of Civil Engineering, MIT, Cambridge, Mass., September 1975.

Baligh, M.M. and Levadoux, J.N., "Pore Pressure Dissipation After Cone Penetration," Publication No. R80-11, Order No. 662, Department of Civil Engineering, MIT, Cambridge, Mass., April, 1980.

Baligh, M.M. and Vivatrat, V., "In Situ Measurements in a Marine Clay," Proceedings, BOSS 79, London, Vol. 1, August 1979, pp. 151-174.

Baligh, M.M., Vivatrat, V., and Ladd, C.C., "Exploration and Evaluation of Engineering Properties for Foundation Design of Offshore Structures," Publication No. R78-40, Order No. 607, Department of Civil Engineering, MIT, Cambridge, Mass., December 1978.

Baligh, M.M., Vivatrat, V., and Ladd, C.C., "Cone Penetration in Soil Profiling," ASCE, Journal of the Geotechnical Engineering Division, Vol. 106, No. GT4, April 1980.

Batchelor, G.K., An Introduction to Fluid Dynamics, Cambridge University Press, 1970.

Bathe, K.J. and Wilson, E.L., Numerical Methods in Finite Element Analysis, Prentis-Hall, Inc., Englewood Cliffs, New Jersey, 1976.

Bishop, A.W. and Henkel, D.J., "Pore Pressure Changes During Shear in Two Undisturbed Clays," Proceedings, 3rd International Conference on Soil Mechanics and Foundation Engineering, Switzerland, Vol. 1, 1953, pp. 94-99.

Bishop, A.W. and Henkel, D.J., The Measurement of Soil Properties in the Triaxial Test, Edward Arnold, 2nd edition, London, 1962.

Bjerrum, L, "Engineering Geology of Norwegian Normally-Consolidated Marine Clays as Related to Settlements of Buildings," 7th Rankine Lecture, Geotechnique, London, Vol. 17, No. 2, 1962, pp. 81-118.

Braathen, N.-F., "Investigation of Effects of Disturbance on Undrained Shear Strength of Boston Blue Clay," Master's thesis, Department of Civil Engineering, MIT, Cambridge, Mass., 1966.

Carter, J.P., Randolph, M.F., and Wroth, C.P., "Stress and Pore Pressure Changes in Clay During and After the Expansion of a Cylindrical Cavity, Report No. TR51, Department of Civil Engineering, University of Cambridge, England, 1978.

Casagrande, A. and Wilson, S.D., "Effect of Rate of Loading on the Strength of Clays and Shales at Constant Water Content," Geotechnique, London, Vol. 2, No. 3, 1951, pp. 251-263.

Clarke, B.G., Carter, J.P., and Wroth, C.P., "In Situ Determination of the Consolidation Characteristics of Saturated Clays," Proceedings, 7th European Conference on Soil Mechanics and Foundation Engineering, Brighton, England, 1979.

D'Appolonia, D.J., "Effects of Foundation Construction on Nearby Structures," Proceedings, 4th Panamerican Conference on Soil Mechanics and Foundation Engineering, Puerto Rico, June 1971, pp. 189-236.

Davis, E.H. and Christian, J.T., "Bearing Capacity of Anisotropic Cohesive Soil," Journal of the Soil Mechanics and Foundations Division, ASCE, Vol. 97, No. SM5, May 1971, pp. 753-769.

Drucker, D.C., "Plasticity," Proceedings, First Symposium on Naval Structural Mechanics, Pergamon Press, New York, 1960.

Drucker, D.C. and Prager, W., "Soil Mechanics and Plastic Analysis or Limit Design," Quarterly of Applied Mathematics, Vol. 10, No. 2, 1952, pp. 157-165.

Esrig, M.I. and Kirby, R.C., "Soil Capacity for Supporting Deep Foundation Members in Clay," Proceedings, ASTM Symposium on Behavior of Deep Foundations, Boston, Mass., June 1978.

Esrig, M.I., Kirby, R.C., and Murphy, B.S., "Advances in General Effective Stress Method for the Prediction of Axial Capacity for Driven Piles in Clay," Proceedings, 11th Offshore Technology Conference, April-May 1979.

Esrig, M.I. et al., "Initial Development of a General Effective Stress Method for the Prediction of Axial Capacity for Driven Piles in Clay," Proceedings, 9th Offshore Technology Conference, 1977.

Fung, Y.C., Foundations of Soil Mechanics, Prentice-Hall, New Jersey, 1965.

Ghionna, V. et al., "Performance of the Self-Boring Pressuremeter in Saturated Cohesive Deposits," Progress Report No. 1, Istituto di Scienza delle Costruzioni, Politecnico di Torino, Joint Research with the Department of Civil Engineering, MIT, Cambridge, Mass., July 1979.

Hagerty, D.J. and Garlanger, J.E., "Consolidation Effects around Driven Piles," Proceedings, Specialty Conference on Performance of Earth and Earth-Supported Structures, Purdue University, June 1972.

Henkel, D.J., "The Relationship Between the Strength, Pore Water Pressure and Volume Change Characteristics of Saturated Clays," Geotechnique, London, Vol. 9, No. 3., 1959, pp. 119-135.

Henkel, D.J., "The Shear Strength of Saturated Remolded Clays," Proceedings, ASCE Specialty Conference on Shear Strength of Cohesive Soils, Boulder, Colorado, 1960.

Henkel, D.J. and Wade, N.H., "Plane Strain Tests on a Saturated Remolded Clay," Journal of the Soil Mechanics and Foundations Division, ASCE, Vol. 92, No. SM6, November 1966, pp. 67-80.

Hight, D.W., El-Ghamrawy, M.K., and Gens, A., "Some Results from a Laboratory Study of a Sandy Clay and Implications Regardings its In Situ Behavior," Proceedings, BOSS 79, London, August 1979.

Hill, R., The Mathematical Theory of Plasticity, Oxford at the Clarendon Press, 1950.

Iwan, W.D., "On a Class of Models for the Yielding Behavior of Continuous and Composite Systems," Journal of Applied Mechanics, Vol. 34, 1967, pp. 612-617.

Janbu, N., "In Situ Measurements of Shear Strength," Proceedings, ASCE Specialty Conference on In Situ Measurement of Soil Properties, Raleigh, North Carolina, 1975, pp. 150-152.

Kavadas, M., personal communication, 1979.

Kirby, R.C. and Esrig, M.I., "Further Development of a General Effective Stress Method for Prediction of Axial Capacity for Driven Piles in Clay," Proceedings, Conference on Recent Developments in the Design and Construction of Piles, The Institute of Civil Engineers, London, March 1979.

Kirby, R.C. and Wroth, C.P., "Application of Critical State Soil Mechanics to the Prediction of Axial Capacity for Driven Piles," Proceedings, 9th Offshore Technology Conference, Paper No. 2942, Vol. 3, 1977, pp. 483-494.

Koizumi, Y. and Ito, K., "Field Tests with Regard to Pile Driving and Bearing Capacity of Piled Foundations," Soils and Foundations, Japan, Vol. 7, No. 3, 1967, pp. 30-53.

Lacasse, SM., Ladd, C.C., and Baligh, M.M., "Evaluation of Field Vane, Dutch Cone Penetrometer and Piezometer Probe Testing Devices," Research Report No. R78-26, Department of Civil Engineering, MIT, Cambridge, Mass., 1978.

Ladd, C.C. and Edgers, L., "Consolidated-Undrained Direct-Simple Shear Tests on Saturated Clays," Contract Report No. 3-101, Phase Report No. 16, Department of Civil Engineering, MIT, Cambridge, Mass., July 1972.

Ladd, C.C. and Foott, R., "New Design Procedure for Stability of Soft Clays," Journal of the Geotechnical Engineering Division, ASCE, Vol. 100, No. GT7, July 1974, pp. 763-786.

Ladd, C.C. and Varallyay, J., "The Influence of Stress System on the Behavior of Saturated Clays During Undrained Shear," Contract Report No. 3-101, Department of Civil Engineering, MIT, Cambridge, Mass., July 1965.

Ladd, C.C. et al., "Consolidated-Undrained Plane Strain Shear Tests on Boston Blue Clay," Contract Report No. 3-101, Phase Report No. 15, Department of Civil Engineering, MIT, Cambridge, Mass., March 1971.

Ladd, C.C. et al., "Stress-Deformation and Strength Characteristics," Proceedings, 9th International Conference on Soil Mechanics and Foundations Engineering, Tokyo, 1977.

Ladd, C.C. et al., "Evaluation of Self-Boring Pressuremeter Tests in Boston Blue Clay," Research Report No. R79-4, Department of Civil Engineering, MIT, Cambridge, Mass., 1979.

Laier, J.E., Schmertmann, J.H., and Schaub, J.H., "Effects of Finite Pressuremeter Length in Dry Sand," Proceedings, ASCE Specialty Conference on the In Situ Measurements of Soil Properties, Raleigh, North Carolina, June 1975.

Lambe, T.W., "The Stress-Path Method," Journal of the Soil Mechanics and Foundations Division, ASCE, Vol. 93, No. SM6, November 1967, pp. 309-331.

Lambe, T.W. and Horn, H.M., "The Influence on an Adjacent Building of Pile Driving for the MIT Material Center," Proceedings, 6th International Conference on Soil Mechanics and Foundation Engineering, Montreal, 1965.

Lambe, T.W. and Marr, W.A., "Stress Path Method: Second Edition," Journal of the Geotechnical Engineering Division, ASCE, Vol. 105, No. GT6, June 1979, pp. 727-738.

Leonards, G.A. and Altschaeffl, A.G., "Compressibility of Clay," Journal of the Soil Mechanics and Foundations Division, ASCE, Vol. 90, No. SM5, 1964, pp. 113-156.

Levadoux, J.N. and Baligh, M.M., "Pore Pressure Dissipation After Cone Penetration," Publication No. R80-11, Order No. 662, Department of Civil Engineering, MIT, Cambridge, Mass., April 1980.

Levadoux, J.N. and Baligh, M.M., "Pore Pressures During Cone Penetration in Clays," Research Report, Department of Civil Engineering, MIT, Cambridge, Mass., 1980 (in preparation).

Levadoux, J.N. and Baligh, M.M., "Radial Consolidation Solutions," Research Report, Department of Civil Engineering, MIT, Cambridge, Mass., 1980 (in preparation).

Lo, K.Y., "Stress-Strain Relationship and Pore Water Pressure Characteristics of a Normally Consolidated Clay," Proceedings, 5th International Conference on Soil Mechanics and Foundation Engineering, Montreal, 1965.

Malvern, L.E., Introduction to the Mechanics of a Continuous Medium, Prentice-Hall, New Jersey, 1969.

Massarch, K.R. and Broms, B.B., "Fracturing of Soil Caused by Pile Driving in Clay," Proceedings, 9th International Conference on Soil Mechanics and Foundation Engineering, Tokyo, 1977.

Mroz, A., "On the Description of Anisotropic Workhardening," Journal of the Mechanics and Physics of Solids, Longon, Vol. 15, 1967, pp. 163-175.

Naghdi, P.M., "Stress-Strain Relations and Thermoplasticity," Proceedings, Second Symposium on Naval Structural Mechanics, Pergamon Press, New York, 1960.

Nadai, Theory of Flow and Fracture of Solids, McGraw-Hill, New York, 1950.

Prager, W., "The Theory of Plasticity: A Survey of Recent Achievements," Proceedings, The Institute of Mechanical Engineering, London, Vol. 169, 1955.

Prevost, J.H., "Soil Stress-Strain-Strength Models Based on Plasticity Theory," Ph.D. thesis, Department of Civil Engineering, Stanford University, 1974.

Prevost, J.H., "Undrained Stress-Strain-Time Behavior of Clays," Journal of the Geotechnical Engineering Division, ASCE, Vol. 102, No. GT12, December 1976, pp. 1245-1259.

Prevost, J.H., "Mathematical Modelling of Monotonic and Cyclic Undrained Clay Behavior," International Journal for Numerical and Analytical Methods in Geomechanics, Vol. 1, 1977, pp. 195-216.

Prevost, J.H., "Anisotropic Undrained Stress-Strain Behavior of Clays," Journal of the Geotechnical Engineering Division, ASCE, Vol. 104, No. GT8 , August 1978, pp. 1075-1090.

Prevost, J.H., Undrained Shear Tests on Clay," Journal of the Geotechnical Engineering Division, ASCE, Vol. 105, No. GT1, January 1979, pp. 49-64.

Prevost, J.H. and Hoeg, K., "Reanalysis of Simple Shear Soil Testing," Canadian Geotechnical Journal, Toronto, Vol. 13, No. 4., November 1976, pp. 418-429.

Randolph, M.F., personal communication, 1979.

Randolph, M.F., Carter, J.P., and Wroth, C.P., "Driven Piles in Clay: (I) Installation, Modelled as the Expansion of a Cylindrical Cavity," Report No. TR53, Department of Civil Engineering, University of Cambridge, England, 1978.

Randolph, M.F., Steenfelt, J.S., and Wroth, C.P., "The Effect of Pile Type of Design Parameters for Driven Piles," Proceedings, 7th European Conference on Soil Mechanics and Foundation Engineering, Brighton, England, September 1979.

Robinsky, E.I. and Morrison, C.F., "Sand Displacement and Compaction around Friction Piles," Canadian Geotechnical Journal, Vol. 1, 1964, pp. 81-93.

"Report of the Subcommittee on Standardization of Penetration Testing in Europe," Proceedings, 9th International Conference on Soil Mechanics and Foundation Engineering, Tokyo, Japan, Vol. 3, 1977, pp. 95-109.

Roscoe, K.H. "An Apparatus for the Application of Simple Shear to Soil Samples," Proceedings, 3rd International Conference on Soil Mechanics and Foundation Engineering, Zurich, 1953.

Roscoe, K.H. and Burland, J.B., "On the Generalized Behavior of 'Wet' Clay," Engineering Plasticity, ed. J. Heyman and F.A. Leckie, Cambridge university Press, England, 1968, pp. 535-609.

Rourk, T.L., "Model Studies of a Pile Failure Surface in a Cohesive Soil," Master's thesis, Department of Civil Engineering, Georgia Institute of Technology, Atlanta, 1961.

Rouse, H., Advanced Mechanics of Fluids, John Wiley & Sons, New York, 1959.

Roy, M. et al., "Behavior of a Sensitive Clay During Pile Driving," Proceedings, 32nd Canadian Geotechnical Conference, Quebec, September 1969.

Schmertmann, J.H., "Measurements of In Situ Shear Strength," Proceedings, ASCE Specialty Conference on In Situ Measurement of Soil Properties, Raleigh, North Carolina, 1975.

Schoefield, A.N. and Wroth, C.P., Critical Soil Mechanics, McGraw-Hill, New York, 1968.

Shames, I.H., Mechanics of Fluids, McGraw-Hill, New York, 1962.

Skempton, A.W., "The Bearing Capacity of Clays," Building Research Congress, the Institute of Civil Engineering, London, 1951.

Skempton, A.W., "The Pore-Pressure Coefficients A and B," Geotechnique, London, Vol. 4, 1954, pp. 143-147.

Szechy, K., "Deformations Around and Below Driven and Vibrated Test Tubes," Acta Technica Acad. Sci, Hungary, Vol. 62, 1968, pp. 97-113.

Taylor, D.W., 9th Progress Report on Shear Strength Research to U.S. Engineers, MIT, 1943.

Terzaghi, K., Theoretical Soil Mechanics, John Wiley & Sons, New York, 1943.

Terzaghi, K. and Peck, R., Soil Mechanics in Engineering Practice, John Wiley & Sons, New York, 1967.

Vaid, Y.P. and Campanella, R.G., "Triaxial and Plane Strain Behavior of Natural Clay," Journal of the Geotechnical Engineering Division, ASCE, Vol. 100, No. GT3, March 1974, pp. 207-224.

Vesic, A.S., "Bearing Capacity of Deep Foundations to Sand," Stresses in Soils and Layered Systems, Highway Research Board No. 39, 1963. pp. 112-.53.

Vijayvergiya, V.N. and Focht, J.A., "A New Way to Predict the Capacity of Piles in Clay," Fourth Annual Offshore Technology Conference, Houston, Texas, Vol. 2, 1972, pp. 865-874.

Weinstein, A., "On Axially Symmetric Flows," Quarterly of Applied Mathematics, Vol. 5, No. 4., 1948, pp. 429-434.

Wissa, A.E.Z., Martin, R.T., and Garlanger, J.E., "The Piezometer Probe," Proceedings, ASCE Specialty Conference on In Situ Measurement of Soil Properties, Raleigh, North Carolina, 1975.

APPENDIX A

STRAIN PATH METHOD - EVALUATION OF TOTAL STRESSES

A.1 SPATIAL INTEGRATION OF EQUILIBRIUM EQUATIONS

In axisymmetric problems, the equilibrium equations in terms of total stresses are:

$$\left.\begin{aligned} \frac{\partial \sigma_r}{\partial r} + \frac{\partial \tau_{rz}}{\partial z} + \frac{\sigma_r - \sigma_\theta}{r} + R = 0 \\ \frac{\partial \tau_{rz}}{\partial r} + \frac{\partial \sigma_z}{\partial z} + \frac{\tau_{rz}}{r} + Z = 0 \end{aligned}\right\} \qquad (A.1)$$

in which:

r = radial coordinate

z = vertical coordinate

σ_r = radial total stress

σ_θ = circumferential total stress

σ_z = vertical total stress

τ_{rz} = radial shear stress acting on the vertical plane

R = radial body force

and, Z = vertical body force

When the z - axis is aligned with the vertical direction (positive upwards), the body forces are: $R = 0$; $Z = \gamma_t$ (γ_t = total unit weight of the clay). In deep quasi-static steady penetration, the radius of the cone (or pile) is small and the effect of gravity (γ_t) on equilibrium near

the tip is negligible* and equations A.1 become:

$$\left.\begin{aligned} \frac{\partial \sigma_r}{\partial r} + \frac{\partial \tau_{rz}}{\partial z} + \frac{\sigma_r - \sigma_\theta}{r} &= 0 \\ \frac{\partial \tau_{rz}}{\partial r} + \frac{\partial \sigma_z}{\partial z} + \frac{\tau_{rz}}{r} &= 0 \end{aligned}\right\} \qquad (A.2)$$

Dividing total stresses into deviatoric and octahedral (or isotropic) stresses:

$$\left.\begin{aligned} \sigma_r &= s_r + \sigma_{oct} \\ \sigma_\theta &= s_\theta + \sigma_{oct} \\ \sigma_z &= s_z + \sigma_{oct} \\ \tau_{rz} &= s_{rz} \end{aligned}\right\} \qquad (A.3)$$

and substituting Eqs. A.3 into Eqs. A.2, we get:

$$\left.\begin{aligned} \frac{\partial \sigma_{oct}}{\partial r} &= -\frac{\partial s_r}{\partial r} - \frac{\partial s_{rz}}{\partial z} - \frac{s_r - s_\theta}{r} \\ \frac{\partial \sigma_{oct}}{\partial z} &= -\frac{\partial s_{rz}}{\partial r} - \frac{\partial s_z}{\partial z} - \frac{s_{rz}}{r} \end{aligned}\right\} \qquad (A.4)$$

In the strain path method described in Chapter 2, the right hand side of Eq. A.4 can be determined from the deviatoric stress soil model knowing the strain path of the soil element. The octahedral stress can then be computed by integrating Eq. A.4 along a path starting at a location where the octahedral stress $(\sigma_{oct})_o$ is known (i.e., in the far field) and utilizing:

$$d\,\sigma_{oct} = \frac{\partial \sigma_{oct}}{\partial r}\,dr + \frac{\partial \sigma_{oct}}{\partial z}\,dz \qquad (A.5)$$

---

*For example, a cone penetrometer (or pile) pushed to a depth of 100 ft in soft clay induces a change in isotropic stresses approximately equal to the total overburden stress at that depth.

where dr and dz are the radial and vertical coordinate increments between two consecutive points on the integration path.

Appendix F provides description and computer codes for a numerical integration scheme applied along two different sets of integration paths.

A.2 IMPLICATIONS OF USING AN APPROXIMATE STRAIN FIELD

Since the strain path method is based on an approximate strain field, it is not surprising that the resulting stresses are also approximate. This is reflected by the fact that the partial differentials of σ_{oct} do not satisfy the relation:

$$\frac{\partial}{\partial z}\left(\frac{\partial \sigma_{oct}}{\partial r}\right) = \frac{\partial}{\partial r}\left(\frac{\partial \sigma_{oct}}{\partial z}\right) \qquad (A.6)$$

In other words the right hand side of Eq. A.5 is not a total differential and integration with Eq. A.5 is path dependent.

More insight into the approximations associated with the strain path method may be gained by recognizing that any material can be forced to follow any strain field (satisfying the boundary and compatibility requirements) as long as an appropriate body force field is superimposed. The deviatoric stresses obtained by the strain path method in the case of deep steady cone penetration are, therefore, the exact solution to the stresses experienced in the soil subjected to both the boundary displacements (at the soil-instrument interface) and an appropriate field of fictitious body forces.

Substituting Eqs. A.3 into Eqs. A.1 we obtain:

$$\frac{\partial \sigma_{oct}}{\partial r} = - \frac{\partial s_r}{\partial r} - \frac{\partial s_{rz}}{\partial z} - \left(\frac{s_r - s_\theta}{r}\right) - \{R\} \qquad (A.7.a)$$

$$\frac{\partial \sigma_{oct}}{\partial z} = - \frac{\partial s_{rz}}{\partial r} - \frac{\partial s_z}{\partial z} - \frac{s_{rz}}{r} - \{Z\} \qquad (A.7.b)$$

in which $\{R\}$ and $\{Z\}$ are the fictitious body forces. These two equations relate, at any point in space, the known deviatoric stresses to three unknowns: σ_{oct}, $\{R\}$ and $\{Z\}$. This indeterminancy of order one, therefore, indicates that an infinite number of body force ($\{R\}$ and $\{Z\}$) and isotropic stress (σ_{oct}) fields can be found to satisfy Eqs. A.7. For example, given a sufficiently smooth σ_{oct} field, the body forces $\{R\}$ and $\{Z\}$ can be evaluated directly by means of Eqs. A.7 to achieve equilibrium.

A.3 EVALUATION OF ACCEPTABLE BODY FORCE FIELDS

The fictitious body force fields in the problem of cone penetration are of interest for two reasons: a) to compare at a selected number of points the magnitude of these body forces to the stress gradients and, thus assess their effect in the overall solution, and; b) to develop an iterative procedure in order to improve the approximate velocity field and therefy, obtain a more accurate solution.

Because of the indeterminancy in the problem, it is necessary to arbitrarily assign predetermined variation in one of the three unknowns: σ_{oct}, $\{R\}$, and $\{Z\}$. A method for evaluating acceptable body force fields consists of:

1) Integrate Eq. A.7.a with $\{R\} = 0$ along radial lines ($dz = 0$). The resulting σ_{oct} field satisfies equilibrium in the radial

direction (Eq. A.7.a);

2) Evaluate at every point the required fictitious body force $\{Z\}$ so that the isotropic stress σ_{oct} previously obtained and the deviatoric stresses satisfy equilibrium in the z direction; i.e., solve Eq. A.7.b for $\{Z\}$.

An equivalent method consists of first assuming $\{Z\} = 0$, integrating Eq. A.7.b along vertical lines (i.e., $dr = 0$) and finally evaluate $\{R\}$ by means of Eq. A.7.a.

Integration along radial ($dz = 0$) or vertical ($dr = 0$) lines is more complicated than the methods of integration along isochronic and streamlines presented in Appendix E. Indeed, such an integration first requires interpolation of the deviatoric stresses along straight (radial or vertical) lines.

APPENDIX B

ESTIMATION OF STRAINS AND DEFORMATIONS DURING CONE PENETRATION - COMPUTER PROGRAM

B.1 PROGRAM DESCRIPTION

This computer program utilizes the theoretical developments presented in Chapter 3 to compute strains and deformations for incompressible, irrotational and inviscid flow around a conical tip attached to a cylindrical shaft during steady cone penetration. The program is coded in FORTRAN IV (double precision) and is intended to be used in an interactive mode (e.g., MULTICS or CMS, with Honeywell or IBM systems, respectively). At each input stage, the user is prompted for the next data to be entered and usage of the program is, therefore, self-explanatory.

B.1.1 General Input

At the beginning of each new problem, the user must provide:

a) the cylinder radius;

b) the half cone angle;

c) the ratio of the cylinder to the cone length;

d) the radius of curvature at the cone-cylinder transition;

e) the number of sources* uniformly spaced over the cone length;

f) the number of sources* uniformly spaced over the cylinder length, and;

---

* The total number of sources along both segments should not exceed 200.

g) a printing control parameter:

= 0; no printing

= 1; only final results are printed

= 2; detailed output

h) a storage control parameter:

= 0, no storage

≠ 0, parameter gives the unit number for storage

All the variables are expressed in F10.3 format.

B.1.2 Sources Strength Evaluation

Once the input phase has been completed, the coordinates of the body points and of the sources centers are computed and stored. Evaluation of the sources strength (Chapter 3) is then accomplished by solving the system of linear equations (Eqs. 3.6) with the elimination method. Three modes of operation are then available.

B.1.3 Modes of Operation

The first mode of operation (MODE = 0) is used to exit the program when computations are completed; the next two modes (MODE = 1,2) are intended for checking stability and accuracy of the solution and; the last mode (MODE = 3) is invoked to carry out computations of deformations, strain increments and strains, along one streamline at a time.

a) MODE = 1

The program computes values of the stream function $\Psi(r,z)$, using Eq. 3.7, at a fixed z-coordinate, for a radius varying from 0 to RMAX (in increments equal to DELR).

b) MODE = 2

The streamline corresponding to a given value of the stream function $\psi(r,z)$ is located in the interval {ZMIN, ZMAX} at equal DELZ increments by solving for r in the implicit Eq. 3.15 by successive trials.

c) MODE = 3

The streamline is defined by the coordinates (RO, ZO) of the particle (to be followed along its path) at time T = 0. Numerical integration of velocities and rates-of-deformation is first carried out (without printing) with a decreasing time increment proportional to $|1/z|$ up to a time equal to TMIN. The time interval is then reduced to DTF and the following quantities are printed at the end of each time interval: relative time, z and r coordinates, strain increment components ($d\varepsilon_{rr}$, $d\varepsilon_{zz}$, $d\varepsilon_{\theta\theta}$ and $d\varepsilon_{rz}$) and, natural strain components (ε_{rr}, ε_{zz}, $\varepsilon_{\theta\theta}$ and ε_{rz}).

Changing the mode of operation is achieved by setting Z > 1000, XPSI = 0, or RO = 0 when the present mode is equal to 1, 2, or 3, respectively.

B.2 PROGRAM LISTING

```
C     ..................................................................
C     PROGRAM TO OBTAIN STREAMLINES, STRAIN INCREMENTS AND STRAINS FOR
C     AN INCOMPRESSIBLE IRROTATIONAL INVISCID FLOW AROUND A CONE
C     ATTACHED TO A CYLINDER.
C     PROGRAMMED BY J.N. LEVADOUX                    M.I.T. (APRIL 1979).
C     ..................................................................
C
      IMPLICIT REAL*8 (A-H,O-Z)
      COMMON /CNTL/ RC,XLCO,XLCY,XR,PI,NCO,NCY,NTOT,IPRINT,ISTORE
      COMMON /STRE/ ETA(200),R(200),Z(200),DL(200)
      COMMON /BIGI/ C(200,201)
C
C.... PARAMETERS DEFINITION
C
C     RC     = CYLINDER RADIUS
C     ALPHA  = HALF CONE ANGLE
C     XLCO   = CONE LENGTH
C     XLCY   = CYLINDER LENGTH
C     XR     = RADIUS OF CURVATURE AT CONE-CYLINDER TRANSITION
C     NCO    = NUMBER OF SOURCES ALONG CONE AXIS
C     NCY    = NUMBER OF SOURCES ALONG CYLINDER AXIS
C     IPRINT : PRINTING CONTROL FOR UNIT 6
C            = 0 NO PRINTING
C            = 1 REDUCED INFORMATION
C            = 2 COMPLETE INFORMATION
C     ISTORE = DEVICE NUMBER TO STORE RESULTS (=0 NO STORAGE)
C     MODE   : MODE OF OPERATION
C            = 0 QUIT
C            = 1 COMPUTE STREAM FUNCTION AT FIXED Z, VARYING R
C            = 2 SEARCH FOR STREAMLINES (IMPLICIT METHOD)
C            = 3 COMPUTE STRAIN INCREMENTS, STRAINS AND DEFORMATIONS
C                ALONG STREAM LINES (INTEGRATION METHOD)
C
      PI=3.1415926536 D0
C
C.... INPUT PARAMETERS
C
      WRITE(6,2000)
      READ(5,1000) RC
      WRITE(6,2001)
      READ(5,1000) ALPHA
      ALPHA=ALPHA*PI/180.0D0
      XLCO=RC*DCOS(ALPHA)/DSIN(ALPHA)
      WRITE(6,2002)
      READ(5,1000) XLCY
      XLCY=XLCY*XLCO
      WRITE(6,2005)
      READ(5,1000) XR
      WRITE(6,2003)
      READ(5,1000) XNCO
      NCO=XNCO
      WRITE(6,2004)
      READ(5,1000) XNCY
      NCY=XNCY
      WRITE(6,2007)
      READ(5,1000) XPRINT
      IPRINT=XPRINT
      WRITE(6,2008)
      READ(5,1000) XSTORE
      ISTORE=XSTORE
      NTOT=NCO+NCY
C
C.... COMPUTE BODY POINTS COORDINATES
C
      CALL BODY
C
C.... COMPUTE SOURCE STRENGTH
C
      CALL STRENG
C
C.... INPUT MODE OF OPERATION
C
    2 WRITE(6,2005)
      READ(5,1000) XMODE
      MODE=XMODE
      IF (MODE.EQ.0) CALL EXIT
C
C.... CHECK STREAM FUNCTION
C
      IF (MODE.EQ.1) CALL CHECK
C
C.... SEARCH STREAM LINES
C
      IF (MODE.EQ.2) CALL STLINE
C
C.... COMPUTE STRAIN INCREMENTS, STRAINS AND DEFORMATIONS
C
      IF (MODE.EQ.3) CALL GRID
      GO TO 2
 1000 FORMAT(F10.3)
 2000 FORMAT(/'  INPUT THE CYLINDER RADIUS (F10.3)'/)
 2001 FORMAT(/'  INPUT THE HALF CONE ANGLE (F10.3)'/)
 2002 FORMAT(/'  INPUT " XLCY/XLCO " (F10.3)'/)
 2003 FORMAT(/'  INPUT THE NUMBER OF SOURCES ALONG CONE AXIS (F10.3)'/)
 2004 FORMAT(/'  INPUT THE NUMBER OF SOURCES ALONG ',
     $       'CYLINDER AXIS (F10.3)'/)
 2005 FORMAT(///'  MODE OF OPERATION ?????'/)
 2006 FORMAT(/'  INPUT RADIUS OF CURVATURE (F10.3)'/)
 2007 FORMAT(/'  COMPLETE PRINTING INFORMATION ????'/)
 2008 FORMAT(/'  STORAGE UNIT NUMBER (=0 NO STORAGE) ????'/)
      END
      SUBROUTINE BODY
C     ..................................................................
C     THIS ROUTINE COMPUTES BODY POINTS COORDINATES.
C     ..................................................................
      IMPLICIT REAL*8 (A-H,O-Z)
      COMMON /CNTL/ RC,XLCO,XLCY,XR,PI,NCO,NCY,NTOT,IPRINT,ISTORE
      COMMON /STRE/ ETA(200),R(200),Z(200),DL(200)
C
      DELCO=XLCO/NCO
      DELCY=XLCY/NCY
      SLOPE=RC/XLCO
      Z(1)=DELCO/2.0 D0
      R(1)=SLOPE*Z(1)
      DL(1)=DELCO
      DO 1 I=2,NCO
      Z(I)=Z(I-1)+DELCO
      R(I)=SLOPE*Z(I)
      DL(I)=DELCO
    1 CONTINUE
```

```
      Z(NCO+1)=XLCO+DELCY/2.0 D0
      R(NCO+1)=RC
      DL(NCO+1)=DELCY
      IS=NCO+2
      DO 2 I=IS,NTOT
      Z(I)=Z(I-1)+DELCY
      R(I)=RC
      DL(I)=DELCY
    2 CONTINUE
C
      IF (XR.EQ.0.0D0) RETURN
C
C.... MODIFY BODY POINTS AT CONE-CYLINDER TRANSITION
C
      ALPHA=DATAN2(RC,XLCO)
      ALPHA2=ALPHA/2.0
      T=DSIN(ALPHA2)/DCOS(ALPHA2)
      ZC=RC*(1.0D0-T*T)/(2.0*T)-XR*T*(1.0-T*T)/(1.0+T*T)
      ZD=RC*(1.0-T*T)/(2.0*T)+XR*T
      DO 3 I=1,NTOT
      IF (Z(I).LT.ZC.OR.Z(I).GT.ZD) GO TO 3
      RAD=XR*XR-(Z(I)-RC*(1.0-T*T)/(2.0*T)-XR*T)**2
      R(I)=RC-XR+DSQRT(RAD)
    3 CONTINUE
      RETURN
      END
      SUBROUTINE CHECK
C     ..................................................................
C     THIS ROUTINE COMPUTES THE STREAM FUNCTION AT A GIVEN Z FOR R
C     VARYING FROM 0 TO RMAX (WITH INCREMENTS EQUAL TO DELR).
C     ..................................................................
      IMPLICIT REAL*8 (A-H,O-Z)
C
    1 WRITE(6,2000)
      READ(5,1000) Z
      IF (Z.GT.1000.0D0) RETURN
      WRITE(6,2001)
      READ(5,1000) RMAX
      WRITE(6,2002)
      READ(5,1000) DELR
      WRITE(6,2003)
      R=-DELR
    2 R=R+DELR
      U=PSI(R,Z)
      WRITE(6,2004) R,Z,U
      IF (R.LT.(RMAX-1.0D-10)) GO TO 2
      GO TO 1
 1000 FORMAT(F10.3)
 2000 FORMAT(/'  INPUT Z (F10.3)'/)
 2001 FORMAT(/'  INPUT RMAX (F10.3)'/)
 2002 FORMAT(/'  INPUT DELTA R (F10.3)'/)
 2003 FORMAT(/10X,'    RR    ',','    ZZ    ',','    PSI'/)
 2004 FORMAT(10X,2F10.3,1PE10.3)
      END
      SUBROUTINE EPS(RR,ZZ,DEPSR,DEPSZ,DEPST,DEPSRZ,VELR,VELZ)
C     ..................................................................
C     THIS ROUTINE COMPUTES VELOCITIES AND STRAIN INCREMENTS AT (RR,ZZ).
C     ..................................................................
      IMPLICIT REAL*8 (A-H,O-Z)
      COMMON /CNTL/ RC,XLCO,XLCY,XR,PI,NCO,NCY,NTOT,IPRINT,ISTORE
      COMMON /STRE/ ETA(200),R(200),Z(200),DL(200)
C
      SUMR = 0.0D0
      SUMZ = 0.0D0
      SUM1 = 0.0D0
      SUM2 = 0.0D0
      R2=RR*RR
C
      DO 1 I=1,NTOT
      ZB = ZZ + DL(I)/2.0D0 - Z(I)
      ZT = ZZ - DL(I)/2.0D0 - Z(I)
      ROB = DSQRT(ZB*ZB+R2)
      ROT = DSQRT(ZT*ZT+R2)
      Q = ETA(I)/DL(I)
      ROB3 = ROB**3
      ROT3 = ROT**3
      SUMR = SUMR + Q*(ZB/ROB-ZT/ROT)
      SUMZ = SUMZ + Q*(1.0D0/ROB-1.0D0/ROT)
      SUM1 = SUM1 + Q*(ZB/ROB3-ZT/ROT3)
      SUM2 = SUM2 + Q*(1.0D0/ROB3 - 1.0D0/ROT3)
    1 CONTINUE
C
      VELR = SUMR/RR
      VELZ = 1.0D0 - SUMZ
      DEPSZ=-SUM1
      DEPST=-SUMR/(RR*RR)
      DEPSR=-(DEPSZ+DEPST)
      DEPSRZ=-SUM2*RR
      RETURN
      END
      SUBROUTINE GRID
C     ..................................................................
C     THIS ROUTINE COMPUTES STRAINS AND DEFORMATIONS ALONG A CHOSEN
C     STREAMLINE.
C     ..................................................................
      IMPLICIT REAL*8 (A-H,O-Z)
      COMMON /CNTL/ RC,XLCO,XLCY,XR,PI,NCO,NCY,NTOT,IPRINT,ISTORE
      COMMON /STRE/ ETA(200),R(200),Z(200),DL(200)
C
      Z1=-0.1D0*XLCO
      Z2=1.5D0*XLCO
C
    1 WRITE(6,2000)
      READ(5,1000) RO
      IF (RO.EQ.0.0) RETURN
      WRITE(6,2001)
      READ(5,1000) ZO
      WRITE(6,2002)
      READ(5,1000) DTC
      WRITE(6,2003)
      READ(5,1000) TMIN
      WRITE(6,2004)
      READ(5,1000) TMAX
      WRITE(6,2005)
      READ(5,1000) DTF
      WRITE(6,2006)
      READ(5,1000) XKF
      KF=XKF
      ZZ=ZO
      RR=RO
```

```
      TMIN=TMIN-DTF
      T=0.0 D0
      EPSR=0.0 D0
      EPSZ=0.0 D0
      EPST=0.0 D0
      EPSRZ=0.0 D0
      IF (TMIN.LE.0.0) GO TO 4
      SLOPE=(DTF-DTC)/TMIN
      IF (IPRINT.NE.0) WRITE(6,2010)
    2 CONTINUE
      DDT = DTC + SLOPE*T
      T=T+DDT
      IF (T.LT.TMIN) GO TO 3
      DDT=TMIN-T+DDT
      T=TMIN
    3 CALL EPS(RR,ZZ,DEPSR,DEPSZ,DEPST,DEPSRZ,VELR,VELZ)
      RR = RR + DDT*VELR
      ZZ = ZZ + DDT*VELZ
      DEPSR=DDT*DEPSR
      DEPSZ=DDT*DEPSZ
      DEPST=DDT*DEPST
      DEPSRZ=DDT*DEPSRZ
      IF (IPRINT.EQ.0) GO TO 10
      EPSR=EPSR+DEPSR
      EPSZ=EPSZ+DEPSZ
      EPST=EPST+DEPST
      EPSRZ=EPSRZ+DEPSRZ
      WRITE(6,2011) T,ZZ,RR,DEPSZ,DEPSR,DEPST,DEPSRZ,EPSZ,EPSR,EPST,
     $              EPSRZ
   10 CONTINUE
      IF (ISTORE.NE.0)
     $WRITE(ISTORE,2012) ZZ,RR,DEPSZ,DEPSR,DEPST,DEPSRZ
      IF (T.LT.TMIN) GO TO 2
    4 CONTINUE
      DDT=DTF/XKF
      KKF=KF
      IF (RO.GT.RC) GO TO 20
      IF (ZZ.LT.Z1.OR.ZZ.GT.Z2) GO TO 20
      KKF=10*KF
      DDT=DDT/10.0D0
   20 SEPSR=0.0D0
      SEPSZ=0.0D0
      SEPST=0.0D0
      SEPSRZ=0.0D0
      DO 5 I=1,KKF
      T=T+DDT
      CALL EPS(RR,ZZ,DEPSR,DEPSZ,DEPST,DEPSRZ,VELR,VELZ)
      RR = RR + DDT*VELR
      ZZ = ZZ + DDT*VELZ
      DEPSR=DDT*DEPSR
      DEPSZ=DDT*DEPSZ
      DEPST=DDT*DEPST
      DEPSRZ=DDT*DEPSRZ
      SEPSR=SEPSR+DEPSR
      SEPSZ=SEPSZ+DEPSZ
      SEPST=SEPST+DEPST
      SEPSRZ=SEPSRZ+DEPSRZ
      IF (IPRINT.EQ.0) GO TO 5
      EPSR=EPSR+DEPSR
      EPSZ=EPSZ+DEPSZ
      EPST=EPST+DEPST
      EPSRZ=EPSRZ+DEPSRZ
    5 CONTINUE
C
      IF (IPRINT.GT.0)
     1WRITE(6,2011) T,ZZ,RR,SEPSZ,SEPSR,SEPST,SEPSRZ,EPSZ,EPSR,EPST,
     2              EPSRZ
      IF (ISTORE.NE.0)
     $WRITE(ISTORE,2012) ZZ,RR,SEPSZ,SEPSR,SEPST,SEPSRZ
      IF (T.LT.TMAX) GO TO 4
      GO TO 1
 1000 FORMAT(F10.3)
 2000 FORMAT(/'  INPUT RADIUS AT INFINITY '/)
 2001 FORMAT(/'  INPUT STARTING Z '/)
 2002 FORMAT(/'  INPUT MAXIMUM COARSE TIME INTERVAL '/)
 2003 FORMAT(/'  INPUT MINIMUM TIME FOR PRINTING '/)
 2004 FORMAT(/'  INPUT MAXIMUM TIME FOR PRINTING '/)
 2005 FORMAT(/'  INPUT FINE TIME INTERVAL '/)
 2006 FORMAT(/'  INPUT SUBINTERVAL NUMBER '/)
 2010 FORMAT(1H1//3X,'TIME',8X,'Z',9X,'R',6X,'DEPSZ',5X,'DEPSR',
     $ 6X,'DEPST',3X,'DEPSRZ',6X,'EPSZ',6X,'EPSR',6X,'EPST',
     $ 5X,'EPSRZ'/)
 2011 FORMAT(F9.3,2F10.5,1X,1P8E10.3)
 2012 FORMAT(F10.5,F10.6,1P4E10.3)
      END
      FUNCTION PSI(RR,ZZ)
C     ..................................................................
C     THIS ROUTINE COMPUTES THE STREAM FUNCTION AT THE POINT (RR,ZZ).
C     ..................................................................
      IMPLICIT REAL*8 (A-H,O-Z)
      COMMON /CNTL/ RC,XLCO,XLCY,XR,PI,NCO,NCY,NTOT,IPRINT,ISTORE
      COMMON /STRE/ ETA(200),R(200),Z(200),DL(200)
C
      SUM=0.0 D0
      DO 1 J=1,NTOT
      XB=DSQRT(RR*RR+(Z(J)-DL(J)/2.0D0-ZZ)**2)
      XT=DSQRT(RR*RR+(Z(J)+DL(J)/2.0D0-ZZ)**2)
      SUM=SUM+ETA(J)*(1.0+(XB-XT)/DL(J))
    1 CONTINUE
      PSI=0.5D0*RR*RR - SUM
      RETURN
      END
      SUBROUTINE SOLVC
C     ..................................................................
C     THIS ROUTINE SOLVES THE LINEAR EQUATIONS WITH THE ELIMINATION
C     METHOD.
C     ..................................................................
      IMPLICIT REAL*8 (A-H,O-Z)
      COMMON /CNTL/ RC,XLCO,XLCY,XR,PI,NCO,NCY,NTOT,IPRINT,ISTORE
      COMMON /STRE/ ETA(200),R(200),Z(200),DL(200)
      COMMON /BIGI/ C(200,201)
C
      N=NTOT
      NP1=N+1
      DO 1 I=1,NTOT
    1 C(I,NP1)=ETA(I)
      NM1=N-1
      DO 5 K=1,NM1
      KP1=K+1
      L=K
```

```
      DO 2 I=KP1,N
    2 IF (DABS(C(I,K)).GT.DABS(C(L,K))) L=I
      IF (L.EQ.K) GO TO 4
      DO 3 J=K,NP1
      TEMP=C(K,J)
      C(K,J)=C(L,J)
    3 C(L,J)=TEMP
    4 DO 5 I=KP1,N
      FACTOR=C(I,K)/C(K,K)
      DO 5 J=KP1,NP1
    5 C(I,J)=C(I,J)-FACTOR*C(K,J)
      ETA(N)=C(N,NP1)/C(N,N)
      I=NM1
    6 IP1=I+1
      SUM=0.0D0
      DO 7 J=IP1,N
    7 SUM=SUM+C(I,J)*ETA(J)
      ETA(I)=(C(I,NP1)-SUM)/C(I,I)
      I=I-1
      IF (I.GE.1) GO TO 6
      RETURN
      END
      SUBROUTINE STLINE
C     ..................................................................
C     THIS ROUTINE COMPUTES THE STREAM FUNCTION AT SELECTED LOCATIONS.
C     ..................................................................
      IMPLICIT REAL*8 (A-H,O-Z)
      COMMON /CNTL/ RC,XLCO,XLCY,XR,PI,NCO,NCY,NTOT,IPRINT,ISTORE
      COMMON /STRE/ ETA(200),R(200),Z(200),DL(200)
C
    1 WRITE(6,2000)
      READ(5,1000) XPSI
      IF (XPSI.EQ.0.0D0) RETURN
      WRITE(6,2001)
      READ(5,1000) ZMIN
      WRITE(6,2002)
      READ(5,1000) ZMAX
      WRITE(6,2003)
      READ(5,1000) DELZ
      WRITE(6,2004)
      ZZ=ZMIN-DELZ
    2 ZZ=ZZ+DELZ
      RR=STR(ZZ,XPSI)
      SPSI=PSI(RR,ZZ)
      WRITE(6,2005)  RR,ZZ,SPSI
      IF (ZZ.LT.(ZMAX-1.0D-10)) GO TO 2
      GO TO 1
 1000 FORMAT (F10.3)
 2000 FORMAT(/'  INPUT THE STREAMLINE CONSTANT (F10.3)'/)
 2001 FORMAT(/'  INPUT THE MINIMUM Z (F10.3)'/)
 2002 FORMAT(/'  INPUT THE MAXIMUM Z (F10.3)'/)
 2003 FORMAT(/'  INPUT DELTA Z (F10.3)'/)
 2004 FORMAT(////10X,'     R     ','     Z     ','   PSI'//)
 2005 FORMAT(10X,2F10.5,1PE10.3)
      END
      FUNCTION STR(ZZ,XPSI)
C     ..................................................................
C     THIS ROUTINE FINDS THE R-COORDINATE WHICH MAKES THE STREAM
C     FUNCTION EQUAL TO XPSI AT THE Z-COORDINATE.
C     ..................................................................
      IMPLICIT REAL*8 (A-H,O-Z)
      COMMON /CNTL/ RC,XLCO,XLCY,XR,PI,NCO,NCY,NTOT,IPRINT,ISTORE
      COMMON /STRE/ ETA(200),R(200),Z(200),DL(200)
C
      RTOL=1.0D-05
      RS=0.99D0
      IF (ZZ.GT.Z(NTOT)) GO TO 2
      RS=DSQRT(2.0D0*XPSI) - 0.01D0
      IF (RS.LT.0.0D0) RS=0.0D0
      DO 1 I=1,NTOT
      IF (ZZ.LE.Z(I)) GO TO 2
      RS=R(I)-0.01
    1 CONTINUE
    2 ISTOP=0
      DELR=0.1D0
      RR=RS
      XE=PSI(RS,ZZ)
      NN=0
      GO TO 4
    3 DELR=DELR/10.0D0
      XE=XS
      RR=RS
      IF (DELR.LT.RTOL) ISTOP=1
    4 XS=XE
      RS=RR
      NN=NN+1
      IF (NN.GE.100) GO TO 5
      RR=RS+DELR
      XE=PSI(RR,ZZ)
      XTEST=(XPSI-XS)*(XPSI-XE)
      IF (XTEST.GT.0.0D0) GO TO 4
      IF (ISTOP.EQ.0) GO TO 3
      STR=RR
      RETURN
    5 STR=999.0
      WRITE(6,2000) ZZ,XPSI
      RETURN
 2000 FORMAT('  RADIUS COULD NOT BE FOUND FOR : Z = ',F10.3,
     $       ' AND  PSI = ',1PE10.3)
      END
      SUBROUTINE STRENG
C     ..................................................................
C     THIS ROUTINE COMPUTES SOURCES' STRENGTH.
C     ..................................................................
      IMPLICIT REAL*8 (A-H,O-Z)
      COMMON /CNTL/ RC,XLCO,XLCY,XR,PI,NCO,NCY,NTOT,IPRINT,ISTORE
      COMMON /STRE/ ETA(200),R(200),Z(200),DL(200)
      COMMON /BIGI/ C(200,201)
C
      ESUM=0.25D0*RC*RC
C
C.... FILL IN 'C' MATRIX AND 'ETA' VECTOR
C
      DO 1 I=1,NTOT
      DO 1 J=1,NTOT
      ZB=DSQRT(R(I)*R(I)+(Z(J)-DL(J)/2.0D0-Z(I))**2)
      ZT=DSQRT(R(I)*R(I)+(Z(J)+DL(J)/2.0D0-Z(I))**2)
      C(I,J)=1.0D0+(ZB-ZT)/DL(J)
      IF (I.EQ.J.OR.I.EQ.NTOT) C(I,J)=1.0D0
    1 CONTINUE
```

```
C
      DO 2 I=1,NTOT
    2 ETA(I)=0.5D0*R(I)*R(I)
      ETA(NTOT)=ESUM
C
C.... COMPUTE SOURCES STRENGTH
C
      CALL SOLVC
C
      IF (IPRINT.LE.1) RETURN
      DO 3 I=1,NTOT
    3 WRITE(6,2000) Z(I),R(I),ETA(I)
      RETURN
 2000 FORMAT(2X,2F12.5,1PE17.8)
      END
```

APPENDIX C

ANISOTROPIC UNDRAINED STRESS-STRAIN MODEL

- COMPUTER PROGRAM

C.1 PROGRAM DESCRIPTION

This computer program utilizes the anisotropic undrained stress-strain model presented in Chapter 4 to compute the deviatoric stresses along an arbitrary strain path for axisymmetric or plane strain problems. The program is coded in FORTRAN IV (double precision).

The input phase consists of two parts:

1. Information specifying the model parameters and the initial conditions. This includes:
   a) the initial radius and the center coordinates of each yield surface along with the initial plastic modulus and a maximum allowable equivalent strain associated to it;
   b) the elastic shear modulus;
   c) the parameters governing changes in size and in plastic moduli of the yield surfaces during plastic flow;
   d) the initial deviatoric stresses, and;
2. Information defining the strain path to be followed. This is achieved by specifying a series of deviatoric strain increment vectors.

For each deviatoric strain increment vector, the program performs the following steps:

(1) Check the loading direction.

(2) Subdivide the strain increment vector into vectors corresponding to the maximum allowable equivalent strain, if necessary.

(3) Compute the deviatoric stress increment vector and update the deviatoric stress vector.

(4) Check if the stress point has crossed the next yield surface.

(5) Update the yield surface parameters.

(6) Print the natural strains, the deviatoric stresses, the current yield surface number and the number of intermediate steps, at the end of each strain increment.

C.2 USER'S MANUAL

C.2.1 MODEL PARAMETERS (UNIT = 5)

CARD 1 (2I5)

Note	Columns	Variable	Entry
(1)	1-5	IN	Device number for strain increment input
(2)	6-10	NY	Number of yield surfaces

CARD 2 (6F10.3)

Note	Columns	Variable	Entry
	1-10	XG	Elastic shear modulus
(3)	11-20	AM	Value of A_m (Eq. 6.13)
(3)	21-30	XLRAT	Value of $H_m'^{\ell}/H_m'^{0}$ (Eq. 6.13)
	31-40	XKOP	Radius of the initial failure surface
	41-50	XKLP	Radius of the residual failure surface
	51-60	AP	Value of A_p (Eq. 6.15)

NOTES:

(1) IN is equal to 5 when the strain increments are input in the same data set.
(2) NY $\leq$ 50
(3) The same value is used for all the yield surfaces.

CARD 3,4,....,(NY + 2) (6F10.3)

Note	Columns	Variable	Entry
	1-10	XA(I,1)	First center coordinate of the I^{th} yield surface
	11-20	XA(I,2)	Second " " " " " " "
	21-30	XA(I,3)	Third " " " " " " "
	31-40	XH(I)	Initial radius of the I^{th} yield surface
	41-50	XH(I)	Initial plastic modulus of the I^{th} yield surface
(1)	51-60	SMAX(I)	Maximum equivalent strain increment to be used in one step

CARD (NY + 3) (4F10.3)

Columns	Variable	Entry
1-10	SIG(1)	Initial value of s_{zz}
11-20	SIG(2)	" " " s_{rr} or s_{xx}
21-30	SIG(3)	" " " $s_{\theta\theta}$ or s_{yy}
31-40	SIG(4)	" " " s_{rz} or s_{xz}

NOTE:

(1) When this field is left blank, the program automatically sets SMAX(I) = 0.0001.

C.2.2 STRAIN PATH INPUT (UNIT = IN)

CARDS 1, 2,....* (4F10.3)

Note	Columns	Variable	Entry
(1)	1-10	DST(1)	$d\varepsilon_{zz}$
(1)	11-20	DST(2)	$d\varepsilon_{rr}$ or $d\varepsilon_{xx}$
(1)	21-30	DST(3)	$d\varepsilon_{\theta\theta}$ or $d\varepsilon_{yy}$
	31-40	DST(4)	$d\varepsilon_{rz}$ or $d\varepsilon_{xz}$

NOTES:

(1) The following equation must be satisfied:

DST(1) + DST(2) + DST(3) = 0

* The program automatically stops after the last card has been read.

C.3 PROGRAM LISTING

```
C     ..................................................................
C     PROGRAM USING PREVOST MODEL TO OBTAIN THE DEVIATORIC STRESSES
C     ALONG AN ARBITRARY STRAINPATH (FOR PLANE-STRAIN AND AXISYMMETRIC
C     UNDRAINED PROBLEMS).
C     PROGRAMMED BY J.N. LEVADOUX                    M.I.T. (APRIL 1979).
C     ..................................................................
      IMPLICIT REAL*8 (A-H,O-Z)
      COMMON /YIELD/ XA(50,3),XK(50),XH(50),XHO(50),SMAX(50),XG,NY,M,NI
      COMMON /STRESS/ SIG(4),SIGD(3),DSIGD(3)
      COMMON /STRAIN/ DST(4),ST(4),DSTD(3),DSAVE(3),DUSE(3),XLAM(50),
     $                AM,XLRAT,XKOP,XKLP,AP
C
C.... INITIALIZE PARAMETERS
C
      M=0
      SUM=0.0D0
      DO 1 I=1,4
    1 ST(I)=0.0D0
      DO 2 I=1,50
    2 XLAM(I)=0.0D0
C
C.... READ MODEL PARAMETERS
C
      READ(5,1001) IN,NY
      READ(5,1000) XG,AM,XLRAT,XKOP,XKLP,AP
      DO 3 I=1,NY
      READ(5,1002) (XA(I,J),J=1,3),XK(I),XH(I),SMAX(I)
      IF (SMAX(I).LE.0.0D0) SMAX(I)=0.0001D0
    3 XHO(I)=XH(I)
C
C.... INPUT INITIAL STRESS DEVIATORS : SZ,SR,ST,SRZ
C
      READ(5,1002) (SIG(I),I=1,4)
      SIGD(1)=SIG(1)*1.5D0
      SIGD(2)=DSQRT(3.0D0)*(SIG(3)-SIG(2))/2.0D0
      SIGD(3)=DSQRT(3.0D0)*SIG(4)
C
C.... READ DEVIATORIC STRAIN INCREMENTS  DEPSZ,DEPSR,DEPST,DEPSRZ
C
      WRITE(6,2001)
    4 READ(IN,1002,END=10) (DST(I),I=1,4)
      DO 5 I=1,4
    5 ST(I)=ST(I)+DST(I)
      SUM=SUM + 100.0D0*DABS(DST(1))
      DSTD(1)=DST(1)
      DSTD(2)=(DST(3)-DST(2))/DSQRT(3.0D0)
      DSTD(3)=2.0D0*DST(4)/DSQRT(3.0D0)
C
C.... COMPUTE DEVIATORIC STRESS INCREMENT
C
      CALL PREVO
C
C.... OUTPUT NEW DEVIATORIC STRESSES
C
      SIG(1) = SIGD(1)/1.5D0
      SIG(2) =-SIGD(2)/DSQRT(3.0D0) - SIGD(1)/3.0D0
      SIG(3) = SIGD(2)/DSQRT(3.0D0) - SIGD(1)/3.0D0
      SIG(4) = SIGD(3)/DSQRT(3.0D0)
      WRITE(6,2000) SUM,ST,SIG,M,NI
      GO TO 4
   10 STOP
 1000 FORMAT(6F10.3)
 1001 FORMAT(2I5)
 1002 FORMAT(6F10.3)
 2000 FORMAT(2X,F10.3,2X,2(1P4E12.3,2X),2I5)
 2001 FORMAT(//6X,'LAMBDA',6X,'EPSZ',8X,'EPSR',8X,'EPST',8X,
     $ 'EPSRZ',8X,'SIGDZ',7X,'SIGDR',7X,'SIGDT',7X,'SIGDRZ',9X,
     $ 'M',3X,'NI'/)
      END
      SUBROUTINE PREVO
C     ..................................................................
C     THIS ROUTINE COMPUTES THE DEVIATORIC STRESS INCREMENTS.
C     ..................................................................
      IMPLICIT REAL*8 (A-H,O-Z)
      COMMON /YIELD/ XA(50,3),XK(50),XH(50),XHO(50),SMAX(50),XG,NY,M,NI
      COMMON /STRESS/ SIG(4),SIGD(3),DSIGD(3)
      COMMON /STRAIN/ DST(4),ST(4),DSTD(3),DSAVE(3),DUSE(3),XLAM(50),
     $                AM,XLRAT,XKOP,XKLP,AP
      DIMENSION DUM(3),P1(3),P2(3),CE(3)
C
C.... INITIALIZE PARAMETERS
C
      NI=0
      ISTOP=0
      DO 1 I=1,3
    1 DSAVE(I)=DSTD(I)
C
C.... CHECK DIRECTION OF LOADING
C
    2 CONTINUE
      IF (ISTOP.EQ.1) RETURN
      NI=NI+1
      VL=0.0D0
      DO 3 I=1,3
      DUSE(I)=DSAVE(I)
      DSAVE(I)=0.0D0
      IF (DABS(DUSE(I)).LT.1.0D-15) GO TO 3
      VL=VL+DUSE(I)*DUSE(I)
    3 CONTINUE
      VL=DSQRT(VL)
      IF (M.EQ.0) GO TO 100
      TEST=0.0D0
      DO 4 I=1,3
    4 TEST=TEST+(SIGD(I)-XA(M,I))*DUSE(I)
      IF (TEST.GT.0.0D0) GO TO 5
      M=0
      GO TO 100
    5 CONTINUE
      IF (VL.LE.SMAX(M)) GO TO 7
      RAT=SMAX(M)/VL
      DO 6 I=1,3
      DSAVE(I)=(1.0D0-RAT)*DUSE(I)
    6 DUSE(I)=RAT*DUSE(I)
      GO TO 8
    7 ISTOP=1
    8 CONTINUE
      IF (M.EQ.NY) GO TO 300
      GO TO 200
C
C.... ELASTIC INCREMENT
```

```
C
  100 CONTINUE
      DO 101 I=1,3
      DSIGD(I)=3.0D0*XG*DUSE(I)
  101 DUM(I)=SIGD(I) + DSIGD(I)
      D=0.0D0
      DO 102 I=1,3
  102 D=D+(DUM(I)-XA(1,I))**2
      D=DSQRT(D)
      IF (D.LT.XK(1)) GO TO 105
      DO 103 I=1,3
      P1(I)=SIGD(I)
      P2(I)=DUM(I)
  103 CE(I)=XA(1,I)
      RAT=RATIO(P1,P2,CE,XK(1))
      DO 104 I=1,3
      DSAVE(I)=DSAVE(I)+(1.0D0-RAT)*DUSE(I)
      DSIGD(I)=RAT*DSIGD(I)
  104 SIGD(I)=SIGD(I) + DSIGD(I)
      M=1
      GO TO 2
  105 CONTINUE
      DO 106 I=1,3
  106 SIGD(I)=DUM(I)
      RETURN
C
C.... ELASTO-PLASTIC INCREMENT
C
  200 CONTINUE
      FACT=0.0D0
      DO 201 I=1,3
  201 FACT=FACT+(SIGD(I)-XA(M,I))*DUSE(I)
      DO 202 I=1,3
  202 DSIGD(I)=3.0D0*XG*DUSE(I) - (3.0D0*XG-1.5D0*XH(M))
     $        *(SIGD(I)-XA(M,I))*FACT/XK(M)**2
      DO 203 I=1,3
  203 DUM(I)=SIGD(I) + DSIGD(I)
      D=0.0D0
      DO 204 I=1,3
  204 D=D+(DUM(I)-XA(M+1,I))**2
      D=DSQRT(D)
      IF (D.LT.XK(M+1)) GO TO 208
      ISTOP=0
      DO 205 I=1,3
      P1(I)=SIGD(I)
      P2(I)=DUM(I)
  205 CE(I)=XA(M+1,I)
      RAT=RATIO(P1,P2,CE,XK(M+1))
      DO 206 I=1,3
      DSAVE(I)=DSAVE(I)+(1.0D0-RAT)*DUSE(I)
      DUSE(I)=RAT*DUSE(I)
      DSIGD(I)=RAT*DSIGD(I)
      IF (DABS(DSIGD(I)).LT.1.0D-10) DSIGD(I)=0.0D0
  206 CONTINUE
      XTEST=0.0D0
      DO 207 I=1,3
  207 XTEST=XTEST+DSIGD(I)**2
      IF (XTEST.GT.1.0D-15) CALL SLIDE
      CALL SOFTEN
      M=M+1
      GO TO 2
  208 XTEST=0.0D0
      DO 209 I=1,3
      IF (DABS(DSIGD(I)).LT.1.0D-15) GO TO 209
      XTEST=XTEST+DSIGD(I)*DSIGD(I)
  209 CONTINUE
      IF (XTEST.GT.1.0D-15) CALL SLIDE
      CALL SOFTEN
      GO TO 2
C
C.... POST FAILURE BEHAVIOR
C
  300 CALL SOFT
      GO TO 2
      END
      FUNCTION RATIO(P1,P2,CE,R)
C     ..................................................................
C     THIS ROUTINE DETERMINES THE INTERSECTION BETWEEN THE STRESS
C     INCREMENT VECTOR AND THE NEXT YIELD SPHERE.
C     ..................................................................
      IMPLICIT REAL*8 (A-H,O-Z)
      DIMENSION P1(3),P2(3),CE(3)
C
      A=0.0D0
      B=0.0D0
      C= - R*R
      DO 1 I=1,3
      A=A+(P2(I)-P1(I))*(P2(I)-P1(I))
      B=B+(P2(I)-P1(I))*(P1(I)-CE(I))
    1 C=C+(P1(I)-CE(I))*(P1(I)-CE(I))
      DELTA=B*B-A*C
      RATIO=0.0D0
      IF (DELTA.GT.0.0D0) RATIO=(-B+DSQRT(DELTA))/A
      RETURN
      END
      SUBROUTINE SLIDE
C     ..................................................................
C     THIS ROUTINE RELOCATES THE YIELD SURFACES AND UPDATES THE
C     DEVIATORIC STRESSES.
C     ..................................................................
      IMPLICIT REAL*8 (A-H,O-Z)
      COMMON /YIELD/ XA(50,3),XK(50),XH(50),XHO(50),SMAX(50),XG,NY,M,NI
      COMMON /STRESS/ SIG(4),SIGD(3),DSIGD(3)
      DIMENSION XMU(3)
C
      XL=XK(M+1)/XK(M)
      DO 1 I=1,3
    1 XMU(I)=XL*(SIGD(I)-XA(M,I)) - (SIGD(I)-XA(M+1,I))
      YA=0.0D0
      YB=0.0D0
      YC=0.0D0
      DO 2 I=1,3
      YA=YA+XMU(I)**2
      YB=YB+(XA(M,I)-SIGD(I)-DSIGD(I))*XMU(I)
    2 YC=YC+2.0D0*(SIGD(I)-XA(M,I))*DSIGD(I)+DSIGD(I)*DSIGD(I)
      DELT=YB*YB-YA*YC
      IF (DELT.GE.0.0D0) GO TO 3
      WRITE(6,2000)
      CALL EXIT
    3 CONTINUE
```

```
      DMU=0.0D0
      IF (YA.EQ.0.0D0.AND.YB.NE.0.0D0.AND.YC.EQ.0.0D0) GO TO 4
      DMU=(-YB-DSQRT(DELT))/YA
    4 CONTINUE
      DO 5 I=1,3
      XA(M,I)=XA(M,I)+DMU*XMU(I)
    5 SIGD(I)=SIGD(I)+DSIGD(I)
      IF (M.EQ.1) RETURN
      MM=M-1
      DO 7 I=1,3
      FACT=(SIGD(I)-XA(M,I))/XK(M)
      DO 6 J=1,MM
    6 XA(J,I)=SIGD(I)-XK(J)*FACT
    7 CONTINUE
      RETURN
 2000 FORMAT(//'  PROBLEM IN SLIDE : REDUCE STRAIN INCREMENT.'//)
      END
      SUBROUTINE SOFT
C     ..................................................................
C     THIS ROUTINE DESCRIBES THE POST-PEAK STRAIN-SOFTENING BEHAVIOR.
C     ..................................................................
      IMPLICIT REAL*8 (A-H,O-Z)
      COMMON /YIELD/ XA(50,3),XK(50),XH(50),XHO(50),SMAX(50),XG,NY,M,NI
      COMMON /STRESS/ SIG(4),SIGD(3),DSIGD(3)
      COMMON /STRAIN/ DST(4),ST(4),DSTD(3),DSAVE(3),DUSE(3),XLAM(50),
     $                AM,XLRAT,XKOP,XKLP,AP
C
C.... UPDATE F(P) AS A FUNCTION OF THE GENERALIZED STRAIN XLAM(NY).
C
      CALL SOFTEN
      OLDK=XK(NY)
      XK(NY)=(XKOP-XKLP)*DEXP(-AP*XLAM(NY)) + XKLP
      XA(NY,1)=XK(NY) - XKLP
      SCALE=XK(NY)/OLDK
C
C.... FIND THE NEW STRESS POINT (NORMALITY RULE).
C
      XLN=0.0D0
      DO 1 I=1,3
      IF (DABS(DUSE(I)).LT.1.0D-15) GO TO 1
      XLN=XLN+DUSE(I)*DUSE(I)
    1 CONTINUE
      XLN=DSQRT(XLN)
      DO 2 I=1,3
    2 SIGD(I)=XA(NY,I) + XK(NY)*DUSE(I)/XLN
C
C.... RELOCATE ALL YIELD SURFACES
C
      NN=NY-1
      DO 4 J=1,NN
      XK(J)=SCALE*XK(J)
      DO 3 I=1,3
    3 XA(J,I)=XA(NY,I)+(1.0D0-XK(J)/XK(NY))*(SIGD(I)-XA(NY,I))
    4 CONTINUE
      RETURN
      END
      SUBROUTINE SOFTEN
C     ..................................................................
C     THIS ROUTINE REDUCES MODULI OF YIELD SURFACES F(1) TO F(M-1).
C     ..................................................................
C
      IMPLICIT REAL*8 (A-H,O-Z)
      COMMON /YIELD/ XA(50,3),XK(50),XH(50),XHO(50),SMAX(50),XG,NY,M,NI
      COMMON /STRAIN/ DST(4),ST(4),DSTD(3),DSAVE(3),DUSE(3),XLAM(50),
     $                AM,XLRAT,XKOP,XKLP,AP
C
      A1=0.0D0
      IF (DABS(DUSE(1)).LT.1.0D-15) GO TO 1
      A1=DUSE(1)*DUSE(1)
    1 A2=0.0D0
      IF (DABS(DUSE(2)).LT.1.0D-15) GO TO 2
      A2=DUSE(2)*DUSE(2)
    2 A3=0.0D0
      IF (DABS(DUSE(3)).LT.1.0D-15) GO TO 3
      A3=DUSE(3)*DUSE(3)
    3 DXL=DSQRT(A1+A2+A3)
      DO 4 I=1,M
      XLAM(I)=XLAM(I)+DXL
      IF (I.EQ.M) GO TO 4
      XH(I)=XHO(I)*DEXP(-AM*XLAM(I))
      TEST=XHO(I)*XLRAT
      IF (XH(I).LT.TEST) XH(I)=TEST
    4 CONTINUE
      RETURN
      END
```

APPENDIX D

SHEAR INDUCED PORE PRESSURE MODEL FOR ANISOTROPIC CLAYS - COMPUTER PROGRAM

D.1 PROGRAM DESCRIPTION

This computer program utilizes the anisotropic shear induced pore pressure model developed and presented in Chapter 5 to compute the shear induced pore pressures along an arbitrary strain path for axisymmetric or plane strain problems. The program is coded in FORTRAN IV (double precision).

The input phase consists of two parts:

1. Information specifying the model parameters. This includes:
   a) the initial center coordinates and the radius of each sphere along with the rate of shear induced pore pressure generation and a maximum allowable equivalent strain associated to it, and;
   b) the maximum shear induced pore pressure that is reached asymptotically in case of unloading, and;
2. Information defining the strain path to be followed. This is achieved by specifying a series of deviatoric strain increment vectors.

For each deviatoric strain increment vector, the program performs the following steps:

(1) Check the loading direction.

(2) Subdivide the strain increment vector into vectors corresponding to the maximum allowable equivalent strain, if necessary.

(3) Compute the shear induced pore pressure increment.

(4) Check if the strain point has crossed the next sphere.

(5) Relocate the appropriate spheres.

(6) Print the natural strains, the shear induced pore pressure, the number of the sphere currently used and the number of intermediate steps, at the end of each strain increment.

D.2 USER'S MANUAL

D.2.1 Model Parameters (UNIT = 5)

CARD 1 (215)

Note	Columns	Variable	Entry
(1)	1-5	NYP	Number of surfaces (spheres)
(2)	5-10	IN	Device number for strain increment input

CARD 2 (F10.3)

Note	Columns	Variable	Entry
(3)	1-10	UMAX	Maximum shear induced excess pore pressure

NOTES:

(1) NYP $\leq$ 50.
(2) IN is equal to 5 when the strain increments are input in the same data set.
(3) See definition of $(\Delta u_s)_{MAX}$ in Section 7.3

CARD 3,4,....,(NY + 2) (6F10.3)

Note	Columns	Variable	Entry
	1-10	XA(I,1)	First center coordinate of the I^{th} sphere
	11-20	XA(I,2)	Second center coordinate of the I^{th} sphere
	21-30	XA(I,3)	Third center coordinate of the I^{th} sphere
	31-40	XKP(I)	Radius of the I^{th} sphere
	41-50	XI(I)	Rate of shear induced pore pressure generation associated to the I^{th} sphere
(1)	51-60	PMAX(I)	Maximum equivalent strain increment to be used in one step

D.2.2 Strain Path Input (UNIT = IN)

CARDS 1,2,....* (4F10.3)

Note	Columns	Variable	Entry
(2)	1-10	DST(1)	$d\varepsilon_{zz}$
(2)	11-20	DST(2)	$d\varepsilon_{rr}$ or $d\varepsilon_{xx}$
(2)	21-30	DST(3)	$d\varepsilon_{\theta\theta}$ or $d\varepsilon_{yy}$
(2)	31-40	DST(4)	$d\varepsilon_{rz}$ or $d\varepsilon_{xz}$

NOTES:

(1) When this field is left blank, the program automatically sets PMAX(I) = 0.001.
(2) The following equation must be satisfied:
DST(1) + DST(2) + DST(3) = 0
* The program automatically stops after the last card has been read.

D.3 PROGRAM LISTING

```
C     ..................................................................
C     PROGRAM TO COMPUTE THE PORE PRESSURES DUE TO SHEAR AS A FUNCTION
C     OF STRAINS.
C     PROGRAMMED BY J.M. LEVADOUX                    M.I.T. (APRIL, 1979).
C     ..................................................................
C
      IMPLICIT REAL*8 (A-H,O-Z)
      COMMON /YPP/ XA(50,3),XKP(50),XI(50),PMAX(50),U,DU,UREF,UMAX,
     $             NYP,M,NI,NREV
      COMMON /STRAIN/ DST(4),ST(4),DSTD(3),STD(3),DSAVE(3),DUSE(3)
C
C.... INITIALIZE PARAMETERS.
C
      UREF=0.0D0
      NREV=0
      M=1
      U=0.0D0
      XLAM=0.0D0
      DO 1 I=1,4
    1 ST(I)=0.0D0
      DO 2 I=1,3
    2 STD(I)=0.0D0
C
C.... READ MODEL PARAMETERS.
C
      READ(5,1000) NYP,IN
      READ(5,1001) UMAX
      WRITE(6,2002) UMAX
      DO 3 I=1,NYP
      READ(5,1001) (XA(I,J),J=1,3),XKP(I),XI(I),PMAX(I)
      IF (PMAX(I).LE.0.0D0) PMAX(I)=0.001D0
    3 CONTINUE
      WRITE(6,2000)
C
C.... READ STRAIN INCREMENT.
C
    4 READ(IN,1001,END=6) DST
      DO 5 I=1,4
    5 ST(I)=ST(I)+DST(I)
      DSTD(1)=DST(1)
      DSTD(2)=(DST(3)-DST(2))/DSQRT(3.0D0)
      DSTD(3)=2.0D0*DST(4)/DSQRT(3.0D0)
C
C.... COMPUTE PORE PRESSURE INCREMENT.
C
      CALL DELU
C
C.... OUTPUT NEW PORE PRESSURE DUE TO SHEAR.
C
      WRITE(6,2001) ST,U,M,NI
      GO TO 4
    6 STOP
 1000 FORMAT(2I5)
 1001 FORMAT(6F10.3)
 2000 FORMAT(////8X,'EPSZ',8X,'EPSX',8X,'EPSY',7X,'EPSXZ',9X,
     1       'DUS',11X,'M',8X,'NI'/)
 2001 FORMAT(2X,1P4E12.3,2X,0PF10.5,2I10)
 2002 FORMAT(//10X,' UMAX = ',F12.5)
      END
      SUBROUTINE DELU
C     ..................................................................
C     THIS ROUTINE COMPUTES THE (SHEAR) PORE PRESSURE INCREMENT.
C     ..................................................................
C
      IMPLICIT REAL*8 (A-H,O-Z)
      COMMON /YPP/ XA(50,3),XKP(50),XI(50),PMAX(50),U,DU,UREF,UMAX,
     $             NYP,M,NI,NREV
      COMMON /STRAIN/ DST(4),ST(4),DSTD(3),STD(3),DSAVE(3),DUSE(3)
      DIMENSION DUM(3),CE(3)
C
C.... INITIALIZE PARAMETERS
C
      NI=0
      ISTOP=0
      DO 1 I=1,3
    1 DSAVE(I)=DSTD(I)
C
C.... CHECK STRAIN INCREMENT VECTOR DIRECTION
C
    2 CONTINUE
      IF (ISTOP.EQ.1) RETURN
      NI=NI+1
      VL=0.0D0
      DO 3 I=1,3
      DUSE(I)=DSAVE(I)
      DSAVE(I)=0.0D0
    3 VL=VL+DUSE(I)*DUSE(I)
      VL=DSQRT(VL)
      IF (M.EQ.1) GO TO 5
      TEST=0.0D0
      DO 4 I=1,3
    4 TEST=TEST+(STD(I)-XA(M,I))*DUSE(I)
      IF (TEST.GE.0.0D0) GO TO 5
C
C.... CHANGE IN STRAINING DIRECTION.
C
      M=1
      NREV=NREV+1
      UREF=U
      GO TO 8
C
C.... NO CHANGE IN STRAINING DIRECTION.
C
    5 CONTINUE
      IF (VL.LE.PMAX(M)) GO TO 7
      RAT=PMAX(M)/VL
      DO 6 I=1,3
      DSAVE(I)=(1.0D0-RAT)*DUSE(I)
    6 DUSE(I)=RAT*DUSE(I)
      GO TO 8
    7 CONTINUE
      ISTOP=1
C
    8 CONTINUE
      IF (NREV.GT.1) RETURN
      DE=0.0D0
      DO 9 I=1,3
    9 DE=DE+DUSE(I)*DUSE(I)
      DE=DSQRT(DE)
      GAMO=0.0D0
```

```
      GAM1=0.0D0
      DO 10 I=1,3
      GAM0=GAM0+STD(I)*STD(I)
      GAM1=GAM1+(STD(I)+DUSE(I))*(STD(I)+DUSE(I))
   10 CONTINUE
      GAM0=DSQRT(GAM0)/DSQRT(2.0D0)
      GAM1=DSQRT(GAM1)/DSQRT(2.0D0)
      DELGAM=GAM1-GAM0
      DU=XRATE(DELGAM)*DELGAM*DSQRT(2.0D0)
      D=0.0D0
      DO 11 I=1,3
      DUM(I)=STD(I)+DUSE(I)
   11 D=D+(DUM(I)-XA(M+1,I))**2
      D=DSQRT(D)
      IF (D.LT.XKP(M+1)) GO TO 15
      DO 12 I=1,3
   12 CE(I)=XA(M+1,I)
      RAT=RATIO(STD,DUM,CE,XKP(M+1))
      ISTOP=0
      XTEST=0.0D0
      DO 13 I=1,3
      DSAVE(I)=DSAVE(I)+(1.0D0-RAT)*DUSE(I)
      DUSE(I)=RAT*DUSE(I)
      IF (DABS(DUSE(I)).LT.1.0D-10) GO TO 13
      XTEST=XTEST+DUSE(I)*DUSE(I)
   13 CONTINUE
      IF (XTEST.GT.1.0D-15) CALL USLIDE
      DU=RAT*DU
      U=U+DU
      IF (U.GT.UMAX) U=UMAX
      M=M+1
      DO 14 I=1,3
      IF (DABS(DUSE(I)).LT.1.0D-10) GO TO 14
      STD(I)=STD(I)+DUSE(I)
   14 CONTINUE
      GO TO 2
   15 CONTINUE
      XTEST=0.0D0
      DO 16 I=1,3
   16 XTEST=XTEST+DUSE(I)*DUSE(I)
      IF (XTEST.GT.1.0D-15) CALL USLIDE
      U=U+DU
      IF (U.GT.UMAX) U=UMAX
      DO 17 I=1,3
   17 STD(I)=STD(I)+DUSE(I)
      GO TO 2
      END
      FUNCTION RATIO(P1,P2,CE,R)
C     ..................................................................
C     THIS ROUTINE FINDS THE INTERSECTION BETWEEN A LINE AND A SPHERE.
C     ..................................................................

      IMPLICIT REAL*8 (A-H,O-Z)
      DIMENSION P1(3),P2(3),CE(3)

      A=0.0D0
      B=0.0D0
      C= - R*R
      DO 1 I=1,3
      A=A+(P2(I)-P1(I))*(P2(I)-P1(I))
      B=B+(P2(I)-P1(I))*(P1(I)-CE(I))
      C=C+(P1(I)-CE(I))*(P1(I)-CE(I))
    1 CONTINUE
      DELTA=B*B-A*C
      RATIO=0.0D0
      IF (DELTA.GT.0.0D0) RATIO=(-B+DSQRT(DELTA))/A
      RETURN
      END
      SUBROUTINE USLIDE
C     ..................................................................
C     THIS ROUTINE RELOCATES THE SURFACES.
C     ..................................................................
C
      IMPLICIT REAL*8 (A-H,O-Z)
      COMMON /YPP/ XA(50,3),XKP(50),XI(50),PMAX(50),U,DU,UREF,UMAX,
     $             NYP,M,NI,NREV
      COMMON /STRAIN/ DST(4),ST(4),DSTD(3),STD(3),DSAVE(3),DUSE(3)
      DIMENSION XMU(3),AUX(3)
C
      IF (M.EQ.1) GO TO 9
      DUM=0.0D0
      DO 1 I=1,3
    1 DUM=DUM+(STD(I)-XA(M,I))**2
      XL=XKP(M+1)/DSQRT(DUM)
      DO 2 I=1,3
    2 XMU(I)=XA(M+1,I)+XL*(STD(I)-XA(M,I))-STD(I)
      YA=0.0D0
      YB=0.0D0
      YC=0.0D0
      DO 3 I=1,3
      YA=YA+XMU(I)**2
      YB=YB+(XA(M,I)-STD(I)-DUSE(I))*XMU(I)
    3 YC=YC+2.0D0*(STD(I)-XA(M,I))*DUSE(I)+DUSE(I)*DUSE(I)
      DELT=YB*YB-YA*YC
      IF (DELT.GE.0.0D0) GO TO 4
      WRITE(6,2000)
      RETURN
    4 CONTINUE
      DMU=0.0D0
      IF (YA.EQ.0.0D0.AND.YB.NE.0.0D0.AND.YC.EQ.0.0D0) GO TO 5
      DMU=(-YB-DSQRT(DELT))/YA
    5 CONTINUE
      DO 6 I=1,3
      XA(M,I)=XA(M,I)+DMU*XMU(I)
    6 AUX(I)=STD(I)+DUSE(I)
      IF (M.EQ.1) RETURN
      MM=M-1
      DO 8 I=1,3
      FACT=(AUX(I)-XA(M,I))/XKP(M)
      DO 7 J=1,MM
      XA(J,I)=AUX(I)-XKP(J)*FACT
    7 CONTINUE
    8 CONTINUE
      RETURN
    9 CONTINUE
      DO 10 I=1,3
      XA(1,I)=XA(1,I)+DUSE(I)
   10 CONTINUE
      RETURN
 2000 FORMAT(//'  PROBLEM IN USLIDE : REDUCE STRAIN INCREMENT.'//)
```

```
      END
      FUNCTION XRATE(DUM)
C     ..................................................................
CC    THIS ROUTINE DETERMINES THE RATE OF PORE PRESSURE SETUP TO BE USED
C     ..................................................................
C
      IMPLICIT REAL*8 (A-H,O-Z)
      COMMON /YPP/ XA(50,3),XKP(50),XI(50),PMAX(50),U,DU,UREF,UMAX,
     $             NYP,M,NI,NREV
C
      XRATE=XI(M)*(UMAX-UREF)/UMAX
      IF (DUM.LT.0.0D0) XRATE=-XRATE
      RETURN
      END
```

APPENDIX E

DETERMINATION OF TOTAL STRESSES FOR THE CONE PENETRATION PROBLEM

E.1 INTRODUCTION

This appendix describes a numerical method for obtaining the field of octahedral total normal stress, σ_{oct} from the field of deviatoric stresses, s_{ij}, by integrating the equilibrium equations. The strain path method leads, in general, to a total stress field which does not satisfy total stress equilibrium and thus, integration of the equilibrium equations is path dependent (see Appendix A). In order to assess the path dependency, integration is performed by two methods: the first method performs integration along isochronic lines,* whereas the second performs integration along streamlines. Comparison of results obtained by the two methods will provide valuable information in order to evaluate deviations form total stress equilibrium. The computer programs necessary to perform numerical integration according to the two methods are listed at the end of this appendix.

E.2 METHOD OF SOLUTION

The total stress equilibrium equations in cylindrical coordinates for the case of axial symmetry without body forces are given by:

---

*An isochronic line is the locus (at a given time) of particles initially located on an horizontal line (normal to the shaft axis).

$$\left.\begin{aligned} \frac{\partial \sigma_r}{\partial r} + \frac{\partial \sigma_{rz}}{\partial z} + \frac{\sigma_r - \sigma_\theta}{r} &= 0 \\ \frac{\partial \sigma_{rz}}{\partial r} + \frac{\partial \sigma_z}{\partial z} + \frac{\sigma_{rz}}{r} &= 0 \end{aligned}\right\} \qquad \text{(E.1)}$$

The total stress σ_{ij} can be expressed in terms of the deviatoric stress s_{ij} and the octahedral total normal stress σ_{oct} by:

$$\sigma_{ij} = s_{ij} + \sigma_{oct} \qquad \text{(E.2)}$$

Substituting Eq. .2 into Eqs. E.1 and rearranging terms, the equilibrium in the radial (r) and vertical (z) directions at any point, in the deformed geometry, are given by:

$$\left.\begin{aligned} \frac{\partial \sigma_{oct}}{\partial r} &= -\frac{\partial s_r}{\partial r} - \frac{\partial s_{rz}}{\partial z} - \frac{s_r - s_\theta}{r} \\ \frac{\partial \sigma_{oct}}{\partial z} &= -\frac{\partial s_{rz}}{\partial r} - \frac{\partial s_z}{\partial z} - \frac{s_{rz}}{r} \end{aligned}\right\} \qquad \text{(E.3)}$$

Figure E.1 illustrate the two integration paths. When integration is performed along isochronic lines (Fig. E.1.a) the value of σ_{oct} is known in the far field ($r \to \infty$) and integration proceeds in the direction of decreasing r. On the other hand, when integration is performed along stream-streamlines (Fig. E.1.b) the value of σ_{oct} is known in the far field ($z \to -\infty$) and integration process in the direction of increasing z.

In both methods, a central difference iterative integration scheme is used. The value of the octahedral stress at point M_{k+1}, $(\sigma_{oct})^{k+1}$, is obtained from $(\sigma_{oct})^{k}$ by means of the equation:

$$(\sigma_{oct})^{k+1} = (\sigma_{oct})^{k} + \frac{\partial \sigma_{oct}}{\partial r} dr + \frac{\partial \sigma_{oct}}{\partial z} dz \qquad (E.4)$$

in which $\frac{\partial \sigma_{oct}}{\partial r}$ and $\frac{\partial \sigma_{oct}}{\partial z}$ are the partial derivatives of the octahedral stress evaluated at point C_k (see Fig. E.1) and dr and dz are related to the coordinates of the points M_k and M_{k+1} by:

$$dr = r_{k+1} - r_k \; ; \quad dz = z_{k+1} - z_k \qquad (E.5)$$

E.3 ISOPARAMETRIC ELEMENT AND INTERPOLATION FUNCTIONS

Evaluation of the various terms in Eq. E.3 at location C_k in Fig. E.1 is carried out by considering a nine node isoparametric element, shown in Fig. E.2, similar to that used in some finite element formulations (e.g., Bathe and Wilson, 1976).

The basic procedure consists of expressing the element coordinates and field functions in the form of interpolations using the natural coordinate system (s,t) of the element. The coordinates interpolations are given by:

$$r(s,t) = \Sigma \, h_i(s,t) \cdot r_i \; ; \; z(s,t) = \Sigma \, h_i(s,t) \cdot z_i \qquad (E.6)$$

in which $h_i(s,t)$ are the interpolation functions given in Table E.1, and r_i and z_i are the physical coordinates at node i.

The isoparametric element shown in Fig. E.2 consists of nine nodes (1 through 9) where the values of the deviatoric stresses, s_{ij}, are known and of 4 nodes (a, b, c and d) where the right hand sides of Eqs. E.3 are numerically evaluated. The relative locations of the points M_k, M_{k+1} and C_k (in Fig. E.1) in the isoparameteric element are given in Table E.2 as a function of the method of integration utilized.

The parabolic interpolation of a field function g in terms of its values g_i at node (i = 1, 2, ..., 9) is given by:

$$g(s,t) = \sum h_i(s,t) \cdot g_i \tag{E.7}$$

After partial differentiation with respect to s and t, Eq. .7 leads to:

$$\begin{aligned} \frac{\partial g(s,t)}{\partial s} &= \sum \frac{\partial h_i(s,t)}{\partial s} \cdot g_i \\ \frac{\partial g(s,t)}{\partial t} &= \sum \frac{\partial h_i(s,t)}{\partial t} \cdot g_i \end{aligned} \tag{E.8}$$

In order to obtain the partial derivatives of g in terms of the physical coordinates, the chain rule of differentation is used:

$$\left.\begin{aligned} \frac{\partial g}{\partial z} &= \frac{\partial g}{\partial s}\frac{\partial s}{\partial z} + \frac{\partial g}{\partial t}\frac{\partial t}{\partial z} \\ \frac{\partial g}{\partial r} &= \frac{\partial g}{\partial s}\frac{\partial s}{\partial r} + \frac{\partial g}{\partial t}\frac{\partial t}{\partial r} \end{aligned}\right\} \tag{E.9}$$

This equation can be written as:

$$\begin{bmatrix} \frac{\partial g}{\partial z} \\ \\ \frac{\partial g}{\partial r} \end{bmatrix} = [J]^{-1} \begin{bmatrix} \frac{\partial g}{\partial s} \\ \\ \frac{\partial g}{\partial t} \end{bmatrix} \qquad \text{(E.10)}$$

in which $[J]^{-1}$ can be readily evaluated by inversion of the Jacobian operator [J] given by:

$$[J] = \begin{bmatrix} \frac{\partial z}{\partial s} & \frac{\partial r}{\partial s} \\ \\ \frac{\partial z}{\partial t} & \frac{\partial r}{\partial t} \end{bmatrix} \qquad \text{(E.11)}$$

In summary, evaluation of the partial derivatives of the octahedral total normal stress σ_{oct} at point C_k proceeds as follows:

1) evaluate s_r, s_θ, s_{rz} and r at C_k (a, b, c, or d in Fig. E.2) using Eqs. E.6 and E.7 together with the known values of the parameters at the 9 adjacent nodes and the numerical values given in Table E.3.a;

2) evaluate and invert the Jacobian at C_k (Eq. E.11);

3) evaluate the partial derivatives with respect to s and t of s_r, s_z and s_{rz} at C_k using Eqs. E.8 and the numerical values given in Table E.3.a and b, and ;

4) evaluate $\frac{\partial \sigma_r}{\partial r}$, $\frac{\partial \sigma_{rz}}{\partial z}$, $\frac{\partial \sigma_{rz}}{\partial r}$ and $\frac{\partial \sigma_z}{\partial z}$ using the results of 2) and 3) and Eq. E.10.

E.4 COMPUTER PROGRAMS: LISTINGS

E.4.1 Integration along Isochronic Lines

```
C     ..................................................................
C     THIS PROGRAM UTILIZES A CENTRAL DIFFERENCE INTEGRATION SCHEME TO
C     DETERMINE THE FIELD OF SIGMA OCTAHEDRAL.
C     INTEGRATION IS CARRIED OUT IN THE R (RADIAL) DIRECTION.
C     PROGRAMED BY J.N. LEVADOUX                      M.I.T.  (MAY, 1979)
C     ..................................................................
C
      DIMENSION DSIG(3,5,389),R(3,389),Z(3,389),DUM(3)
      COMMON DS(9,4),RR(9),ZZ(9)
C
      READ(5,1000) NFL,NEQ
      READ(5,1001) (Z(2,I),R(2,I),(DSIG(2,J,I),J=1,5),I=1,NEQ)
      READ(5,1001) (Z(3,I),R(3,I),(DSIG(3,J,I),J=1,5),I=1,NEQ)
C
      DO 7 N=1,NFL
C
      DO 3 K=1,2
      DO 2 I=1,NEQ
      Z(K,I)=Z(K+1,I)
      R(K,I)=R(K+1,I)
      DO 1 J=1,5
    1 DSIG(K,J,I)=DSIG(K+1,J,I)
    2 CONTINUE
    3 CONTINUE
C
      READ(9,1002) (Z(3,II),R(3,II),(DSIG(3,JJ,II),JJ=1,4),II=1,NEQ)
C
      NEQ1=NEQ-1
C
      DO 6 L=2,NEQ1
C
      RR(1)=R(1,L+1)
      RR(2)=R(1,L-1)
      RR(3)=R(3,L-1)
      RR(4)=R(3,L+1)
      RR(5)=R(1,L)
      RR(6)=R(2,L-1)
      RR(7)=R(3,L)
      RR(8)=R(2,L+1)
      RR(9)=R(2,L)
C
      ZZ(1)=Z(1,L+1)
      ZZ(2)=Z(1,L-1)
      ZZ(3)=Z(3,L-1)
      ZZ(4)=Z(3,L+1)
      ZZ(5)=Z(1,L)
      ZZ(6)=Z(2,L-1)
      ZZ(7)=Z(3,L)
      ZZ(8)=Z(2,L+1)
      ZZ(9)=Z(2,L)
C
      DO 4 JN=1,4
      DS(1,JN)=DSIG(1,JN,L+1)
      DS(2,JN)=DSIG(1,JN,L-1)
      DS(3,JN)=DSIG(3,JN,L-1)
      DS(4,JN)=DSIG(3,JN,L+1)
      DS(5,JN)=DSIG(1,JN,L)
      DS(6,JN)=DSIG(2,JN,L-1)
      DS(7,JN)=DSIG(3,JN,L)
      DS(8,JN)=DSIG(2,JN,L+1)
    4 DS(9,JN)=DSIG(2,JN,L)
C
      CALL DIFF(DMEAN)
C
      DSIG(3,5,L)=DSIG(2,5,L)+DMEAN
C
      DO 5 JN=1,3
    5 DUM(JN)=DSIG(3,JN,L) + DSIG(3,5,L)
C
      WRITE(10,2000) Z(3,L),R(3,L),(DUM(JJ),JJ=1,3),DSIG(3,4,L),
     $ DSIG(3,5,L)
    6 CONTINUE
C
    7 CONTINUE
      STOP
 1000 FORMAT(2I5)
 1001 FORMAT(7F10.3)
 1002 FORMAT(6F10.3)
 2000 FORMAT(0PF10.5,0PF10.6,1P5E10.3)
      END
      SUBROUTINE DIFF(DMEAN)
C
      COMMON DS(9,4),R(9),Z(9)
      DIMENSION CO(9,2),XH(9),XJ(2,2),XJI(2,2)
      DATA CO /-0.0625,0.0625,-0.1875,0.1875,0.0,-0.375,0.0,0.375,0.0,
     $         0.0,0.0,0.0,0.0,0.0,0.0,0.0,-1.0,0.0,1.0/
      DATA XH /0.0,0.0,0.0,0.0,-0.125,0.0,0.375,0.0,0.75/
C
C.... COMPUTE JACOBIAN AT THE PRESCRIBED NODE
C
      DO 1 I=1,2
      DO 1 J=1,2
    1 XJ(I,J)=0.0
C
      DO 2 I=1,9
      XJ(1,1)=XJ(1,1)+Z(I)*CO(I,1)
      XJ(1,2)=XJ(1,2)+R(I)*CO(I,1)
      XJ(2,1)=XJ(2,1)+Z(I)*CO(I,2)
    2 XJ(2,2)=XJ(2,2)+R(I)*CO(I,2)
C
C.... INVERT JACOBIAN
C
      DET=XJ(1,1)*XJ(2,2) - XJ(1,2)*XJ(2,1)
      IF (DET.NE.0.0) GO TO 3
      WRITE(6,2000)
      CALL EXIT
C
    3 XJI(1,1)=XJ(2,2)/DET
      XJI(1,2)=-XJ(1,2)/DET
      XJI(2,1)=-XJ(2,1)/DET
      XJI(2,2)=XJ(1,1)/DET
C
C.... COMPUTE IN SEQUENCE : DSR/DR, DSRZ/DZ, DSRZ/DR, AND DSZ/DZ
C
      DRS=0.0
      DRT=0.0
      DRZS=0.0
      DRZT=0.0
      DZS=0.0
      DZT=0.0
```

```
C
      DO 4 I=1,9
      DRS=DRS + DS(I,2)*CO(I,1)
      DRT=DRT + DS(I,2)*CO(I,2)
      DRZS=DRZS + DS(I,4)*CO(I,1)
      DRZT=DRZT + DS(I,4)*CO(I,2)
      DZS=DZS + DS(I,1)*CO(I,1)
      DZT=DZT + DS(I,1)*CO(I,2)
    4 CONTINUE
C
      D1=DRS*XJI(2,1) + DRT*XJI(2,2)
      D2=DRZS*XJI(1,1) + DRZT*XJI(1,2)
      D3=DRZS*XJI(2,1) + DRZT*XJI(2,2)
      D4=DZS*XJI(1,1) + DZT*XJI(1,2)
C
C.... EVALUATE R, SR, ST, AND SRZ AT PRESCRIBED NODE
C
      RR=0.0
      SR=0.0
      ST=0.0
      SRZ=0.0
C
      DO 5 I=1,9
      RR=RR+R(I)*XH(I)
      SR=SR+DS(I,2)*XH(I)
      ST=ST+DS(I,3)*XH(I)
    5 SRZ=SRZ+DS(I,4)*XH(I)
C
      DSIGR=-D1-D2-(SR-ST)/RR
      DSIGZ=-D3-D4-SRZ/RR
C
      DELR=R(7)-R(9)
      DELZ=Z(7)-Z(9)
C
      DMEAN=DSIGR*DELR+DSIGZ*DELZ
      RETURN
 2000 FORMAT(//10X,'****  DET. OF JACOBIAN = 0.0 ****'//)
      END
```

E.4.2 Integration along Streamlines

```
C     ..................................................................
C     THIS PROGRAM UTILIZES A CENTRAL DIFFERENCE INTEGRATION SCHEME TO
C     DETERMINE THE FIELD OF SIGMA OCTAHEDRAL.
C     INTEGRATION IS CARRIED OUT IN THE Z (VERTICAL) DIRECTION.
C     PROGRAMED BY J.N. LEVADOUX                    M.I.T.  (MAY, 1979)
C     ..................................................................
C
      DIMENSION DSIG(3,5,46),R(3,46),Z(3,46),DUM(3,46)
      COMMON  DS(9,4),RR(9),ZZ(9)
C
      READ(5,1000) NFL,NEQ
      READ(5,1001) (Z(2,I),R(2,I),(DSIG(2,J,I),J=1,5),I=1,NFL)
      READ(9,1002) (Z(3,I),R(3,I),(DSIG(3,J,I),J=1,4),I=1,NFL)
C
      DO 1 I=1,NFL
    1 DSIG(3,5,I)=DSIG(2,5,I)
C
      NEQ1=NEQ-1
C
      DO 9 N=2,NEQ1
      DO 4 K=1,2
      DO 3 I=1,NFL
      Z(K,I)=Z(K+1,I)
      R(K,I)=R(K+1,I)
      DO 2 J=1,5
    2 DSIG(K,J,I)=DSIG(K+1,J,I)
    3 CONTINUE
    4 CONTINUE
C
      READ(9,1002) (Z(3,II),R(3,II),(DSIG(3,JJ,II),JJ=1,4),II=1,NFL)
C
      DO 6 L=1,NFL
      NODE=2
      IF (L.EQ.1) NODE=3
      IF (L.EQ.NFL) NODE=1
      M=NODE-1
C
      RR(1)=R(3,L+M)
      RR(2)=R(1,L+M)
      RR(3)=R(1,L+M-2)
      RR(4)=R(3,L+M-2)
      RR(5)=R(2,L+M)
      RR(6)=R(1,L+M-1)
      RR(7)=R(2,L+M-2)
      RR(8)=R(3,L+M-1)
      RR(9)=R(2,L+M-1)
C
      ZZ(1)=Z(3,L+M)
      ZZ(2)=Z(1,L+M)
      ZZ(3)=Z(1,L+M-2)
      ZZ(4)=Z(3,L+M-2)
      ZZ(5)=Z(2,L+M)
      ZZ(6)=Z(1,L+M-1)
      ZZ(7)=Z(2,L+M-2)
      ZZ(8)=Z(3,L+M-1)
      ZZ(9)=Z(2,L+M-1)
C
      DO 5 JN=1,4
      DS(1,JN)=DSIG(3,JN,L+M)
      DS(2,JN)=DSIG(1,JN,L+M)
      DS(3,JN)=DSIG(1,JN,L+M-2)
      DS(4,JN)=DSIG(3,JN,L+M-2)
      DS(5,JN)=DSIG(2,JN,L+M)
      DS(6,JN)=DSIG(1,JN,L+M-1)
      DS(7,JN)=DSIG(2,JN,L+M-2)
      DS(8,JN)=DSIG(3,JN,L+M-1)
    5 DS(9,JN)=DSIG(2,JN,L+M-1)
C
      CALL DIFF(DMEAN,NODE)
      DSIG(3,5,L)=DSIG(2,5,L)+DMEAN
    6 CONTINUE
C
      DO 8 L=1,NFL
      DO 7 JN=1,3
    7 DUM(JN,L)=DSIG(3,JN,L) + DSIG(3,5,L)
      WRITE(10,2000) Z(3,L),R(3,L),(DUM(JJ,L),JJ=1,3),DSIG(3,4,L),
     $ DSIG(3,5,L)
    8 CONTINUE
C
    9 CONTINUE
      STOP
 1000 FORMAT(2I5)
 1001 FORMAT(7F10.3)
 1002 FORMAT(6F10.3)
 2000 FORMAT(0PF10.5,0PF10.6,1P5E10.3)
      END
      SUBROUTINE DIFF(DMEAN,NODE)
C
      COMMON  DS(9,4),R(9),Z(9)
      DIMENSION CO(9,2,3),XH(9,3),XJ(2,2),XJI(2,2)
C
      DATA CO /1.0,0.0,0.0,0.0,-1.0,0.0,0.0,0.0,0.0,
     $ 0.5625,-0.1875,-0.0625,0.1875,1.125,0.25,0.375,-0.75,-1.5,
     $ 0.0,0.0,0.0,0.0,0.0,0.0,0.0,0.0,0.0,1.0,-1.0,
     $ 0.1875,-0.0625,0.0625,-0.1875,0.375,0.0,-0.375,0.0,0.0,
     $ 0.0,0.0,0.0,1.0,0.0,0.0,0.0,-1.0,0.0,0.0,0.0,
     $ -0.1875,0.0625,0.1875,-0.5625,-0.375,-0.25,-1.125,0.75,1.5/
      DATA XH /0.375,-0.125,0.0,0.0,0.75,0.0,0.0,0.0,0.0,0.0,
     $ 0.0,0.0,0.0,0.0,0.0,0.0,-0.125,0.0,0.375,0.75,
     $ 0.0,0.0,-0.125,0.375,0.0,0.0,0.0,0.75,0.0,0.0/
C
C.... COMPUTE JACOBIAN AT THE PRESCRIBED NODE
C
      DO 1 I=1,2
      DO 1 J=1,2
    1 XJ(I,J)=0.0
C
      DO 2 I=1,9
      XJ(1,1)=XJ(1,1)+Z(I)*CO(I,1,NODE)
      XJ(1,2)=XJ(1,2)+R(I)*CO(I,1,NODE)
      XJ(2,1)=XJ(2,1)+Z(I)*CO(I,2,NODE)
    2 XJ(2,2)=XJ(2,2)+R(I)*CO(I,2,NODE)
C
C.... INVERT JACOBIAN
C
      DET=XJ(1,1)*XJ(2,2) - XJ(1,2)*XJ(2,1)
      IF (DET.NE.0.0) GO TO 3
      WRITE(6,2000)
      CALL EXIT
C
```

```
    3 XJI(1,1)=XJ(2,2)/DET
      XJI(1,2)=-XJ(1,2)/DET
      XJI(2,1)=-XJ(2,1)/DET
      XJI(2,2)=XJ(1,1)/DET
C
C.... COMPUTE IN SEQUENCE : DSR/DR, DSRZ/DZ, DSRZ/DR, AND DSZ/DZ
C
      DRS=0.0
      DRT=0.0
      DRZS=0.0
      DRZT=0.0
      DZS=0.0
      DZT=0.0
C
      DO 4 I=1,9
      DRS=DRS + DS(I,2)*CO(I,1,NODE)
      DRT=DRT + DS(I,2)*CO(I,2,NODE)
      DRZS=DRZS + DS(I,4)*CO(I,1,NODE)
      DRZT=DRZT + DS(I,4)*CO(I,2,NODE)
      DZS=DZS + DS(I,1)*CO(I,1,NODE)
      DZT=DZT + DS(I,1)*CO(I,2,NODE)
    4 CONTINUE
C
      D1=DRS*XJI(2,1) + DRT*XJI(2,2)
      D2=DRZS*XJI(1,1) + DRZT*XJI(1,2)
      D3=DRZS*XJI(2,1) + DRZT*XJI(2,2)
      D4=DZS*XJI(1,1) + DZT*XJI(1,2)
C
C.... EVALUATE R, SR, ST, AND SRZ AT PRESCRIBED NODE
C
      RR=0.0
      SR=0.0
      ST=0.0
      SRZ=0.0
C
      DO 5 I=1,9
      RR=RR+R(I)*XH(I,NODE)
      SR=SR+DS(I,2)*XH(I,NODE)
      ST=ST+DS(I,3)*XH(I,NODE)
    5 SRZ=SRZ+DS(I,4)*XH(I,NODE)
C
      GO TO (6,7,8), NODE
    6 DELR=R(1)-R(5)
      DELZ=Z(1)-Z(5)
      GO TO 9
    7 DELR=R(8)-R(9)
      DELZ=Z(8)-Z(9)
      GO TO 9
    8 DELR=R(4)-R(7)
      DELZ=Z(4)-Z(7)
C
    9 CONTINUE
      DSIGR=-D1-D2-(SR-ST)/RR
      DSIGZ=-D3-D4-SRZ/RR
C
      DMEAN=DSIGR*DELR+DSIGZ*DELZ
      RETURN
 2000 FORMAT(//10X,'****  DET. OF JACOBIAN = 0.0 ****'//)
      END
```

i	g_i	$\frac{\partial g_i}{\partial s}$	$\frac{\partial g_i}{\partial t}$
1	$\frac{1}{4}\,st(1+s)(1+t)$	$\frac{1}{4}\,t(1+t)(1+2s)$	$\frac{1}{4}\,s(1+s)(1+2t)$
2	$-\frac{1}{4}\,st(1-s)(1+t)$	$-\frac{1}{4}\,t(1+t)(1-2s)$	$-\frac{1}{4}\,s(1-s)(1+2t)$
3	$\frac{1}{4}\,st(1-s)(1-t)$	$\frac{1}{4}\,t(1-t)(1-2s)$	$\frac{1}{4}\,s(1-s)(1-2t)$
4	$-\frac{1}{4}\,st(1+s)(1-t)$	$-\frac{1}{4}\,t(1-t)(1+2s)$	$-\frac{1}{4}\,s(1+s)(1-2t)$
5	$\frac{1}{2}\,t(1-s^2)(1+t)$	$-\frac{1}{2}\,st(1+t)$	$\frac{1}{2}\,(1-s^2)(1+2t)$
6	$-\frac{1}{2}\,s(1-s)(1-t^2)$	$-\frac{1}{2}\,(1-t^2)(1-2s)$	$st\,(1-s)$
7	$-\frac{1}{2}\,t(1-s^2)(1-t)$	$st(1-t)$	$-\frac{1}{2}\,(1-s^2)(1-2t)$
8	$\frac{1}{2}\,s(1+s)(1-t^2)$	$\frac{1}{2}\,(1-t^2)(1+2s)$	$-\,st(1+s)$
9	$(1-s^2)(1-t^2)$	$-\,2s(1-t^2)$	$-\,2\,t(1-s^2)$

Table E.1 Interpolation Functions and Their Derivatives

Method of Integration	M_k	M_{k+1}	C_k
along isochronic lines	9	7	d
along streamlines			
outmost streamline	5	1	a
central streamline	9	8	b
inmost streamline	7	4	c

Table E.2 Relative Location of the 9 Node Isoparametric Element for Different integration Methods

a)

Node	g								
	g_1	g_2	g_3	g_4	g_5	g_6	g_7	g_8	g_9
a	$\frac{3}{8}$	$-\frac{1}{8}$	0	0	$\frac{3}{4}$	0	0	0	0
b	0	0	0	0	0	$-\frac{1}{8}$	0	$\frac{3}{8}$	$\frac{3}{4}$
c	0	0	$-\frac{1}{8}$	$\frac{3}{8}$	0	0	$\frac{3}{4}$	0	0
d	0	0	0	0	$-\frac{1}{8}$	0	$\frac{3}{8}$	0	$\frac{3}{4}$

b)

Node	$\frac{\partial g}{\partial s}$								
	g_1	g_2	g_3	g_4	g_5	g_6	g_7	g_8	g_9
a	1	0	0	0	- 1	0	0	0	0
b	0	0	0	0	0	0	0	1	- 1
c	0	0	0	1	0	0	- 1	0	0
d	$-\frac{1}{16}$	$\frac{1}{16}$	$-\frac{3}{16}$	$\frac{3}{16}$	0	$-\frac{3}{6}$	0	$\frac{3}{8}$	0

c)

Node	$\frac{\partial g}{\partial t}$								
	g_1	g_2	g_3	g_4	g_5	g_6	g_7	g_8	g_9
a	$\frac{9}{16}$	$-\frac{3}{16}$	$-\frac{1}{16}$	$\frac{3}{16}$	$\frac{9}{8}$	$\frac{1}{4}$	$\frac{3}{8}$	$-\frac{3}{4}$	$-\frac{3}{2}$
b	$\frac{3}{16}$	$-\frac{1}{16}$	$\frac{1}{16}$	$-\frac{3}{16}$	$\frac{3}{8}$	0	$-\frac{3}{8}$	0	0
c	$-\frac{3}{16}$	$\frac{1}{16}$	$\frac{3}{16}$	$-\frac{9}{16}$	$-\frac{3}{8}$	$-\frac{1}{4}$	$-\frac{9}{8}$	$\frac{3}{4}$	$\frac{3}{2}$
d	0	0	0	0	0	0	- 1	0	1

Table E.3 Values of Interpolations Functions and Their Derivatives at the Nodes of Interest.

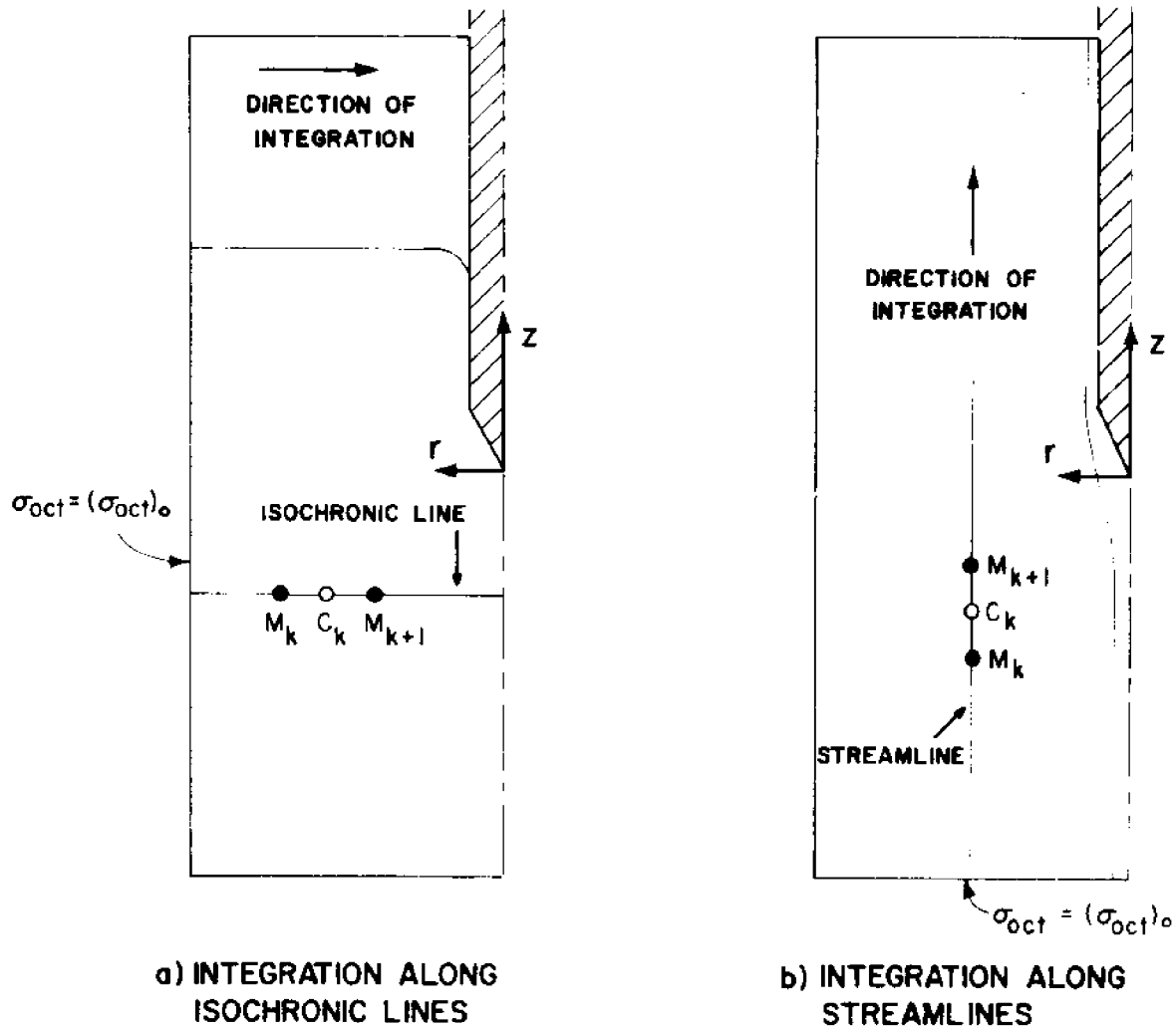

Figure E.1 Integration schemes.

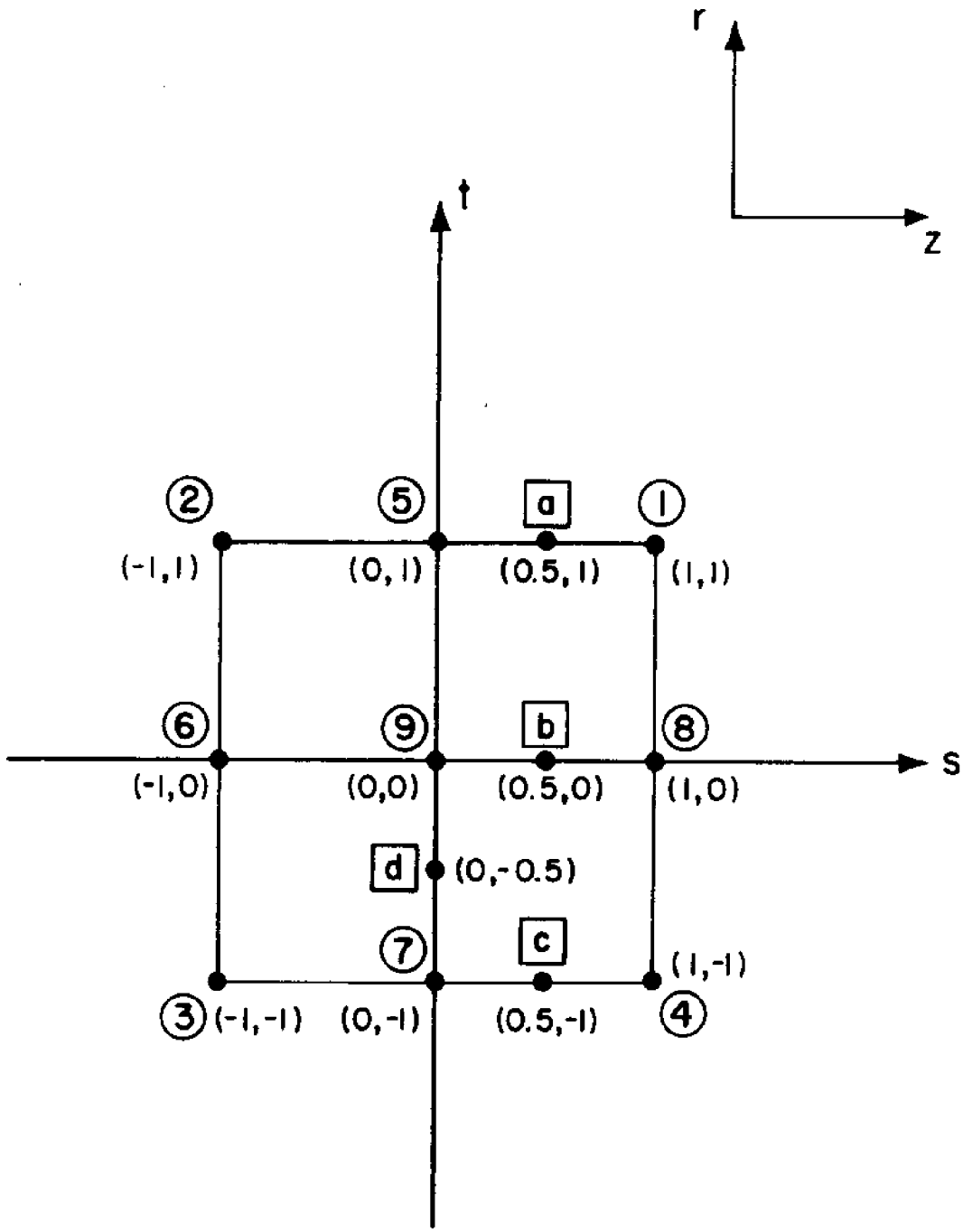

NOTE: Point coordinates are indicated in parentheses

Figure E.2 Isoparametric element.